UNIVERSITY OF CALIFORNIA

Santa Barbara

Bio-Inspired Adhesion, Friction and Lubrication

A dissertation submitted in partial satisfaction of the

requirements for the degree Doctor of Philosophy

in

Chemical Engineering

by

Saurabh Basudeb Das

Committee in charge:

Professor Jacob N. Israelachvili, Chair

Professor Todd M. Squires

Professor Michael J. Gordon

Professor Kimberly L. Turner

December 2014

The dissertation of Saurabh Basudeb Das is approved.

_____

Professor Todd M. Squires

_____

Professor Michael J. Gordon

_____

Professor Kimberly L. Turner

_____

Professor Jacob N. Israelachvili, Chair

December 2014

Bio-Inspired Adhesion, Friction and Lubrication

ACKNOWLEDGEMENTS

During my stint as a doctoral researcher at UCSB, I investigated multiple problems in interfacial science and engineering along with collaborators from mechanical engineering, materials science, chemistry, and molecular and marine biology. All this would have not been possible without the support and guidance of my PhD advisor Prof. Jacob Israelachvili. He encouraged and cultivated a collaborative research environment in his group and this has immensely contributed to my success as a PhD student. He taught me to ask the right questions and I express my gratitude and respect to him for enabling me to grow as a Scientist.

I would also like to thank my many other lab members who supported me from a professional perspective. I am grateful to Travers Anderson, Stephen Donaldson, Xavier Banquy, Wren Greene and Jing Yu who taught me the SFA technique. I worked together with Nadine Martinez, Nick Cadirov and Kollbe Ahn on many different projects and resolved technical and scientific challenges efficiently in matters of weeks. I am thankful to Wei Wei and Dusty Miller for providing mussel foot proteins and peptides. I greatly appreciate the company of my very close friends (and colleague) Himanshu Mishra and Yair Kaufman for their support and advice. I am thankful to Sandy Chen, Alex Schrader and Dong Woog Lee who made work for me a fun-filled and an entertaining experience.

Many thanks to Kai Kristiansen and Greg Carver who helped me troubleshoot technical problems with the instruments in the lab. Nancy Emerson was my guardian in the States and I appreciate all her support for numerous occasions. Prof. Herbert Waite gave countless suggestions and insightful thoughts into the biochemistry aspect of my research. I want to thank my committee members, Prof. Todd Squires, Prof. Mike Gordon and Prof.

Kim Turner for taking the time to review my research progress annually and providing helpful suggestions.

I dedicate this Dissertation to my parents and cannot thank them enough for all of their love and support during my PhD studies and throughout my life. I am grateful to all of my local and international friends at UCSB with whom I share many sweet memories for years to come, esp., with Rodrigo Nery Azevedo and Aviel Chaimovich.

Finally I thank the funding agencies: Procter & Gamble, Institute of Collaborative Biotechnologies, National Institute of Health and The Department of Energy.

VITA of SAURABH BASUDEB DAS

December, 2014

EDUCATION

2009 Bachelor of Chemical Engineering
Chemical Engineering
University Institute of Chemical Technology, Mumbai

2014 Doctor of Philosophy
Chemical Engineering
University of California, Santa Barbara

PEER-REVIEWED JOURNAL ARTICLES

Das, S.; Rodriguez, N. R. M.; Wei, W.; Waite, J. H.; Israelachvili, J. N. Peptide length and Dopa Contribution to Metal Mediated Chelation of Peptides. *Submitted* **2014**.

Das, S.; Miller, D. R.; Kaufman, Y.; Rodriguez, N. R. M.; Israelachvili, J.; Waite, J. H. Tough Coating proteins: Subtle Sequence Variation Modulates Cohesion. *Submitted* **2014**.

Das, S.; Miller, D. R.; Huang, K. Y.; Han, S.; Israelachvili, J.; Waite, J. H. Mussel-Inspired Complex Coacervate Provide Enhanced Wear Protection to Surfaces. *Submitted* **2014**.

Das, S.; Cadirov, N.; Chary, S.; Kaufman, Y.; Hogan, J.; Turner, K.; Israelachvili, J. Stick-slip Friction of Gecko Mimetic Flaps on Smooth and Rough Surfaces. *Submitted* **2014**.

Das, S.; Ahn, B. K.; Rodriguez, N. R. M.; Rinstadt, R.; Kaufman, Y.; Kesselman, E.; Mirshafian, R.; Lipshutz, B.; Talmon, Y.; Israelachvili, J.; Waite, J. H. Small Molecular Underwater Adhesives Inspired by Mussel Foot Proteins. *Submitted* **2014**.

Rodriguez, N. R. M.; **Das, S.**; Kaufman, Y.; Israelachvili, J.; Waite, J. H. Interfacial pH During Mussel Adhesive Plaque Formation. *Submitted* **2014**.

Rodriguez, N. R. M.; **Das, S.**; Kaufman, Y.; Wei, W.; Israelachvili, J.; Waite, J. H. Mussel adhesive protein provides cohesive matrix for collagen type-1α. *Biomaterials (accepted)* **2014**.

Lee, D. W.; Banquy, X.; **Das, S.**; Cadirov, N.; Jay, G.; Israelachvili, J. Effects of Molecular Weight of Grafted Hyaluronic Acid on Wear Initiation. *Acta Biomater* **2014,** *10* (5), 1817-1823.

Banquy, X.; Lee, D. W.; **Das, S.**; Hogan, J.; Israelachvili, J. N. Shear-Induced Aggregation of Mammalian Synovial Fluid Components under Boundary Lubrication Conditions. *Adv Funct Mater* **2014,** *24* (21), 3152-3161.

Rapp, M.; Donaldson, S.; Gebbie, M.; **Das, S.**; Kaufman, Y.; Gizaw, Y.; Koenig, P. H.; Israelachvili, J. Hydrophobic, Electrostatic, and Dynamic Polymer Forces at Silicone Surfaces Modified with Long-Chain Bolaform Surfactants. *Small* **2014,** in press.

Yu, J.; Kan, Y. J.; Rapp, M.; Danner, E.; Wei, W.; **Das, S.**; Miller, D. R.; Chen, Y. F.; Waite, J. H.; Israelachvili, J. N. Adaptive Hydrophobic and Hydrophilic Interactions of Mussel Foot Proteins with Organic Thin Films. *P Natl Acad Sci USA* **2013,** *110* (39), 15680-15685.

Nicklisch, S. C. T.; **Das, S.**; Rodriguez, N. R. M.; Waite, J. H.; Israelachvili, J. N. Antioxidant Efficacy and Adhesion Rescue by a Recombinant Mussel Foot Protein-6. *Biotechnol Progr* **2013,** *29* (6), 1587-1593.

Israelachvili, J. N.; Kristiansen, K.; Gebbie, M. A.; Lee, D. W.; Donaldson, S. H.; **Das, S.**; Rapp, M. V.; Banquy, X.; Valtiner, M.; Yu, J. The Intersection of Interfacial Forces and Electrochemical Reactions. *J Phys Chem B* **2013,** *117* (51), 16369-16387.

Israelachvili, J.; Donaldson, S.; **Das, S.**; Gebbie, M.; Rapp, M. Interactions of Soft-particles (vesicles, etc.) in Complex Fluid Systems. *Abstr Pap Am Chem S* **2013,** *246*.

Donaldson, S. H.; **Das, S.**; Gebbie, M. A.; Rapp, M.; Jones, L. C.; Roiter, Y.; Koenig, P. H.; Gizaw, Y.; Israelachvili, J. N. Asymmetric Electrostatic and Hydrophobic-Hydrophilic Interaction Forces between Mica Surfaces and Silicone Polymer Thin Films. *Acs Nano* **2013,** *7* (11), 10094-10104.

Donaldson, S.; Valtiner, M.; Kristiansen, K.; Royne, A.; Gebbie, M.; Rapp, M.; **Das, S.**; Chmelka, B.; Israelachvili, J. Development of a General Interaction Potential for Hydrophobic and Hydrophilic Interactions. *Abstr Pap Am Chem S* **2013,** *246*.

Das, S.; Donaldson, S. H.; Kaufman, Y.; Israelachvili, J. N. Interaction of Adsorbed Polymers with Supported Cationic Bilayers. *Rsc Adv* **2013,** *3* (43), 20405-20411.

Das, S.; Chary, S.; Yu, J.; Tamelier, J.; Turner, K. L.; Israelachvili, J. N. JKR Theory for the Stick Slip Peeling and Adhesion Hysteresis of Gecko Mimetic Patterned Surfaces with a Smooth Glass Surface. *Langmuir* **2013,** *29* (48), 15006-15012.

Das, S.; Banquy, X.; Zappone, B.; Greene, G. W.; Jay, G. D.; Israelachvili, J. N. Synergistic Interactions between Grafted Hyaluronic Acid and Lubricin Provide Enhanced Wear Protection and Lubrication. *Biomacromolecules* **2013,** *14* (5), 1669-1677.

Yu, J.; Chary, S.; **Das, S.**; Tamelier, J.; Turner, K. L.; Israelachvili, J. N. Friction and Adhesion of Gecko-Inspired PDMS Flaps on Rough Surfaces. *Langmuir* **2012,** *28* (31), 11527-11534.

Yu, J.; Chary, S.; **Das, S.**; Tamelier, J.; Pesika, N. S.; Turner, K. L.; Israelachvili, J. N. Gecko-Inspired Dry Adhesive for Robotic Applications. *Adv Funct Mater* **2011,** *21* (16), 3010-3018.

Tamelier, J.; Chary, S.; Turner, K.; Yu, J.; **Das, S.**; Israelachvili, J. Millimeter Size Patch Behavior of Gecko-Inspired Reversible Adhesive. *2011 Ieee Sensors* **2011**, 1819-1822.

BOOK CHAPTER

Greene, G. W.; Lee, D. W.; Yu, J.; **Das, S.**; Banquy, X.; Israelachvili, J. N., Lubrication and Wear Protection of Natural (Bio)Systems. In Polymer Adhesion, Friction, and Lubrication, John Wiley & Sons, Inc.: 2013; pp 83-133.

SELECTED CONFERENCE PRESENTATIONS

Das, S., Miller, D., Kaufman, Y., Martinez, N., Isralelachvili, J.N., Waite, H., "Tough Coating proteins: Subtle Sequence Variation Modulates Cohesion", 2nd International Conference on Biological and Biomimetic Adhesives, Istanbul, Turkey, 2014.

Das, S.; Chary, S.; Tamelier, J.; Hogan, H.; Yu, J.; Turner, K.; Israelachvili, J., "Frictional Adhesion and Stick-slip Friction of Patterned Surfaces with Smooth and Rough Glass Surfaces", International Nanotribology Forum, Kochi, Kerala, Jan 2014.

Das, S.; Yu, J.; Chary, S.; Tamelier, J.; Turner, K.; Israelachvili, J., "A Modified JKR Theory for the Adhesion of Patterened Surfaces Against Smooth Glass Surface", Gordon Research Conference of Adhesion, South Hadley MA, July 2013.

Das, S.; Donaldson Jr., S.; Israelachvili, J., "Polyacrylamide Induced Thinning and Increase in Head Group Area of Supported Cationic Bilayers", AIChE, Pittsburgh PA, Nov 2012.

Das, S.; Banquy, X.; Zappone, B.; Greene, G.; Jay, G.; Israelachvili, J., "Synergistic Interactions between Grafted Hyaluronic acid and Lubricin Provide Enhanced Wear Protection and Lubrication", Gordon Research Conference of Tribolgy, Waterville ME, July 2012.

Das, S.; Yu, J.; Chary, S.; Tamelier, J.; Turner, K.; Israelachvili, J., "Gecko-Inspired Dry Adhesive for Robotic Applications", Gordon Research Conference of Adhesion, Lewiston ME, July 2011.

HONORS AND AWARDS

Best Poster award in the International Nanotribology Forum (by Springer), Kochi (2014)

Best Poster award in Surface Forces Apparatus Conference, Cancun (2014)

MRL-Dow fellowship (2012-2014)

Doctoral Student Travel Grant (2012)

Institute award for standing third at the Third Year Bachelor of Chemical Engineering (2008)

Sir Ratan Tata Scholarship for academic excellence (2005-2008)

Institute award for standing third at the Second Year Bachelor of Chemical Engineering (2007)

Institute award for standing third at the First Year Bachelor of Chemical Engineering (2006)

Gujarat Ambuja Educational Institute Award (2006)

FIELDS OF STUDY

Major Field: Chemical Engineering
Interfacial and Colloid Science
Wet adhesion
Biomaterials

Advisor: Jacob N. Israelachvili

ABSTRACT

Bio-Inspired Adhesion, Friction and Lubrication

by

Saurabh Basudeb Das

Biological systems have developed elegant adaptations during its evolution to survive and perform its functions efficiently under specific environmental constrains with enormous physical demands. In this dissertation, I make an effort to understand tribological phenomena in biology and translate them into a synthetic system for engineering applications. I emphasize on adhesion, friction and lubrication in three different biologically inspired soft condensed matter as described below.

Dopa (3,4-dihydroxyphenylalanine), a post-translational modification from tyrosine (Tyr), features prominently in the mussel foot proteins (mfps), ranging from less than 5 mol % in mfp-4 to 30 mol % in mfp-5. The binding ability of the mfps to different substrates has been mostly attributed to the Dopa functionality in the protein and the role of the other peptide residues in the adhesive properties of the protein remains elusive. Here we have discovered that the adhesion between mfp-1 decapeptide films ($[AKPSYPPTYK]_2$) and mica remained unchanged with or without the Dopa residue. This is a paradigm shift in our understanding of the molecular mechanisms underlying adhesive properties of the mfps and calls for further inquiry into the effects of peptide residues beyond Dopa chemistry. We also developed a systematic body of work linking the adhesive performance to lengths and architectures of peptides. Dopa in a peptide sequence does not necessarily lead to the formation of cross-links between peptide films through metal chelation, and the length of the peptide is a crucial parameter for enabling metal ion mediated bridging between surfaces.

More recently, we have been working on designing and characterizing small molecules that mimic the properties of the adhesive mussel foot proteins. The wet adhesion and coacervation of an adhesive protein (mfp-5) was recapitulated in an order of magnitude smaller length scale which shows cohesive properties superior to the mfps. We believe that the resulting insights into the molecular structure-function relationships will enable rational design of synthetic bio-inspired adhesives that would enable *de novo* (suture less) sealants for injuries and surgeries and nano-scale-adhesive applications in the semiconductor industry.

Geckos can attach and detach their toes reversible in matters of milliseconds from most surfaces regardless of its roughness due to the hierarchical structure of their foot-pads. Micro-flaps mimicking the function of the micron sized setae on the gecko foot pad were fabricated and investigated for its adhesion and frictional properties in a modified surface forces apparatus (SFA). A Johnson-Kendall-Roberts (JKR) model with an effective stiffness and adhesion energy parameters quantitatively described the 'contact mechanics' of the tilted micro-flaps against a smooth silica surface at the macro and micro-scales. Constant attachments and detachments occurred between the surfaces during shearing and were described by an *Avalanche* mechanism. These results demonstrate the significance of preload, shearing velocity, shearing distances, commensurability, and shearing direction of gecko-mimetic adhesives and provide a simple model for analyzing and/or designing such systems.

Biolubrication systems show ultralow friction coefficients, remarkable wear resistance properties and are far superior to any artificial system designed to date. In this work, the role of proteins (e.g., Lubricin, Lub) and polysaccharides (e.g., Hyaluronic acid, HA) found in articular joints, and mfp-1 inspired coacervates were investigated to determine

the lubrication and wear protection mechanisms conferred by the naturally occurring polymers to a mica surface. We find that Lub penetrates into a *chemically* bound HA on mica to form a visco-elastic gel that reduces the coefficient of friction as well as boosts the strength of the surface against abrasive wear, however, *physically* adsorbed HA-Lub complex were poor at conferring wear protection to mica even though it showed low friction coefficients. Similarly, coacervated mfp-1/HA rescues mica from shear induced damage only when the protein is modified with Dopa, which is responsible for attaching the coacervate to the surface. Absence of Dopa resulted in severe abrasive wear to the surfaces even under low loads (< 10 mN) during shearing. These results show that strong anchoring of polymers is crucial to protect surfaces from shear induced damage. We also demonstrate that friction coefficient is not correlated to wear.

TABLE OF CONTENTS

1. INTRODUCTION

Since the very beginning, humankind has been constantly struggling to improve its quality of life through *Engineering* and developing new technologies. The word *Engineering* is derived from the Latin word 'Ingenium' which means 'to device craft-fully'. The very first known 'Engineering' marvel dates back to the early Neolithic age (~9500 B.C.) when cereals were first farmed and Beer was brewed. Another wonder that changed human civilization for good was during 3500 B.C. when the Mesopotamian civilization first invented 'wheel and the axel' to mobilized heavy objects and reduce friction during translationary motion. This was followed by the evolution of the lubrication technology at around 1800 B.C. when the Egyptians used water and oil to reduce the frictional stress between surfaces to move heavy sledges. Today, we have the tools and capabilities to manipulate and perceive scientific phenomena from the nanoscopic (~10^{-9} m) to megascopic scales and further beyond. The human civilization has been constantly struggling to explore more and learn from biology and nature to enhance his luxury of life and live a utopian dream. He has indeed succeeded partially in achieving his goal and the curiosity to learn allows him to uncover the many unknown mysteries of life and science. Engineering developments in chemistry, physics, biology and material science has indeed led man to determine the origin of time, space, life and invent devices to make daily life pleasant and comfortable.

A branch of engineering that is a star alliance in uniting all the different fields of engineering viz., mechanical, civil, electrical, materials etc. is *Chemical engineering*. They pioneer valuable materials and techniques which plays a crucial role in related fields such as biotechnology, nanotechnology, bioengineering and biomaterials. This dissertation is no different and will apply the principles of chemical engineering to interpret the area of surface sciences with the key goal of understanding biologically inspired adhesion, friction and lubrication. Based on the interpretations, design rules will be suggested to build molecules that can be tailored for different applications.

The 21st century has witnessed the development of many force measuring, microscopy and material characterization techniques that has played a vital role to help corroborate theories with experimental observations. These include the surface forces apparatus (SFA), atomic force microscope (AFM), scanning electron microscope (SEM), scanning tunneling microscopy (STM), X-ray photoelectron spectroscopy (XPS), infrared spectroscopy (IR) and many more. These techniques has made it possible to visualize the dynamics and statics of intermolecular and surface forces which in turn enriched our fundamental understanding of behavior of elements and hence has led to a rational development of materials for different applications. The theme of this dissertation will revolve around the measurement and understanding of interfacial forces in a few bio-inspired materials and propose design rules for developing molecules for adhesive/lubrication applications.

1.1 Inspiration from biology

Organisms in nature have adapted to their complex biotic and abiotic environments for their survival under extreme conditions. For example, marine mussels have evolved both, an energy-tolerant and dissipative byssus, to manage the significant lift and drag forces imposed upon them in the harsh intertidal zone. Geckos can run on walls and ceilings of practically any material and roughnesses. The adhesive foot pads of a gecko exploit frictional-adhesion to attach and detach quickly from surfaces and we struggle to understand and mimic this behavior through synthetic analogs. Sand-castle worms deploy their tentacles to capture and glue sand particles and secure its habitat under deep sea waters. These organisms thus inspire the fabrication and synthesis of wet and dry adhesive materials that can work under any environment and will be further discussed in this dissertation in chapters 3 to 6.

Another miracle of biology that we try to understand and mimic is the super-lubricity and wear protection properties conferred by the complex synergy between the various proteins, polysaccharides and lipids in the synovial fluid between articular joints in animals. As with any ‘well oiled’ machine, the optimal performance and functionality of biomechanical systems are contingent upon effectual lubrication of motile surfaces. Nature has developed surprisingly varied, and, at times, rather ingenious lubrication strategies for controlling and regulating the interaction forces, friction, and wear at sheared interfaces. Chapter 7 and 8 in this dissertation will we narrow our focus to the area of biolubrication and discuss a few probable mechanisms of the many solutions nature has devised for controlling friction and preventing wear. It will also demonstrate the use of mussel inspired complex coacervation as a strategy to provide enhanced wear protection to surfaces.

1.1.1 Biomimetic wet adhesion: The marine mussels

Marine mussels are experts at 'wet' adhesion, achieving strong and durable attachment to a variety of surfaces in their marine habitat. Adhesion is mediated by a byssus, essentially a bundle of leathery threads that emerge from living mussel tissue at one end and tipped by flat adhesive plaques at the other (Fig. 1.1). The byssal plaques consist of a complex array of proteins (mostly mussel foot proteins, mfps), each of which has a distinct localization and function in the structure, but all share the unusual modified amino acid 3,4-dihydroxyphenylalanine (Dopa).

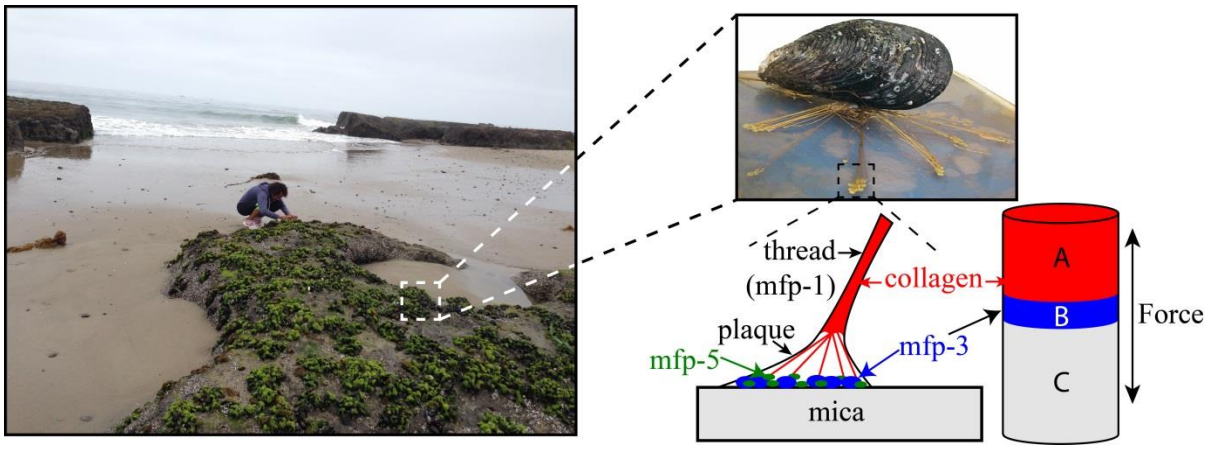

Figure 1.1 A colleague, Dr. Nadine Martinez, picking up mussel from the wave sept beach shore at UCSB campus point during low tide (*Left*, Photo credits: Saurabh Das). A mussel secured to a mineral surface (*Right inset*). Adhesive mfps such as mfp-3 (blue circles) and mfp-5 (green circles) binds the plaque to a mineral surface. In mussel byssal threads, collagens known as preCOLs mediate the transfer of load between the mussel plaque and the thread. PreCOLs come within a few nm of the mica surface, thus may bind directly to adhesive mfps such as mfp-3 and mfp-5. The preCOLs are protected by a coating protein,

mfp-1, that can accommodate high strains while simultaneously contributing to its disparate stiffness.

The mussel foot proteins, mfp-1, mfp-3, and mfp-5, have been shown to exhibit remarkable binding to mineral surfaces such as mica and TiO_2 (1, 2). The versatility of mussel adhesion to surfaces with wide-ranging chemical and physical properties has inspired much research dedicated to understanding the mechanism of mussel adhesion as well as developing biomimetic coatings and adhesives for wide-ranging industrial and biomedical applications, the latter including paints for coronary arteries (3), fetal membrane sealants (4), cell encapsulants (5), and for securing transplants for diabetics (6).

Several studies with Dopa functionalized polymers have demonstrated a strong positive linear correlation between Dopa content and adhesion to different surfaces (7-11). The binding ability of the mfps to different substrates thus has been mostly attributed to the Dopa functionality in the protein and the role of the other peptide residues in the adhesive properties of the protein remains elusive. The goal of this research was to understand the adhesion capabilities of the mfps beyond Dopa chemistry. The surface forces apparatus (SFA) was used to measure the adhesive properties of mfp-1, a natural coating protein that forms the major constituent of the protective cuticle covering all exposed portions of the byssus including the plaques. Partial recombinant constructs of mfp-1 (rmfp-1, mass~14 kDa) and short decapeptides dimers, with and without Dopa were also assessed for its adhesive and cohesive properties. A systematic body of work linking the adhesive performance to lengths and architectures of peptides was also developed. This work recapitulated the wet adhesion and coacervation of an adhesive protein (mfp-5) in an order of

magnitude smaller length scale (small zwitterionic molecules) which shows adhesive properties superior to the mfps.

1.1.2 Biomimetic dry adhesion: Geckos

The supreme ability of the gecko to attach and detach quickly to any surface has been fascinating man for over two millennia. They are super climbers with impeccable dexterity of attaching and detaching their toes in matters of milliseconds (12) while running with wantonness on surfaces, be it vertical or inverted. This exceptional feature of the species of quick attachment and equally quick detachment to any surface is still a challenge that no conventional adhesive is capable of meeting. The bottom up design of the hierarchical gecko foot structure (Fig. 1.2) (13) helps in an adhesive mechanism robust enough to maneuver on unknown rough surfaces irrespective of its inclination.

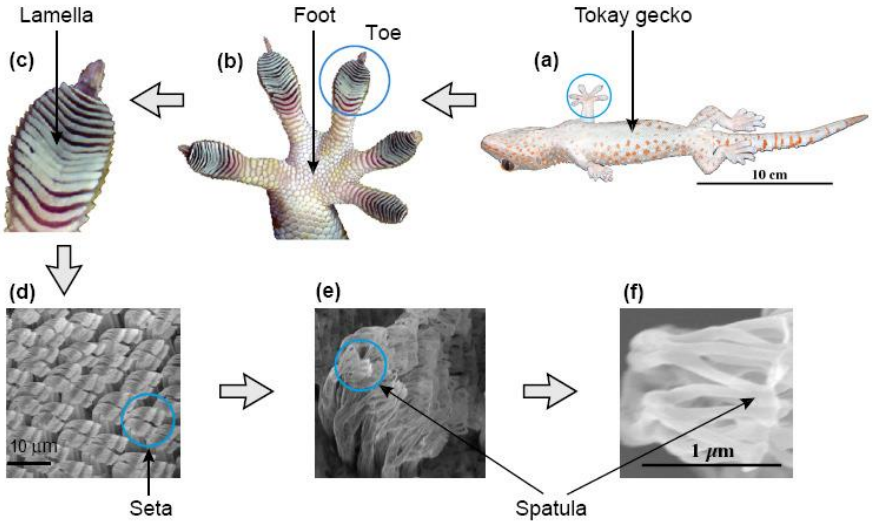

Figure 1.2 Hierarchical structures of a Tokay gecko. (a) Optical image of a Tokay gecko at rest. (b) A gecko foot. (c) A gecko toe. (d) Scanning electron microscope images of a setal array, (e) the spatula pads, and (f) a magnified view of a spatula pad.

Each gecko foot has 5 toes; each toe has about 20 arrays (lamellae) of micron-scale hair (setae), with each seta being ~5 μm in diameter and approximately 110 μm in length on average. Each seta splits into 100-1000 nano-scale spatula, of 200 nm length and width at the tip, forming the fine structure of the gecko adhesive system (14). The setae are formed out of β-keratin (15). The setae further branches out into spatulae. These spatulae, by conforming to both micro- and nano-scale asperities, achieve a large true area of contact, so that geckos can adhere to different surfaces via the weak van der Waals force together with other types of non-covalent forces such as capillary forces (16, 17). Conventional pressure sensitive adhesives (PSAs) are good in adhering to different surfaces since they are soft and sticky but they do not have the control over issues such as fouling, self-adhering, degradation and accidental attachment to inappropriate surfaces. They both stick too strongly to surfaces and are difficult to remove (e.g. Duct tapes) or adhere weakly to surfaces and peel of easily (e.g. Sticky notes). The gecko setae, however, shows directional adhesion, quick attachment and detachment (16) irrespective of the surface profile and strong adhesion with a small preload, self-cleaning property, non-sticky and does not self-adhere. The properties of the gecko adhesive system have been known but the basic principles behind these complex behaviors are still not well understood.

This dissertation will address the 'frictional-adhesion' properties of gecko-mimetic fabricated structures against smooth and rough surfaces. The combined effects of preloads, shearing speeds and, surface roughness (topography) on adhesion and frictional properties of adhesives mimicking the functional properties of a gecko foot-pad will be discussed. The results from these studies will help determine the design and operating principles for gecko-mimetic adhesives. This work will also suggest a design idea for a prototype 'robotic foot

placement device' that can create an actuating mechanism at low energy inputs and enables high speed and versatile climbing and movement. The gecko-mimetic adhesives can also be employed for the transportation and manipulation of fragile micro/macro object, especially to handle delicate wafers in the semiconductor industry.

1.1.3 Bio-lubrication

Nature has managed to create biolubrication systems that shows ultralow friction coefficients, remarkable wear resistance properties and is far superior to any artificial system designed to date. The collagen fibril network in the cartilage in animal joints are 'well' lubricated through the physical immobilization of polysaccharides via mechanical trapping of the molecules partially trapped in the cartilage pores (18). Biolubrication systems are dynamic with the tribological factors such as loads, shear forces, fluid flux, shear rates and sliding velocities can change quickly with time. Nonetheless, the natural biolubrication systems are robust and are exceptional in maintaining low shear stresses and protecting sliding interfaces from damage.

Boundary lubrication and hydrodynamic lubrication mechanisms are thought to be mainly responsible for the efficient operation of animal joints. Hyaluronic acid (HA), a polysaccharide that forms the major component of the synovial fluid in the joints acts synergistically with proteins (e.g., Lubricin), mucopolysaccarides (e.g., GAGs) and lipids to provide boundary lubrication and wear protection to the cartilage surfaces while maintaining ultralow friction forces. This dissertation will explore the role of a protein 'lubricin' and HA in protecting surfaces from wear and maintain lubrication.

The lubrication property of mussel inspired complex coacervates has also been investigated in this thesis. Protein and polymer solubilization in aqueous environments can be detrimental to the delivery of materials to target surfaces. The marine mussel appears to overcome this problem via exploiting complex coacervation during delivery of the proteins onto target surfaces to attach securely. Hence, complex coacervation can serve as a potential strategy for delivery of adhesive and coating materials to target surfaces through the ability of mfp-1, a natural coating protein, and hyaluronic acid (HA), a natural lubricant found in synovial fluid, to coacervate. The interfacial properties of the HA/mfp-1 coacervate have been investigated with the SFA in order to determine their potential as protective and/or functional coatings and as a lubricant material. Particularly, the role of Dopa in the wear protection property conferred by the coacervate to a model mica surface will be addressed here.

1.2 Organization of this dissertation

I will provide a brief description of the important forces in biology that are relevant to this work in chapter 2. Additionally, I will describe the main experimental techniques that I used for measuring forces and characterization of surfaces viz., surface forces apparatus (SFA), atomic force microscopy (AFM), cyclic voltammetry (CV), X-ray photoelectron spectroscopy (XPS) and quartz crystal microbalance (QCM). Other solution phase techniques such as dynamic light scattering (DLS), Infrared Raman techniques etc. will be described in the later chapters where they were used. Chapter 3 proposes a mechanism of protein- and Fe^{3+} concentration-dependent cohesion and metal chelation in mussel foot protein-1 (mfp-1) from two homologous mussel species and ferric cation. The role of peptide length and Dopa

content in a peptide sequence in the formation of cross-links, metal chelation and interaction with hydrophobic silicones has been discussed in chapter 4. Chapter 5 and 6 reviews the frictional adhesion properties of gecko-mimetic patterned surfaces against smooth and rough silica surfaces. The role of proteins, polysaccharides and mussel inspired complex coacervate has been investigated in chapter 7 and 8. In chapter 9, I propose the designing of mussel protein inspired single molecular zwitterionic molecules that surpasses the adhesive properties of mussel foot proteins (mfps) and recently developed adhesive protein amyloids (19). In this chapter, I also explain the challenges to develop gecko-mimetic robotic devices and show a simple mechanism that can be exploited to integrate gecko-mimetic flaps for robotic applications.

1.3 References

1. Lin Q, *et al.* (2007) Adhesion mechanisms of the mussel foot proteins mfp-1 and mfp-3. *Proceedings of the National Academy of Sciences of the United States of America* 104(10):3782-3786.
2. Yu J, *et al.* (2013) Adhesion of Mussel Foot Protein-3 to TiO2 Surfaces: the Effect of pH. *Biomacromolecules* 14(4):1072-1077.
3. Kastrup CJ, *et al.* (2012) Painting blood vessels and atherosclerotic plaques with an adhesive drug depot. *Proceedings of the National Academy of Sciences* 109(52):21444-21449.
4. Haller C, *et al.* (2011) Mussel-mimetic tissue adhesive for fetal membrane repair: a standardized ex vivo evaluation using elastomeric membranes. *Prenatal diagnosis* 31(7):654-660.

5. Yang SH, *et al.* (2011) Mussel-inspired encapsulation and functionalization of individual yeast cells. *Journal of the American Chemical Society* 133(9):2795-2797.

6. Brubaker CE, Kissler H, Wang L-J, Kaufman DB, & Messersmith PB (2010) Biological performance of mussel-inspired adhesive in extrahepatic islet transplantation. *Biomaterials* 31(3):420-427.

7. Anderson TH, *et al.* (2010) The Contribution of DOPA to Substrate-Peptide Adhesion and Internal Cohesion of Mussel-Inspired Synthetic Peptide Films. *Advanced Functional Materials* 20(23):4196-4205.

8. Heo J, *et al.* (2012) Improved Performance of Protected Catecholic Polysiloxanes for Bioinspired Wet Adhesion to Surface Oxides. *Journal of the American Chemical Society* 134(49):20139-20145.

9. Chung HY & Grubbs RH (2012) Rapidly Cross-Linkable DOPA Containing Terpolymer Adhesives and PEG-Based Cross-Linkers for Biomedical Applications. *Macromolecules* 45(24):9666-9673.

10. Liu B, Burdine L, & Kodadek T (2006) Chemistry of periodate-mediated cross-linking of 3,4-dihydroxylphenylalanine-containing molecules to proteins. *Journal of the American Chemical Society* 128(47):15228-15235.

11. Saxer S, *et al.* (2010) Surface Assembly of Catechol-Functionalized Poly(L-lysine)-graft-poly(ethylene glycol) Copolymer on Titanium Exploiting Combined Electrostatically Driven Self-Organization and Blomimetic Strong Adhesion. *Macromolecules* 43(2):1050-1060.

12. Autumn K, *et al.* (2006) Dynamics of geckos running vertically. *Journal of Experimental Biology* 209(2):260-272.

13. Tian Y, *et al.* (2006) Adhesion and friction in gecko toe attachment and detachment. *Proceedings of the National Academy of Sciences of the United States of America* 103(51):19320-19325.

14. Ruibal R & Ernst V (1965) Structure of Digital Setae of Lizards. *Journal of Morphology* 117(3):271-&.

15. Russell LD (1982) Morphological Evaluation of the Effects of Environmental Agents on Testicular Function in Experimental-Animals. *Archives of Andrology* 9(1):45-46.

16. Autumn K, *et al.* (2002) Evidence for van der Waals adhesion in gecko setae. *Proceedings of the National Academy of Sciences of the United States of America* 99(19):12252-12256.

17. Huber G, *et al.* (2005) Evidence for capillarity contributions to gecko adhesion from single spatula nanomechanical measurements. *Proceedings of the National Academy of Sciences of the United States of America* 102(45):16293-16296.

18. Greene GW, *et al.* (2011) Adaptive mechanically controlled lubrication mechanism found in articular joints. *Proceedings of the National Academy of Sciences* 108(13):5255-5259.

19. Zhong C, *et al.* (2014) Strong underwater adhesives made by self-assembling multi-protein nanofibres. *Nature nanotechnology*.

2. SURFACE INTERACTIONS IN BIOLOGY

2.1 Overview of important interactions

In the macroscopic world, the forces between matter is mainly governed by gravity for big separation distances, i.e., in the range of several meters to light years. However, as the size scale of an object becomes small, i.e., in the order of several nano-meters and less, the surface area to volume ratio increases and surface forces play a dominant role in determining the interactions between the molecules and role of gravity becomes negligible. This is due to the fact that the mass of the molecules gets smaller and the surface area for interaction increases for the interfacial forces to act upon as the objects start getting smaller. These interfacial surface forces that determine the intermolecular interactions are classified as dispersion forces, van der Waals (VDW) forces, London forces, charge fluctuation forces, electro-dynamic forces and induced dipole–induced–dipole forces. The basic origin of all these forces is electrostatics and it manifests itself into the so called *dispersion forces* (1). When we refer to the strength of interaction between two surfaces or molecules, we often tend to confuse between interaction *forces* (*F*) and *energies* (*W*). The two are related by $F = -\mathrm{d}W/\mathrm{d}D$ where D is the separation distance between the surfaces under consideration. It should be noted that even if the energy of interaction between two surfaces is the same, the force required to separate them could be completely different and depends on the rate of

separation and the path taken to separate the surfaces apart. This has important implications in peeling process that a gecko employs to quickly release its foot-pads from a surface.

Interactions in biological systems are very complicated and involve the interplay of many different forces such as the van der Waals force, electrostatic force, hydrogen bonding, steric forces, hydration and hydrophobic forces. Since the theme of this dissertation revolves around measuring interaction forces, a few of the relevant ones will be described briefly in this chapter. I will also describe a few experimental techniques that were used for measuring interfacial forces between protein and polymer surfaces and surface characterization techniques.

2.1.1 Van der Waals (VDW) interactions

VDW forces occur between all bodies and originate due to fluctuations in the electric dipole moment and are also known as *dispersion* force. They occur regardless of the properties of the molecule and are quantum mechanical in origin. It can be intuitively understood by considering two neutral atoms or molecules interacting in vacuum, e.g., helium atoms. For non-polar helium atoms, the time averaged dipole moment is zero, however, at any given instant of time, the dipole moment of one of the atoms will be non-zero due to the instantaneous position of its electrons with respect to its nucleus. This instantaneous dipole moment creates an electric field that induces a similar dipole moment in the nearby helium atom and gives rise to a net attractive force of interaction between the two atoms when averaged over time. These forces are long-ranged and can be either attractive or repulsive depending on the system but are always attractive between similar materials.

The van der Waals forces are non-additive and are influenced by other nearby bodies. The Lifshitz theory circumvented this complexity by assuming a continuum approach and derived the equation in terms of measurable bulk properties of the material. Thus, Lifshitz proposed a simple equation for to determine the VDW force between spheres of the same material and it takes the form

$$F(D) = \frac{AR}{6D^2} \qquad (2.1)$$

where r is the radius of the spheres, D is the distance at the point of smallest separation between the spheres, and A is the Hamaker constant which depends on the electric and optical properties of the materials and medium of the system.

The Hamaker constant A is given by the Lifzhitz theory and has been described by Israelachvili in Ref. (1). The Hamaker constant for medium 1 interacting with medium 2 across medium 3, A_{132}, is given by

$$A_{132} = \frac{3}{4}kT\left(\frac{\varepsilon_1 - \varepsilon_3}{\varepsilon_1 + \varepsilon_3}\right)\left(\frac{\varepsilon_2 - \varepsilon_3}{\varepsilon_2 + \varepsilon_3}\right) + \frac{3h\nu_e}{8\sqrt{2}}\frac{(n_1^2 - n_3^2)(n_2^2 - n_3^2)}{(n_1^2 + n_3^2)^{1/2}(n_2^2 + n_3^2)^{1/2}\left\{(n_1^2 + n_3^2)^{1/2} + (n_2^2 + n_3^2)^{1/2}\right\}} \qquad (2.2)$$

where ε_1, ε_2 and n_1, n_2 are the static dielectric constant and refractive index of the interacting surfaces, ε_3 and n_3 are the static dielectric constant and refractive index of the medium between the surfaces, ν_e is the absorption frequency, k_B is the Boltzmann constant and T is the temperature. A, the Hamaker constant is typically 10^{-19} for materials interacting in dry air. The value of A can be one half to one third of this value for polymer-polymer interaction or may get reduced by an order of magnitude in presence of water. The VDW forces are long-ranged (and can extend upto $D \sim 10$ nm) and can be either attractive or repulsive depending on the system but are always attractive between similar materials. A qualitative magnitude

of VDW forces compared to the other interfacial forces is shown in Fig. 2.1. VDW forces can get quite strong at small separation distances between molecules and surfaces. VDW plays an important role in play a role in a number of phenomena such as adhesion, surface tension, wetting, structure of condensed macromolecules, the properties of gases and liquids, the strength of solids, and the flocculation of particles.

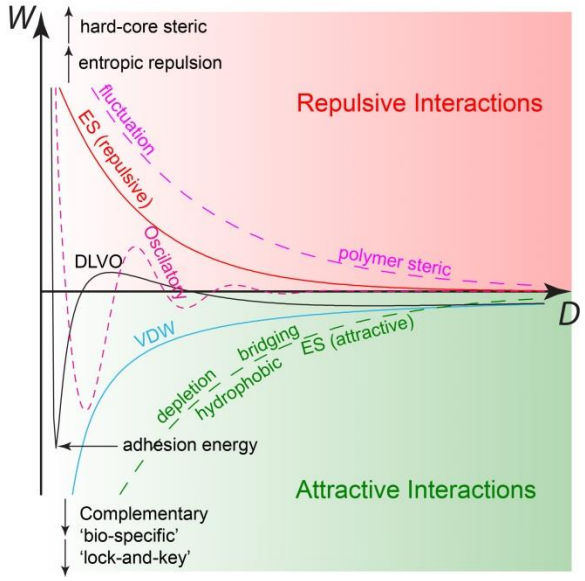

Figure 2.1 Illustration of the common surface interactions in aqueous solution, plotted as a function of distance *D*. Figure adapted from Leckband and Israelachvili (2)..

2.1.2 Electrostatic interactions

The electrostatic force of interaction (F_{ES}) between two charged bodies is given by Coulomb's inverse square law and can be mathematically written as

$$F_{ES}(D) = \frac{Q_2 Q_1}{4\pi\varepsilon\varepsilon_0 D^2} \qquad (2.3)$$

where Q_1, Q_2 are the charges on the bodies, ε_0 is the permittivity of free space, ε is the dielectric constant of the medium between the bodies and D is the distance of separation.

When a surface is immersed in an electrolytic solution, adsorption of ions charges the surface and gives rise to an electric double layer near its vicinity. Thus two charged surfaces in a solution will electrostatically interact with each other according to eq. (2.3). The charging mechanism of the surfaces were first proposed by Helmholtz in his 'Electric Double' theory and proposed that charged interfaces behave as a molecular dielectric and stores energy. Later Louis Guoy and David Chapman introduced the 'Guoy-Chapman' model of electric double layer and used the Poisson-Boltzmann (PB) equation to calculate the charge distribution near an electrode interface. The force of interaction between two charged double layers can be obtained by solving the PB equation and applying constant charge or constant potential boundary conditions (3, 4). For dissimilar surfaces, an analytical solution to the PB equation is not available and the equation needs to be solved numerically to calculate the interaction energy between the surfaces. In an aqueous solution the surface potential sets up a diffuse layer of counter-ions in solution, distributed close to the charged surface to balance out the surface charges. The double-layer extends from each surface with a characteristic decay length called the Debye length κ^{-1} that is given by

$$\kappa^{-1} = \left(\frac{\varepsilon \varepsilon_0 k_B T}{2 \mathrm{N_A} I \mathrm{e}^2} \right)^{1/2} = \frac{0.304}{\sqrt{[\mathrm{NaCl}]}} \text{ nm (for NaCl at 25°C)} \qquad (2.4)$$

where ε is the dielectric constant of water, ε_0 is the permittivity of free space, $\mathrm{N_A}$ is Avogadro's number, I is the ionic strength of the electrolyte (in mole per liter), e is the fundamental electric charge, and [NaCl] the concentration given in units of mole per liter (1).

Electrostatic double layer interactions between surfaces are similar to VDW interaction but longer ranged depending on the solution conditions (1, 5). The sum of the double-layer and VDW interactions together make up DLVO interactions (Fig. 2.1) and is

named after Derjaguin & Landau (1941) and Verwey & Overbeek (1948) who developed it independently while working on colloidal stability. Biological interfaces such as proteins, membranes and tissues are mostly submerged in an aqueous environment and electrostatic forces regulate many different biological processes (6-8).

2.1.3 Hydrogen bonding and hydrophobic forces

Hydrogen bonds are a particular case of strong dipole-dipole interactions. It is an outcome of an electrostatic attraction between polar molecules due to partial charging of hydrogen atom bound to a highly electronegative atom such as oxygen, nitrogen or halogens that result in the formations of molecular dipoles. Hydrogen bonding interactions are stronger than VDW interactions, but weaker than a covalent bond. In fact the bond length of a hydrogen bond in water (H---O) is 0.176 nm, which is much less than a VDW radii but larger than a covalent bond. The average strength of a hydrogen bond is about 5-10 kT per bond. Water, the most important biological molecule shows extensive hydrogen bonding network and this explains the high boiling/melting points and accounts for its anomalous behavior. Hydrogen bonds play an important role in giving the DNA its helical structure (1), protein folding (9, 10), enzymatic catalytic activities (11) and adhesive interaction of proteins to surfaces (12, 13) and interaction of collagen with mussel foot proteins (Martinez, Das et al., submitted, Fig. 1.1).

The hydrogen bonding capability of water is compromised in presence of a vapor cavity or non-polar molecules or hydrophobic surfaces. It is no longer able to form its hydrogen bonding network around the vicinity of such surfaces or molecules. In case of a small hydrophobic moiety (< 1nm size), water can still form its hydrogen bonding cage

around the molecule at the cost of entropy, but favorable energetically. However the hydrogen bond network of water completely fails around a big hydrophobic interface and the exact mechanism for the same is still not understood. Some workers claim that hydrophobic surfaces increase the fluctuation of the water density around the interface whereas some other proposes the formation of excluded volume where the water density fades out (14-17). Hydrophobic interactions play a crucial role in biological processes like protein folding, stability of the DNA(1), mussel foot coating protein cohesion, self-assemble processes.

2.1.4 Polymer mediated interactions

Proteins or polymers can adsorb to surfaces through VDW and electrostatic interactions or could be chemically grafted to a surface through the formation of covalent bonds between the polymer and the surface. Surface adsorbed polymer can rearrange to form a mushroom like structure, polymer brushes, and random coils or may simply lay down flat on the surface. When such polymer decorated surfaces are brought close to another surface, the molecules experience entropic loss due to the compression of the polymer chains. This causes a repulsive steric force of interaction between the polymer decorated surface and the approaching surface. The magnitude of the steric repulsion depends on the molecular weight of polymer, surface grafting density, temperature and solution conditions. The repulsive steric interaction between polymer chains showing brush and mushroom like configurations has been proposed by Alexander De Gennes (18) and Edward-Dolan (19) respectively.

When two polymer coated surfaces or blobs are brought into a compressive contact, they may interact physically through the through VDW interaction or specific coulombic interactions. Coulombic (or electrostatic) interactions might involve the formation of

hydrogen bonds, pi-pi stacking (20) between aromatic residues in the polymer, cation-pi (21) interactions between the aromatic residues and charged cations residues or hydrophobic interactions. An example of such interactions between collagen and a mussel foot protein-3 (mfp-3) is shown in Fig. 2.2. Bridging interactions between polymer chains can also be induced externally through metal chelation and will be discussed in details with regards to the bridging between mfp-1 films in chapter 3.

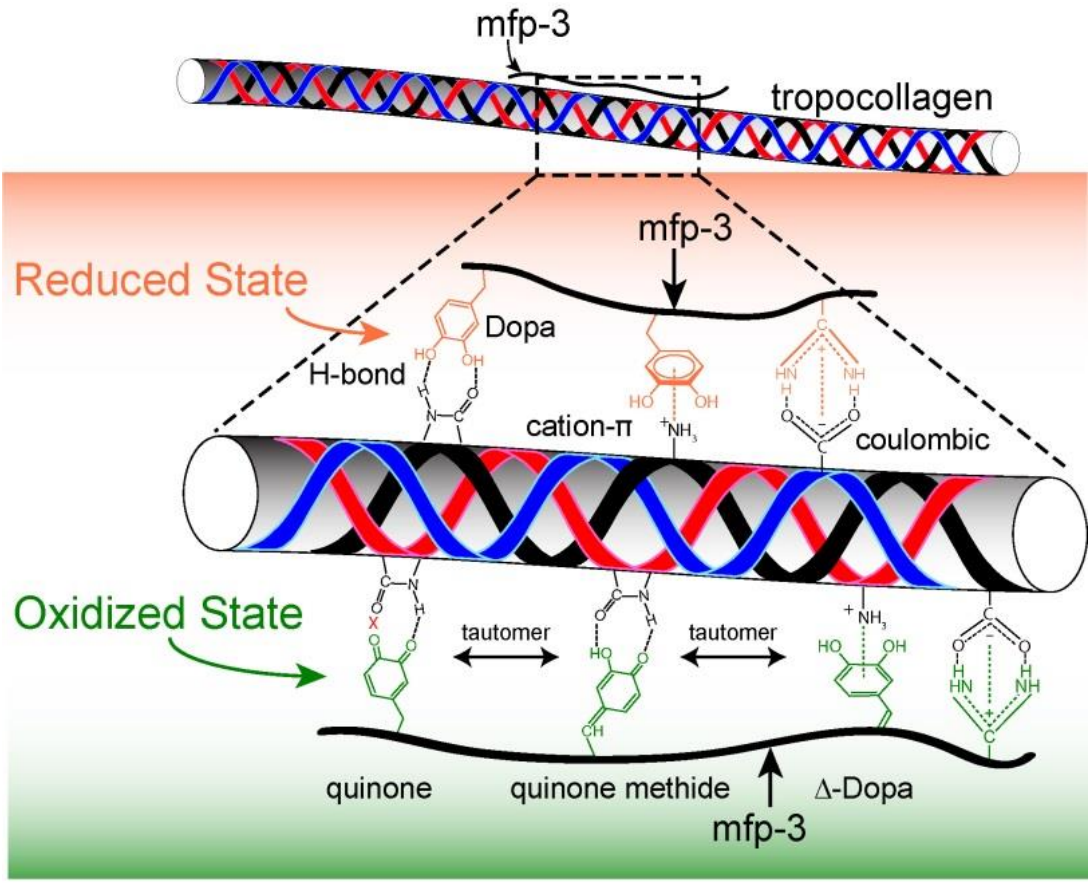

Figure 2.2 Hydrogen bonding and cation-pi interactions between collagen and mfp-3 appear to mediate the strong but reversible binding between these molecules (Martinez, Das et al., Submitted).

2.2 Measuring surface interactions: The Surface Forces Apparatus (SFA)

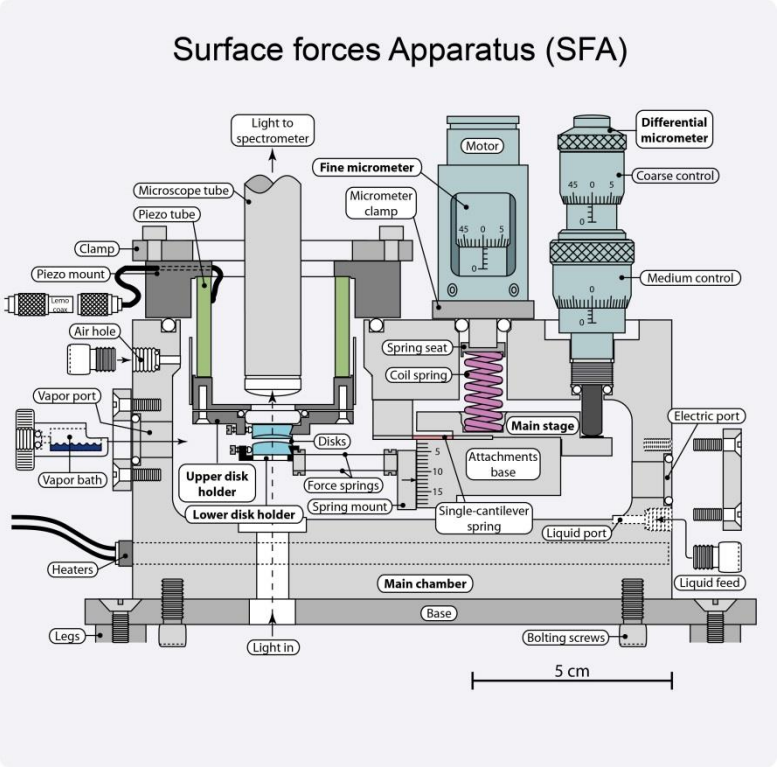

Figure 2.3 A schematic diagram of the side view of the SFA 2000.

Measuring surface interactions in biologically relevant systems and bio-inspired surfaces is fundamental to this dissertation. Hence I used the surface forces apparatus (SFA, SurForce LLC, Santa Barbara) (Fig. 2.3) for directly measuring forces as a function of distance between two surfaces. The SFA technique was first developed in the late 1960s by Tabor and Winterton (22) to directly measure the VDW forces between mica surfaces. It was later modified by Israelachvili and Tabor (23, 24) to measure normal and shear forces between molecularly thin films. In fact, the first report on the direct measurement of the hydrophobic forces was made using the SFA by Israelachvili and Pashley (25). SFA can be used to control and measure distances between two surfaces with sub-nanometer accuracy and resolution independently of the force while simultaneously record the shape of the

contact interface. It can also measure the refractive index of the material of interest and its tribological properties. In this dissertation, I used the SFA to measure normal and shear forces using both, optical technique and strain gauges (digital signal). I will describe both in this section.

In a SFA, the surfaces that are to be studied are mounted opposite each other in the main chamber (Fig. 2.3). The upper surface is mounted on the upper disk holder that consists of a piezo-electric tube for very fine distance control for the movement of the upper surface. The other surface is mounted on the lower disk holder which is coupled directly to a double cantilever spring that upon deflection bends normally. The double cantilever spring is held by the attachment base as shown in fig. 2.3 and allows for three levels of controlling the position of the lower surface. A differential micrometer that is directly coupled to the attachment base can be used for coarse and medium distance control. Fine control for the movement of the lower surface can be achieved by a spring gear mechanism. This mechanism involves a motor driven micro-meter that pushes a weak spring which in turn forces a stiffer spring (single cantilever spring) to deflect. The ratio of the spring constant between the stiff and the weak spring is in the order of 10^3 and that allows for the movement and fine distance control of the lower surface to approximately 1 nm. The distance between the surfaces is determined by multiple beam interferometry (MBI) (26) technique and will be discussed later in this section. This technique requires white light to pass normally through the surfaces and this is allowed for by a window at the bottom of the main chamber and in each holder which is passed through a microscope and directed into a spectrometer for light wavelength analysis.

2.2.1 Measuring normal forces

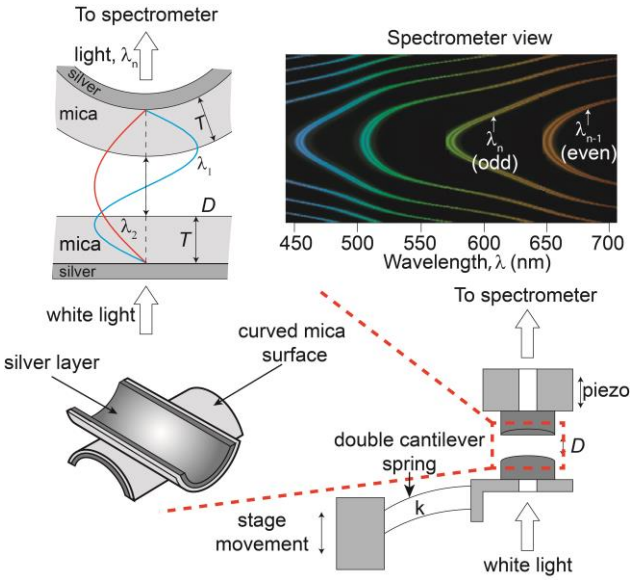

Figure 2.4 Schematic of the multiple beam interferometry (MBI) technique used in the SFA showing the fringes of equal chromatic order (FECO).

In a typical SFA experiment, the distance and the force between the surfaces are measured simultaneously. To begin with, the instrument is calibrated at large separation distances. When the two surfaces are not interacting, i.e., they are separated by large distances, the change in the separation between them is equal to the distance through which the motor moves the lower surface towards or away from the upper surface (or the upper surface driven by the piezo-tube moves towards the lower surface). However, once the surfaces are close enough to start interacting with each other, the measured separation distance deviates from the expected separation calibrated when there is no force between the surfaces. This deviation is due to the deflection of the double cantilever spring and is directly proportional to the force acting normally between the two opposing surfaces. Thus the normal force can be measured using Hooke's law, $F = k\Delta x$, where k is the spring constant of

the double-cantilever spring and $\Delta x = D_{\text{actual}} - D_{\text{applied}}$ is the deflection of the spring, determined by taking the difference between the applied change in position of one of the surfaces D_{applied} and the actual change in distance measured between the surfaces D_{actual}. The actual distance, D_{actual}, between the surfaces can be measured by multiple beam interferometry (MBI) and will be discussed below.

2.2.2 Measuring distance: Multiple beam interferometry (MBI)

The distance between the surfaces, shape of the interface and the refractive index of the media between the surfaces can be accurately determined by MBI technique (27). In this technique, white light is directed through two back silvered mica surfaces (or uniform and same thickness). As a white light passes between the mica surfaces, it undergoes interference due to the optical trap set up by the back silver on each of these surfaces giving rise to discrete wavelengths of light (Fig. 2.4). These wavelengths of light are resolve in a spectrometer creating interference fringes known as 'fringes of equal chromatic order' (FECO). Since mica is birefringent, the FECO appears as doublets and termed as β and γ. Alternate fringes are termed as odd and even fringes with odd fringes having nodes at the center and even fringes with anti-nodes in the center. The FECO is then recorded on a camera and analyzed to determine the distance between the surfaces using the following equations:

$$\tan\left(\frac{2\pi\mu_2 D}{\lambda_n^D}\right) = \frac{2\bar{\mu}\sin\left(\frac{1-\lambda_n^0/\lambda_n^D}{1-\lambda_n^0/\lambda_{n-1}^0}\pi\right)}{\left(1+\bar{\mu}^2\right)\cos\left(\frac{1-\lambda_n^0/\lambda_n^D}{1-\lambda_n^0/\lambda_{n-1}^0}\pi\right)\pm\left(\bar{\mu}^2-1\right)} \qquad (2.5)$$

$$T = n\lambda_{\mathrm{n}}^{0} / 4\mu_1 \tag{2.6}$$

$$n = \frac{\lambda_{\mathrm{n-1}}^{0}}{F_{\mathrm{n}}\left(\lambda_{\mathrm{n-1}}^{0} - \lambda_{\mathrm{n}}^{0}\right)} \tag{2.7}$$

where D is the separation distance between the surfaces, n is the fringe order (n = 1,2,3,…) λ_{n}^{0} is the wavelength of the n$^{\mathrm{th}}$ order fringe (0 refers to the distance between the mica, D = 0, or mica-mica contact reference), T is the thickness of each of the mica surfaces, μ_1 is the refractive index of mica, μ_2 is the refractive index of the medium, $\bar{\mu} = \mu_1 / \mu_2$, and the - is used for odd fringes and the + is used for the even fringes, F_{n} is a correction factor that depends on the phase changes at the mica-silver interface and dispersion effects that can be estimated as $F_{\mathrm{n}} \approx 1.024 + 1/\mathrm{n}$ for odd fringes measured near $\lambda \sim 550$ nm (27).

For small separation distance (D < 30 nm) between the surfaces, eq. 2.5 can be approximated as

$$D = \frac{\lambda_{\mathrm{n-1}}^{0}\left(\lambda_{\mathrm{n}}^{D} - \lambda_{\mathrm{n}}^{0}\right)}{2\mu_1\left(\lambda_{\mathrm{n-1}}^{0} - \lambda_{\mathrm{n}}^{0}\right)}, \text{ for n odd} \tag{2.8}$$

$$D = \frac{\mu_1\lambda_{\mathrm{n-1}}^{0}\left(\lambda_{\mathrm{n}}^{D} - \lambda_{\mathrm{n}}^{0}\right)}{2\mu_2^{2}\left(\lambda_{\mathrm{n-1}}^{0} - \lambda_{\mathrm{n}}^{0}\right)}, \text{ for n even} \tag{2.9}$$

It should be noted that the distance calculated with the equation for the odd fringes (eq. 2.8) is independent of the refractive index between the two surfaces whereas that calculated with even (eq. 2.9) is not. This allows for simultaneous measurement of refractive index along with the force and separation distance between the surfaces.

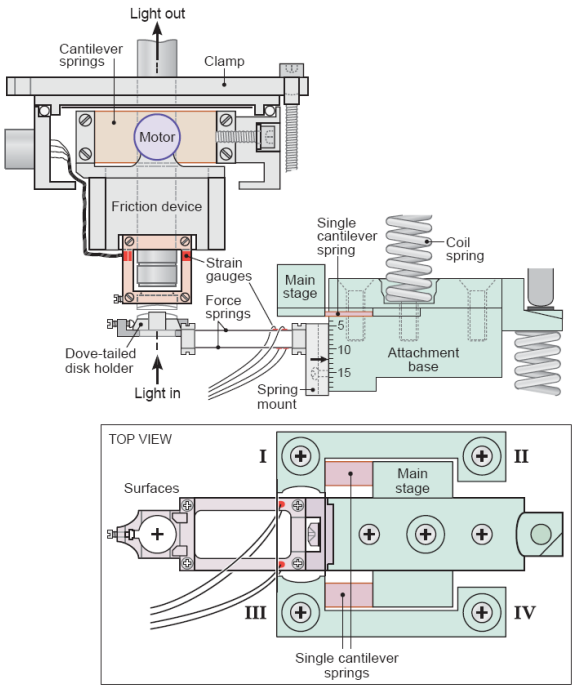

Figure 2.5 Schematic of the experimental set-up showing the main features of the 3D force-displacement-sensor attachment to the SFA 2000. This attachment allows 3D translation and (independent) force sensing.

2.2.3 Measuring normal and lateral force using strain gauges

In order to quantify the adhesion (normal forces) and friction (lateral forces) properties of surfaces, a 3D displacement and force sensing probe attachment for the surface forces apparatus (SFA) 2000 was developed (Fig. 2.5). The new attachment can generate both normal and lateral movement of surfaces, and measures the resulting normal and lateral forces independently (26). It was designed to do both, load/pull and load/drag/pull tests on fabricated micro-structures or polymer coated surfaces on a small scale with a contact area of around 0.1~1 mm^2. The actual contact area depends on the applied normal load. The bottom disk is mounted in a normal load sensor in the SFA 2000 (Fig. 2.5). The sensor has 4 foil

strain gauges (Vishay Micro- Measurements) glued symmetrically to the bending arms of the double cantilever spring, forming a Wheatstone bridge strain gauge system. When a normal force is applied to the surfaces, the strain gauges are used to measure the deflection of the spring with a signal conditioning amplifier (Vishay Measurements, 2300), which outputs the signal to either a computer data acquisition system or a chart recorder. The voltage signal is then calibrated against known weights. The top surface is held by a friction device that can move laterally with a sliding distance of between 200 and 500 μm. Driven by a reversible dc motor, the friction device can slide the upper disk back and forth smoothly with respect to the lower disk at different constant or variable speeds (1-10 μm/s) using a function generator. With the same force sensing mechanism as the normal load sensor, the friction device can measure the lateral shearing force (friction) during the sliding of the top surface (Fig. 2.5). The surfaces can also be sheared with a bimorph device that can slide laterally over a distance of 1-700 μm at different sliding speeds (0.01-200 μm/s). The bimorph device provides superior distance and velocity control over several orders of magnitude over the friction device.

2.3 Other experimental techniques

A number of other surface sensitive and solution phase techniques were used in this dissertation to complement the SFA experiments and investigate the physicochemical interactions in biological systems. I will describe few of the major techniques that were used in this section.

2.3.1 Atomic force microscope (AFM)

Atomic force microscope (AFM) is microscopy technique that can produce very high resolution three dimensional images of surfaces while simultaneously measuring the forces with nano-Newton resolution. The forces are measured by monitoring the deflection of a cantilever beam with a sharp tip or colloidal probe attached on the force measuring end of the beam. AFM was developed by Gerd Binnig and Heinrich Rohrer who shared the Nobel Prize in physics in 1986 for the scanning tunneling microscope (STM). While STM requires an electrically conductive surface, AFM can operate on all types of surfaces regardless of its conductivity. In this dissertation, AFM technique was used to investigate and characterize the properties of surfaces with adsorbed proteins and for determining the roughness of surfaces.

2.3.2 X-Ray Photoelectron Spectroscopy (XPS)

X-Ray Photoelectron Spectroscopy (XPS) is a surface sensitive spectroscopic technique that can be used to measure quantitatively the elemental composition of surfaces upto a depth of ~ 20 nm from the external interface. It can be used to determine the composition, empirical formula, chemical state and electronic state of the atoms in a material. XPS spectra are obtained by irradiating a sample with high energy X-rays at different grazing angles while simultaneously measuring the number and the kinetic energy of the electrons that are emitted. This data can be translated into the binding energy of the electrons in the molecules that make the material and used to determine the elemental compositions and the bonding states of the constituent elements. In this dissertation, XPS was used to characterize the chemistry of the surfaces used for SFA experiments.

2.3.3 Cyclic voltammetry (CV)

Cyclic voltammetry (CV) is an electrochemical technique that used electric potential energy to investigate the oxidation-reduction behavior of molecules in a solution. It is a potentiodynamic technique and many workers refer to it as linear sweep voltammetry (LSV). A CV set up consists of a three electrode system: Working electrode (WE), counter electrode (CE) and a reference electrode (RE). WE can be made of a carbon paste material or could be a gold electrode. In a typical CV experiment, the potential of the working electrode is cycled between two set potentials boundaries in a triangular wave fashion at different rates (typically 1 mV/s to 1 V/s) and the resulting current at the working electrode is measured with time. These experiments have proven to be very useful in obtaining useful information about complicated reactions at an electrode surface. Here, I used CV measurements to determine the redox stability of proteins and synthetic molecules.

2.3.4 Quartz crystal microbalance with dissipation (QCM-D)

Quartz crystal microbalance (QCM) is a surface sensitive technique that measures the change in resonant frequency of a vibrating quartz crystal upon adsorption of material to a surface. The quartz crystal is vibrated by applying a voltage across it at its resonant frequency. The resonant frequency of the crystal decreases when the mass of the chip increases (due to adsorption of molecules on its surface), which can be converted to adsorbed mass Δm using the Sauerbrey equation:

$$\Delta m = -\frac{A_c \Delta f \sqrt{\rho_q \mu_q}}{2 f_0^2} \qquad 2.10$$

where A_c is the area of the crystal, Δf is the change in frequency, ρ_q is the density of quartz (2.648 g/cm^3), μ_q is the shear modulus of quartz (2.947×10^{11} g/cm·s^2) and f_0 is the resonant

frequency of the crystal. The Sauerbrey equation assumes the adsorbed mass is rigid, uniformly distributed across the crystal and the frequency shift is less than 2% of the resonant frequency. Quartz crystal microbalance with dissipation (QCM-D) is an extension to the QCM technique developed by Q-Sense® and can be used to determine the rigidity/softness and the viscoelastic properties of the adsorbed material. The QCM quartz crystal can be coated with different rigid materials (e.g., metals, polymers, dielectrics) and the adsorption kinetics can be monitored on these materials in liquid environment. Modeling of the Δf and ΔD at different overtones also allows for the calculation of thin film viscosities, shear modulus, thicknesses, hydrations etc. of the adsorbed layers. In this dissertation, QCM-D was used to measure the adsorption of proteins, peptides and synthetic molecules onto titania and silica surfaces.

2.4 References

1. Israelachvili JN (2011) Intermolecular and Surface Forces, 3rd Edition. *Intermolecular and Surface Forces, 3rd Edition*:1-674.
2. Leckband D & Israelachvili J (2001) Intermolecular forces in biology. *Quarterly reviews of biophysics* 34(02):105-267.
3. Hogg R, Healy T, & Fuerstenau D (1966) Mutual coagulation of colloidal dispersions. *Transactions of the Faraday Society* 62:1638-1651.
4. Wiese G & Healy T (1970) Effect of particle size on colloid stability. *Transactions of the Faraday Society* 66:490-499.
5. Das S, Donaldson SH, Kaufman Y, & Israelachvili JN (2013) Interaction of adsorbed polymers with supported cationic bilayers. *Rsc Advances* 3(43):20405-20411.

6. Sheinerman FB, Norel R, & Honig B (2000) Electrostatic aspects of protein–protein interactions. *Current opinion in structural biology* 10(2):153-159.

7. Riccardi D, König P, Guo H, & Cui Q (2008) Proton transfer in carbonic anhydrase is controlled by electrostatics rather than the orientation of the acceptor. *Biochemistry* 47(8):2369-2378.

8. Träuble H & Eibl H (1974) Electrostatic effects on lipid phase transitions: membrane structure and ionic environment. *Proceedings of the National Academy of Sciences* 71(1):214-219.

9. Grantcharova VP, Riddle DS, Santiago JV, & Baker D (1998) Important role of hydrogen bonds in the structurally polarized transition state for folding of the src SH3 domain. *Nature Structural & Molecular Biology* 5(8):714-720.

10. Perrin CL & Nielson JB (1997) "Strong" hydrogen bonds in chemistry and biology. *Annual review of physical chemistry* 48(1):511-544.

11. Gerlt JA, Kreevoy MM, Cleland W, & Frey PA (1997) Understanding enzymic catalysis: the importance of short, strong hydrogen bonds. *Chemistry & biology* 4(4):259-267.

12. Nicklisch SCT, Das S, Rodriguez NRM, Waite JH, & Israelachvili JN (2013) Antioxidant Efficacy and Adhesion Rescue by a Recombinant Mussel Foot Protein-6. *Biotechnology Progress* 29(6):1587-1593.

13. Lin Q, *et al.* (2007) Adhesion mechanisms of the mussel foot proteins mfp-1 and mfp-3. *Proceedings of the National Academy of Sciences of the United States of America* 104(10):3782-3786.

14. Garde S & Patel AJ (2011) Unraveling the hydrophobic effect, one molecule at a time. *Proceedings of the National Academy of Sciences* 108(40):16491-16492.

15. Setny P, Baron R, Kekenes-Huskey PM, McCammon JA, & Dzubiella J (2013) Solvent fluctuations in hydrophobic cavity–ligand binding kinetics. *Proceedings of the National Academy of Sciences* 110(4):1197-1202.

16. Dill KA, Truskett TM, Vlachy V, & Hribar-Lee B (2005) Modeling water, the hydrophobic effect, and ion solvation. *Annu. Rev. Biophys. Biomol. Struct.* 34:173-199.

17. Chandler D (2005) Interfaces and the driving force of hydrophobic assembly. *Nature* 437(7059):640-647.

18. De Gennes P (1987) Polymers at an interface; a simplified view. *Advances in Colloid and Interface Science* 27(3):189-209.

19. Dolan A & Edwards S (1974) Theory of the stabilization of colloids by adsorbed polymer. *Proceedings of the Royal Society of London. A. Mathematical and Physical Sciences* 337(1611):509-516.

20. Hunter CA & Sanders JK (1990) The nature of. pi.-. pi. interactions. *Journal of the American Chemical Society* 112(14):5525-5534.

21. Mecozzi S, West AP, & Dougherty DA (1996) Cation-pi interactions in aromatics of biological and medicinal interest: electrostatic potential surfaces as a useful qualitative guide. *Proceedings of the National Academy of Sciences* 93(20):10566-10571.

22. Tabor D & Winterton R (1969) The direct measurement of normal and retarded van der Waals forces. *Proceedings of the Royal Society of London. A. Mathematical and Physical Sciences* 312(1511):435-450.

23. Israelachvili J & Tabor D (1972) The measurement of van der Waals dispersion forces in the range 1.5 to 130 nm. *Proceedings of the Royal Society of London. A. Mathematical and Physical Sciences* 331(1584):19-38.

24. Israelachvili J & Tabor D (1973) The shear properties of molecular films. *Wear* 24(3):386-390.

25. Israelachvili J & Pashley R (1982) The hydrophobic interaction is long range, decaying exponentially with distance.

26. Israelachvili J, *et al.* (2010) Recent advances in the surface forces apparatus (SFA) technique. *Reports on Progress in Physics* 73(3).

27. Israelachvili J (1973) Thin-Film Studies Using Multiple-Beam Interferometry. *Journal of Colloid and Interface Science* 44(2):259-272.

3. TOUGH COATING PROTEINS: SUBTLE SEQUENCE VARIATION MODULATES COHESION

3.1 Abstract

Mussel foot protein-1 (mfp-1) is an essential constituent of the protective cuticle covering all exposed portions of the byssus (plaque and the thread) that marine mussels use to attach to intertidal rocks. The reversible complexation of Fe^{3+} by the 3, 4-dihydroxyphenylalanine (Dopa) side-chains in mfp-1 in *Mytilus californianus* cuticle is speculated to be responsible for its high extensibility (120%) as well as its stiffness (2 GPa). We have investigated the interactions between Fe^{3+} and mfp-1 from two mussel species, *M. californianus* (*Mc*) and *M. edulis* (*Me*), using both surface sensitive and solution phase techniques. Our results show that although *mfp-1* homologs from both species bind Fe^{3+}, *mfp-1* (*Mc*) contains Dopa with two distinct Fe^{3+}-binding tendencies and prefers to form intramolecular complexes with Fe^{3+}. In contrast, *mfp-1* (*Me*) is better adapted to intermolecular Fe^{3+} binding by Dopa. Addition of Fe^{3+} did not significantly increase the cohesion energy between the *mfp-1* (*Mc*) films at pH 5.5. However, iron appears to stabilize the cohesive bridging of *mfp-1* (*Mc*) films at the physiologically relevant pH of 7.5, where most other *mfps* lose their ability to adhere reversibly. Understanding the molecular mechanisms underpinning the capacity of *M. californianus* cuticle to withstand twice the

strain of *M. edulis* cuticle is important for engineering of tunable strain tolerant composite coatings for biomedical applications.

3.2 Introduction: Mussel foot coating protein

Protective coatings are used in manufacturing to improve the abrasion, scratch, corrosion, and ultraviolet-light resistance of target surfaces and thereby adds significantly to product performance and value. Current coating applications based on polymers are limited by the high modulus/low strain (epoxies) or low modulus/high strain (polyurethanes) of available polymers (1, 2) but could be significantly diversified with polymers that were both stiff and extensible. The naturally occurring polymeric coatings of mussel byssus have a modulus of 2 GPa and strains of about 75% and 120 % in *Mytilus galloprovincialis* (*Mg*) (3) and *Mytilus californianus* (*Mc*) (4), respectively, making them among the most energy tolerant coatings known. Previous characterizations of byssal coatings have detected Fe^{3+} and a 3, 4-dihydroxyphenylalanine (Dopa) -containing protein known as mussel foot protein 1 (mfp-1) (5, 6). Resonance Raman microscopy indicates that Fe^{3+} and Dopa are coupled as tris-catecholato-Fe^{3+} complexes in the coatings and are proposed to provide reversible protein cross-links between mfp-1 proteins (7). This cross-linking has been recapitulated in vitro in mixtures of isolated mfp-1 and Fe^{3+} (8) and increases the stiffness of mfp-1 gels (9). Similar results were obtained with synthetic and natural catechol-functionalized polymers and Fe^{3+} (10-12) and metal cations (13). More recently, Dopa -Fe^{3+} complexes were proposed to contribute to the strong and reversible iron-dependent cohesion energy (~4 mJ/m^2) between two monolayers of mfp-1 from *M. edulis* (14).

Homologous proteins from closely related species often provide unique opportunities for gaining mechanistic insights into structure-function relationships (15, 16). In this spirit, we investigated the cohesive and adhesive properties of an mfp-1 homolog from a related mussel, *M. californianus* (*Mc*), whose byssal coating has an ultimate strain in excess of 120% (3, 4) and also contains Dopa -Fe^{3+} complexes. Mfp-1 from both species consists of tandem decapeptide repeats: the consensus decapeptide PKISYP**P*TY*K (where P*, P**, and Y* denote *trans*-4-hydroxyproline, dihydroxyproline, and Dopa, respectively) in *Mc* is highly similar to AKPSYP**P*TY*K in *Me* and *Mg* (17, 18); indeed, apart from the inverted order of the first three amino acids, the only net change is an A$\rightarrow$ I substitution. A preliminary study of cohesion in two symmetric *Mc* mfp-1 monolayers using the surfaces forces apparatus (SFA) showed significantly greater intrinsic cohesion than its homolog from *Me* (cohesion energy, W_c ~ 1.7-3.4 mJ/m^2 in *Mc* vs W_c ~ 0 in *Me*) (19). Given the prominence of *mfp-1* and iron in the composite structure of byssal cuticle, we investigated the protein- and Fe^{3+} concentration-dependent cohesion of *mfp-1* at different pH values. Despite their similar sequences, *mfp-1* (*Mc*) and *mfp-1* (*Me*) films exhibit strikingly different cohesive properties with and without Fe^{3+} in the surface forces apparatus. Understanding these differences will help inspire the design of future biomimetic polymers or recombinant mfp-1 proteins for bio-medical and functional coatings (20).

3.3 Materials and Methods

3.3.1 Purification of *mfp-1*

Mfp-1 (*Mc*) was purified as described previously (21) with some modifications. Breifly, mussels were harvested off Goleta Pier, (Santa Barbara, CA), and held in circulation

tanks. The mussles were shucked and the foot was severed from the body and frozen to -70°C before fileting off the pigmeted epithelium. Approximately 50 prepared feet were homoginized in four equivalets (w/v) of 5% acetic acid (v/v), 10 μM leupeptin, 10 μM pepstatin, and 1mM EDTA in a glass Kontes tissue grinder (Vineland, NJ) on ice and centrifuged at 20,000 X g, 4°C for 40 min. The supernatant was acidified with 70 % perchloric acid to a final concentration of 1.5% (v/v). After centrifugation at 20,000 X g, 4°C for 40 min, the supernatant was dyalized 4 X 4L of 5% acetic acid (v/v) for four hours and overnight with in Spectrum Industries 1,000 KDa molecular weight cutoff dialysis tubing (Los Angeles, Ca) before freeze drying. The lyophilized protein was resuspended in 200 μl of 5% acetic acid (v/v) and 50 μl aliquots were run over a Shodex KW-803 size exclusion column (5 μm, 8 x 300 mm) (New York, NY). Fractions were monitored at 280 nm and those positive for protein were subjected to acid-urea polyacrylamide gel electrophoresis (7.5% acrylamide and 0.2% N, N-methylenebisacrylamide) containing 5% acetic acid and 8 M urea (22). After electrophoresis, gels were stained with Sigma-Aldrich Coomassie Blue R-250 (Brooklyn, NY). Pure *mfp-1* (*Mc*) fractions were pooled and aliquoted before freeze-drying and stored at -70°C for future use.

3.3.2 Measuring the adhesive/cohesive interactions

The surface forces apparatus (SFA, SurForce LLC) was used to measure the normal forces between two mica surfaces in a cross-cylindrical geometry as a function of the separation distance, *D*, between them and has been described elsewhere (23, 24). *Mfp-1* (*Mc*) films were made by adsorbing 50 μL of the protein from a C_{fp1} = 10-100 μg/ml in a buffer solution (0.1 M sodium acetate buffer, pH 5.5, 0.25 M KNO_3, and 1 mM bis-tris) onto the

mica surfaces for 30 minutes, then rinsing the excess protein with the same buffer. During the protein adsorption, the discs were kept in a saturated Petri dish to minimize evaporation of the water from the surfaces. The discs were then mounted in the SFA in one of two configurations. In an asymmetric configuration, the mussel protein was adsorbed on one surface in order to measure the interaction (*adhesion*) between the *mfp-1* (*Mc*) film and the mica surface.

In a symmetric configuration (Fig. 3.1), the mussel protein film was deposited on both surfaces in order to measure *cohesion* between the protein films. Cohesion was tested with and without iron. Iron solutions 1, 10, 100 μM $FeCl_3$ in acetate buffer (as above) were freshly made and added to the symmetrically deposited protein by injection of progressively higher concentrations of Fe^{3+} between the surfaces. The pH of the solution between the surfaces was increased to 7.5 by rinsing with a phosphate buffer (0.1 M potassium phosphate, pH 7.5, 0.25 M KNO_3).

The protein films were always hydrated (i.e. never allowed to dry) and a droplet of the acetate buffer was injected between the surfaces immediately after loading in the SFA. During a typical approach-separation force measurement cycle, the surfaces were first moved towards each other (approach) until reaching a "hardwall" and then separated. The hardwall distance is the separation distance between the two mica surfaces upon compression that does not change with increased compression. The energy of interaction between two crossed-cylinder geometry, roughly corresponds to a sphere of radius R approaching a flat surface based on the Derjaguin approximation, $W(D) = F(D) / 2\pi R$ where, $W(D)$ is the energy of interaction per unit area between two flat surfaces and $F(D)$ is the measured force of interaction in the SFA. The measured adhesion (or cohesion) force F_{ad} (or F_c) is related to the

adhesion (or cohesion) energy per unit area by $W_{ad} = F_{ad} / 2\pi R$ for rigid surfaces with weak adhesive interactions, and by $W_{ad} = F_{ad} / 1.5\pi R$ (used in this study) for soft deformable surfaces with strong adhesion or cohesion (25, 26).

3.3.3 AFM imaging proteins at the interface

Images were acquired using MFP-3D-Bio Atomic Force Microscope **(**AFM, Asylum Research) using SNL probe (Bruker) in tapping mode at room temperature (22 °C). *Mfp-1* (*Mc*) was deposited on a mica surface (area ~ 1 cm^2) by adsorbing 50 µL of the protein from a 10, 25, 50 and 100 µg/ml in the buffer solution at pH 5.5.

3.3.4 Cyclic Voltammetry (CV)

The CV measurements were performed using a three electrode electrochemical setup consisting of a carbon paste working electrode (WE), platinum counter electrode (CE) and a Ag|AgCl (3N KCl) reference electrode (RE) and has been described elsewhere (27). The electrochemical potential was controlled using a Gamry potentiostat (Reference 600 Series). 5 µL of 50 µg/ml of the *mfp-1* (*Mc*) (or 10 µL of 20-100 µg/ml *mfp-1* (*Me*) was dissolved in 1 ml buffer solution (10 mM NaCl and pH 3.7) and a triangular wave potential sweep was applied on the WE between chosen negative and positive limits and the cycle was repeated 3 times form measuring CV profiles. Higher concentrations of *mfp-1* (*Me*) were used for the measurements to get a Dopa oxidation current peak similar or more than the *mfp-1* (*Mc*). This strategy provides a better understanding of the Dopa-Fe complexation mechanism in the proteins and has been discussed in the results and discussion sections. The measurements

were also done in the buffer solution with 10 μM Fe^{3+} to test the effect of ferric ions on the oxidation behavior of the proteins.

3.4 Results

3.4.1 Cohesive interactions between the *mfp-1* (*Mc*) films

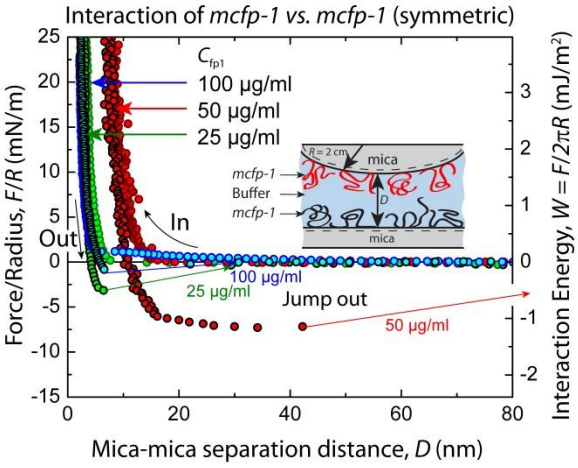

Figure 3.1 Cohesion between two symmetric *mfp-1* (*Mc*) films. Representative force *vs.* distance plots for *mfp-1* (*Mc*) films at three protein concentrations (C_{fp1} = 25, 50 and 100 μg/ml in 0.1 M sodium acetate buffer, pH 5.5, 0.25 M KNO_3, and 1 mM bis-tris).

Our first challenge in any study involving surface forces between symmetric films was to optimize protein concentrations for film deposition. The cohesion between two symmetrically deposited *mfp-1* (*Mc*) films on the mica surfaces was measured using the SFA (symmetric system, see Fig. 3.1). Protein deposition from a solution concentration of C_{fp1} = 10 μg/ml resulted in no attraction between the protein films. Increasing the protein solution concentration to 25 μg/ml resulted in a cohesion energy of W_c = 0.59 ± 0.20 mJ/m^2 between the films (Fig. 3.2). A further increase to 50 μg/ml doubled the cohesion (W_c = 1.24 ± 0.40

mJ/m^2). At C_{fp1} = 100 µg/ml, cohesion decreased significantly to W_c = 0.18 ± 0.04 mJ/m^2 (Fig. 3.2). The surfaces exhibited poor bridging *cohesion* (28) at C_{fp1} = 25 and 100 µg/ml compared with *mfp-1* (*Mc*) bridging at C_{fp1} ~ 50 µg/ml (Fig. 3.1).

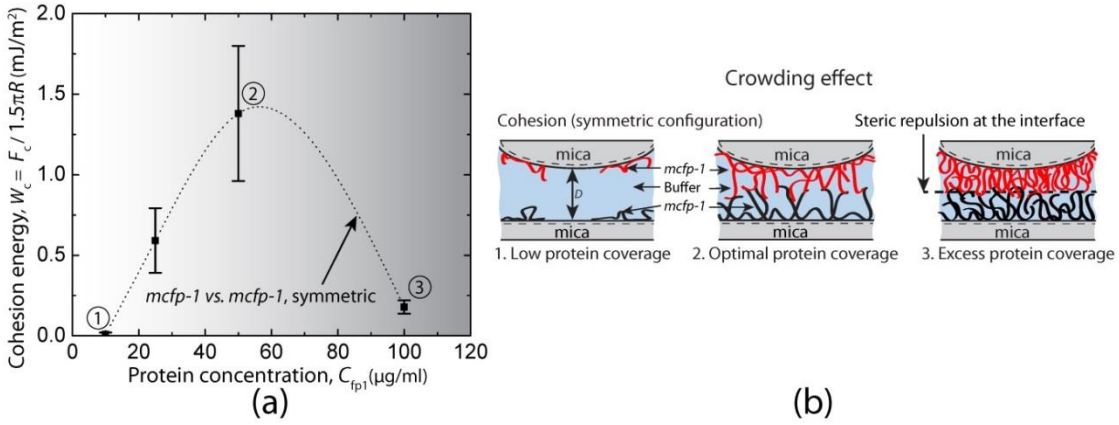

Figure 3.2 Concentration-dependence of cohesion between two symmetric *mfp-1* (*Mc*) films. (a) Effect of protein deposition concentration on the cohesion (*mfp-1* (*Mc*) *vs. mfp-1* (*Mc*), symmetric) energies of interaction between the surfaces. (b) Schematic representations of the crowding effect for cohesion. For clarity, the protein molecules on the upper and lower mica surfaces are shown in red and black colors, respectively.

Interestingly, addition of Fe^{3+} did not change the cohesion force measured between the *mfp-1* (*Mc*) films significantly for C_{Fe3+} = 0-100 µM (Fig. S3.1). These results are in stark contrast to the behavior of *mfp-1* (*Me*), a homolog from *M. edulis*, where at pH 5.5, 10 µM Fe^{3+} caused two non-interacting *mfp-1* (*Me*) protein films to bridge (14). In any given experiment, Fe^{3+} expanded the *mfp-1* (*Mc*) film on the mica surface progressively with increasing C_{Fe3+}. The thickness of the *mfp-1* (*Mc*) film deposited at 50 µg/ml increased from 8.5 nm to 15 nm between C_{Fe3+} = 0 µM and 100 µM, respectively (Fig. S3.1).

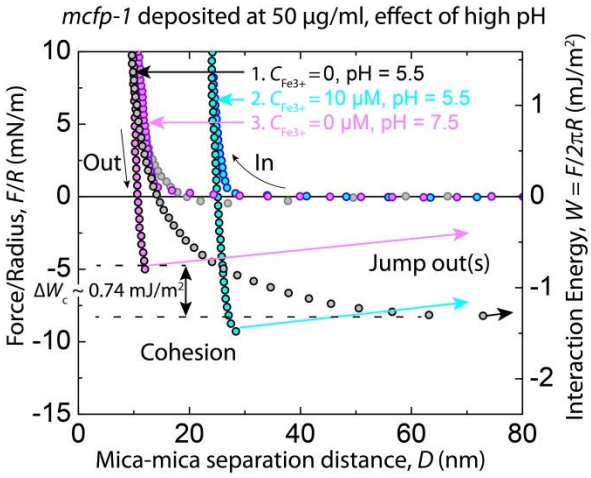

Figure 3.3 pH dependence of Fe^{3+}-mediated cohesion between two symmetric *mfp-1* (*Mc*) films. Representative force *vs.* distance plot showing the interaction between two symmetric *mfp-1* (*Mc*) films deposited at 50 µg/ml in 0.1 M sodium acetate buffer, pH 5.5, 0.25 M KNO_3, and 1 mM bis-tris with C_{Fe3+} = 0 µM (gray), and 100 µM (blue) at pH 5.5. The cohesion between the *mfp-1* (*Mc*) films was preserved after increasing the pH to 7.5 (magenta).

Addition of Fe^{3+} has a peculiar effect on cohesion between the protein films even after increasing the pH of the solution to 7.5 (Fig. 3.3). Previous studies of a variety of *mfps* have reported a short-term cohesion loss that was attributed to the oxidation of Dopa to Dopa-quinone (29-31) but these were done without added Fe^{3+}. With *mfp-1* (*Mc*) alone, cohesion at pH 5.5 was robust (W_c ~ 1.4 mJ/m^2) with a gradually increasing separation force. Addition of Fe^{3+} at pH 5.5 expanded the mfp-1 films from 8 to about 15 nm and stiffened them without changing the cohesion energy. This is consistent with extensive mono-complexation of Fe^{3+} leading to *mfp-1* (*Mc*) film swelling. Switching the pH up to 7.5 will flush out the unbound iron but increase Dopa complexation to the tris catecholate-Fe^{3+} mode

hence condensing the films back to ~8 nm. There was no correlation between the *mfp-1* (*Mc*) film thickness and the protein film deposition concentration (C_{fp1}) for different experiments; however, the measured trends in the adhesive/cohesive forces of interaction were consistent between experiments for similar deposition conditions.

3.4.2 Atomic Force Microscopy (AFM) images

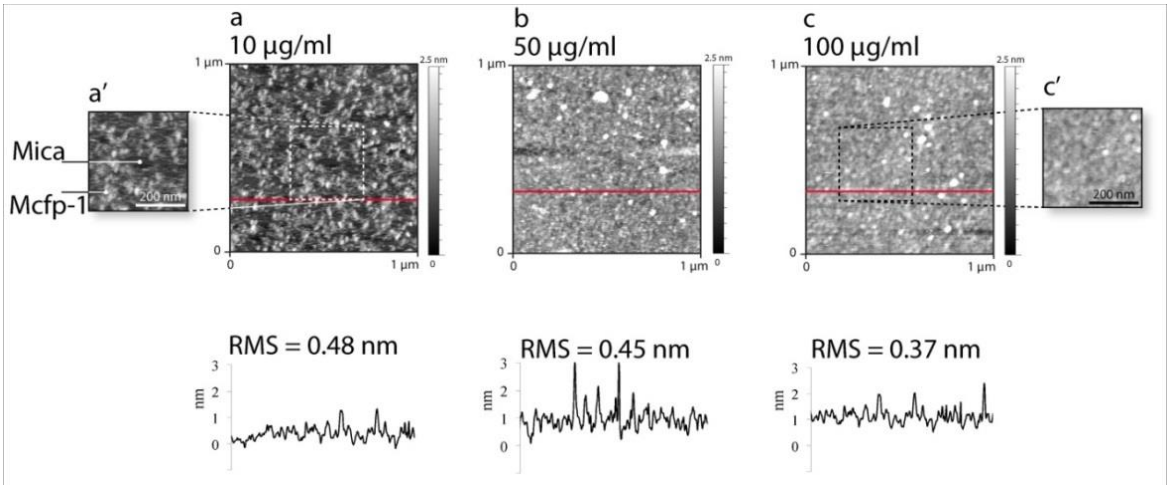

Figure 3.4 *Mfp-1* (*Mc*) films adsorbed to mica. AFM topography images and their respective cross sections (below) of *mfp-1* (*Mc*) on mica in pH 5.5 acetate buffer at different C_{fp1} = (a) 10 µg/ml (b) 50 µg/ml and (c) 100 µg/ml.

AFM was used to investigate the protein coverage on the mica surface for different C_{fp1}. Protein film deposited from a solution concentration of 10 µg/ml resulted in a partial coverage of the mica surface (Fig. 3.4a and a'). At higher C_{fp1} of 50 and 100 µg/ml, the mica surface was completely covered with the protein film (Fig. 3.4b, c and c').

3.4.3 Cyclic Voltammetry (CV) on mfp-1

CV measurements were performed on mfp-1 to investigate the oxidation behavior of the coating protein. *Mfp-1* (*Mc*) showed an oxidation peak at E_O = 0.385 V corresponding to the oxidation of Dopa to Dopa-quinone. Dopa-quinone gets reduced back to Dopa reversibly at E_R = 0.310 V (Fig. 5). *Mfp-1* (*Me*), in contrast, exhibited Dopa with slightly lower redox stability at the same conditions (E_O = 0.365 V, E_R = 0.320 V). The differences in current (*I*) merely reflect the difference in total Dopa content in the two samples.

The current amplitude (*I*) of the oxidation peak current of *mfp-1* (*Mc*) was decreased by approximately 60% when excess Fe^{3+} (10 µM) was added (Fig. 3.5). This indicates that ~1/3 of the Dopa in *mfp-1* (*Mc*) does not chelate iron and at pH 3.7 remains unbound in the protein even with excess Fe^{3+}. However, current for the Dopa *mfp-1* (*Me*) decreased by ~90% following 10 µM Fe^{3+} addition suggesting that nearly all the Dopa residues in *mfp-1* (*Me*) chelate Fe^{3+} at pH 3.7 (Fig. 3.5).

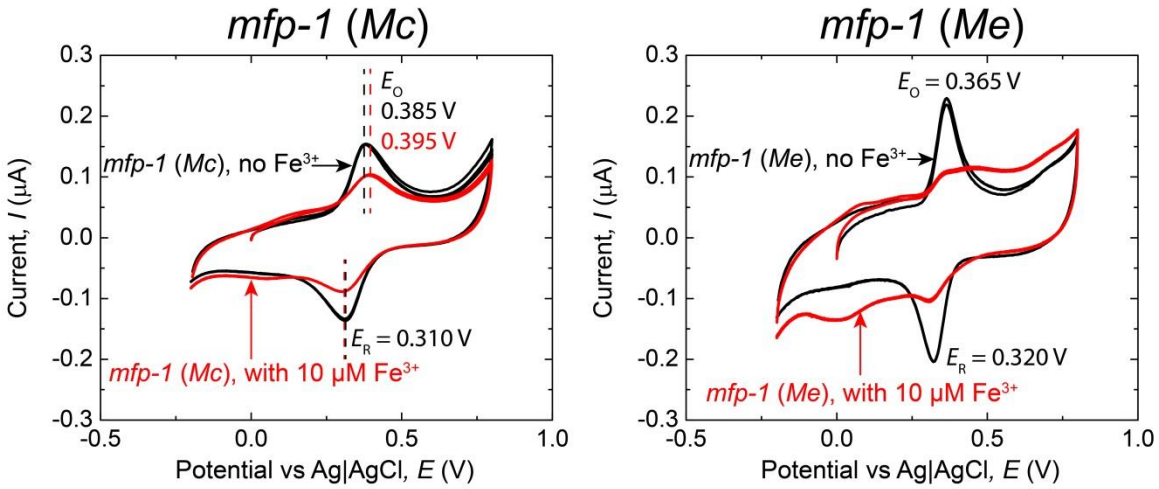

Figure 3.5 Cyclic voltammograms of *mfp-1* (*Mc*) and *mfp-1* (*Me*) with and without 10 µM ferric nitrate in the buffer solution pH 3.7 at a scan rate of 50 mV/s.

3.4.4 In solution Fe^{3+} binding by Dynamic Light Scattering (DLS)

In solution, size comparisons of *mfp-1* (*Me*) and *mfp-1* (*Mc*) by DLS (Fig. S3.2) showed similar size for *mfp-1* (*Mc*) (Diameter, d = 35 nm, Std. Dev. 20 nm) and *mfp-1* (*Me*) (d = 41 nm, Std. Dev. 22 nm) aggregates in the absence of Fe^{3+} (Fig. S3.2). Upon addition of excess iron, *mfp-1* (*Me*) showed an increase in the peak intensity corresponding to the larger aggregate size (d ~ 277 nm), whereas *mfp-1* (*Mc*) showed no change in size. However, the peak intensity corresponding to the smaller aggregate size increased upon the addition of iron to the *mfp-1* (*Mc*) solution suggesting that *mfp-1* (*Mc*) monomers are stabilized by Fe^{3+}. The increase in the peak intensities of the larger aggregates in *mfp-1* (*Me*)–iron solution is consistent with its tendency to form intermolecular Fe^{3+} bonds.

3.5 Discussion

M. edulis and *M. californianus* both make byssal threads coated with a hard energy-tolerant cuticle. That the toughness of *M. californianus* coating is much greater than that of *M. edulis* is due in large part to the former's greater breaking strain (~120% *vs*. 75%). The coatings of both species are particle-filled composites; however, average particle diameters in *M. californianus* cuticle are less than a quarter of those in *M. edulis*. This is important because strain in both cuticles is enabled by micro-cracking at the interface between the matrix and particles and, because *M. californianus* affords 5 times more particle surface area per unit volume, more interfacial cracks can occur resulting in greater overall strain. Presented in this light, the overarching engineering question can be reduced to 'how does *M. californianus* make smaller particles'?

As the particles or granules are enriched in Fe^{3+} and mfp-1 relative to the continuous matrix (7), a reasonable hypothesis is that the assembly of *mfp-1* in the two species into small or large granules is protein-templated. As established in the Introduction, molecular differences between the two *mfp-1s* seem slight: both consist of tandemly repeated decapeptides that are 80% identical and have a net change of only one amino acid side chain, that is, Ala (in *Me*) to Ile (in *Mc*). Conformation of the repeat decapeptide sequence has been investigated only for the *Me* sequence. A polyproline II or bent-helix has been proposed (32, 33) in which Dopa-5 is less solvent exposed than Dopa-9 (34). Dopa exposure is important for forming the *mono-*, *bis-*, and *tris*-catecholate complexes with Fe^{3+} (8) with a cumulative log stability of $K_s \sim 10^{45}$ (35), thereby effectively cross-linking mfp-1 (7, 14).

In contrast to previous SFA studies of mfps, we optimized conditions for *mfp-1* (*Mc*) deposition from stock solutions (range 0-100 µg/ml) in order to obtain the highest adhesion or cohesion. Following these regimens, SFA testing of symmetric *mfp-1* (*Mc*) films showed significant cohesion (up to -1.5 mJ/m^2) in contrast to *mfp-1* (*Me*), which had little to no tendency for self-interaction at similar conditions (14). As with other mfps, cohesion was compromised at pH 7.5 (due to Dopa oxidation), however, with added Fe^{3+}, intrinsic cohesion was maintained. Notably, the strong Fe^{3+}-mediated bridging of symmetric *mfp-1* (*Mc*) films of the type associated with *Me* (W_c = 4 mJ/m^2) was absent. This absence persisted at all conditions tested for Fe^{3+} (C_{Fe3+} = 1-100 µM) and *mfp-1* (*Mc*) C_{fp1} = 50-100 µg/ml (Fig. S3.1 and S3.5).

Effective load bearing and load transfer between the opposing *mfp-1* films on mica require both, strong cohesion between the two *mfp-1* films and *mfp-1* adhesion to mica. Generally speaking, at pH 5.5, *mfp* adhesion to mica is strong and attributed to electrostatic

attraction between cationic amines (Lys) and surface siloxy anions as well as extensive bidentate hydrogen bonding between the Dopa and the polysiloxy mica surface (26, 29, 30). The cohesion typically observed between symmetrically deposited *mfp* films is attributed to π-cation interactions between the positively charged Lys residues and the aromatic Dopa and Tyr groups as well as π– π interactions between the phenyl groups (19, 25, 26, 36), however, this cohesion is weak in symmetric *mfp-1* (*Me*) (37). Perhaps, *mfp-1* (*Me*) over-recruits Dopa groups to the mica surface, leaving only the Lys groups to face one another in repulsion (37). Given the sequence similarity of *mfp-1* in the two species this should be a cohesive problem for both proteins. As *mfp-1*(*Mc*) has good cohesion and *mfp-1* (*Me*) does not, the subtle sequence difference may result from fewer Dopa groups recruited to mica leaving more to contribute to cohesion in *mfp-1* (*Mc*).

3.5.1 Effect of Fe^{3+} on the cohesive interactions between the *mfp-1* (*Mc*) films

Most notably, Fe^{3+} addition (C_{Fe3+} = 1-100 μM) did not affect the cohesive energy measured between the *mfp-1* (*Mc*) films deposited at C_{fp1} = 50-100 μg/ml (Fig. S3.1 and S3.5). This is in stark contrast to the Fe^{3+} mediated bridging energy between two *mfp-1* (*Me*) films at ~2-5 mJ/m^2 (Fig. S3.6) (14). DLS results (Fig. S3.2) show that Fe^{3+} addition enhances aggregation in *mfp-1* (*Me*), but not in *mfp-1* (*Mc*). Cyclic voltammetry suggests that only half of the Dopa groups in *mfp-1* (*Mc*) are engaged in forming catecholato-Fe^{3+}-complexes at pH 3.7. At least 30-40 % of the Dopa in *mfp-1* (*Mc*) remains unbound and available for oxidation to Dopaquinone or coordinates Fe^{3+} only at higher pH. The latter is more probable. Dopa certainly occurs in two slightly different repeat sequences within *mfp-1*, *i.e.* P*-S-Dopa-P for Dopa-5 and P*-T-Dopa-K for Dopa-9, but these are common to both

Me and *Mc* homologs. The only evidence for a functional difference between the two sequence motifs is that the 9-position is 2-3 times more accessible enzymatic modification than the 5-position in *mfp-1* (*Me*) (38).

The increased accessibility of Dopa-9, particularly as Dopa-Lys, is likely to be an important factor in *mfp* adhesion as measured by the SFA. More than half the Dopa in the strongly adhesive proteins, *mfp-3f* and *mfp-5*, has Lys or Arg groups flanking Dopa on one or both sides. If the same accessibility that helps Dopa chelate Fe^{3+} in *mfp-1* (*Mc*) also helps binding to the mica crystal lattice, then, when a surface and Fe^{3+} are both present, there will be competition for accessible Dopa. In pre-adsorbing *mfp-1* (*Mc*) to mica, many of the accessible Dopa residues are recruited to bind mica. Are the bound and/or unbound Dopa groups available for coordination to Fe^{3+}? According to resonance Raman spectroscopy (Fig.S8), the shifts associated with Dopa-Fe^{3+} complexes have similar intensities in mfp-1 films prepared from both *Me* and *Mc*. Cyclic voltammetry, however, identifies distinct Dopa groups in *mfp-1* (*Mc*) that do not bind iron (Fig. 5). The contribution of the non-Fe^{3+} binding Dopa to cohesion between opposing *mfp-1* (*Mc*) films must be significant.

It is now possible to model cohesive interactions with and without Fe^{3+} in *mfp-1* for the two species (Fig. 3.6). Without added Fe^{3+}, *mfp-1* (*Mc*) has fewer Dopa groups recruited to the mica surface, so Dopa is available for H-bonding, π-cation and π-π interactions with the opposing face. With added Fe^{3+}, *mfp-1* films of both species are endowed with extensive mono-, bis-, and tris-catecholate-Fe^{3+} complexes, however, these are primarily intermolecular in *mfp-1* (*Me*) and intramolecular in *mfp-1* (*Mc*) (Fig. 6). As a result, only *mfp-1* (*Mc*) exhibits significant cohesive bridging without Fe^{3+}, whereas only *mfp-1* (*Me*) has Fe^{3+}-mediated bridging in the presence of Fe^{3+}.

Taken together, the results suggest that although *mfp-1s* from both species complex Fe^{3+} (confirmed by resonance Raman analysis), *mfp-1* (*Mc*) is better adapted to accumulate Fe^{3+} as a monomer, whereas *mfp-1* (*Me*) aggregates as it accumulates Fe^{3+}. These differences in Fe^{3+} binding predict that symmetric films of *mfp-1* (*Me*) in the SFA should show excellent bridging cohesion with Fe^{3+}, whereas *mfp-1* (*Mc*) should not. The differences might also predict that granules made from *mfp-1* (*Me*) would grow to a larger size that those from *mfp-1* (*Mc*). Both predictions are realized.

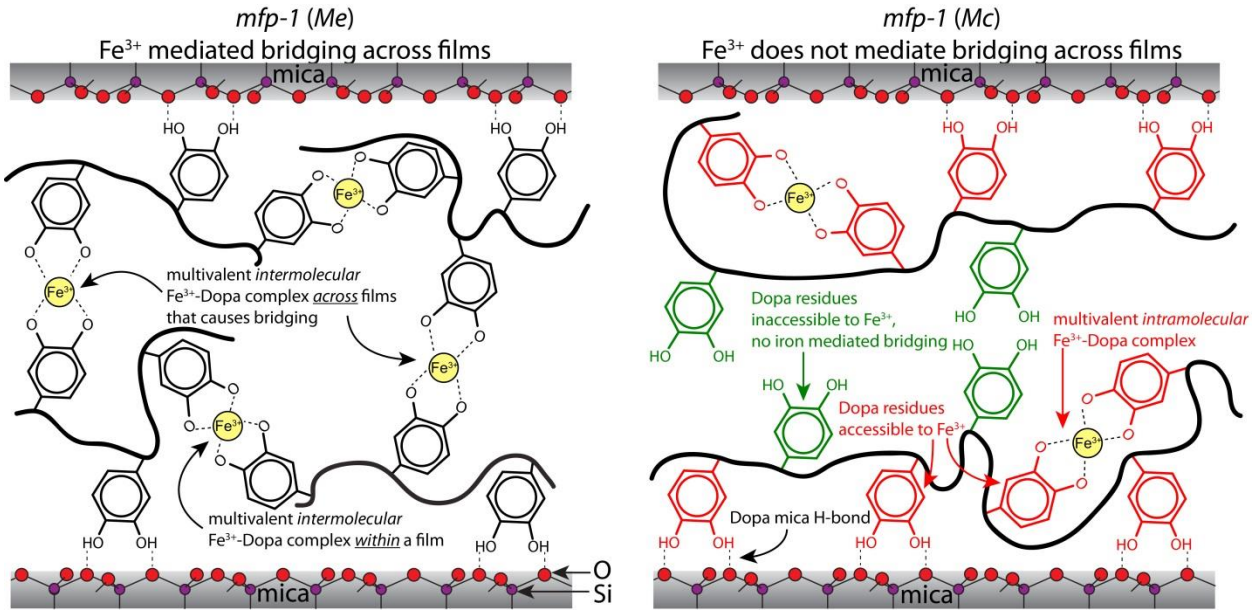

Figure 3.6 Molecular schematics of *mfp-1* (*Me*) and *mfp-1* (*Mc*) films on mica showing the interaction of the Dopa side chain with Fe^{3+}. The multivalent Fe^{3+}-Dopa complex is indicative of bis and/or tris mode of catecholato-Fe^{3+} coordination. The contribution of Lys and other amino acid residues is not shown for the sake of clarity.

In the presence of Fe^{3+}, each *mfp-1* (*Mc*) molecule is inclined to collapse whereas *mfp-1* (*Me*) reaches out to share Fe^{3+} with other *mfp-1* (*Me*)s. cDNA-deduced protein sequences of *mfp-1* (*Mc*) (39) and *mfp-1* (*Me*) (40) show that there is a subtle difference in

the decapeptide repeat in the two proteins (See supporting Fig. S3.9). The Ala→ Ile substitution in the consensus decapeptide repeat of *mfp-1* (*Mc*) could be responsible for limiting the accessibility of Dopa to Fe^{3+}. Possibly, the hydrophobic interaction between Ile-3 and Dopa-5 in *mfp-1* (*Mc*) results in a different assembly. An intriguing biological consequence of this is that the granules in the *M. californianus* (*Mc*) byssal cuticle are much smaller (~80%) than those in *M. edulis* (*Me*, and its congener *Mg*) (4) and able to withstand almost twice the strain of those in *M. edulis* (3, 4).

3.6 Conclusions

Cohesive interactions between thin films of *mfp-1* (*Mc*) were shown to depend strongly on the protein concentrations used for surface deposition and are maximal on mica at C_{fp1} ~ 50 µg/ml. Cohesion of mfp-1 revealed striking differences upon Fe^{3+} addition. In the range of C_{Fe3+} = 0-100 µM at pH 5.5, *mfp-1* (*Mc*) films seem well adapted for intramolecular iron binding in contrast to the intermolecular binding of *mfp-1* (*Me*). However, stabilizes the bridging between the *mfp-1* (*Mc*) films at pH 7.5, where most of the mussel foot proteins lose adhesion. The Lys residues flanking Dopa in mfp-1 sequences may be critical to determining the accessibility of Dopa for surface interactions and Fe^{3+} binding. Also the Alanine (A) → Isoleucine (I) substitution in the consensus decapeptide repeat may be responsible for creating two electrochemically distinct Dopa reactivities. Thus, metal chelation, with the right molecular architecture for a peptide chain can be used as a potential strategy to exploit mfp-1 mimetic biomacromolecules at physiological pH for wet adhesive applications.

3.7 Appendix

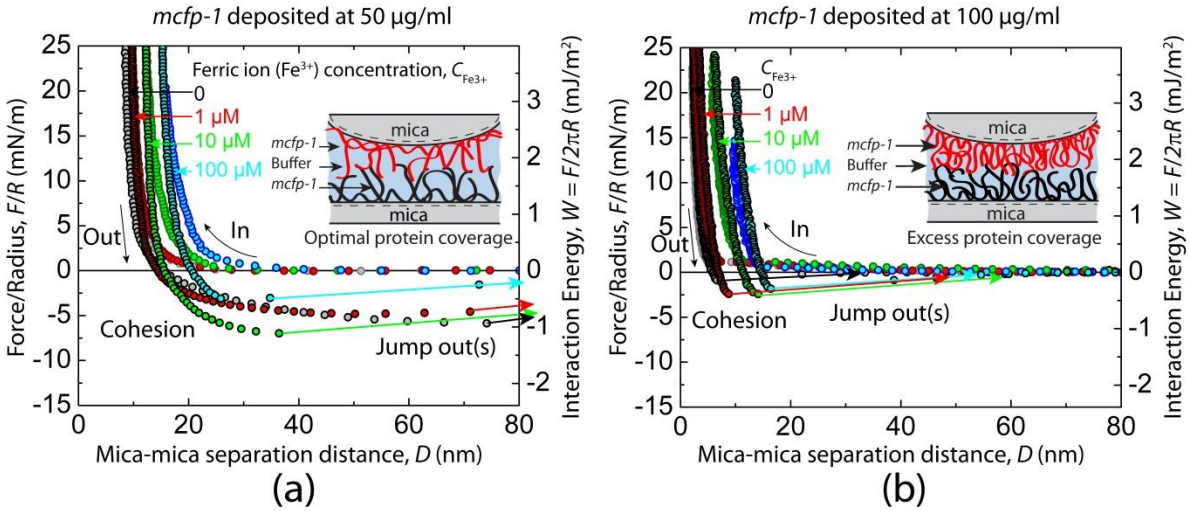

Figure S3.1 Representative force *vs.* distance plot showing cohesion between two symmetric *mfp-1*(*Mc*) films deposited at (a) C_{fp1} = 50 µg/ml and (b) 100 µg/ml in 0.1 M sodium acetate buffer, pH 5.5, 0.25 M KNO_3, and 1 mM bis-tris with C_{Fe3+} = 0 µM (gray), C_{Fe3+} = 1µM (red), 10 µM (green) and 100 µM (blue). In all cases the surfaces were brought into short contact (1-2 min).

Cohesive interactions between *mfp-1* (*Mc*) films. At low protein deposition concentrations ($C_{fp1} \leq$ 10 µg/ml), *mfp-1* (*Mc*) forms a patchy film (Fig. 3.4a and a') on the mica surface with all or most of the Dopa and Lys ε-amino (─NH_3^+) groups bound to the mica crystal lattice and robustly binding the mfp-1 film to mica. Hence, few of the Dopa and Lys side-chains in the *mfp-1* (*Mc*) film on one of the mica surfaces are available for adhering the protein to the opposing surface, resulting in low or no adhesion/cohesion between the surfaces for $C_{fp1} \leq$ 10 µg/ml. At the optimal protein deposition concentration (C_{fp1} = 50 µg/ml) for cohesion, some of the Dopa and Lys residues help to bind the protein film to the mica surface whereas the

others not bound to mica are available to adhere the film to the opposing mica surface (asymmetric) or the protein film (symmetric) on the other surface.

The energy of adhesion between the *mfp-1* (*Mc*) film and the opposing mica surface initially increases (Fig. S3.3, S3.4) from C_{fp1} = 10 to 50 μg/ml, then levels off for C_{fp1} > 50 μg/ml presumably because the number of exposed Dopa and Lys side-chains responsible for the adhesion of the protein film to the mica surface increases with increase in C_{fp1} and does not change for higher protein film deposition concentrations (C_{fp1} > 50 μg/ml). Refractive index (n_F) measurements (Table S3.2) of the confined protein film showed that at high protein deposition concentrations (C_{fp1} > 50 μg/ml), the surface gets crowded with the protein molecules. Thus, the volume fraction of *mfp-1* (*Mc*) in the hydrated protein film increased progressively from 9 to 71 % as C_{fp1} was increased from 10 to 100 μg/ml, implying that at higher protein film deposition concentrations, the density of *mfp-1* (*Mc*) in the film increases.

Hence, for two interacting protein films (symmetric), a smaller cohesive force was measured between the surfaces although the number of Dopa and Lys groups interacting across interface stays constant due to the steric repulsion induced by the *mfp-1* (*Mc*) molecules crowding the mica surfaces (Fig. 3.2). Hence for the cohesion measurements, W_c reaches a maximum value as C_{fp1} is increased.

Adhesive interactions of *mfp-1* (*Mc*) film to mica. A surfaces forces apparatus (SFA) was used to investigate the adhesive interactions of *mfp-1* (*Mc*) to a mica surface (i.e., asymmetric configuration, see Fig. S3.3a and S3.4) at various protein deposition concentrations (C_{fp1} = 10, 25, 50 and 100 μg/ml). The forces measured on approach of the surfaces were purely repulsive for protein deposition at C_{fp1} = 10-100 μg/ml (Fig. S3.3a and S3.4). Negligible

adhesion was measured between the *mfp-1* (*Mc*) film and the mica surface during separation for C_{fp1} = 10 μg/ml (Fig. S3.3b and S3.4).

Increasing the protein film deposition concentration C_{fp1} to 25 μg/ml resulted in a "jump out" when separating the surfaces (Fig. S3.3a) indicating adhesive contact between the *mfp-1* (*Mc*) film and the mica surface with an adhesion energy, W_{ad} = 0.79 ± 0.25 mJ/m^2 (Fig. S3.3b). For C_{fp1} = 50 μg/ml, the protein film adhered to the opposing mica surface with W_{ad} = 2.5 ± 0.74 mJ/m^2 showing signatures of bridging *adhesion* (28). The adhesion force between the protein film and the mica surface did not change significantly for C_{fp1} > 50 μg/ml. A similar bridging *adhesion* was measured for C_{fp1} = 100 μg/ml with W_{ad} = 2.61 ± 0.31 mJ/m^2 between the *mfp-1* (*Mc*) film and the mica surface. Protein films deposited at C_{fp1} = 25 μg/ml, however, did not show bridging *adhesion* against the mica surface and a sharp jump-out instability was measured during the separation of the surfaces (Fig S3.3a).

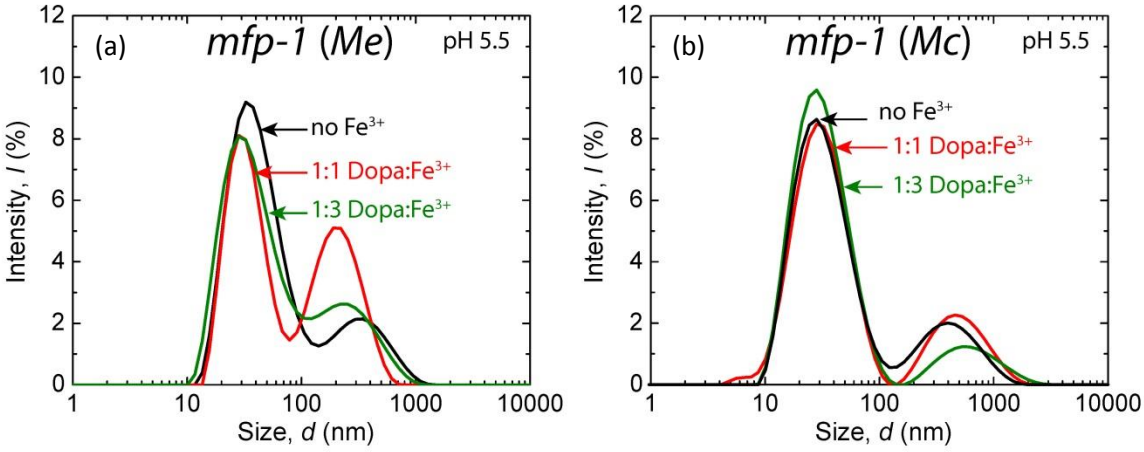

Figure S3.2 Effect of Fe^{3+} on aggregate size of *mfp-1* (*Me*) and *mfp-1*(*Mc*) by DLS measurements. In-solution aggregate size comparison of (a) *mfp-1*(*Me*) and (b) *mfp-1* (*Mc*) at 70 μg/ml were done in 0.1 M acetic acid, pH 5.5. Measurements were made with sequential increase in Fe^{3+} from 0 (no iron) to 1:1 and 3:1 (excess ratio) of iron to Dopa.

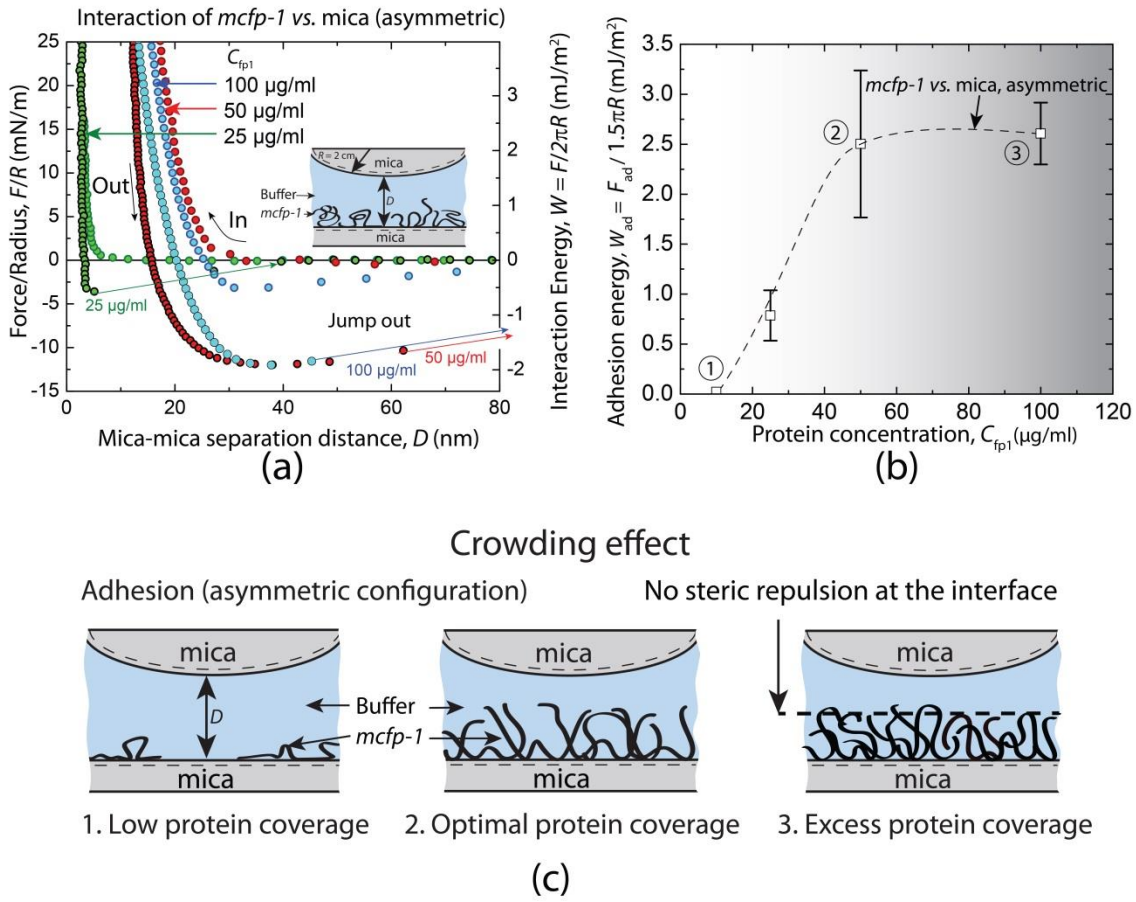

Figure S3.3 (a) Representative force *vs.* distance plot for different protein deposition concentrations (C_{fp1} = 25, 50 and 100 µg/ml in 0.1 M sodium acetate buffer, pH 5.5, 0.25 M KNO_3, and 1 mM bis-tris) showing adhesion between *mfp-1* (*Mc*) film and mica. (b) Effect of protein deposition concentration on the adhesion (*mfp-1*(*Mc*) *vs.* mcia, asymmetric) energies of interaction between the surfaces. (b) Schematic representations of the crowding effect for adhesion. The quality of the protein coverage (*viz*., low, optimal and excess) is based on the cohesion energy measred between protein films deposited at different bulk concentrations.

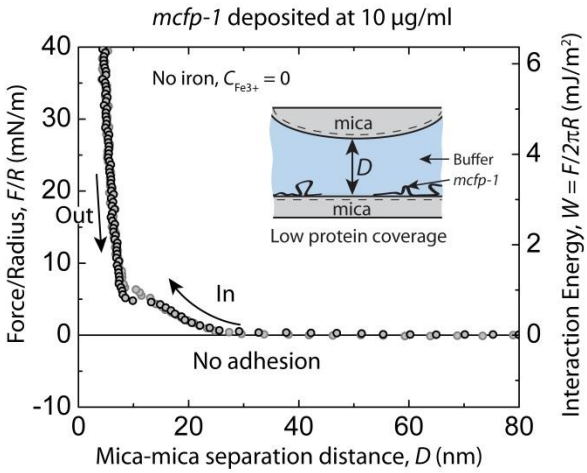

Figure S3.4 Representative force *vs.* distance plot showing the interaction between a bare mica surface and *mfp-1*(*Mc*) film deposited at 10 µg/ml in 0.1 M sodium acetate buffer, pH 5.5, 0.25 M KNO_3, and 1 mM bis-tris with C_{Fe3+} = 0 µM.

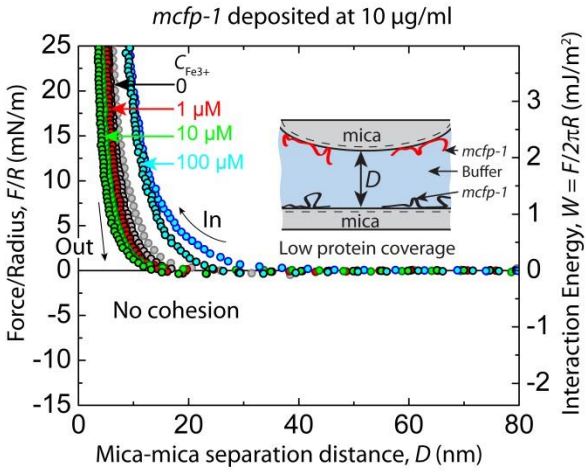

Figure S3.5 Representative force *vs.* distance plot showing the interaction between two symmetric *mfp-1* (*Mc*) films deposited at 10 µg/ml in 0.1 M sodium acetate buffer, pH 5.5, 0.25 M KNO_3, and 1 mM bis-tris with C_{Fe3+} = 0 µM (gray), C_{Fe3+} = 1 µM (red), 10 µM (green) and 100 µM (blue).

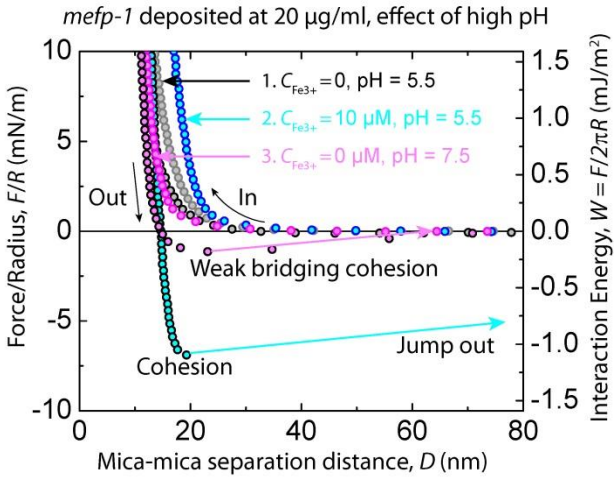

Figure S3.6 (a) Representative force *vs.* distance plot showing the interaction between two symmetric *mfp-1*(*Me*) films deposited at 20 µg/ml in 0.1 M sodium acetate buffer, pH 5.5, 0.25 M KNO_3, and 1 mM bis-tris with C_{Fe3+} = 0 µM (gray), and 100 µM (blue) at pH 5.5. The surfaces showed a weak bridging cohesion (W_c < 0.2 mJ/m^2) after increasing the pH to 7.5 (magenta).

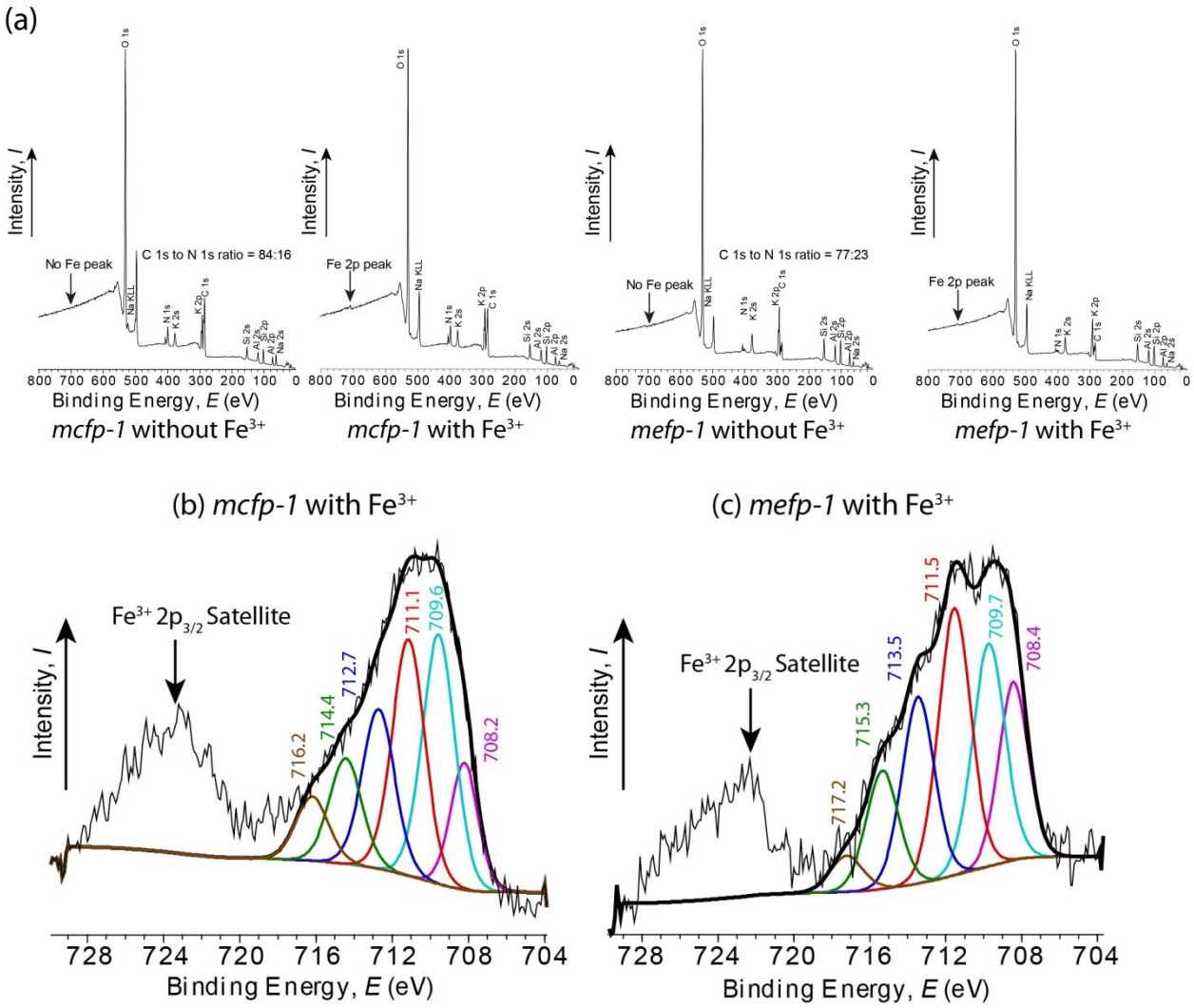

Figure S3.7 (a) XPS survey spectra on *mfp*-1(*Mc*) and *mfp*-1(*Me*) films deposited on mica surfaces at 50 µg/ml and 20 µg/ml respectively with and without preadsorbed Fe^{3+}. High resolution XPS Fe^{3+} 2p spectra on *mfp-1*(*Mc*) (b) and *mfp-1* (*Me*) (c) films with preadsorbed 50 µL of 10 µM Fe^{3+}, with Gaussian fits to the peaks.

X-ray photoelectron spectroscopy (XPS). The interaction of Fe^{3+} with the Dopa groups in *mfp-1* (*Mc*) and *mfp-1* (*Me*) were investigated by XPS (Axis Ultra XPS, Kratos Analytical, UK) spectrometer. A wide spectrum scan (Binding energy, E = 0 - 800 eV) was obtained with a pass energy of 160 eV (Fig. S3.7a). The binding energies were corrected to 285 eV for

the C 1s peak. High resolution elemental analysis of the N 1s and Fe 2p peaks were obtained at 40 eV pass energy with a step size of 0.1 eV and averaged over 2 scans (Fig. S3.7). The experimental data was fitted to a Gaussian function.

Full spectrum scans of the *mfp-1*(*Mc*) and *mfp-1* (*Me*) films on mica surface are shown in Fig. S3.7a and no Fe peaks are detected in the protein films without pre adsorbed iron. High resolution XPS spectrum of the protein films with pre adsorbed Fe^{3+} shows that the coordination state of Fe^{3+} in the two adsorbed protein films is different (41). The multiplets fitted to the Fe^{3+} $2p_{3/2}$ peak (Fig. S3.7b and c) shows higher energy peak fits to the Fe^{3+} coordinated to *mfp-1*(*Me*) compared to *mfp-1*(*Mc*) film. Decreased coordination will lower the electron density around ferric ion resulting in a higher energy needed to produce a photoelectron. Thus, the measurements made in the XPS demonstrate that *mfp-1*(*Me*) is better at wrapping Fe^{3+} compared to *mfp-1*(*Mc*).

Raman spectroscopy. Prior to testing with Raman spectroscopy, lyophilized protein samples were resuspended in 5 mM acetic acid to a concentration of 1 mg/ml. 1mM $FeCl_3$ was added to a droplet of the protein solution in a ratio of 3 DOPA residues to 1 Fe^{3+} ion and the pH was raised with NaOH. Raman micro spectroscopy was performed using a confocal Raman microscope (alpha300; WITec, Ulm, Germany) equipped with a piezoelectric scan stage (P-500, Physik Instrumente, Karlsruhe, Germany) and a Nikon objective (20X). A green laser (λ = 532 nm) was focused on the solution and Raman scattering was detected using a CCD camera (DV401-BV; Andor, Belfast, North Ireland) behind a spectrometer (UHTS 300; WITec) with a spectral resolution of 3 cm^{-1}. The Scan Ctrl Spectroscopy Plus software (version 1.38, Witec) was used for measurement setup and acquisition. Resonance Raman

spectra were measured from several different regions in the solution with an integration time of 0.5 s and 30 accumulations. For each sample, at least 4 spectra were averaged. Averaged spectra were baseline corrected and smoothed using OPUS software (Bruker, version 7.0).

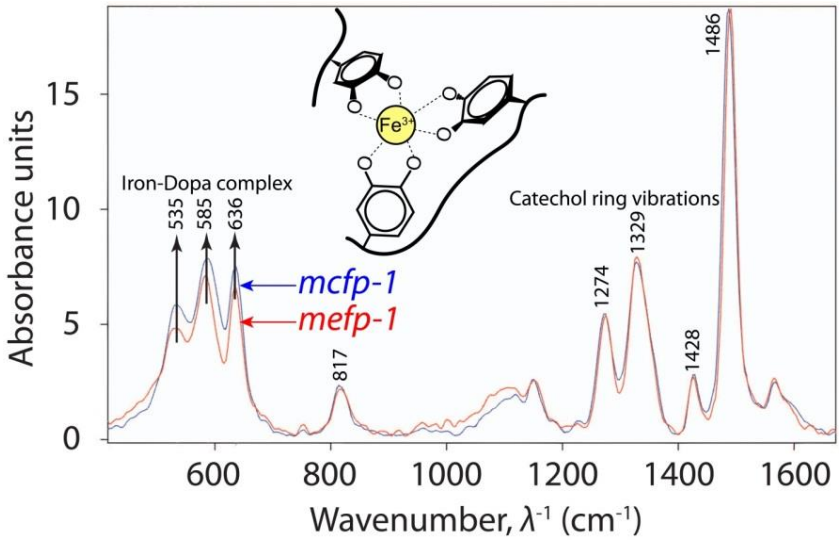

Figure S3.8 Resonance Raman microscopy of *mfp-1* (*Me*) and *mfp-1* (*Mc*) with Fe^{3+}. Prior to testing with Raman spectroscopy, samples were resuspended in 5 mM acetic acid to a concentration of 1 mg/ml. 1mM $FeCl_3$ was added to a droplet of the protein solution in a ratio of 3 Dopa residues to 1 Fe^{3+} ion. The pH was raised with NaOH (although it was possible to measure similar spectra even before adding the NaOH). Spectra were measured from different regions in the solution and at least 4 spectra were averaged. Data were background corrected and smoothed in OPUS.

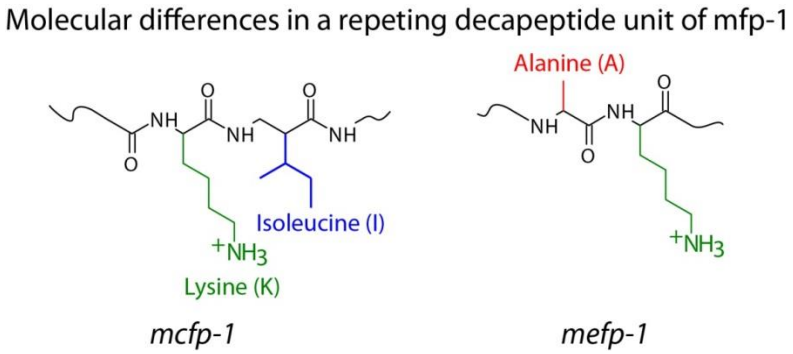

Figure S3.9 Molecular difference in the consensus decapeptide repeat unit of *mfp-1*(*Mc*) and *mfp-1*(*Me*).

Resolving the protein concentration values. The literature reports adhesion (asymmetric configuration) and cohesion (symmetric configuration) of *mfp-1* (*Mc*) protein films deposited at 10 μg/ml (14, 19). However, it should be noted that the *mfp-1* (*Mc*) protein concentrations in the previous works were measured indirectly through Bradford protein assay. This work used a scalar method. Therefore, Bradford concentration assay standard curves were created with both bovine serum albumin (BSA) and *mfp-1* (*Mc*) to determine the dye binding capacity of *mfp-1* (*Mc*) compared to BSA, the standard protein used for making calibration curves for Bradford concentration assays. Comparing BSA binding to that of *mfp-1* (*Mc*) shows that *mfp-1* (*Mc*) has a 2.5 fold lower binding capacity than BSA, resulting in a 2.5 fold lower concentration reading than its BSA counterpart for the same protein concentration. Therefore, what previous studies indicate as 10 μg/ml, this study would indicate as 25 μg/ml (Fig. S3.10).

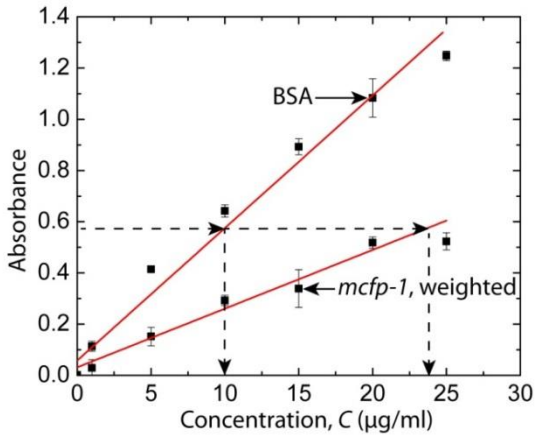

Figure S3.10 Bradford assay for *mfp-1* (*Mc*) and comparison to Bovine Serum Albumin (BSA).

Estimation of refractive index (n_P) of pure non-hydrated *mfp*-1(*Mc*)

Table S3.1. Molecular weight (M_A) and Refractive indices (n_A) of Amino Acids.

Amino acid	Molecular weight, M_A (g/mol)	Refractive Index, n_A
P*	131.1	1.540
K	146.2	1.615
I	131.2	1.568
S	105.1	1.676
Y*	197.2	1.654
P**	147.1	1.599
T	119.1	1.618

Mfp-1(*Mc*) from *M. californianus* has a mass of about 108 kDa and consists largely of tandem repeats of a decapeptide [P*KISY*P**P*TY*K], in which P*, P**, and Y* denote trans-4-hydroxyproline, trans-2,3,cis-3,4-dihydroxyproline, and 3,4-dihydroxyphenylalanine (Dopa), respectively (4). The refractive index of the pure non-hydrated protein can be

estimated from equation 1 as the weight average of the contribution from the individual amino acids refractive indices, n_A (42).

$$n_P = \frac{\sum_A n_A M_A}{\sum_A M_A} \qquad [S3.1]$$

Hence, for pure non-hydrated *mfp-1*(*Mc*), $n_P = 1.611$

Estimation of volume fraction of *mfp-1* (*Mc*) in the protein film from refractive index (n_F) measurements of the film

The refractive index, n_F, of the hydrated protein film was measured using Multiple Beam Interferometry (MBI) technique in the SFA experiments (24). The volume fraction (V_P) of *mfp-1* (*Mc*) in the hydrated protein film confined between the mica surfaces under hard compression (F/R > 30 mN/m) was calculated using equation S3.2.

$$V_P = \frac{n_F - n_W}{n_P - n_W} \qquad [S3.2]$$

where $n_W = 1.333$ (refractive index of water)

Table S3.2. Volume fraction (V_P) of *mfp-1*(*Mc*) in the hydrated protein film confined between the mica surfaces.

C_{mcfp-1} (µg/ml)	n_F	Volume fraction, V_P (%)
10	1.359	9
25	1.448	41
50	1.468	49
100	1.531	71

3.8 References

1. Jacob GC, Starbuck JM, Fellers JF, Simunovic S, & Boeman RG (2004) Strain rate effects on the mechanical properties of polymer composite materials. *Journal of Applied Polymer Science* 94(1):296-301.
2. Jayabalan M, Lizymol PP, & Thomas V (2000) Synthesis of hydrolytically stable low elastic modulus polyurethane-urea for biomedical applications. *Polymer International* 49(1):88-92.
3. Holten-Andersen N & Waite JH (2008) Mussel-designed protective coatings for compliant substrates. *Journal of Dental Research* 87(8):701-709.
4. Holten-Andersen N, Zhao H, & Waite JH (2009) Stiff Coatings on Compliant Biofibers: The Cuticle of Mytilus californianus Byssal Threads. *Biochemistry* 48(12):2752-2759.
5. Sever MJ, Weisser JT, Monahan J, Srinivasan S, & Wilker JJ (2004) Metal-mediated cross-linking in the generation of a marine-mussel adhesive. *Angewandte Chemie-International Edition* 43(4):448-450.
6. Sun CJ & Waite JH (2005) Mapping chemical gradients within and along a fibrous structural tissue, mussel byssal threads. *Journal of Biological Chemistry* 280(47):39332-39336.
7. Harrington MJ, Masic A, Holten-Andersen N, Waite JH, & Fratzl P (2010) Iron-Clad Fibers: A Metal-Based Biological Strategy for Hard Flexible Coatings. *Science* 328(5975):216-220.

8. Taylor SW, Chase DB, Emptage MH, Nelson MJ, & Waite JH (1996) Ferric ion complexes of a DOPA-containing adhesive protein from Mytilus edulis. *Inorganic Chemistry* 35(26):7572-7577.

9. Monahan J & Wilker JJ (2003) Specificity of metal ion cross-linking in marine mussel adhesives. *Chemical Communications* (14):1672-1673.

10. Holten-Andersen N, *et al.* (2011) pH-induced metal-ligand cross-links inspired by mussel yield self-healing polymer networks with near-covalent elastic moduli. *Proceedings of the National Academy of Sciences of the United States of America* 108(7):2651-2655.

11. Ejima H, *et al.* (2013) One-Step Assembly of Coordination Complexes for Versatile Film and Particle Engineering. *Science* 341(6142):154-157.

12. Smith JJ, Thomson AJ, Proudfoot AEI, & Wells TNC (1997) Identification of an Fe(III)-dihydroxyphenylalanine site in recombinant phosphomannose isomerase from Candida albicans. *European Journal of Biochemistry* 244(2):325-333.

13. Stewart RJ, Ransom TC, & Hlady V (2011) Natural Underwater Adhesives. *Journal of Polymer Science Part B-Polymer Physics* 49(11):757-771.

14. Zeng HB, Hwang DS, Israelachvili JN, & Waite JH (2010) Strong reversible Fe^{3+}-mediated bridging between dopa-containing protein films in water. *Proceedings of the National Academy of Sciences of the United States of America* 107(29):12850-12853.

15. Tooney NM (1980) Biophysical chemistry - part I: The conformation of biological, macromolecules, Cantor and Schimmel, W. H. Freeman and Company, San

Francisco, 1980, 341 pp. *Journal of Polymer Science: Polymer Letters Edition* 18(9):643-644.

16. Berglin M, Hedlund J, Fant C, & Elwing H (2005) Use of surface-sensitive methods for the study of adsorption and cross-linking of marine bioadhesives. *Journal of Adhesion* 81(7-8):805-822.

17. Inoue K & Odo S (1994) The Adhesive Protein Cdna of Mytilus-Galloprovincialis Encodes Decapeptide Repeats but No Hexapeptide Motif. *Biological Bulletin* 186(3):349-355.

18. Waite JH & Tanzer ML (1981) Polyphenolic Substance of Mytilus-Edulis - Novel Adhesive Containing L-Dopa and Hydroxyproline. *Science* 212(4498):1038-1040.

19. Lu QY, Hwang DS, Liu Y, & Zeng HB (2012) Molecular interactions of mussel protective coating protein, mcfp-1, from Mytilus californianus. *Biomaterials* 33(6):1903-1911.

20. Pogula SD, *et al.* (2007) Continuous silica coatings on glass fibers via bioinspired approaches. *Langmuir* 23(12):6677-6683.

21. Zhao H & Waite JH (2006) Linking adhesive and structural proteins in the attachment plaque of Mytilus californianus. *Journal of Biological Chemistry* 281(36):26150-26158.

22. Waite JH & Benedict CV (1984) Assay of Dihydroxyphenylalanine (Dopa) in Invertebrate Structural Proteins. *Methods in Enzymology* 107:397-413.

23. Das S, *et al.* (2013) Synergistic Interactions between Grafted Hyaluronic Acid and Lubricin Provide Enhanced Wear Protection and Lubrication. *Biomacromolecules* 14(5):1669-1677.

24. Israelachvili J, *et al.* (2010) Recent advances in the surface forces apparatus (SFA) technique. *Reports on Progress in Physics* 73(3).

25. Israelachvili JN (2011) Intermolecular and Surface Forces, 3rd Edition. *Intermolecular and Surface Forces, 3rd Edition*:1-674.

26. Nicklisch SCT, Das S, Rodriguez NRM, Waite JH, & Israelachvili JN (2013) Antioxidant Efficacy and Adhesion Rescue by a Recombinant Mussel Foot Protein-6. *Biotechnology Progress* 29(6):1587-1593.

27. Israelachvili JN, *et al.* (2013) The Intersection of Interfacial Forces and Electrochemical Reactions. *Journal of Physical Chemistry B* 117(51):16369-16387.

28. Yu J, *et al.* (2013) Adaptive hydrophobic and hydrophilic interactions of mussel foot proteins with organic thin films. *Proceedings of the National Academy of Sciences of the United States of America* 110(39):15680-15685.

29. Anderson TH, *et al.* (2010) The Contribution of DOPA to Substrate-Peptide Adhesion and Internal Cohesion of Mussel-Inspired Synthetic Peptide Films. *Advanced Functional Materials* 20(23):4196-4205.

30. Anderson T & Israelachvili J (2010) Adhesion Mechanisms of the Mussel Foot Proteins mfp-1 and mfp-3. *Biophysical Journal* 98(3):594a-594a.

31. Gieseg SP, Simpson JA, Charlton TS, Duncan MW, & Dean RT (1993) Protein-Bound 3,4-Dihydroxyphenylalanine Is a Major Reductant Formed during Hydroxyl Radical Damage to Proteins. *Biochemistry* 32(18):4780-4786.

32. Kanyalkar M, Srivastava S, & Coutinho E (2002) Conformation of a model peptide of the tandem repeat decapeptide in mussel adhesive protein by NMR and MD simulations. *Biomaterials* 23(2):389-396.

33. Haemers S, van der Leeden MC, & Frens G (2005) Coil dimensions of the mussel adhesive protein Mefp-1. *Biomaterials* 26(11):1231-1236.

34. Williams T, Marumo K, Waite JH, & Henkens RW (1989) Mussel Glue Protein Has an Open Conformation. *Archives of Biochemistry and Biophysics* 269(2):415-422.

35. Taylor SW, Luther GW, & Waite JH (1994) Polarographic and Spectrophotometric Investigation of Iron(III) Complexation to 3,4-Dihydroxyphenylalanine-Containing Peptides and Proteins from Mytilus-Edulis. *Inorganic Chemistry* 33(25):5819-5824.

36. Greene GW, *et al.* (2013) Lubrication and Wear Protection of Natural (Bio)Systems. *Polymer Adhesion, Friction, and Lubrication*, (John Wiley & Sons, Inc.), pp 83-133.

37. Lin Q, *et al.* (2007) Adhesion mechanisms of the mussel foot proteins mfp-1 and mfp-3. *Proceedings of the National Academy of Sciences of the United States of America* 104(10):3782-3786.

38. Marumo K & Waite JH (1986) Optimization of Hydroxylation of Tyrosine and Tyrosine-Containing Peptides by Mushroom Tyrosinase. *Biochimica Et Biophysica Acta* 872(1-2):98-103.

39. Waite JH (1986) Mussel Glue from Mytilus-Californianus Conrad - a Comparative-Study. *Journal of Comparative Physiology B-Biochemical Systemic and Environmental Physiology* 156(4):491-496.

40. Filpula DR, Lee SM, Link RP, Strausberg SL, & Strausberg RL (1990) Structural and Functional Repetition in a Marine Mussel Adhesive Protein. *Biotechnology Progress* 6(3):171-177.

41. Grosvenor AP, Kobe BA, Biesinger MC, & McIntyre NS (2004) Investigation of multiplet splitting of Fe 2p XPS spectra and bonding in iron compounds. *Surface and Interface Analysis* 36(12):1564-1574.

42. Mcmeekin TL, Groves ML, & Wilensky M (1962) Refractive Indices of Proteins in Relation to Amino Acid Composition and Specific Volume. *Biochemical and Biophysical Research Communications* 7(2):151-156.

4. PEPTIDE LENGTH AND DOPA DETERMINE IRON MEDIATED COHESION OF MUSSEL FOOT PROTEINS

4.1 Abstract

Mussel adhesion to mineral surfaces is widely attributed to 3, 4-dihydroxyphenylalanine (Dopa) functionalities in the mussel foot proteins (mfps). For example, Dopa is proposed to bind mica and titania surfaces through bidentate hydrogen and coordination bonds. Many mfps, however, show a broad range (30-100%) of Tyrosine (Tyr) to Dopa conversion suggesting that Dopa is not the only desirable outcome for adhesion. Here, we used a partial recombinant construct of mussel foot protein-1 (rmfp-1, mass~14 kDa) and a short decapeptide dimer with and without Dopa and assessed both its cohesive and adhesive properties on mica using a surface forces apparatus (SFA). Our results demonstrate that at low pH (pH = 3.7), both the unmodified and Dopa-containing rmfp-1s show similar adhesion energies to mica (W_{ad} ~ 9 mJ/m^2) and a cohesion or self-interaction energy of W_c = 4.9 ± 0.6 mJ/m^2. Cohesion between two Dopa-containing rmfp-1 surfaces can be doubled by Fe^{3+} chelation (W_c ~ 10 mJ/m^2), but remains unchanged with unmodified rmfp-1. At the same low pH, the Dopa modified short decapeptide dimer showed superior cohesion compared to rmfp-1 and did not show any change in the cohesive interaction (W_c = 9.4 ± 1.2 mJ/m^2) even with ferric ions. Strong adhesion was also observed between

unmodified rmfp-1 and silicone surfaces (W_{ad} = 15 ± 7 mJ/m^2), compared with the Dopa-containing rmfp-1 (W_{ad} = 7.9 ± 0.9 mJ/m^2). In contrast, at physiological pH 7.5, the Dopa modified rmfp-1 showed significant adhesion (W_{ad} = 3.6 ± 0.8 mJ/m^2) to the silicone surface, whereas the unmodified rmfp-1 (W_{ad} = 0.5 ± 0.1 mJ/m^2) did not. It has been previously proposed that mfp adhesion to surfaces is mainly due to bidentate hydrogen bonding. Our results suggest that the bonding interactions are more due to electrostatic and hydrophobic interactions. We also show that Dopa in a peptide sequence does not necessarily lead to the formation of cross-links between peptide films through metal chelation, and the length of the peptide is a crucial parameter for enabling metal ion mediated bridging between surfaces.

4.2 Introduction

Mussels assemble a battery of proteins known as mussel foot proteins (mfp) into a byssus (plaque and the thread) to adhere to solid surfaces in the high-energy intertidal zone. Dopa (3,4-dihydroxyphenylalanine), a post-translational modification from tyrosine (Tyr), features prominently in mfps, ranging from less than 5 mol % in mfp-4 to 30 mol % in mfp-5 (1-6). Single molecule tensile tests using an atomic force microscope (AFM) where Dopa was tethered to a cantilever tip showed Dopa contributes to nano-Newton adhesion on iron oxide, titania, and amine-functionalized surfaces (7). Moreover, several studies with Dopa functionalized polymers have demonstrated a strong positive linear correlation between Dopa content and adhesion to different surfaces (8-13). Notwithstanding these trends, much debate persists regarding two critical issues of mfp-mediated adhesion: (1) the actual interfacial chemistry of Dopa side-chains on model surfaces, and (2) the contribution of residues other than Dopa to adhesion. The first issue has seen significant progress by the application of

resonance Raman microscopy to detect the pH-dependent formation of bidentate binuclear Ti^{IV} coordination complexes between Dopa-containing mfp-1 (14) and mfp-3 (15) on titania surfaces. The adhesive and cohesive contributions of residues in addition to Dopa are addressed here.

A significant challenge to assessing the adhesive contributions of other amino acids is the complexity of most native mfp sequences, which are polar with high charge density and little to no 2˚ structure in solution (16). The sequences are further complicated by the highly variable post-translational modification by enzymes. In purified native mfp-1, for example, Tyr→Dopa and Pro→Hyp conversion can range from 50 to 80%. To reduce sequence complexity, we used a recombinant mfp-1 (rmfp-1) analog that contains 12 tandem repeats of the decapeptide sequence AKPSYPPTYK. This is less than a sixth of the 75 decapeptide repeats in native mfp-1 from *Mytilus edulis* (17), has no post-translational modifications, and limits Tyr to a simple repeating consensus sequence P-T/S-Y-X, where X is P or K. More than 80% of the Tyr in rmfp-1 can be converted to Dopa by tyrosinase (18), enabling a separate assessment of contributions by Dopa. In this work, rmfp-1 with and without Dopa were tested for the adhesion and cohesion on mica and silicone surfaces using a surface forces apparatus (SFA). We also tested short decapeptide dimers (two repeats of the decapeptide sequence, monomer = AKPSYPPTYK) with and without the hydroxylation of Tyrosine (Y) to Dopa (Y*) and Proline (P) to Hydroxyproline (P*) for its cohesive properties in metal ion (Fe^{3+}) environments to assess the role of peptide length in the formation of metal-protein complexes.

Our results are remarkable in showing that rmfp-1 without Dopa achieves adhesion comparable to Dopa-modified rmfp-1 on mica and silicone surfaces. Cohesive interactions

are also comparable except when Fe^{3+} is added to symmetric surfaces of rmfp-1 with Dopa. However, the cohesive interactions between short decapeptide dimers remained the same regardless of presence or absence of Dopa. The results stress the importance of understanding the molecular parameters beyond Dopa that contribute to mussel adhesion.

4.3 Materials and Methods

4.3.1 Modification of rmfp-1

Rmfp-1 used in this work is a shorter synthetic analogue of the natural mussel foot protein mfp-1 from *Mytius edulis* with 12 tandem repeat units of the mefp-1 consensus decapeptide AKPSYPPTYK. The protein was obtained from DS Hwang (POSTECH) and had a $M+H^+$ of 13,619 Da by MALDI TOF mass spectrometry. Tyr in rmfp-1 was converted to Dopa by mushroom tyrosinase (Sigma-Aldrich) using the borate capture method (18) and then purified by C-8 HPLC and Shodex (Bruker Microflex LRF). Tyr in rmfp-1 was converted to Dopa by mushroom tyrosinase (Sigma-Aldrich) using the borate capture method (18) and then purified by C-18 reverse phase HPLC column, eluted with a linear gradient of aqueous acetonitrile. Eluent was monitored continuously at 230 and 280 nm, and 0.33 ml fractions containing peptides were pooled and freeze-dried. Sample purity and hydroxylation were assessed by MALDI-TOF. $M+H^+$ was 13,939 Da with > 83% conversion efficiency.

4.3.2 Measuring the adhesive/cohesive interactions

The surface forces apparatus (SFA, SurForce LLC®) was used to measure the normal forces between two mica surfaces in a cross-cylindrical geometry as a function of the separation distance, *D*, between them and has been described elsewhere (19, 20). The protein

films were made by adsorbing 50 μL of the protein from a 50 μg/ml in a buffer solution (10 mM sodium acetate buffer, pH 3.7) onto the mica surfaces for 15 minutes, then rinsing the excess protein with the same buffer. During the protein adsorption, the discs were kept in a saturated Petri dish to minimize evaporation of the water from the surfaces. The discs were then mounted in the SFA in one of two configurations. In a symmetric configuration (Fig. 4.1a), the mussel protein film was deposited on both surfaces in order to measure *cohesion* between the protein films. Cohesion was tested with and without iron. To test the effect of Fe^{3+}, a 10 μM $FeCl_3$ in acetate buffer (as above) was freshly made and added to the reservoir between the symmetrically deposited protein films on mica.

In an asymmetric configuration (Fig. 4.1b**)**, the mussel protein was adsorbed on one surface in order to measure the interaction (*adhesion*) between the rmfp-1 film and a model silicone surface (21) or mica. In a separate experiment, the pH of the solution between the surfaces was increased to 7.5 by rinsing with a phosphate buffer saline (0.1 M potassium phosphate, pH 7.5, 0.25 M KNO_3) to investigate the effect of physiological conditions on the cohesive and adhesive force of interaction of the protein film with different surfaces.

The protein films were always hydrated (i.e. never allowed to dry) and a droplet of the acetate buffer was injected between the surfaces immediately after loading in the SFA. During a typical approach-separation force measurement cycle, the surfaces were first moved towards each other (approach) until reaching a "hardwall" and then separated. The hardwall distance, D_H, is the separation distance between the two mica surfaces upon compression that does not change with increased compression. The energy of interaction between two crossed-cylinder geometry, roughly corresponds to a sphere of radius R approaching a flat surface based on the Derjaguin approximation, $W = F / 2\pi R$ where, $W(D)$ is the energy of interaction

per unit area between two flat surfaces and $F(D)$ is the measured force of interaction in the SFA. The measured adhesion (or cohesion) force F_{ad} (or F_c) is related to the adhesion (or cohesion) energy per unit area by $W_{ad} = F_{ad} / 2\pi R$ for rigid surfaces with weak adhesive interactions, and by $W_{ad} = F_{ad} / 1.5\pi R$ (used in this study) for soft deformable surfaces with strong adhesion or cohesion.

4.3.3 Protein adsorption experiments

Quartz Crystal Microbalance (QCM) experiments were done with a Q-Sense E4 open module to characterize the adsorption of rmfp-1 (Dopa modified and unmodified) to TiO_2 surfaces independently of the SFA experiments. The QCM crystals were cleaned in 3% SDS solution, rinsed in distilled water, cleaned with ethanol and then treated with UV-Ozone for 10 min. Frequency and dissipation baselines were established in 100 μL of acetate buffer solution on the crystal followed by injection of 25 μL of 50 μg/ml rmfp-1.

4.4 Results and Discussion

4.4.1 Cohesion between the protein films and interaction with mica

The cohesive force of interaction between two symmetric rmfp-1 films, Dopa modified and unmodified, was measured in a SFA (Fig. 4.1a) at two different pH values, pH 3.7 and 7.5 (Fig. 4.2). The effect of Fe^{3+} on the cohesive force between the protein films was also investigated (Fig. 4.3).

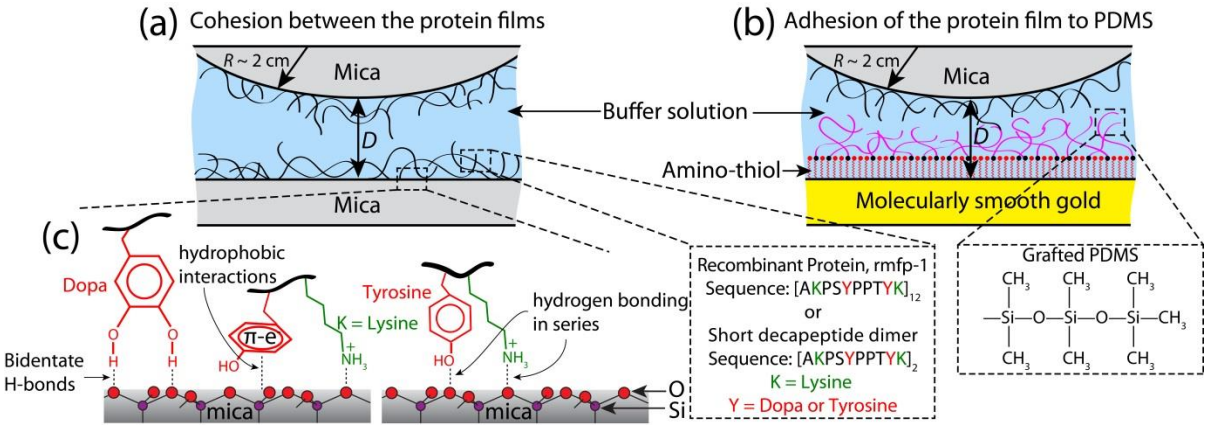

Figure 4.1 Scheme of the surfaces analyzed by the surface forces apparatus. (a) rmfp-1 with or without Dopa is adsorbed as a thin film on one or both mica surfaces; (b) PDMS is grafted to an amino functionalized SAM layer on one mica surface and rmfp-1 with or without Dopa is adsorbed to the other mica surface; (c) Schematics of the bidentate H-bonds, electrostatic and hydrophobic interactions between the protein and mica surface.

At pH 3.7, similar cohesive interactions were measured for Dopa-containing and unmodified rmfp-1 (no Dopa) when surfaces were kept under compressive contact at $t \geq 10$ min (W_c = 4.9 ± 0.6 mJ/m^2) (Fig. 4.2a, b). For short contact times, t_c ~ 2 min, the Dopa modified rmfp-1 showed almost 60 % higher cohesion (W_c = 2.40 ± 0.6 mJ/m^2) compared to the unmodified protein film (W_c = 1.5 ± 0.8 mJ/m^2). This suggests that Dopa may accelerate the development of cohesion between the protein films; however, given enough interaction time, Dopa adds little to the magnitude of cohesive strength between the protein films at equilibrium.

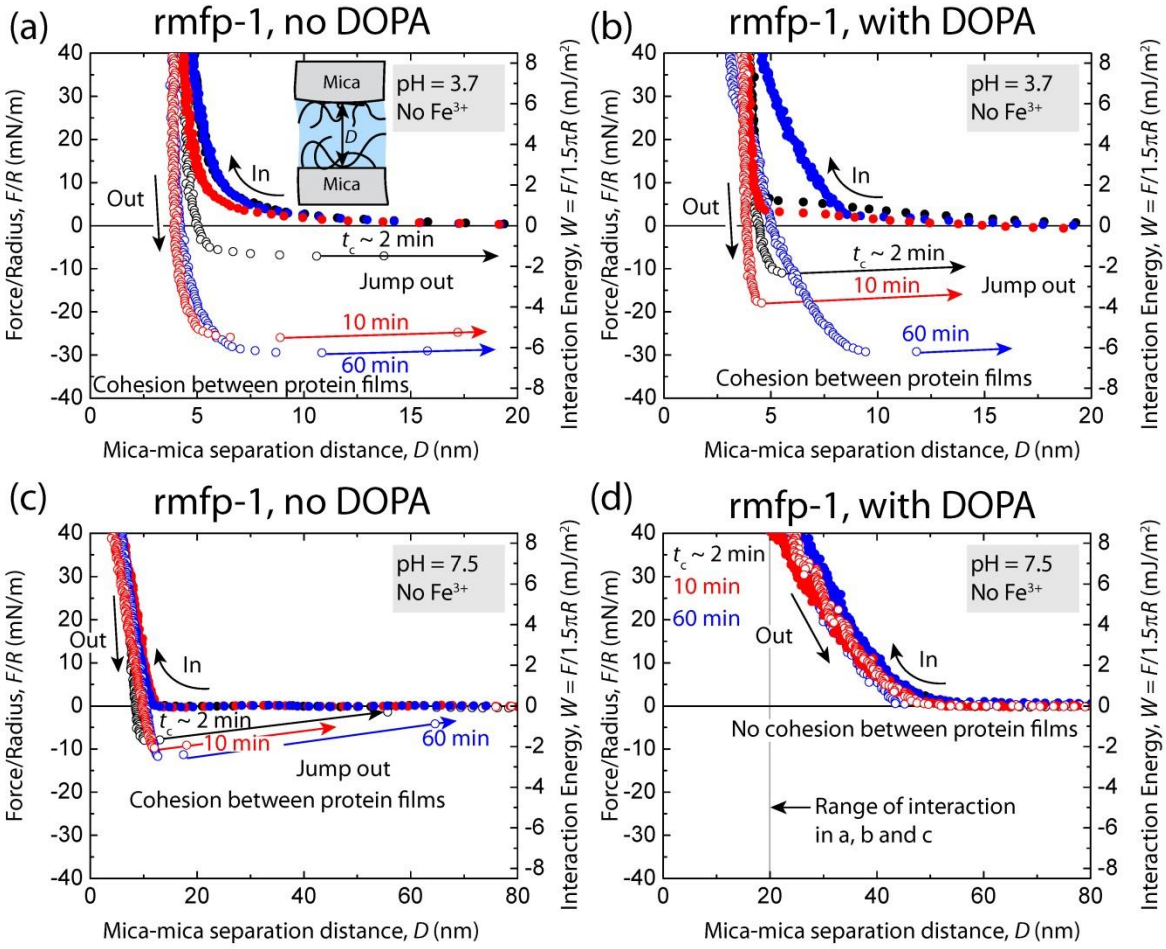

Figure 4.2 Representative force *vs.* distance plots showing the effect of contact time, t_c, on the cohesion between two symmetric rmfp-1 films without Dopa (a, c) as well as two Dopa-containing rmfp-1 films (b, d) at pH 3.7 and, pH 7.5, respectively.

The cohesion between the unmodified rmfp-1 films was completely recovered when the pH of the buffer was switched from 3.7 to 7.5 and back to 3.7 unlike the Dopa modified rmfp-1 where the protein underwent pH-induced irreversible structural changes and cohesion could not be recovered. At low pH and low salt concentrations, π–cation (22) and hydrophobic (21) interactions are strong and these interactions tend to get weaker at higher pH and high salt conditions. Thus, the reversible cohesive behavior of the unmodified rmfp-1

film demonstrates that cohesion in rmfp-1 films could be due to electrostatic (e.g., π–cation) (23-26) and hydrophobic interactions (π–π stacking) and that Dopa is not essential for cohesion.

Another intriguing finding was related to the adhesion of the unmodified (no Dopa) and the Dopa modified rmfp-1 film to mica. Both the proteins showed similar time dependence and adhesion energies to mica. Unmodified rmfp-1 adhered to mica with W_{ad} = 8.0 ± 0.1 mJ/m^2 whereas, the Dopa modified rmfp-1 showed similar adhesion energy of W_{ad} = 9.8 ± 1.2 mJ/m^2 at t_c = 60 min (Fig. S4.1). Protein adsorption experiments in a Quartz Crystal Microbalance (QCM) further established that presence of Dopa in the protein does not change the mass of the adsorbed protein (m ~ 80 ng/cm^2) to a TiO_2 surface (Fig. S4.2). The negligible change in the dissipation of the quartz crystal (Fig. S4.2) upon the adsorption of the protein at pH 3.7 indicates that rmfp-1, both with and without Dopa, forms a stiff film on TiO_2, and bidentate coordination bond of the Dopa to the crystalline TiO_2 is not the dominant mechanism that adheres the protein to the surface. It should be noted that the thickness of the rmfp-1 film with Dopa was about 4 – 5 nm compared to 0.7 – 1.5 nm for the rmfp-1 film without Dopa as measured in the SFA (Fig. S4.1). The presence of Dopa might affect the structure of the adsorbed rmfp-1 film on the surface, however, both films showed similar adhesive/cohesive properties (SFA studies) and stiffness (QCM measurements).

The similar adhesion energies of Dopa modified and unmodified protein to mica also suggest that the primary interaction between the protein film and mica could be due to specific coulombic interactions between the lysine and negatively charged mica or mono-dentate hydrogen bonding in series with Lysine-mica interactions (Fig. 4.1a). Hydrophobic interactions between the aromatic residues and the hydrophobic domains in the mica crystal

(21) could also cause a strong adhesion between protein and the surface. π–cation interaction between the aromatic residues of the peptides in the protein and the K^+ in the mica crystal lattice could also possibly cause enhanced interaction between the protein and the surface and bidentate bonds between Dopa and the polysiloxane lattice of mica might play a minor role in the adhesion. Similar π–cation interaction was previously observed between lignin and gold (27) and bilayers and proteins (28). The work of adhesion between the mica and rmfp-1 was approximately W_{ad} = 7.8 ± 0.6 mJ/m^2 for both Dopa modified and unmodified rmfp-1 at short contact times t_c ~ 2 min (Fig. S4.1) which suggests that bidentate Dopa bond to mica cannot be the primary mode of binding to mica surfaces by rmfp-1.

There was no material transfer between the surfaces during the force measurements because the approach force run profiles for the very first contact between the surfaces were similar to the successive runs repeated at least 6 times at the same contact point. The measured cohesive force also didn't change significantly (< 1 %) for the successive force measurements at a given contact point. The failure during the separation of the protein films was determined to be the protein-protein interface and not the mica-protein interface as the adhesion measured between rmfp-1 (unmodified or Dopa-containing rmfp-1) and mica was significantly higher (W_{ad} = 8.4 ± 0.8 mJ/m^2) than the cohesive energies (W_c = 3.9 ± 1.7 mJ/m^2) of symmetric rmfp-1 films at t_c = 2 to 60 min (Fig. 4.2 and S4.1).

Introduction of 10 μM Fe^{3+} into the gap between rmfp-1 surfaces did not change the cohesion between the unmodified rmfp-1 films (W_c = 5.9 ± 0.8 mJ/m^2 for t_c = 60 mins with and without Fe^{3+}). However, Fe^{3+} doubled the cohesion energy between the Dopa –containing rmfp-1 after similar contact times (Fig. 4.3) and the forces measured were reversible. Contact time t_c, between the surfaces significantly changed the cohesive energy from W_c = 3.3 ± 0.4

mJ/m^2 for t = 2 min to W_c = 10.0 ± 2.8 mJ/m^2 at 60 min for the Dopa-containing rmfp-1 surfaces apparently due to Fe^{3+} bridging. This indicates that it takes time for the Fe^{3+} to recruit two or more Dopa and bridge them across the surfaces. These results also show that Fe^{3+} is involved in chelating only the Dopa moieties in the rmfp-1 films by forming multivalent catecholate-Fe complexes across the surfaces; however, other hard Lewis acid donors such as the –OH of the Tyrosine or the $–NH_2$ of Lysine between rmfp-1 surfaces are not coordinated. The ligand number of the Fe^{3+}-Dopa complex depends on the pH and the ratio of Dopa to Fe^{3+} (29), and the bridging of rmfp-1 surfaces is by bis- and tris-catecholato-Fe^{3+} complex formation. The local pH within the protein film can be different from the bulk pH (30) (*rmfp-1 has a pI of ~10*); hence determining the ratio of bis to tris complexes at an interface is challenging and beyond the scope of this work. The magnitude of Fe^{3+} mediated cohesion between the Dopa modified rmfp-1 films measured in this work is comparable with biotin-avidin interfacial bond energy (W_{ad} ~ 10 mJ/m^2) (31), the strongest known non-covalent interaction between a protein and ligand. Two to three Dopa residues of mfp-1 in the cuticle of the marine mussels complex with a single Fe^{3+} (32), thereby creating a stable complex that can, in principle, be translated to cross-link other structural proteins. These iron-protein complexes have a breaking force nearly half that of covalent bonds (as measured in our experiments), but unlike covalent bonds they can form and break reversibly, making them ideal for creating sacrificial cross-links to prevent catastrophic failure of a material.

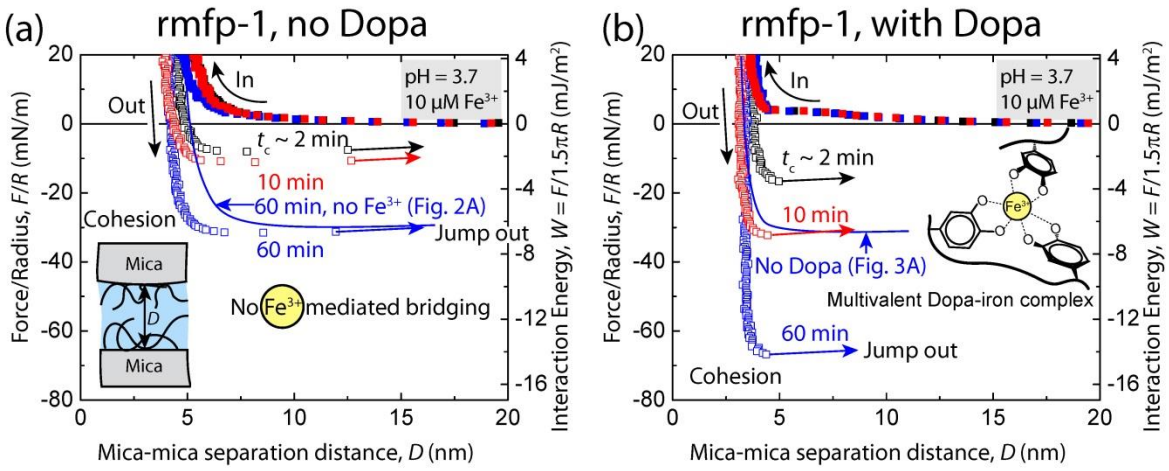

Figure 4.3 Representative force *vs.* distance plots showing the effect of contact time, t_c, on the cohesion between two symmetric (a) unmodified rmfp-1 and (b) Dopa-containing rmfp-1 films at pH 3.7 with 10 μM Fe^{3+} between the surfaces.

4.4.2 Cohesive interactions between mfp-1 short peptide dimers with Dopa

Cohesive interactions between short decapeptide dimers (Pro-pep, $[AKPSYPPTYK]_2$) of the consensus decapeptide repeat unit of mfp-1 were measured to determine the effect of peptide length on the energy of interaction between the protein films uniformly deposited on mica surfaces. We investigated the effect of Fe^{3+} on the change in cohesive energy between the short peptide films. Another short decapeptide dimer (Hyp-Pep, $[AKP^*SYP^*P^*TYK]_2$, P* = trans-4-hydroxyproline) with Hydroxyproline modification was also tested for cohesion. Hyp-pep dimer is a closer mimic of the consensus decapeptide repeat unit of mfp-1 which has *trans*-4-hydroxyproline modification at P-1, P-6 and P-7 of the decapeptide (additional *trans*-3 modification occurs at P-6, but was not tested here). We also assessed if hydroxylation of proline has an effect on the cohesive and metal chelating properties between the protein films.

At pH 3.7, the cohesive energy of interaction between unmodified mfp-1 Pro-pep (Proline containing dimer) film was W_c = 8.1 ± 1.1 mJ/m^2 at short contact times, t_c = 2 min (Fig. 4.4a), and did not change when the surfaces were kept under compressive contact for *t* = 10-60 min unlike rmfp-1 (Fig. 4.2a, b). Dopa-modified Pro-pep dimer showed cohesion energy similar to the unmodified dimer. The forces measured between unmodified mfp-1 Pro-pep dimer films on approach were purely repulsive due to steric and hydration forces (33) (Fig. 4.4a).

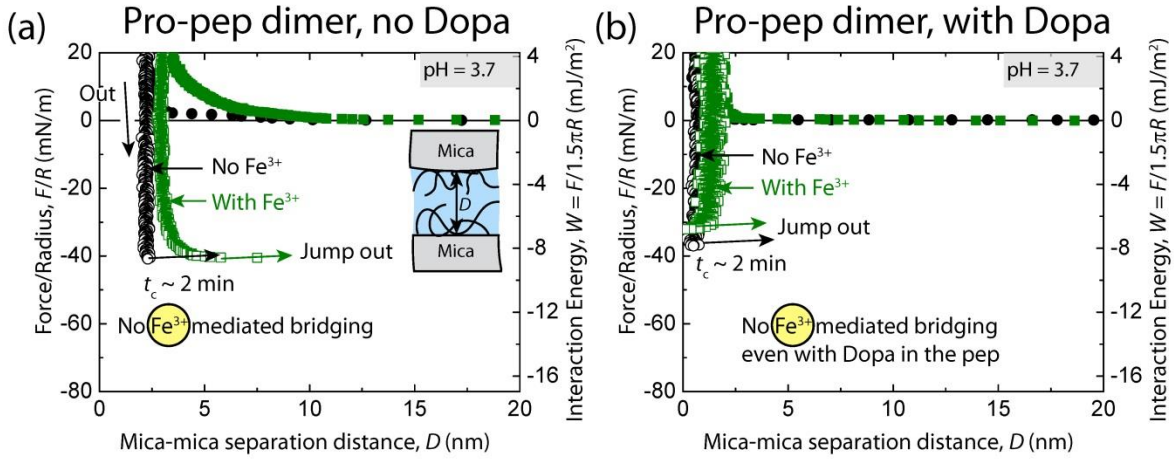

Figure 4.4 Representative force *vs.* distance plots of cohesion between two symmetric (a) unmodified (no Dopa) and (b) Dopa-containing mfp-1 peptide dimer (with proline, Pro-pep) films at pH 3.7 with (black points) and without (green points) 10 μM Fe^{3+} between the surfaces.

The cohesion energy between the mfp-1 peptide films did not change on introducing 10 μM Fe^{3+} between the surfaces regardless of the Dopa modification of the decapeptide dimers (Fig. 4.4). This is contrary to the commonly observed property of ferric ions to chelate Dopa containing protein films across surfaces as shown in our rmfp-1 films (Fig. 4.3) experiments and previously seen in natural mussel foot protein films (34). Perhaps the Dopa

needed to coordinate and form Fe^{3+}-mediated bridges between the films is unavailable by virtue of interacting with the mica surface through various interactions as shown in Fig. 4.1b.

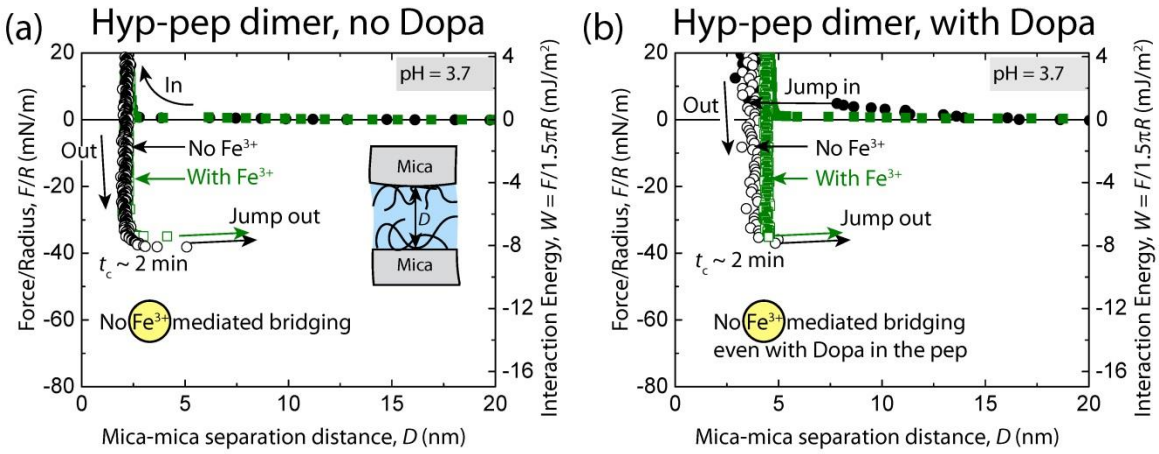

Figure 4.5 Representative force *vs.* distance plots of cohesion between two symmetric (a) unmodified (no Dopa) and (b) Dopa-containing mfp-1 peptide dimer (with trans-4-hydroxyproline, Hyp-pep) films at pH 3.7 with (black points) and without (green points) 10 μM Fe^{3+} between the surfaces.

Interestingly, the peptide dimers with hydroxyproline (Hyp-pep) showed cohesion energies similar to the Pro-pep dimers (W_c = 9.4 ± 1.2 mJ/m^2) and Dopa did not have an effect on the interaction energies between the films (Fig. 4.5). Fe^{3+} was also unable to enhance the cohesive interactions between the Hyp-pep films. These results suggest that peptide length is a critical design parameter for Fe^{3+}-mediated cohesive bridging. We showed that there is a critical number for the repeating decapeptide unit of the monomer between 2 and 12 necessary to trigger metal chelation between the peptide films and that incorporating Dopa into a peptide sequence does not necessarily guarantee the formation of metal mediated cross-links between the peptide films.

4.4.3 Adhesive interaction between rmfp-1 and silicone (PDMS) films

To investigate the effect of Dopa on the adhesive interaction of rmfp-1 to a hydrophobic surface, forces were measured between rmfp-1 films uniformly deposited on mica and an uncross-linked silicone surface of thickness D_{PDMS} ~ 4 – 7 nm prepared on a molecularly smooth gold surface (21).

At pH 3.7, the adhesive energy of interaction between unmodified rmfp-1 and PDMS was W_{ad} = 5.4 ± 1.5 mJ/m^2 at contact time, t < 10 min, and increased to W_{ad} = 15 ± 7 mJ/m^2 at t = 60 min (Fig. 4.6a). A long-range weak jump-in instability was measured for the unmodified rmfp-1 at a distance of 30 nm from the hardwall contact due to hydrophobic interactions and fluctuating silicone and rmfp-1 molecules on the surfaces. Increasing the pH to 7.5 caused significant loss in adhesion between the unmodified rmfp-1 and PDMS surfaces (W_{ad} = 0.5 ± 0.1 mJ/m^2). The forces measured on approach were also purely repulsive (Fig. 4.6c) due to steric and hydration forces (33). However, the adhesion was recovered completely on readjusting the pH to 3.7 indicating that the protein did not undergo any irreversible structural or chemical change.

It has previously been reported that at low pH, the PDMS surface is weakly charged and there is a weak hydrophobic attraction between bare mica and PDMS, whereas at high pH it is negatively charged due to the adsorption of anions from the solution leading to a weak hydration repulsion between the two surfaces (21). The unmodified rmfp-1 film, at pH 3.7, adheres to PDMS mainly through hydrophobic interactions involving the alanine/tyrosine/proline residues in rmfp-1 and the silicone chains of the PDMS. The contribution of electrostatic force to the observed adhesion is minor at low pH since the silicone film is weakly charged (Surface potential, ψ_{PDMS} ~ -3 ± 5 mV) at pH 3.7 and its

interaction with the positively charged lysine in the protein film is therefore small. At physiological pH 7.5 (150 mM salt), electrostatic interactions between the silicone and the unmodified rmfp-1 film are weak due to the screening of the surface charge at such high salt concentrations (35). Strong hydration of the silicone also results in poor adhesion between the rmfp-1 and silicone films (21).

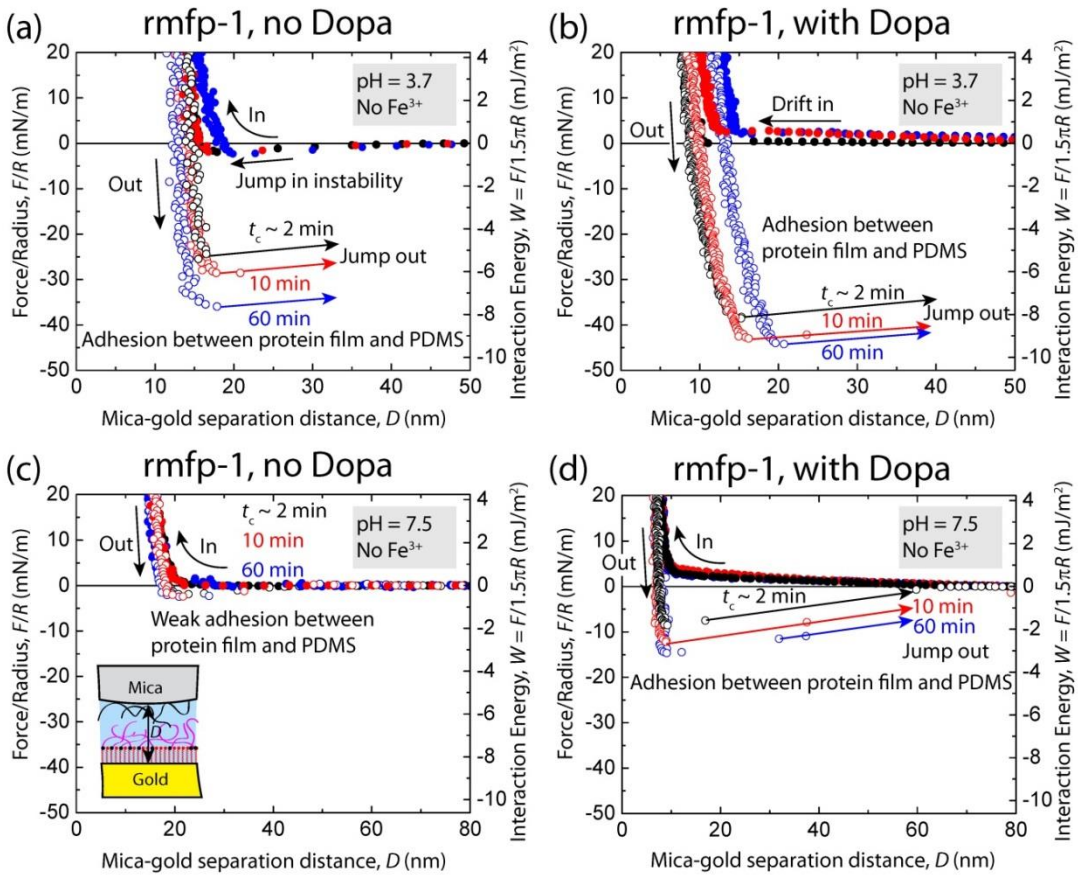

Figure 4.6 Representative force *vs.* distance plots showing the effect of contact time, t_c, on adhesion between unmodified and Dopa-containing rmfp-1 films and a PDMS monolayer at pH 3.7 (a, b) and, pH 7.5 (c, d), respectively.

The Dopa-containing rmfp-1 showed an adhesion energy of W_{ad} = 8 ± 1 mJ/m^2 (Fig. 4.6) to the silicone film (PDMS) at pH 3.7 at t_c = 2 – 60 min (Fig. 4.6b). The forces measured

were reversible after multiple approaches and separations of the surfaces at the same contact point. Unlike the unmodified rmfp-1, a weak repulsive force was measured at about 30 nm from contact; however, an attractive force caused the surfaces to drift into contact (Fig. 4.6b). The adhesion energy between the Dopa-containing rmfp-1 and silicone films resembled the unmodified rmfp-1 at pH 3.7, but under physiological conditions (pH 7.5, 150 mM salt), the Dopa-containing rmfp-1 film showed significant adhesion to the silicone surface (W_{ad} = 3.6 ± 0.8 mJ/m^2) (Fig. 4.6d, 4.7) and was weakly dependent on t_c. Long range repulsive forces were measured between the silicone surface and the Dopa-containing rmfp-1 film during approach at pH 7.5. This is due to the steric repulsion between the cross-linked protein film (due to pH induced oxidation of Dopa to Dopa quinone) and the silicone surface. However, once the surfaces are brought into compression (Fig. 4.6d), the uncross-linked silicone chains entangle and intercalate into the cross-linked protein network and cause the surfaces to adhere through an entanglement trapping mechanism by the formation of knots (36).

An adhesion energy of W_{ad} = 5.3 ± 1.2 mJ/m^2 was measured between the two surfaces (~70% recovery of adhesion) on reversing back the pH to 3.7 from 7.5 (Fig. S4.3). A long ranged repulsive force was recorded ~50 nm from contact (D_H = 10 nm) followed by a jump in to contact during approach (Fig. S4.3). The long-range repulsion is due to the irreversible pH-induced swelling and cross-linking of the Dopa-containing rmfp-1 film similar to that observed during the cohesion measurements (Fig. 4.2d). Nevertheless, once this cross-linked protein film is pushed into the silicone layer, intercalation and entanglement occurs and this phenomenon is enhanced by the increased hydrophobicity of the silicone film at pH 3.7 resulting in a higher adhesion compared to that at pH 7.5. These results suggest that silicone

interacts strongly with Dopa functionalized proteins under physiological conditions and can be used to design coatings for functional biomaterials.

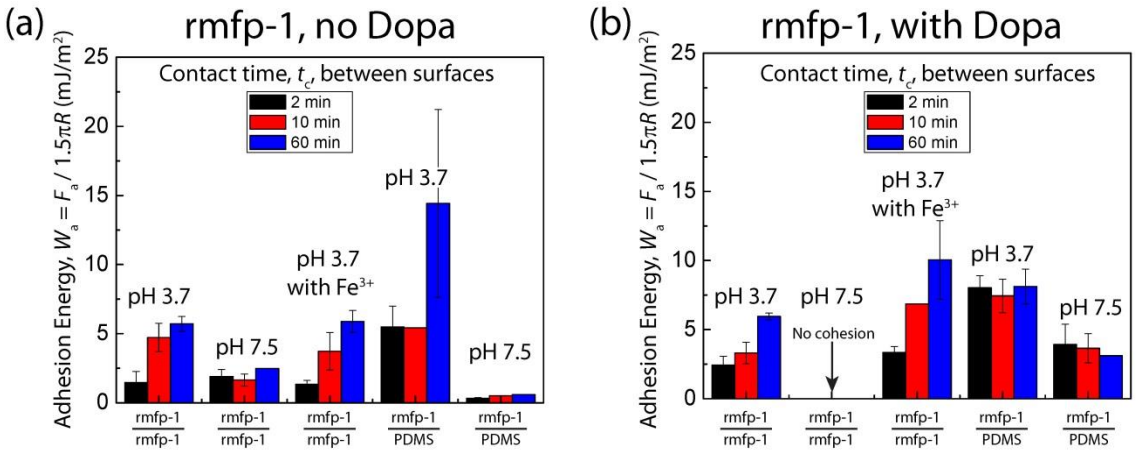

Figure 4.7 Effect of contact time (t_c = 2, 10, 60 mins), pH and Fe^{3+} on the adhesion (cohesion) energy, W_a of (a) unmodified and (b) Dopa-containing rmfp-1 to different surfaces.

4.5 Conclusions

In this work, we demonstrate that bidentate hydrogen bonding by Dopa plays only a minor role in the adhesion of a protein to mica (or adsorption to titania surface). The adhesion of the proteins or peptides to a mica surface is more due to specific coulombic interactions between lysine and the negative mica surface or mono-dentate hydrogen bonding in series with Lysine-mica interactions. Hydrophobic interaction between the aromatic residues and the hydrophobic domains in the mica crystal lattice or π–cation between the aromatic rings in the protein and the ions adsorbed to the mica interface are possibly responsible for the adhesion. As the catechol group did not influence the cohesive strength

between the protein films, π–π stacking, hydrophobic and π–cation interactions are more likely to contribute to the strong cohesion at pH 3.7.

Cohesion between Dopa-containing rmfp-1 surfaces can be doubled through Fe^{3+} mediated chelation resulting in an interfacial energy of $W_c \sim 10$ mJ/m^2 which is equivalent to biotin-avidin interfacial adhesion energy, the strongest known non-covalent interaction; but unlike the protein and ligand interaction, the iron mediated cohesive bond can be broken and formed reversibly. This interaction is absent without Dopa in the protein. Incorporating Dopa into a peptide sequence does not guarantee the formation of metal mediated cross-links between peptide films and the length of the peptide is a crucial parameter that determines the performance of the materials that involve coordination chemistry.

Unmodified rmfp-1 showed a stronger adhesion ($W_{ad} = 15 \pm 7$ mJ/m^2) to the silicone surface at pH 3.7 compared with the Dopa-containing rmfp-1 ($W_{ad} = 8 \pm 1$ mJ/m^2). Under physiological conditions (pH = 7.5, 150 mM salt), Dopa-containing rmfp-1 displayed significant adhesion to silicone film due to entanglement trapping type of interaction between the cross-linked rmfp-1 and the uncross-linked silicone surfaces, whereas the unmodified rmfp-1 adhered weakly to the silicone surface, possibly through weak hydrophobic and electrostatic interactions. We show that Dopa containing proteins can bind strongly to silicone surfaces under a wide range of pH. Hence, Dopa containing proteins and peptides with appropriate length could be used as tunable systems for applications in strain resistant coatings, drug delivery and bio-adhesives.

4.6 Appendix

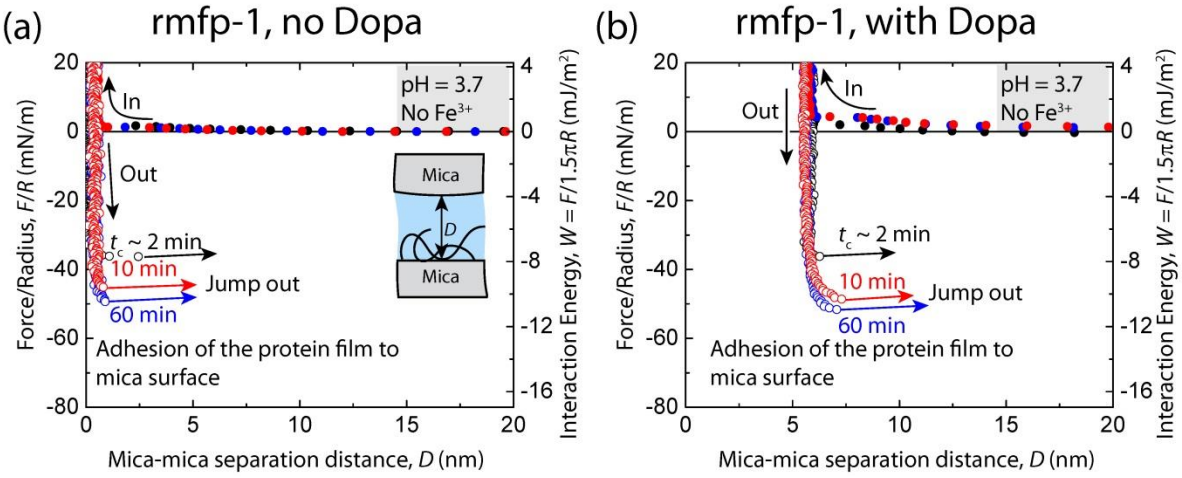

Figure S4.1 Representative force *vs.* distance plot showing the effect of contact time, t_c, on the adhesion between (A) non Dopalated and (B) Dopalated rmfp-1 film and a mica surface respectively.

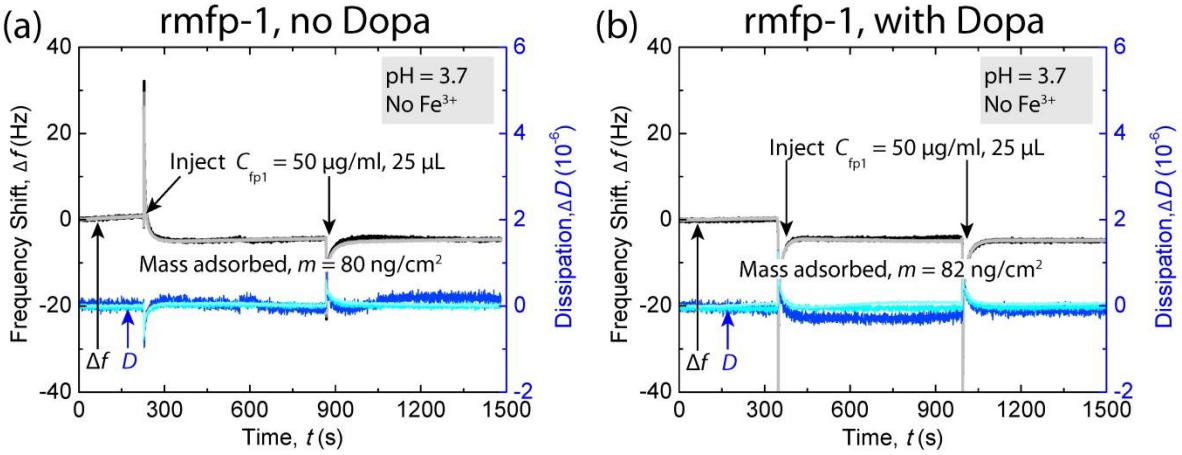

Figure S4.2 Frequency and dissipation change in a Quartz Crystal Microbalance (QCM) upon adsorption of (A) non Dopalated and (B) Dopalated rmfp-1 respectively. In this two-step adsorption, 25 µL of 50 µg/ml of the protein was adsorbed to a TiO_2 surface as indicated

in the figure. The QCM was calibrated to zero with an acetate buffer addition of pH 3.7 used to dilute the proteins.

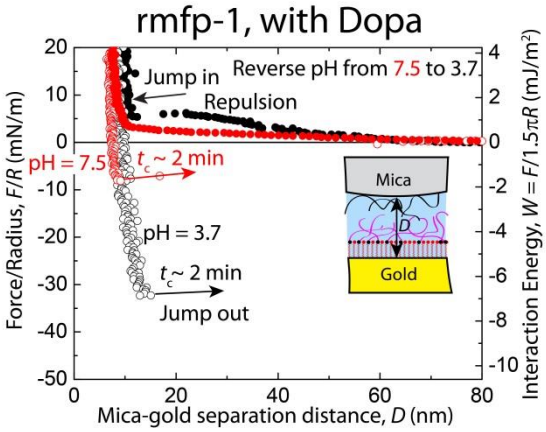

Figure S4.3 Representative force *vs.* distance plot showing the effect of reversing pH from 7.5 to 3.5 on the adhesion between Dopalated rmfp-1 film and silicone film (PDMS).

4.7 References

1. Taylor SW, Luther GW, & Waite JH (1994) Polarographic and Spectrophotometric Investigation of Iron(III) Complexation to 3,4-Dihydroxyphenylalanine-Containing Peptides and Proteins from Mytilus-Edulis. *Inorganic Chemistry* 33(25):5819-5824.
2. Papov VV, Diamond TV, Biemann K, & Waite JH (1995) Hydroxyarginine-Containing Polyphenolic Proteins in the Adhesive Plaques of the Marine Mussel Mytilus-Edulis. *Journal of Biological Chemistry* 270(34):20183-20192.
3. Rzepecki LM & Waite JH (1995) Wresting the muscle from mussel beards: Research and applications. *Molecular Marine Biology and Biotechnology* 4(4):313-322.

4. Sun CJ & Waite JH (2005) Mapping chemical gradients within and along a fibrous structural tissue, mussel byssal threads. *Journal of Biological Chemistry* 280(47):39332-39336.

5. Vreeland V, Waite JH, & Epstein L (1998) Polyphenols and oxidases in substratum adhesion by marine algae and mussels. *Journal of Phycology* 34(1):1-8.

6. Zhao H & Waite JH (2006) Linking adhesive and structural proteins in the attachment plaque of Mytilus californianus. *Journal of Biological Chemistry* 281(36):26150-26158.

7. Lee H, Scherer NF, & Messersmith PB (2006) Single-molecule mechanics of mussel adhesion. *Proceedings of the National Academy of Sciences of the United States of America* 103(35):12999-13003.

8. Anderson TH, *et al.* (2010) The Contribution of DOPA to Substrate-Peptide Adhesion and Internal Cohesion of Mussel-Inspired Synthetic Peptide Films. *Advanced Functional Materials* 20(23):4196-4205.

9. Heo J, *et al.* (2012) Improved Performance of Protected Catecholic Polysiloxanes for Bioinspired Wet Adhesion to Surface Oxides. *Journal of the American Chemical Society* 134(49):20139-20145.

10. Chung HY & Grubbs RH (2012) Rapidly Cross-Linkable DOPA Containing Terpolymer Adhesives and PEG-Based Cross-Linkers for Biomedical Applications. *Macromolecules* 45(24):9666-9673.

11. Liu B, Burdine L, & Kodadek T (2006) Chemistry of periodate-mediated cross-linking of 3,4-dihydroxylphenylalanine-containing molecules to proteins. *Journal of the American Chemical Society* 128(47):15228-15235.

12. Saxer S, *et al.* (2010) Surface Assembly of Catechol-Functionalized Poly(L-lysine)-graft-poly(ethylene glycol) Copolymer on Titanium Exploiting Combined Electrostatically Driven Self-Organization and Blomimetic Strong Adhesion. *Macromolecules* 43(2):1050-1060.

13. Fichman G, *et al.* (2014) Seamless Metallic Coating and Surface Adhesion of Self-Assembled Bioinspired Nanostructures Based on Di-(3,4-dihydroxy-l-phenylalanine) Peptide Motif. *ACS Nano*.

14. Hwang DS, *et al.* (2012) Mussel foot protein-1 (mcfp-1) interaction with titania surfaces. *Journal of Materials Chemistry* 22(31):15530-15533.

15. Yu J, *et al.* (2013) Adhesion of Mussel Foot Protein-3 to TiO2 Surfaces: the Effect of pH. *Biomacromolecules* 14(4):1072-1077.

16. Hwang DS & Waite JH (2012) Three intrinsically unstructured mussel adhesive proteins, mfp-1, mfp-2, and mfp-3: Analysis by circular dichroism. *Protein Science* 21(11):1689-1695.

17. Laursen R (1992) Reflections on the Structure of Mussel Adhesive Proteins. *Structure, Cellular Synthesis and Assembly of Biopolymers*, Results and Problems in Cell Differentiation, ed Case S (Springer Berlin Heidelberg), Vol 19, pp 55-74.

18. Taylor SW (2002) Chemoenzymatic synthesis of peptidyl 3,4-dihydroxyphenylalanine for structure-activity relationships in marine invertebrate polypeptides. *Analytical Biochemistry* 302(1):70-74.

19. Das S, *et al.* (2013) Synergistic Interactions between Grafted Hyaluronic Acid and Lubricin Provide Enhanced Wear Protection and Lubrication. *Biomacromolecules* 14(5):1669-1677.

20. Israelachvili J, *et al.* (2010) Recent advances in the surface forces apparatus (SFA) technique. *Reports on Progress in Physics* 73(3).

21. Donaldson SH, *et al.* (2013) Asymmetric Electrostatic and Hydrophobic-Hydrophilic Interaction Forces between Mica Surfaces and Silicone Polymer Thin Films. *ACS Nano* 7(11):10094-10104.

22. Kearney PC, *et al.* (1993) Molecular Recognition in Aqueous-Media - New Binding-Studies Provide Further Insights into the Cation-Pi Interaction and Related Phenomena. *Journal of the American Chemical Society* 115(22):9907-9919.

23. Hwang DS, Zeng HB, Lu QY, Israelachvili J, & Waite JH (2012) Adhesion mechanism in a DOPA-deficient foot protein from green mussels. *Soft Matter* 8(20):5640-5648.

24. Lu QY, Hwang DS, Liu Y, & Zeng HB (2012) Molecular interactions of mussel protective coating protein, mcfp-1, from Mytilus californianus. *Biomaterials* 33(6):1903-1911.

25. Lu QY, *et al.* (2013) Nanomechanics of Cation Interactions in Aqueous Solution. *Angewandte Chemie-International Edition* 52(14):3944-3948.

26. Sangsik Kim AF, Yongjin Lee, Yongseok Jho, Hongbo Zeng, Dong Soo Hwang (Cation-π interaction in DOPA-deficient mussel adhesive protein mfp-1. *Unpublished*.

27. Pillai KV & Renneckar S (2009) Cation-pi Interactions as a Mechanism in Technical Lignin Adsorption to Cationic Surfaces. *Biomacromolecules* 10(4):798-804.

28. Grauffel C, *et al.* (2013) Cation-pi Interactions As Lipid-Specific Anchors for Phosphatidylinositol-Specific Phospholipase C. *Journal of the American Chemical Society* 135(15):5740-5750.

29. Holten-Andersen N, *et al.* (2011) pH-induced metal-ligand cross-links inspired by mussel yield self-healing polymer networks with near-covalent elastic moduli. *Proceedings of the National Academy of Sciences of the United States of America* 108(7):2651-2655.

30. Longo GS, de la Cruz MO, & Szleifer I (2012) Molecular theory of weak polyelectrolyte thin films. *Soft Matter* 8(5):1344-1354.

31. Helm CA, Knoll W, & Israelachvili JN (1991) Measurement of Ligand Receptor Interactions. *Proceedings of the National Academy of Sciences of the United States of America* 88(18):8169-8173.

32. Harrington MJ, Masic A, Holten-Andersen N, Waite JH, & Fratzl P (2010) Iron-Clad Fibers: A Metal-Based Biological Strategy for Hard Flexible Coatings. *Science* 328(5975):216-220.

33. Das S, Donaldson SH, Kaufman Y, & Israelachvili JN (2013) Interaction of adsorbed polymers with supported cationic bilayers. *Rsc Advances* 3(43):20405-20411.

34. Zeng HB, Hwang DS, Israelachvili JN, & Waite JH (2010) Strong reversible Fe^{3+}-mediated bridging between dopa-containing protein films in water. *Proceedings of the National Academy of Sciences of the United States of America* 107(29):12850-12853.

35. Israelachvili JN (2011) Intermolecular and Surface Forces, 3rd Edition. *Intermolecular and Surface Forces, 3rd Edition*:1-674.

36. Brown HR (1991) The Adhesion between Polymers. *Annual Review of Materials Science* 21:463-489.

5. STICK-SLIP PEELING AND ADHESION HYSTERESIS OF GECKO-MIMETIC PATTERNED SURFACES WITH A SMOOTH GLASS SURFACE

5.1 Abstract

Geckos are highly efficient climbers and can run over any kind of surface with impeccable dexterity due to the typical design of their hierarchical foot structure. We have fabricated tilted, i.e., asymmetric, poly(dimethylsiloxane) (PDMS) micro-flaps of two different densities that mimic the function of the micron sized setae on the gecko foot pad. The adhesive properties of these micro-flaps were investigated in a modified surface forces apparatus (SFA); both for normal pure loading and unloading (detachment), as well as unloading after the surfaces were sheared, both along and against the tilt direction. The tilted micro-flaps showed directional, i.e., anisotropic adhesive behavior when sheared against an optically smooth (RMS roughness ~ 10±8 nm) SiO_2 surface. Enhanced adhesion was measured after shearing the flaps along the tilted (gripping) direction and low adhesion when sheared against the tilted (releasing) direction. A Johnson-Kendall-Roberts (JKR) theory using an effective surface energy and modulus of rigidity (stiffness) quantitatively described the contact mechanics of the tilted micro-flaps against the SiO_2 surface. We also find an increasing adhesion and stick-slip of the surfaces during detachment which we explain

qualitatively in terms of the density of flaps, considering it to increase from 0% (no flaps, smooth surface) to 100% (close-packed flaps, effectively smooth surface). Large energy dissipation at the PDMS-silica interface caused by the viscoelastic behavior of the polymer results in stick-slip peeling and hence an enhanced adhesion energy is observed during the separation of the micro-flaps surface from the smooth SiO_2 surface after shearing of the surfaces. For structured multiple contact surfaces, hysteresis as manifested by different loading and unloading paths can be due entirely to the *elastic* JKR micro contacts. These results have important implications in the design of bio-mimetic adhesives.

5.2 Introduction

The supreme ability of geckos to attach and detach quickly to any surface has been fascinating man for over two millennia. They can attach and detach their toes in matters of milliseconds (1) on surfaces, be they vertical or inverted. This exceptional feature of quick attachment and equally quick detachment to any surface is attributed to the typical hierarchical structure of their foot-pad (2) and is still a challenge that no conventional adhesive is capable of meeting. A considerable number of studies have been performed to understand the mechanism of the gecko adhesive system (3-8) and mimic the same for functional surfaces and articulated robotic devices (9-12).

It has been shown that the geckos employ the universal van der Waals force of adhesion (6, 13) and possibly capillary forces (14-18) to attach to surfaces and a peeling mechanism for quick detachment (4). It has been demonstrated that the hierarchical structure of the gecko foot hair not only allows it to conform to micro and nano scale asperities maintaining high adhesion force on surfaces but also has anisotropic/directional frictional-

adhesion properties (13, 19, 20). Various types of patterned hierarchical structures mimicking the gecko foot pad have been fabricated for enhanced adhesion to smooth and rough surfaces (10, 11, 21-30). Previous works have shown that tilted micro structures perform most closely to the gecko adhesive system (11, 12, 21, 22, 31, 32). However, little effort has been made to understand the effect of the geometry and the areal density of the flaps at the micro level which is crucial in determining the contact mechanics of the arrays of the flaps to a surface.

Here, we report the mechanism of adhesion of the tilted poly(dimethylsiloxane) PDMS micro flaps to a smooth silica surface with and without prior shearing of the surfaces. Shearing significantly changes the effective adhesion energy (twice of the theoretical value) of the flaps to the silica surface and its magnitude is dependent on the sliding direction. The unloading of the (asymmetric and structured) flaps from the silica surface with multiple micro contacts is well described by the classic Johnson-Kendall-Roberts (JKR) theory, unlike the peeling of two smooth PDMS surfaces and, the observed hysteresis and stick-slip has a different origin to that seen between two smooth (unstructured) single contact geometries (33). We demonstrate that the effective stiffness of the arrays of the flaps play minor role in determining the adhesion energy. Stick-slip peeling instabilities during separation after prior sliding of the flaps along the direction of the tilt could rationalize the measured high adhesion energies of the PDMS flaps on the silica surface.

5.3 Materials and Methods

5.3.1 Fabricated patterned surfaces

Large arrays of tilted PDMS flaps of two different densities (Fig. 5.1), were fabricated using micro fabrication techniques described elsewhere (10). The low (1X) and the high (3.5X) areal density flaps have 1850 flaps/mm^2 and 6410 flaps/mm^2 respectively. The flaps are tilted at an angle of $\phi = 20°$ from the vertical. Schematic top-view orthographic diagrams show that the flaps are arranged in a hexagonal packing geometry (Fig. 5.1 b and d).

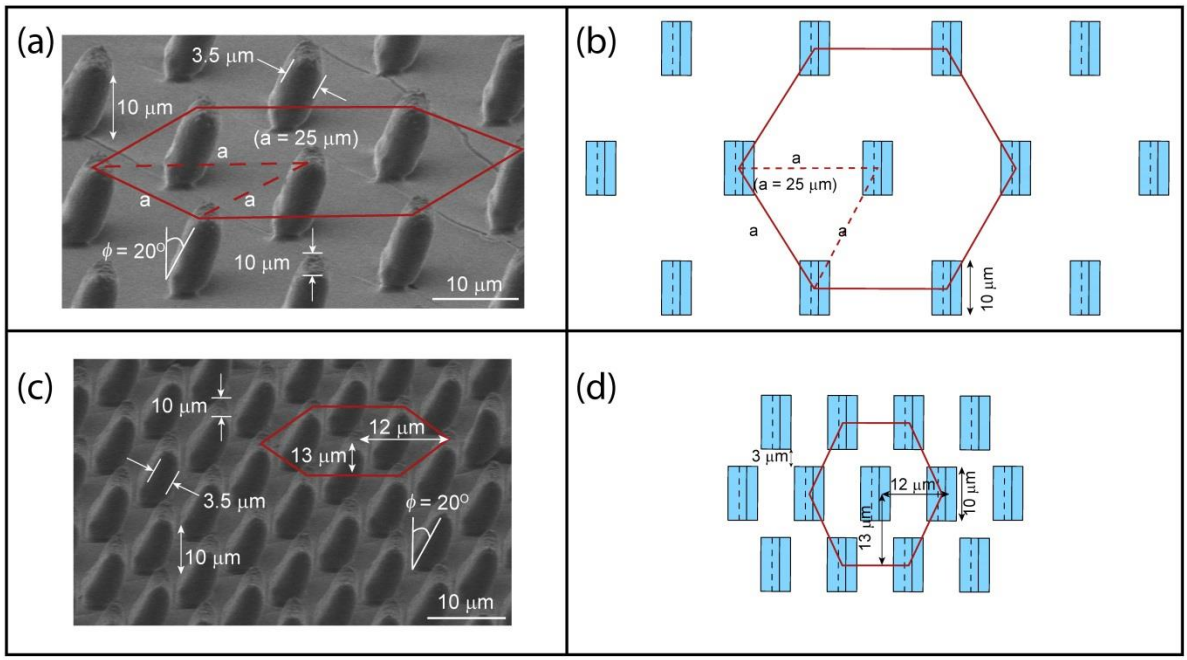

Figure 5.1 SEM images of the (a) low areal density (1850 flaps/mm^2), 1X tilted PDMS flaps and (c) high areal density (6410 flaps/mm^2), 3.5X tilted PDMS flaps. The flaps are tilted at an angle of 20° from the vertical. Schematic top-view orthographic diagrams showing the positions of the flaps relative to each other for both the (b) 1X flaps and (d) 3.5X flaps.

5.3.2 Normal and lateral force measurements

A modified surface forces apparatus (SFA) (34) was used to measure the normal $F_{\perp}$ (adhesion and loads) and the lateral forces $F_{\parallel}$ between the arrays of the fabricated micro-flaps and a spherical silica disk of radius of curvature, R = 2 cm, and RMS roughness ~ 10 ± 8 nm. The full details of the force measurements have been described in previous work (10, 11). As a summary, the spherical glass disk was mounted to the top friction device, which can slide laterally over a distance of 100-500 μm at different sliding speeds (1-10 μm/s). The PDMS flaps were glued to a flat glass disk, which sits on a double cantilever spring with strain gauges that can measure the normal forces. A CCD camera was mounted on a microscope to visualize the contact area during loading, unloading and sliding of the spherical silica disk against the arrays of the fabricated PDMS micro-flaps (Fig. 5.2).

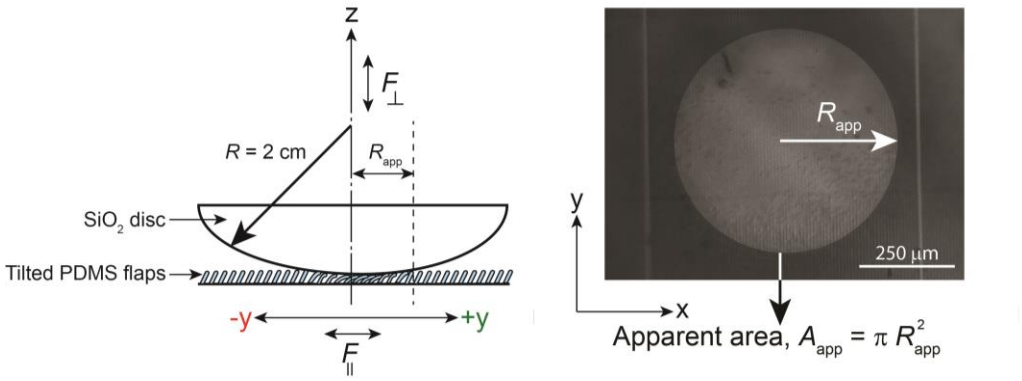

Figure 5.2 The apparent area, A_{app} of contact when the arrays of PDMS micro-flaps are compressed against a spherical silica disk of radius of curvature, R = 2 cm. The bright circular area* shows the region of flaps that is in the deformed state. *Contrast has been enhanced for clarity.

In the SFA experiment, the top spherical silica disk was pressed against the PDMS micro-flaps at a constant speed of ~ 10 μm/s until the desired pre-load, $F_{\perp}^{P}$ was reached.

Adhesion tests were performed by separating the two surfaces, without them being sheared against each other (no prior shearing). Adhesion was also measured after the surfaces were sheared against each other at a velocity of 10 μm/s along the + y direction (along the direction of the tilt) and - y direction (against the direction of the tilt). Shearing was stopped after sliding for ~ 300 μm while the surfaces were still under a shear stress (Fig. 5.3). The flaps did not get damage even after many sliding cycles (50-100) at a given contact point and the adhesion tests were reproducible at different contact points. Measurements and surface preparations were performed in a clean dust free environment (sealed SFA or in Laminar flow hood).

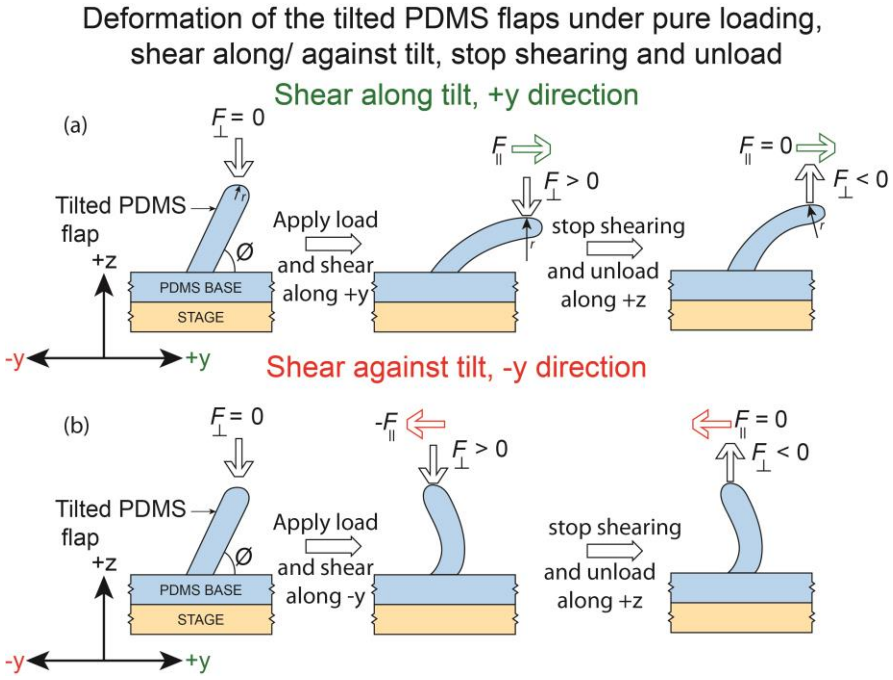

Figure 5.3 Schematics of a single flap deformation showing the separation of the flap with the upper silica surface after the flaps are sheared (a) along the direction of the tilt (+y direction) (b) against the direction of the tilt (-y direction). The adhesion forces, $-F_{\perp}$ measured after sliding the top surface in the +y direction are significantly higher than the values measured after sliding in the -y direction.

5.4 Theoretical background

A brief description of the contact mechanics between two bodies in adhesive contact will be helpful in interpreting the experimental data, since this work investigates the effect of shear on the change in the adhesion properties of a patterned surface against a smooth silica disk.

Classical mechanics deals solely with bulk materials whereas contact mechanics takes into account the bulk properties along with the surface and geometry of contact. Geometric effects of local elastic deformation was first considered by Hertz (35) and the effect of adhesive interactions were neglected. An improvement over the Hertzian theory is the Johnson-Kendall-Roberts (JKR) theory (36) in which the contact surfaces are considered to be adhesive. The adhesion force (F_{ad}) between a sphere of radius *r* and a plane in the JKR model is given by

$$F_{\mathrm{ad}} = \frac{3}{2}\pi r W_{12} \tag{5.1}$$

where $W_{12} = \gamma_1 + \gamma_2 - \gamma_{12}$ is the thermodynamic work of adhesion, and γ_1, γ_2 and γ_{12} are the surface and interfacial energies of two interacting surfaces.

A JKR experiment involves bringing two surfaces (a sphere and a plane) into contact by applying an external load followed by retraction until the contact is broken. The deformation of the surfaces at a specified load $F_{\perp}$ is described by the contact area *a* of radius *r* as a result of compression (and adhesion). The expression for *a* is given by (36)

$$a = \pi\left\{\frac{r}{K_{\mathrm{eff}}}\left[F_{\perp} + 6\pi r W_{12} + \left(12\pi r W_{12} F_{\perp} + \left(6\pi r W_{12}\right)^2\right)^{1/2}\right]\right\}^{2/3} \tag{5.2}$$

$$\frac{1}{K_{\mathrm{eff}}} = \frac{3}{4}\left(\frac{1-\nu_1^{\,2}}{E_1} + \frac{1-\nu_2^{\,2}}{E_2}\right) \tag{5.3}$$

where K_{eff} is the effective stiffness, ν_i and E_i are the Young's modulus and the Poisson's ratio of the samples 1 and 2, respectively.

5.5 Results and Discussion

5.5.1 Adhesion force measurement with no prior shearing

The adhesion behavior of the low (1X) and the high (3.5X) areal density PDMS micro-flaps were tested against a smooth spherical silica disk at different pre-loads of $F_{\perp}^{P}$ = 1 – 40 mN. The 1X flaps showed no measurable adhesion (F_{ad} < 0.1 mN) to the silica surface which is consistent with our previous work (Fig. 5.4) (11). The graph of apparent area, A_{app} vs. the normal actual load, $F_{\perp}^{P}$ for the 1X flaps showed no hysteresis between the loading and unloading curves (Fig. 5.4), which is a characteristic signature of non-adhesive contact. This observation is attributed to the high surface roughness (RMS roughness ~ 250 nm) of the top edge of the 1X flaps (as visualized in the SEM) that reduces the real area of contact between the flaps and the spherical silica surface. The effective stiffness, K_{eff} of the 1X (low density) PDMS micro-flaps was calculated to be 1 MPa by JKR sphere on flat geometry fit (Eq. 5.1-5.3) to the experimental data (Fig. 5.4). The calculated value for K_{eff} is significantly higher than the expected value for bulk PDMS (~ 300 kPa) and is attributed to the non-linear strain response to the applied stress for the PDMS material (see supporting Fig. S5.1).

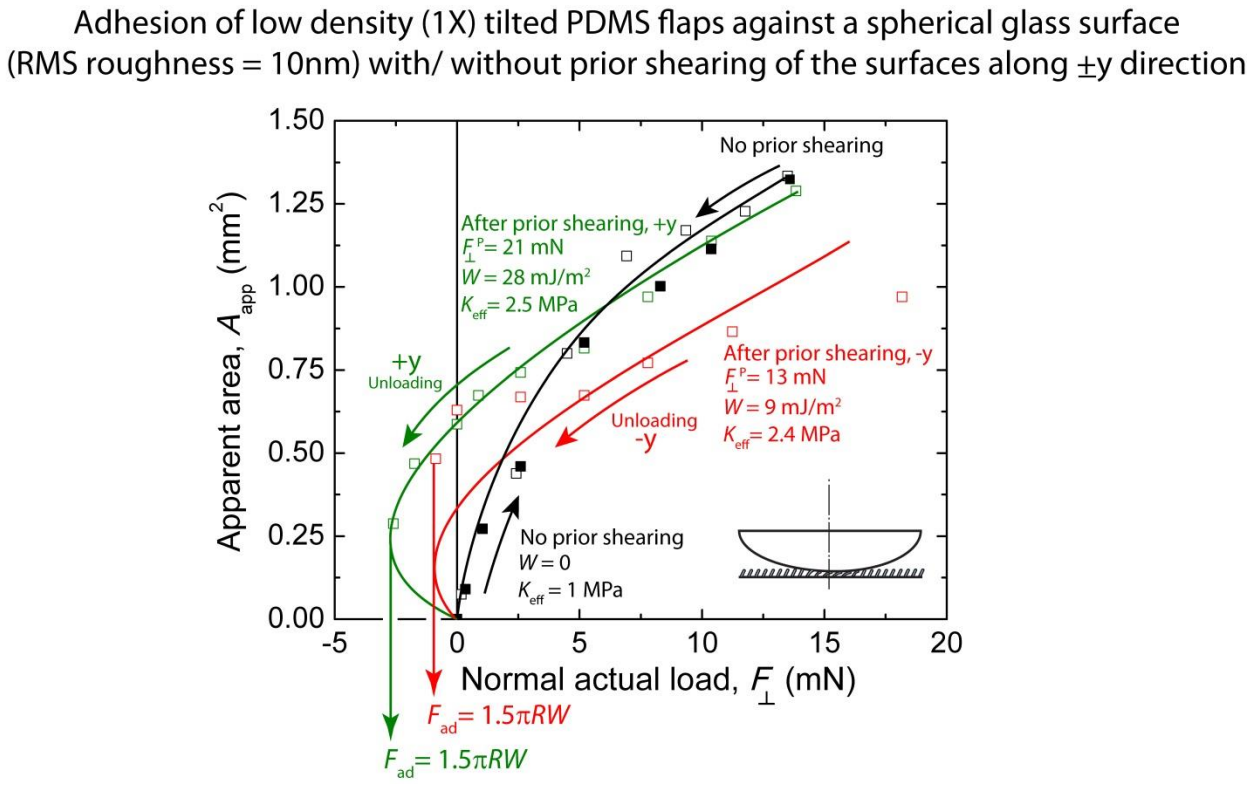

Figure 5.4 The apparent area, A_{app} *vs* the normal actual load, $F_\perp$ for the 1X tilted PDMS micro-flaps as they are separated (unloaded) from the spherical silica surface of radius of curvature, R = 2 cm. The open squares represent the experimentally observed A_{app} when unloading the flaps from the silica surface. The curves show the JKR fits to the experimental data.

The 3.5X (high density) PDMS micro-flaps showed an adhesion force of F_{ad} = 0.8 mN against the silica disk (Fig. 5.5). SEM images show that these flaps have lower surface roughness for the top edge of the flaps (RMS roughness ~ 170 nm). The lower surface roughness and the high areal density result in better commensurability between the surfaces and hence superior adhesion of the 3.5 X PDMS micro-flaps against the silica surface. The plot of A_{app} vs. $F_\perp^P$ for the 3.5X flaps was hysteretic with K_{eff} = 6 MPa and an effective value for the work of adhesion of W = 8 mJ/m^2. This effective work of adhesion is an outcome of

the decreasing energy due to the formation of bonds between the surfaces at the expense of the elastic deformation energy which reduces the binding energy.

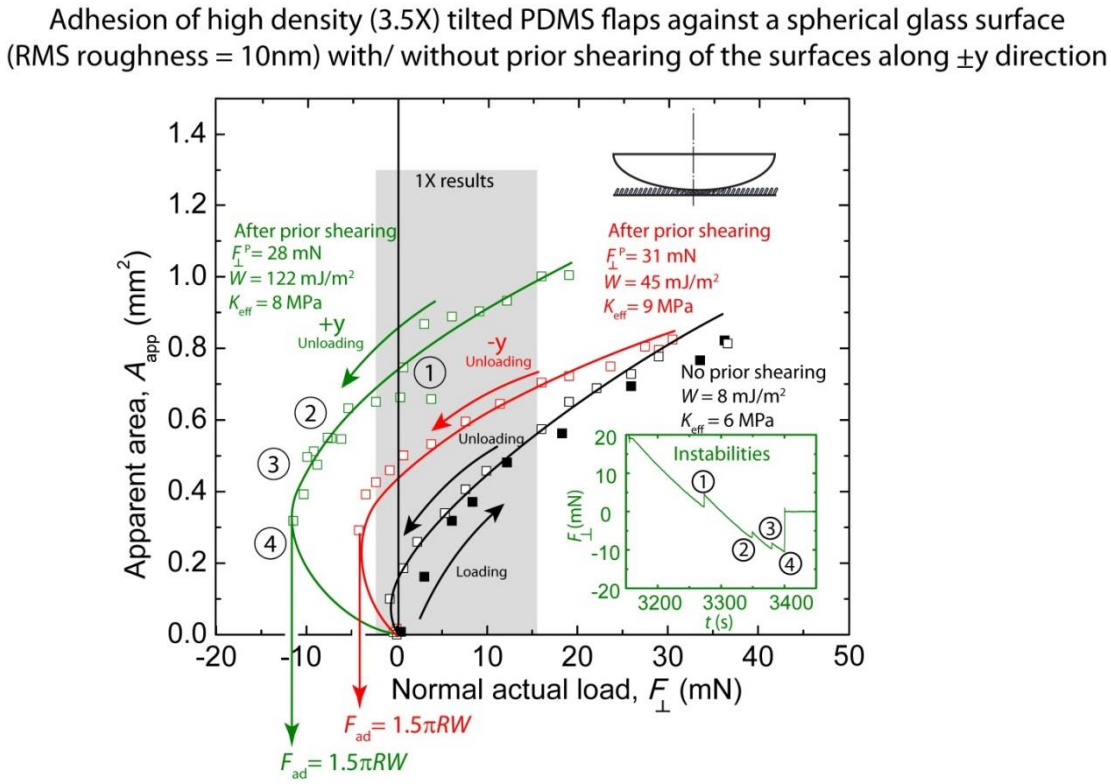

Figure 5.5 The apparent area, A_{app} *vs* the normal actual load, $F_\perp$ for the 3.5X tilted PDMS micro-flaps as they are separated (unloaded) from the spherical silica surfaceof radius of curvature, R = 2 cm. The open squares represent the experimentally observed A_{app} when unloading the flaps from the silica surface. The curves show the JKR fits to the experimental data. As a comparison, the area of the plot occupied by the curves for the 1X tilted PDMS micro-flaps is also shown by the shaded gray box.

The adhesion force per flap, f_{ad} was calculated to be 1 μN with a real area of contact per flap of a_{real} = 5 μm^2 and the local radius of curvature at pull-off was r = 5 μm (Table 5.1) for the 3.5X flaps during pure loading and unloading (no shear). The Hamaker constant for

PDMS and silica interacting across dry air is 5.3 x 10^{-20} J (37). Hence, the adhesive pressure, P_{ad} between PDMS and silica is, $P_{ad} = \frac{A}{6\pi D^3} = 6.3\times10^8$ N/m^2 where D = 0.165 nm is the intermolecular distance. Thus, the theoretically calculated force of interaction between one flap and the silica surface due to van der Waals force is $f_{ad}^{theory} = a_{real}P_{ad} = 3\text{mN}$. This is about 3 orders of magnitude bigger than the experimentally observed value for f_{ad} and shows how roughness can significantly decrease the adhesive force of interaction between two surfaces (10, 38, 39).

Table 5.1. Sphere on flat JKR model for individual flap deformation

Per flap JKR parameters	**1X tilted PDMS flaps (± 15 %)**			**3.5X tilted PDMS flaps (± 15 %)**		
	No shear	+y shear	-y shear	No shear	+y shear	-y shear
Calculated number of flaps at pull off, n [1]	-	**530**	830	640	**2040**	1870
Calculated adhesion force, f_{ad} (μN) [2]	-	**5**	1	1	**6**	2
JKR radius of curvature, r (μm) [3]	-	20	4	5	23	9
Calculated real area of contact, a_{re} (μm^2) [4]	-	**31**	4	5	**37**	11

1. Calculated from the measured apparent area of contact, A_{app} using the equation, $n = \frac{A_{app}}{\sigma}$ where σ^{-1} = Flap density (1850 flaps/mm^2 for 1X tilted PDMS flaps and 6410 flaps/mm^2 for 3.5X tilted PDMS flaps)

2. Calculated from the measured force at pull off (total adhesion force), F_{ad} using the equation, $f_{ad} = \frac{F_{ad}}{n}$

3. Calculated from the JKR sphere on a flat model using equation (1).

4. Calculated from the JKR sphere on a flat model using equation (2), where,

$$\frac{1}{K} = \frac{3}{4}(k_{\text{PDMS}} + k_{\text{glass}})$$

Now, $k_{\text{PDMS}} = \frac{1-\nu^2_{\text{PDMS}}}{E_{\text{PDMS}}}; k_{\text{glass}} = \frac{1-\nu^2_{\text{glass}}}{E_{\text{glass}}}$

Since, $E_{\text{PDMS}}(1.8\text{ MPa}) << E_{\text{glass}}(50\text{ GPa})$

Hence, $\frac{1}{K} \sim \frac{3}{4}k_{\text{PDMS}} = \frac{3}{4}\left(\frac{1-\nu^2_{\text{PDMS}}}{E_{\text{PDMS}}}\right) = \frac{3}{4}\left(\frac{1-0.5^2}{1.8}\right)$

$\rightarrow K = 3.2$ MPa

Therefore, the fitted stiffness, K to the JKR sphere on flat model in equation (2) for the individual flaps is 3.2 MPa.

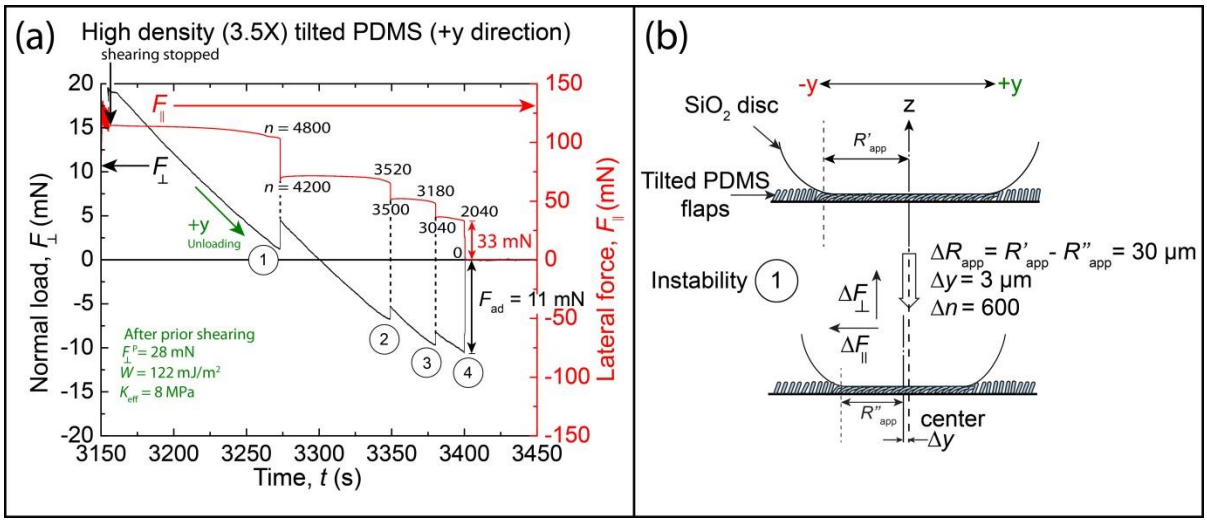

Figure 5.6 (a) Real time normal load and lateral force (friction) measurement of the high density (3.5X) tilted PDMS flaps against a spherical glass surface (RMS roughness = 1 nm) with prior shearing of the surfaces along the +y direction. Here, *n* gives the number of the tilted micro-flaps in contact with the glass surface just before and after the instability jumps. (b) Schematics of the contact just before and after the instability jump at 1.

The measured pull off force depends on the modulus of rigidity of the surfaces as well as the surface roughness (40), and the length scale, $\lambda = W / K_{eff}$ determines the range over which the attractive adhesive force dominates the repulsive elastic force (41, 42). The higher the value for λ, the more compliant the surfaces are and the stronger the adhesive force of interaction is between the surfaces. The effective stiffness of the 3.5X (high density) PDMS micro-flaps is ~3.5 times larger than that of the 1X (low density) micro-flaps, however, the former flaps showed adhesion to the silica surface and the later one does not. This is because, λ for the 1X and the 3.5X PDMS micro-flaps are ~ 0 and 1.3 nm respectively, i.e., the elastic strain energy between the 1X PDMS micro-flaps and the silica surface always dominates over the adhesive energy if the surfaces are separated without prior sliding.

5.5.2 Adhesion force measurement with prior shearing

Shearing the arrays of the tilted PDMS micro-flaps against the silica sphere significantly increased the adhesive force of interaction between the two surfaces. For the 1X (low density) micro-flaps, effective adhesion energies of W = 28 mJ/m^2 and 9 mJ/m^2 were obtained for prior shearing of the flaps against the silica surface along the +y (along the tilted direction or gripping direction) and the –y directions (against the tilted direction or releasing direction) respectively (Fig. 5.4). The high density 3.5X micro-flaps exhibited much larger W of 122 mJ/m^2 and 45 mJ/m^2 respectively for prior shearing the flaps against the silica surface along the +y and –y directions (Fig. 5.5). The experimentally observed W for the 3.5X micro-flaps is higher than that expected between a smooth PDMS and silica surface calculated by van der Waals theory (W = 50 mJ/m^2) (37). This can be attributed to the bond formation due

to local molecular adhesion between the siloxane groups of the PDMS with the silica surface and has been previously observed in rubber sliding on hard surfaces (43).

Slip instabilities were observed at the PDMS flaps-silica interface during unloading after prior shearing along the +y direction (along the direction of the tilt) for both the flap densities (Fig. 5.6). The magnitudes of these instabilities were bigger for the 3.5X (high density) micro-flaps relative to the 1X (low density) micro-flaps (see supporting Fig. S5.2). This can be attributed to the larger number of flaps detaching from the PDMS-SiO_2 interface for the 3.5X micro-flaps compared to the 1X micro-flaps during the separation of the two surfaces, as illustrated in Fig. 5.7. Theoretically, the stick-slip instability should reach a maximum value on increasing the flaps coverage, then decrease and eventually disappear for 100% coverage (close-packed flaps) which can be considered to be an effectively smooth surface, as in the case of zero coverage (Fig. 5.7). No slip instabilities were recorded for unloading after prior shearing along the –y direction (against the direction of the tilt). Hence, another possible explanation for the high observed value of W for the 3.5X micro-flaps after prior shearing along the +y direction could be large energy dissipation at the PDMS-silica interface close to the crack tip caused by the viscoelastic behavior of the polymer (44). The later possibility is more probable since the separation of the surfaces causes local elastic instabilities close to the crack tip and this is evident from the graph of $F_{\perp}$ *vs.* t (Fig. 5.6).

Thus, if a material disperses its elastic energy in the form of waves into the bulk during separation of the surfaces with prior sliding along a specific direction, high adhesion energy will be attained maintaining good bonding to the surface. Alternatively, if prior sliding in a different direction causes the crack tip to move slowly during unloading of the

two surfaces, the elastic energy would help assist the detachment process thus mimicking the gecko adhesive system.

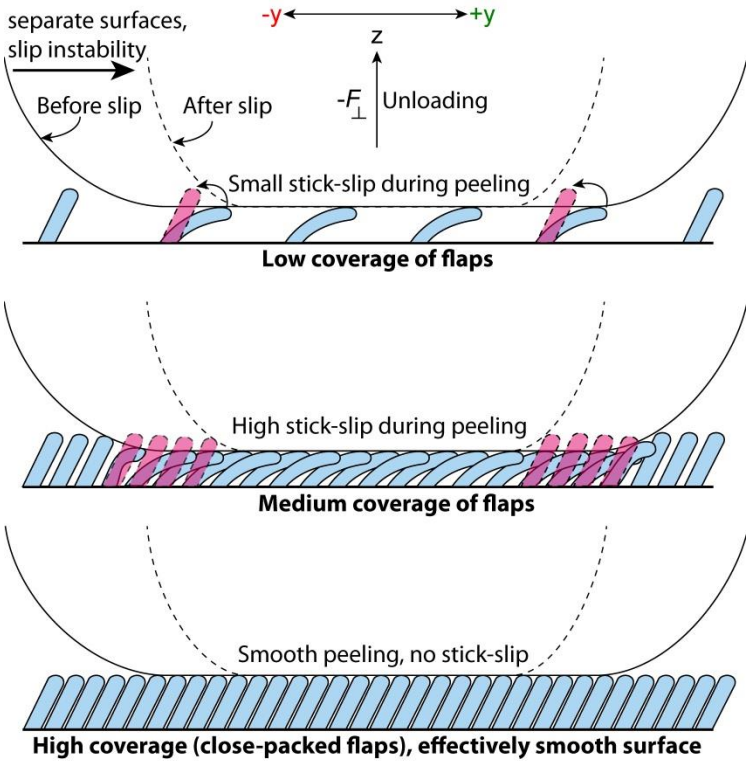

Figure 5.7 The magnitude of stick-slip instabilities observed in the load and friction forces (See Fig. 6a and S2) during the peeling of the spherical glass disk from the patterned surface increases with increase in the flap density and would disappear eventually resulting in smooth peeling. This observation can be attributed to the number of flaps undergoing detachment during slip instability in the system. The flaps undergoing slip during instability is shown in red.

Shearing induced a significant change in the K_{eff} for the arrays of the micro-flaps (for both the 1X (low density) and the 3.5X (high density)) compared to pure loading and unloading with no prior shearing against the silica surface. This large value for the observed K_{eff} is due to the high elastic strain energy stored in the severely deformed flaps as a result of

shearing of the surfaces. The stiffness was found to be similar for unloading of the flaps with prior shearing along the +y (along the direction of the tilt) or –y directions (against the direction of the tilt) for the 1X (Fig. 5.4) and the 3.5X (Fig. 5.5) respectively, meaning that the elastic energies for the deformation of the flaps along the +y and –y directions are similar. The observed effective degrees of stiffness were similar along both the directions (±y) since the flaps underwent severe deformations during the sliding of the surfaces and the inelastic property of the PDMS material determines the stiffness of the system. The tilt is important in determining the bending modulus only for small deflection of the flaps (45).

This implies that the disparity in the adhesive strengths due to shearing of the surfaces along the two different directions is due to different real areas of contact between the PDMS flaps and silica surface during the sliding cycles and/or elastic instabilities as explained above and not due to the difference in the bending energies of the flaps as hypothesized previously (11).

5.6 Conclusions

Our experimental results demonstrate that the Johnson-Kendall-Roberts (JKR) theory using an effective surface energy and stiffness at the macro scale quantitatively describes the contact mechanics of the micro-flaps ensemble against a smooth silica surface. The effective stiffness and the surface energy depend on the ratio of real to apparent contact areas, which can be measured in the SFA experiments. Inserting these values in the JKR theory yielded normal load *vs* area curves close to those measured thereby validating this model. We also find an increasing adhesion and stick-slip of the surfaces during detachment, which we explain qualitatively in terms of the density of flaps, considering it to increase from 0% (no

flaps, smooth surface) to 100% (close-packed flaps, effectively smooth surface). Our results and interpretations should be applicable to other rough and patterned surfaces and could serve as a model for designing and fabrication of gecko mimetic surfaces.

5.7 Appendix

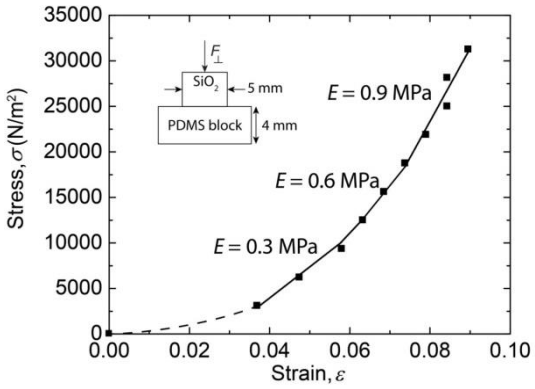

Figure S5.1 The measured stress *vs* strain relationship for the PDMS material used to fabricate the micro-flaps. PDMS shows a nonlinear response to the applied load and the elastic modulus is dependent on the amount of strain it has been subjected to.

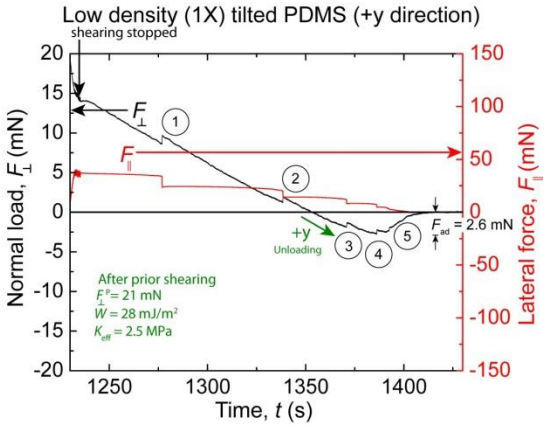

Figure S5.2 Real time normal load and lateral force (friction) measurement of the low density (1X) tilted PDMS flaps against a spherical glass surface (RMS roughness = 1 nm)

with prior shearing of the surfaces along the +y direction. The magnitude of the instability jumps for the 1X flaps are lower than that of the 3.5X tilted PDMS flaps (see Fig. 5.6).

5.8 References

1. Autumn K, *et al.* (2006) Dynamics of geckos running vertically. *Journal of Experimental Biology* 209(2):260-272.
2. Ruibal R & Ernst V (1965) Structure of Digital Setae of Lizards. *Journal of Morphology* 117(3):271-&.
3. Tian Y, *et al.* (2006) Adhesion and friction in gecko toe attachment and detachment. *Proceedings of the National Academy of Sciences of the United States of America* 103(51):19320-19325.
4. Pesika NS, *et al.* (2007) Peel Zone Model of Tape Peeling Based on the Gecko Adhesive System. *Journal of Adhesion* 83(4):383-401.
5. Pesika NS, *et al.* (2009) The Crowding Model as a Tool to Understand and Fabricate Gecko-Inspired Dry Adhesives. *Journal of Adhesion* 85(8):512-525.
6. Autumn K, *et al.* (2002) Evidence for van der Waals adhesion in gecko setae. *Proceedings of the National Academy of Sciences of the United States of America* 99(19):12252-12256.
7. Hansen WR & Autumn K (2005) Evidence for self-cleaning in gecko setae. *Proceedings of the National Academy of Sciences of the United States of America* 102(2):385-389.
8. Autumn K & Peattie AM (2002) Mechanisms of adhesion in geckos. *Integrative and Comparative Biology* 42(6):1081-1090.

9. Zhou M, *et al.* (2012) Design of gecko-inspired fibrillar surfaces with strong attachment and easy-removal properties: a numerical analysis of peel-zone. *Journal of the Royal Society Interface* 9(75):2424-2436.

10. Yu J, *et al.* (2012) Friction and Adhesion of Gecko-Inspired PDMS Flaps on Rough Surfaces. *Langmuir* 28(31):11527-11534.

11. Yu J, *et al.* (2011) Gecko-Inspired Dry Adhesive for Robotic Applications. *Advanced Functional Materials* 21(16):3010-3018.

12. Jin K, *et al.* (2012) Design and Fabrication of Gecko-Inspired Adhesives. *Langmuir* 28(13):5737-5742.

13. Autumn K, Dittmore A, Santos D, Spenko M, & Cutkosky M (2006) Frictional adhesion: a new angle on gecko attachment. *Journal of Experimental Biology* 209(18):3569-3579.

14. Huber G, *et al.* (2005) Evidence for capillarity contributions to gecko adhesion from single spatula nanomechanical measurements. *Proceedings of the National Academy of Sciences of the United States of America* 102(45):16293-16296.

15. Kim TW & Bhushan B (2008) The adhesion model considering capillarity for gecko attachment system. *Journal of the Royal Society Interface* 5(20):319-327.

16. Niewiarowski PH, Lopez S, Ge L, Hagan E, & Dhinojwala A (2008) Sticky Gecko Feet: The Role of Temperature and Humidity. *PLoS One* 3(5).

17. Prowse MS, Wilkinson M, Puthoff JB, Mayer G, & Autumn K (2011) Effects of humidity on the mechanical properties of gecko setae. *Acta Biomaterialia* 7(2):733-738.

18. Sun WX, Neuzil P, Kustandi TS, Oh S, & Samper VD (2005) The nature of the gecko lizard adhesive force. *Biophysical Journal* 89(2):L14-L17.

19. Autumn K, *et al.* (2000) Adhesive force of a single gecko foot-hair. *Nature* 405(6787):681-685.

20. Zhao BX, *et al.* (2008) Adhesion and friction force coupling of gecko setal arrays: Implications for structured adhesive surfaces. *Langmuir* 24(4):1517-1524.

21. Campolo D, Jones S, & Fearing RS (2003) Fabrication of gecko foot-hair like nano structures and adhesion to random rough surfaces. *Nanotechnology, 2003. IEEE-NANO 2003. 2003 Third IEEE Conference on*, pp 856-859 vol. 852.

22. Murphy MP, Kim S, & Sitti M (2009) Enhanced Adhesion by Gecko-Inspired Hierarchical Fibrillar Adhesives. *ACS Applied Materials & Interfaces* 1(4):849-855.

23. Kamperman M, Kroner E, del Campo A, McMeeking RM, & Arzt E (2010) Functional Adhesive Surfaces with "Gecko" Effect: The Concept of Contact Splitting. *Advanced Engineering Materials* 12(5):335-348.

24. Canas N, *et al.* (2012) Effect of nano- and micro-roughness on adhesion of bioinspired micropatterned surfaces. *Acta Biomaterialia* 8(1):282-288.

25. Lee H, Lee BP, & Messersmith PB (2007) A reversible wet/dry adhesive inspired by mussels and geckos. *Nature* 448(7151):338-341.

26. Murphy MP, Aksak B, & Sitti M (2009) Gecko-inspired Directional and Controllable Adhesion. *Small* 5(2):170-175.

27. He LW, Yan SP, Li BQ, & Chu JR (2012) Directional adhesion behavior of a single elastic fiber. *Journal of Applied Physics* 112(1):013516.

28. Qu LT, Dai LM, Stone M, Xia ZH, & Wang ZL (2008) Carbon nanotube arrays with strong shear binding-on and easy normal lifting-off. *Science* 322(5899):238-242.

29. Yurdumakan B, Raravikar NR, Ajayan PM, & Dhinojwala A (2005) Synthetic gecko foot-hairs from multiwalled carbon nanotubes. *Chemical Communications (Cambridge, United Kingdom)* (30):3799-3801.

30. Jeong HE, Kwak MK, & Suh KY (2010) Stretchable, Adhesion-Tunable Dry Adhesive by Surface Wrinkling. *Langmuir* 26(4):2223-2226.

31. Geim AK, *et al.* (2003) Microfabricated adhesive mimicking gecko foot-hair. *Nature Materials* 2(7):461-463.

32. Persano L, *et al.* (2013) High performance piezoelectric devices based on aligned arrays of nanofibers of poly(vinylidenefluoride-co-trifluoroethylene). *Nature Communications* 4.

33. Silberzan P, Perutz S, Kramer EJ, & Chaudhury MK (1994) Study of the Self-Adhesion Hysteresis of a Siloxane Elastomer Using the JKR Method. *Langmuir* 10(7):2466-2470.

34. Israelachvili J, *et al.* (2010) Recent advances in the surface forces apparatus (SFA) technique. *Reports on Progress in Physics* 73(3).

35. Bhushan B (2002) *Introduction to tribology* (John Wiley & Sons, New York) pp xix, 732 p.

36. Johnson KL, Kendall K, & Roberts AD (1971) Surface Energy and Contact of Elastic Solids. *Proceedings of the Royal Society of London Series a-Mathematical and Physical Sciences* 324(1558):301-313.

37. Israelachvili JN (2011) Intermolecular and Surface Forces, 3rd Edition. *Intermolecular and Surface Forces, 3rd Edition*:1-674.

38. Yang C, Persson BNJ, Israelachvili J, & Rosenberg K (2008) Contact mechanics with adhesion: Interfacial separation and contact area. *EPL* 84(4):46004.

39. Benz M, Rosenberg KJ, Kramer EJ, & Israelachvili JN (2006) The deformation and adhesion of randomly rough and patterned surfaces. *Journal of Physical Chemistry B* 110(24):11884-11893.

40. Fuller KNG & Tabor D (1975) Effect of Surface-Roughness on Adhesion of Elastic Solids. *Proceedings of the Royal Society of London Series a-Mathematical Physical and Engineering Sciences* 345(1642):327-342.

41. Maugis D (1992) Adhesion of Spheres - the JKR-DMT Transition Using a Dugdale Model. *Journal of Colloid and Interface Science* 150(1):243-269.

42. Carpick RW, Ogletree DF, & Salmeron M (1999) A general equation for fitting contact area and friction vs load measurements. *Journal of Colloid and Interface Science* 211(2):395-400.

43. Schallamach A (1963) A theory of dynamic rubber friction. *Wear* 6(5):375-382.

44. Mulakaluri N & Persson BNJ (2011) Adhesion between elastic solids with randomly rough surfaces: Comparison of analytical theory with molecular-dynamics simulations. *EPL* 96(6):66003.

45. Autumn K, Majidi C, Groff RE, Dittmore A, & Fearing R (2006) Effective elastic modulus of isolated gecko setal arrays. *Journal of Experimental Biology* 209(18):3558-3568.

6. STICK-SLIP FRICTION OF GECKO-MIMETIC FLAPS ON SMOOTH AND ROUGH SURFACES

6.1 Abstract

The discovery and understanding of gecko's 'frictional-adhesion' adhering and climbing mechanism has allowed researchers to mimic and create gecko-inspired adhesives. A few experimental and theoretical approaches have been taken to understand the effect of surface roughness on synthetic adhesive performance, and the implications of stick-slip friction during shearing. This work extends previous studies by utilizing a modified Surface Forces Apparatus (SFA) to quantitatively measure and model frictional forces between arrays of polydimethylsiloxane (PDMS) gecko footpad-mimetic tilted micro-flaps against smooth and rough glass surfaces. Constant attachments and detachments occur between the surfaces during shearing, as described by an *Avalanche* model. These detachments ultimately result in failure of the adhesion interface and have been characterized in this study. Stick-slip friction disappears with increasing velocity when the flaps are sheared against a smooth silica surface; however, stick-slip was always present at all velocities and loads tested when shearing the flaps against rough glass surfaces. These results demonstrate the significance of preload, shearing velocity, shearing distances, commensurability, and shearing direction of gecko-mimetic adhesives and provide a simple model for analyzing and/or designing such systems.

6.2 Introduction

Reversible adhesives, which exhibit high adhesion and minimal effort to detach, are vital to systems that need to stick and detach repeatedly with high speeds for fast movement. Smart and reversible adhesives are in growing demand for use in responsive robotics that can climb on walls and ceilings in precarious environments. The motivation for this specialized type of adhesive comes from the long observed ability of geckos to effortlessly run and climb on trees, rocks, walls, and ceilings and maintain attachment while stationary and in motion. The gecko's ability to adhere and climb so flawlessly stems from the hierarchical structure of their toe pads and the mechanism they use to actuate and disengage this very high adhesion. The hierarchical system of the toe pads can form and adhere to micro- and nano- asperities on rough surfaces and create a clean contact, and the reliance of van der Waals forces can allow geckos to adhere to hydrophobic and hydrophilic surfaces as long as the polarizability of the surface is not low (e.g., Teflon) (1-3).

The mechanisms for attachment and high adhesive forces of gecko spatula and setae have been measured and modeled by Johnson-Kendall-Roberts (JKR)-type theories (4, 5), while the ease of detachment from surfaces requires a peel-off theory (6-8). It has been found that the frictional forces (parallel to the surface) also contribute to the adhesive force (perpendicular to the surface), giving rise to the model of frictional-adhesion. According to this model, the adhesion of a gecko foot-pad (9) or its mimic to a substrate depends on the applied shear force (4, 6) and explains the very low detachment forces observed in climbing geckos. Anisotropic fibrillar synthetic adhesives mimicking the gecko footpad functionality have been previously fabricated (5, 10-19) and were used to study adhesion and frictional properties on silica surfaces. The mechanism of operation of these structures involved

application of a small preload (several milli-Newtons) followed by shearing the structures against the surface of interest for several microns to allow the real surface area of contact to be maximized and hence, attain a good grip. However, the stick-slip between the structured surface and the substrate was not taken into consideration during the shearing process. Stick-slip sliding of surfaces is an undesirable property which can cause catastrophic failure if slip occurs while a robotic device is moving on an inclined surface or inverted ceiling. When a constant force (gravity) is acting on the surfaces, there is no restoring force to 'catch' and reattach the failed adhesion contact. Hence, determining the conditions (sliding velocities, preloads, sliding distance of the microstructures during movement of the robot, etc.) for avoiding stick-slip motion during the shearing of structured or patterned surfaces on a substrate is essential.

A common form of friction, stick-slip friction, occurs when the static friction force is higher than the kinetic friction force and is found in everyday phenomena such as squeaking doors or the sound produced from a bow sliding across a violin string. Stick-slip friction can arise by three different mechanisms during frictional sliding (1) a rough surface mechanism (20) (topography), (2) distance-dependent mechanism, and (3) a phase transition mechanism (21). The first model describes when a rapid slip occurs as one surface goes over the top of an asperity on the opposing surface after "sticking" for the period due to interlocks prior to the slip. The distance-dependent model describes how a characteristic distance and time scale are observed as two surfaces increase adhesion strength after coming into contact, which may occur for smooth or rough surfaces. During shearing, the surfaces creep the characteristic distance before sliding occurs. These systems are related to the Deborah Number, De, which relates the intrinsic relaxation times of the materials to the time scales of movement and

measurement in the system. The time scales can easily be converted to a characteristic relaxation velocity and sliding velocity in the system. Lastly, the phase transition model is typically only present in lubricated systems or thin films confined between two surfaces which does not pertain to the presented system.

In this study, the friction properties of tilted biomimetic gecko flaps were investigated by measuring and characterizing the friction force as a function of the applied loads and shearing velocities using a Surface Forces Apparatus (SFA) in order to determine the optimum shearing conditions against smooth and rough surfaces. Here we also propose an *Avalanche mechanism* of stick-slip friction. We attribute the stick-slip behavior in our system to be a combination of surface topography effects as well as characteristic length and time scales related to the material properties of PDMS and intermolecular forces between PDMS and SiO_2.

6.3 Materials and Methods

Large arrays of tilted PDMS micro flaps with an areal density of 6410 flaps/mm^2 mimicking the adhesive and frictional properties of a gecko foot pad were fabricated and have been described elsewhere (13, 22). A modified surface forces apparatus (SFA, SurForce LLC) (13, 23) was used to measure the normal $F_{\perp}$ (adhesion and loads) and the lateral forces $F_{\parallel}$ between the arrays of the fabricated micro-flaps and a spherical silica disk of radius of curvature, R = 2 cm, and three different RMS roughnesses of 10 ± 8 nm (smooth), 133 ± 20 nm (rough) and 308 ± 56 nm (very rough). The detailed characterization of the roughnesses is given in Table 6.1. Details of the force measurements have been described in previous work (13, 22). Briefly, the spherical glass disk was mounted to the top friction device that

measures the lateral forces $F_{\parallel}$ on the fabricated flaps. The PDMS flaps were glued to a flat glass disk, which sits on a double cantilever spring with strain gauges that can measure the normal forces. The double cantilever spring was mounted on a bimorph device that can slide laterally over a distance of 1-700 μm at different sliding speeds (0.01-200 μm/s). A CCD camera was mounted on a microscope to visualize the contact area during loading, unloading and sliding of the spherical silica disk against the arrays of the fabricated PDMS micro-flaps.

In the SFA experiment, the PDMS micro-flaps were pressed against the top spherical silica disk at a constant speed of ~ 10 μm/s until the desired pre-load, L was reached. The flaps were then sheared against the smooth and the rough spherical glass disk at different velocities (0.08-200 μm/s). Stick-slip friction force and the instantaneous normal loads $F_{\perp}$ were measured simultaneously. The measured normal load $F_{\perp}$ was different from the applied pre-load L during sliding due to the deformation of the micro-flaps and adhesion/interlocking of the flaps to the glass surface. The flaps did not get damaged even after many sliding cycles (100-1000) at a given contact point and the friction force was reproducible between different contact points on the flap surface. The surfaces were prepared in a clean dust free environment (under Laminar flow hood).

6.4 Results

The effect of normal loads ($F_{\perp}$) and driving velocities (v) on the stick-slip frictional properties of the synthetic tilted PDMS flaps against a silica surface of different roughnesses (Table 6.1) were tested in a modified Surface Forces Apparatus (SurForce®, LLC) (Fig. 6.1). Here, we characterize the surfaces with different roughness based on the height of the surface

features (asperities), the spacing between them, and the slope of the features as shown in Table 6.1.

Table 6.1. Comparison of roughness of borosilicate glass disks used to shear against the gecko-mimetic adhesive flaps. Roughness values were measured in an AFM.

Disk	Avg. height of asperities (μm)	Avg. distance between asperities (μm)	Avg. slope of asperity edges
Smooth	<0.01	N/A	N/A
Rough	0.33 ± 0.06	6.7 ± 3.5	0.80 ± 0.45
Very Rough	0.52 ± 0.09	1.5 ± 1.5	1.2 ± 0.9

The fluctuations in the lateral force (or friction force, $F_{\parallel}$) were measured in the SFA and the changes in the friction properties of the flaps shearing against the silica surface were monitored as v was increased at a given compressive force in the normal direction (pre-load, $F_{\perp} = L$). A close look at the measured friction forces as a function of time indicates that $F_{\parallel}$ can be resolved into three different components, (1) f_{st}, the stiction spike, (2) f_s, the static friction force, and (3) f_k, the kinetic friction force (Fig. 6.2).

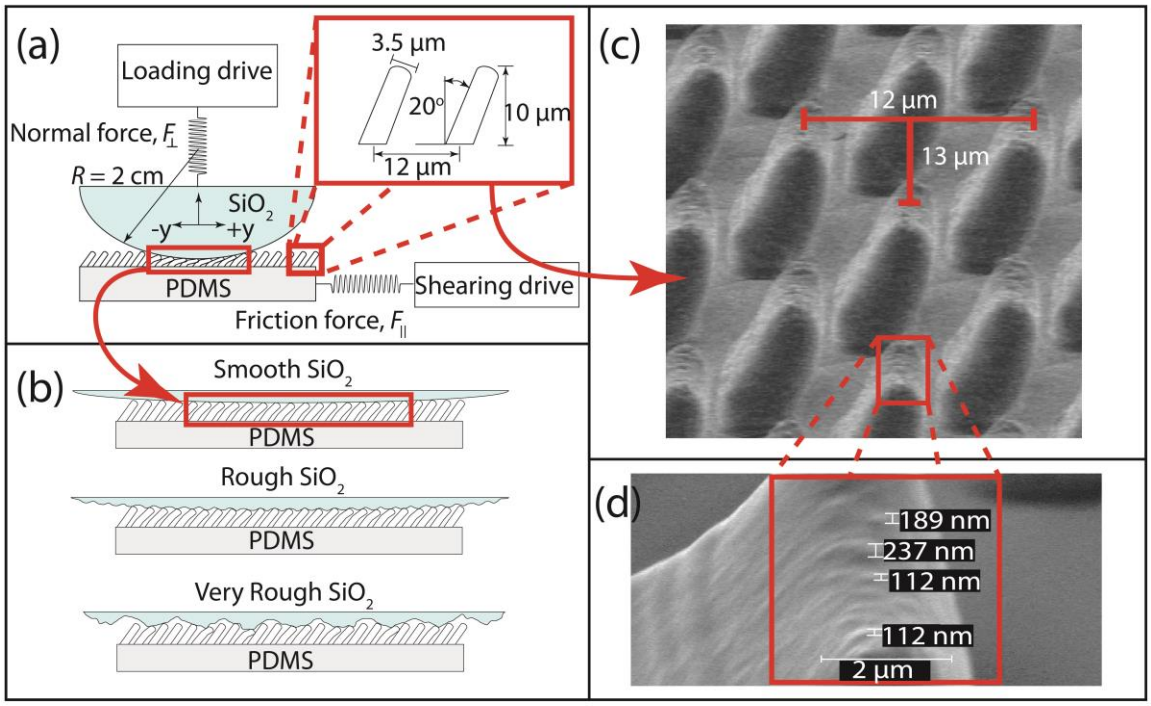

Figure 6.1 (a) Schematic representation of experimental setup in the SFA. Two opposing surfaces are sheared against each other: the bottom being the tilted PDMS gecko flaps and the top as the smooth or rough glass disk. (b) Schematic of the fitting of PDMS flaps into the different rough disk asperities. There is an interlocking mechanism due to spacing of the roughness on the glass disk that occurs with the rough (middle) disk. (c) SEM image of the biomimetic flaps depicting the in-plane distribution of the fibrillar structures. (d) A zoom in on the tip of one pillar depicting submicron scale roughness on its surface.

The stiction spike (f_{st}) is the static friction force that must be overcome before any sliding begins between two stationary surfaces and could be higher or lower than the rest of the friction forces measured during shearing. The kinetic friction force (f_k) and the static friction force (f_s) are the minimal and the maximum magnitude of the measured lateral

stresses respectively when the surfaces are in relative motion during shearing. The kinetic friction force and static friction force are equal during smooth sliding ($f_s = f_k$). When referring to stick-slip friction, the static force is the maxima of the friction trace (the "stick") and the kinetic friction force is the minima where interfacial sliding occurs (the "slip"). This distinction between kinetic friction in smooth and stick-slip sliding is important to note because the measured value of f_k in stick-slip is not necessarily the "true" value of f_k experienced between the surfaces (24).

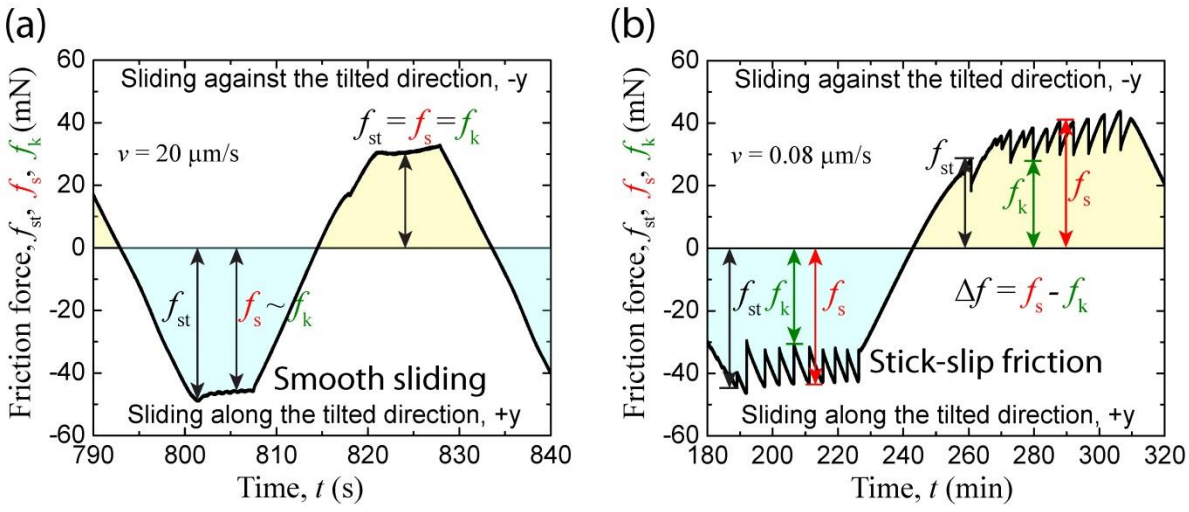

Figure 6.2 Friction traces of the smooth glass disks with a pre-load, L ~10 mN against gecko-mimetic tilted flaps, where friction forces,($F_{\parallel} = f_{st}, f_s, f_k$) were measured as a function of time. Note that negative forces are not negative in magnitude, but result from the direction of shear during measurement. Smooth sliding (a) is observed at velocities greater than 20 μm/s compared to stick-slip friction which is present at lower drive velocities less than 20 μm/s (b) for the given pre-load.

6.4.1 Effect of load on friction force at a constant driving velocity

The tilted PDMS micro-flaps exhibited smooth sliding ($\Delta f = f_s - f_k = 0$) against a smooth silica disk for $F_\perp \leq$ 20 mN and v > 20 μm/s (Fig. 3a). Stick-slip friction is always observed for the shearing of the flaps against the rough and the very rough silica surfaces for all loads (Fig. 6.3b, c). The friction forces ($F_\parallel$) are proportional to the normal loads ($F_\perp$) indicating that Amontons' law is followed (25) in the system under consideration (Fig. 6.3a and c). The coefficient of friction, μ (slope of $F_\parallel$ vs. $F_\perp$) , is higher for sliding of the flaps against the rough and the very rough silica surfaces (μ = 3.1—3.4) compared to the smooth surface (μ = 1.7). The magnitude of stick-slip friction increased as the load increased when shearing the flaps against the rough and the very rough surfaces. Interestingly, the flaps demonstrated similar (within 35% of the highest difference) magnitudes of $F_\parallel$ for a given $F_\perp$ on the smooth and the very rough silica surface which is significantly smaller than the $F_\parallel$ measured on the rough surface. However, when comparing the magnitude of stick-slip friction, Δf (triangle in lower plots in Fig. 6.3), the very rough surface exhibits high values of stick-slip compared to the smooth surface where no stick-slip is observed at any loads ($F_\perp \leq$ 20 mN) at v = 20 μm/s. The flaps display maximum stick-slip during sliding on the rough silica surface, which is as high as double that of the very rough disk. At higher loads, the magnitude of stick-slip is greater for shearing along the –y direction (against the tilt of the flaps) compared to the +y direction (along the tilt of the flaps).

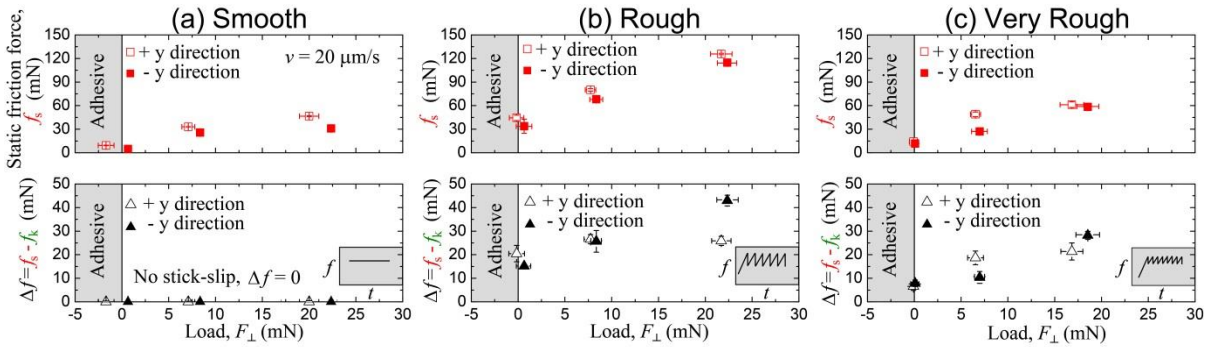

Figure 6.3 Plots of the static friction force (f_s "red") as a function of the load, $F_\perp$, for three varying levels of rough surfaces (a,b,c) sheared at a constant velocity, v = 20 μm/s, in the direction along the tilt of the gecko-mimetic flaps (+y) and against the direction of tilt (-y). The lower plots depict the magnitude of stick-slip friction by the relation $\Delta f = f_s - f_k$ where f_s is the static friction force and f_k is the kinetic friction force.

6.4.2 Effect of shear drive velocity on friction force

The tilted PDMS micro-flaps do not undergo stick-slip sliding ($\Delta f = f_s - f_k = 0$) against a smooth silica surface for $F_\perp \leq$ 20 mN and $v \geq 20$ μm/s, however at lower driving velocities (v = 0.08-20 μm/s), the surfaces exhibit stick-slip motion ($\Delta f > 0$) (Fig. 4). Stick-slip is always present for shearing the micro-flaps against the rough and the very rough silica surfaces. The rough surface displayed an increasing and then decreasing magnitude of stick-slip with increasing velocity (red triangles in Fig. 6.4). The magnitude of Δf is similar for shearing the flaps along the +y and –y direction on the rough surface. The very rough surface shows a higher magnitude of Δf along the +y direction relative to the –y direction of shear. Interestingly, even though the magnitude of stick-slip friction typically decreases with increasing velocities, the static friction force does not change significantly. This is contrary to a typical stick-slip phenomenon between sliding surfaces where the static force decreases

to the magnitude of kinetic friction. In these experiments, the kinetic friction force is thus increasing to match the static friction force values.

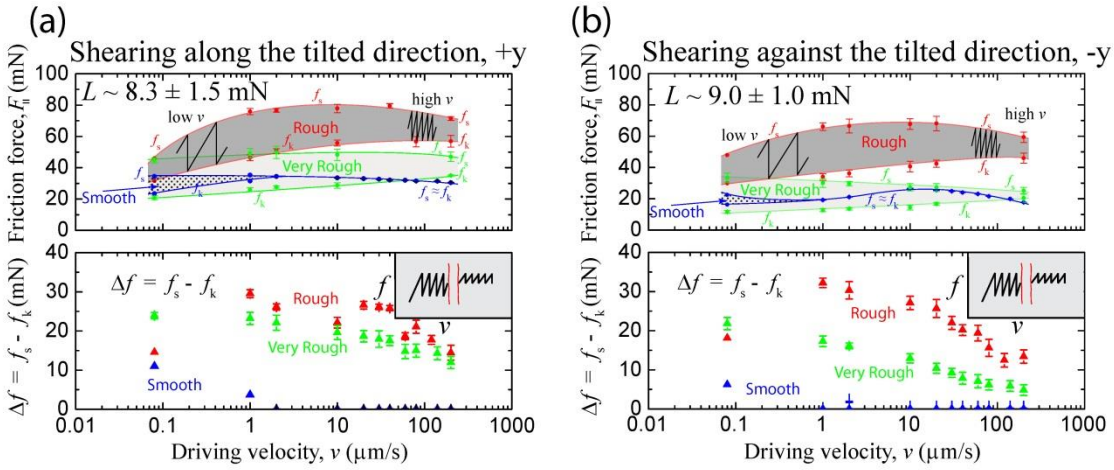

Figure 6.4 Plots of the static friction force (f_s) and kinetic friction force (f_k) from the friction traces as a function of the shear driving velocity, v, for three different rough surfaces of varying roughness (smooth (blue), rough (red), and very rough (green)) sheared at a constant load in the direction (a) along (+y direction) and (b) against (-y direction) the tilt of the tilted PDMS flaps. The lower plot depicts the magnitude of stick-slip friction by the relation $\Delta f = f_s - f_k$ where f_s is the static friction force and f_k is the kinetic friction force.

6.4.3 Friction map

Depending on the nature of motion between the micro-flaps and the silica surface, a map can be constructed to indicate the regime of smooth sliding conditions and stick-slip friction (Fig. 6.5). The transition from stick-slip motion to smooth sliding is observed only when the micro-flaps are sheared against a smooth silica surface. The surfaces always show stick-slip friction between the flaps and the rough or the very rough surfaces in the velocity

regime of the measurements. However, it should be noted that the magnitude of stick-slip decreases with increasing velocity during shearing, indicating that the sliding will eventually show a smooth motion for high shearing velocities. The regions under the friction map may be interpreted as an indicator for the operating conditions of sliding velocities when actuating the foot of a robot with the gecko-mimetic pad attached to enable a secure stick to a surface and easy release. These results also stress the importance of the sliding distance during the operation of a gecko-mimetic footpad on robotic devices and are discussed later.

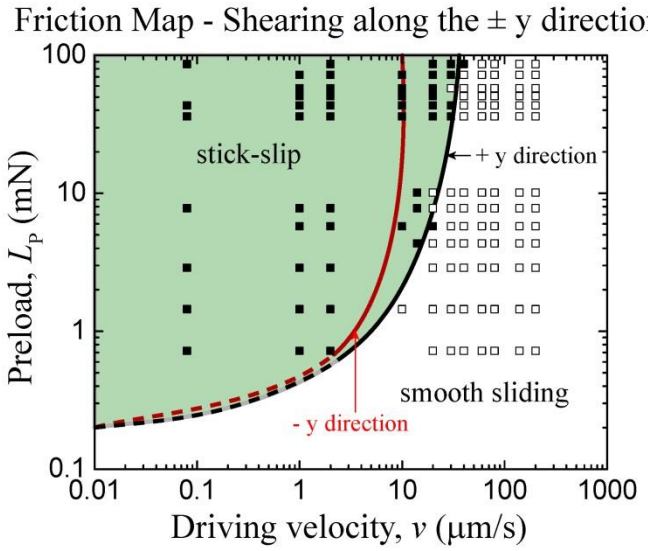

Figure 6.5 Friction map depicting stick-slip and smooth sliding regimes for the +y (along the tilt) and –y (against the tilt) shearing directions as a function of preload and driving velocity, *v*, for a smooth glass disk. Increasing driving velocity leads to smooth sliding. The dashed line indicates the limit of the measuring capability, but smooth sliding is predicted at such low loads and sliding velocities.

6.5 Discussion

Two very interesting phenomena are evident from the friction force measurements as a function of load. First, the rough surfaces exhibit the highest friction forces and stick-slip magnitude. This can be explained through an interlocking mechanism (22) (Fig. 6.6) where the roughness of the surface matches with the interspacing of the array of flaps. Based on the values in Table 6.1, the average distance between asperities on the rough surface (6.7 ± 3.5 μm) shows that it is possible to fit the flap dimensions (10 μm × 3.5 μm) in between some spots where the asperities are more spread out. The interlocking mechanism and fitting of flaps between surface asperities are compared in Fig. 6.6. The smooth surface does not have these asperities and the very rough surface has asperities too large and close together to allow for interlocking to occur. Another feature present in the data is that the friction values for the smooth and very rough surfaces are very comparable. It appears that the friction between the flaps and the pair of surfaces (smooth and very rough) follow Amontons' law, which states that friction forces are independent of the apparent area of contact. Molecular Dynamics (MD) simulations suggest that for non-adhering surfaces above a certain load, the coefficient of friction is independent of the detailed nature of the surface roughness (26). These surfaces have previously been tested for adhesion and exhibit adhesion only once the surfaces have been sheared (4, 13). The very rough surfaces contain asperities that are too close together and too large for the full interlocking mechanism to take place, thus allowing Amontons' law to hold true.

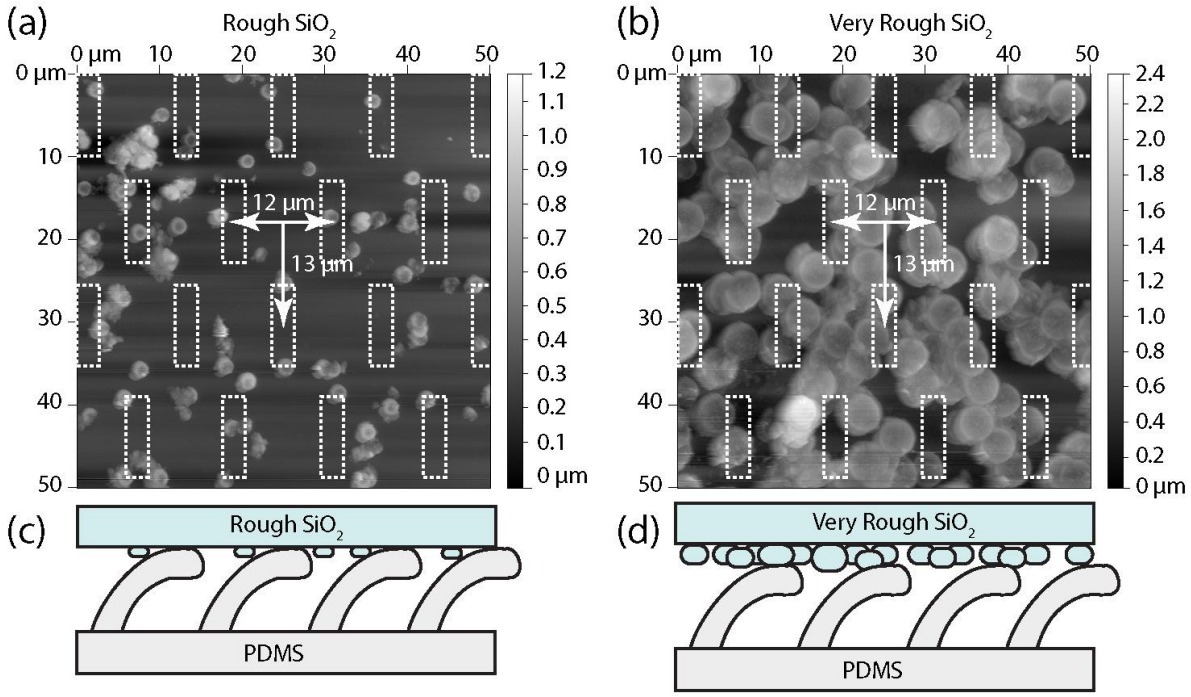

Figure 6.6 AFM images of the rough surfaces ((a) rough and (b) very rough) with an overlay of the gecko flap tip dimensions and spacing. The interlocking mechanism is displayed schematically where the rough disk (c) and PDMS flaps have commensurate spacing compared with the very rough disk (d), starting to approximate a "smooth" surface.

6.5.1 Stick-slip mechanism: *The Avalanche Mechanism*

Here we present the *Avalanche Model* which explains that stick-slip instabilities at the macro level are initiated by the micro-instabilities at the contact junction between the individual micro-flaps and the silica surface (Fig. 6.7a, b). Stick-slip at individual micro contacts between two 'dry' surfaces in relative motion ensues due to creep instabilities (27, 28), brittle fracture (29, 30) or viscoelastic shear failure (31) of the interlocked asperities as they detach (Fig. 6.7a).

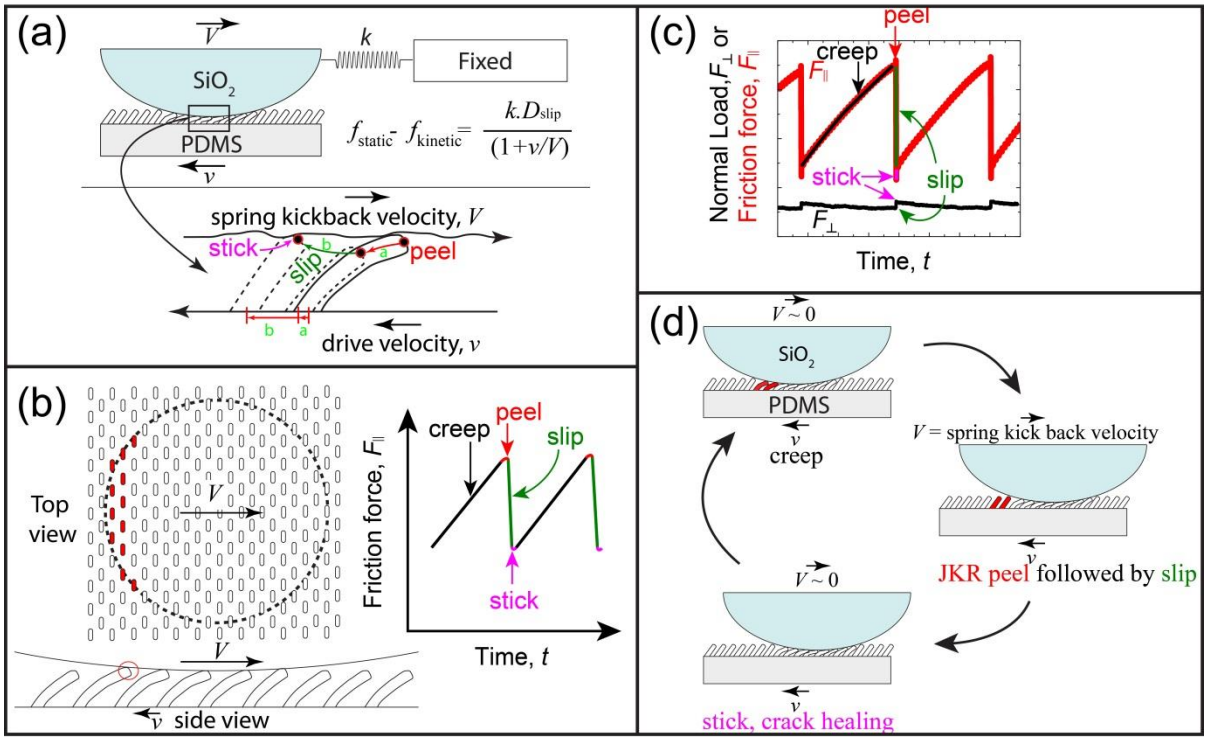

Figure 6.7 The *Avalanche* stick-slip of the arrays of PDMS flaps from the silica surface. (a) The PDMS micro-flaps peeling (JKR) from the silica surface during the *Avalanche* slip at the micro-scale that causes the force measuring spring to kick-back with a velocity *V*. (b) The flaps that are about to detach from the silica surface are shown in red along with a cartoon of the stick-slip friction trace showing the creep, JKR-peel, slip and stick regimes. (c) An illustration of the normal load ($F_\perp$) and friction force ($F_\parallel$) measured in the SFA during shearing of the micro-flaps against a silica surface showing the different regimes (creep, JKR-peel, slip and stick) during the *Avalanche* slip. (d) *Avalanche* slip as visualized at the macro-scale when the spherical silica surface is sheared against the PDMS micro-flaps.

The creep instability mechanism assumes that the stick-slip magnitude ($\Delta f = f_s - f_k$) is determined by the size of the contact area and not by f_s or the shear force required to break the adhesive interface. Even though the *apparent* area of the contact between the smooth

silica surface and the PDMS flaps is larger than that between the rough/very rough disks for the same load, stick-slip sliding disappears when shearing the PDMS flaps against the smooth silica surface, unlike sliding on the rough/very rough surface. Hence, creep instability is not a plausible explanation for the stick-slip in our system. A brittle fracture mechanism can also be ruled out since the contact under consideration is soft and deformable. During sliding of the PDMS flaps on the silica surface, viscoelastic instability causes the contact junction to grow when the surfaces slide past each other and the friction force (or stress) increases during this stage from f_k to f_s. Depending on the relative displacement between the sliding surfaces, the contact junction dilates and breaks when a critical stress is reached, leading to a crack-like contact instability followed by the release of the elastic strain energy at the contact junction.

The trailing edge of a contact junction is associated with detachment of the individual flaps from the silica surface in a JKR peeling fashion (4, 5). The flaps that are about to detach from the silica surface are shown in red in Fig. 6.7b, d. When a critical stress is reached for a few micro-flaps at the contact boundary, they detach and trigger other near critical detachments, and the surfaces slip for a distance d or nd where d = distance between the arrays of the flaps or rough asperities and n is an integer (See supporting Fig. S6.1). The slip is also associated with the propagation of Schallamach (32, 33) waves from the front to the rear end of the contact. This propagation causes the viscoelastic PDMS flaps to release the shear stresses at the trailing edge of the contact junction and stick at the advancing edge of the contact to the silica surface. Hence, each slip is associated with a Schallamach wave and the frequency of stick-slip (φ) is equal to the rate of propagation of the waves. Each of these

slips is associated with an increase and decrease in the apparent contact junction area and is evident from the sliding video footage.

When Schallamach waves are responsible for the peeling (JKR mechanism) (4, 5) and sticking of an adhesive interface, the work of adhesion can be estimated by,

$$F_{\parallel} v \sim \frac{f_s + f_k}{2} v = A_{app} \Delta W \varphi \tag{6.1}$$

where φ = frequency of the Schallamach waves (s^{-1}), ΔW = Work of adhesion during *Avalanche stick-slip* (or energy dissipated during *Avalanche rupture* of the adhesive interface, not the thermodynamic work of adhesion) between the surfaces (J/m^2), v = velocity of the driving surface (m/s), and A_{app} is the apparent area of contact (m^2).

The work of adhesion for the shearing of the flaps against the silica surfaces was estimated using eq. (6.1). It should be noted that the rate of shearing affects the work of adhesion drastically over five orders of magnitude (See supporting Fig. S6.2). Energy dissipation (ΔW) during sliding of the surfaces is maximal for the rough silica surface compared to the smooth and the very rough silica for similar loads and shearing velocities. The calculated ΔW for $v < 1$ μm/s is less than the thermodynamic work of adhesion between silica and PDMS since thermal energy provides a mechanism for the interfacial bonds between the surfaces to overcome a fixed energy barrier during the slow shearing process (34, 35). We also find that the energy dissipation shows a linear relationship with the sliding velocity (v) (Fig. S6.2).

The relative slip distance, D_{slip}, between the flaps and the silica surface is given by

$$t_v = \frac{D_{slip}}{v + V} \tag{6.2}$$

$$V = \frac{f_s - f_k}{kt_v} \tag{6.3}$$

where t_v = slip time (s), V = spring kick-back velocity (m/s), i.e., the average speed at which the lateral force measuring spring retracts back during the slip between the surfaces, k = spring constant of the lateral force measuring spring (N/m).

The friction forces can be correlated to D_{slip} through

$$f_s - f_k = \frac{kD_{slip}}{\left(1 + \frac{V}{v}\right)} \tag{6.4}$$

In our experiments, we measured t_v, v, k, f_s and f_k and thereby calculated D_{slip}.

The slip time (t_v) in our experiments was 60-80 μs for $v \leq 10$ μm/s and 40 μs for $v \geq 20$ μm/s when shearing against silica surfaces of different roughnesses. Thus, the *Avalanche* slip is characterized by a specific slip distance ($D_{slip} = nd$) and slip times (t_v).

For shearing the PDMS micro-flaps against the silica surfaces (both smooth and rough), $f_s - f_k$ decreased and f_k increased as v was increased (Fig. 6.4). For sliding against the smooth surface, $f_s - f_k \rightarrow 0$ for $v > 20$ μm/s (Fig. 6.4 and 6.5). However, we did not observe smooth sliding for the rough and the very rough silica surfaces for v = 0.08-200 μm/s. Higher sliding velocities are required to reach the smooth sliding regime ($\Delta f = f_s - f_k = 0$). Hence, an approach to eliminate stick-slip between the rough/very rough surfaces and the flaps is to shear the surfaces for a distance $D < 400$ μm and stop sliding before the maximum value of friction is attained, i.e., $f < f_s$. In our experiments, based on the sliding distances and the number of stick-slip spikes (which depends on the velocity of shearing, v), we calculate this critical sliding distance to be $D_c \leq 40$ μm for the rough surface and ≤ 15 μm for the very

rough surface at v = 0.08-200 μm/s. Thus to avoid *slip* failure on a rough surface, a robot with the reversible gecko-mimetic adhesive footpads should be sheared for a distance less than the critical sliding distance.

6.6 Conclusions

In this work, we demonstrate the effect of roughness and shearing velocities (v = 0.08-200 μm/s) on the stick-slip friction between tilted PDMS micro-flaps and silica surfaces. We show that Amontons' law is obeyed when the shearing between both smooth and very rough silica surfaces against the tilted micro-flaps. The flaps showed similar values for the static friction for shearing against the smooth and the very rough silica surfaces, and were characterized with an *Avalanche* stick-slip friction model with energy dissipation showing a linear relationship with the sliding velocity. Stick-slip sliding was always observed ($\Delta f = f_s - f_k > 0$) when shearing the flaps on the rough and very rough surfaces. Sliding the micro-flaps on the rough surface showed maximum Δf due to the interlocking-detachment cycles of the flaps with the surface asperities.

Stick-slip friction is detrimental to the performance of the gecko-mimetic adhesives since slipping would result in the failure of the contact, and not allow the surfaces to grip again in the absence of a restoring force. Stick-slip friction of flaps on smooth surfaces can be eliminated by increasing the sliding velocity above a critical value (v_c = 20 μm/s in our experiments). The friction between the micro-flaps and the smooth silica surface was translated into a 'friction' map that may be interpreted as an indicator for the conditions of desirable sliding velocities when actuating the foot of a robot with the gecko-mimetic pad to enable both a secure stick to a surface and easy release. Stick-slip between the rough surfaces

and the flaps can be eliminated by shearing the surfaces for a critical distance D_c of 40 μm and 15 μm for the rough and the very rough surfaces respectively. However, quantitative micromechanical mechanisms that can predict the critical distances (D_c) and sliding velocities (v_c) to circumvent stick-slip friction need further investigation and theoretical modeling based on the interface stiffness and topographical commensurability of the interacting surfaces. Our results stress the importance of the preloads, shearing distance, commensurability, sliding direction and velocities for the safe operation of gecko-mimetic footpads on robotic devices.

6.7 Appendix

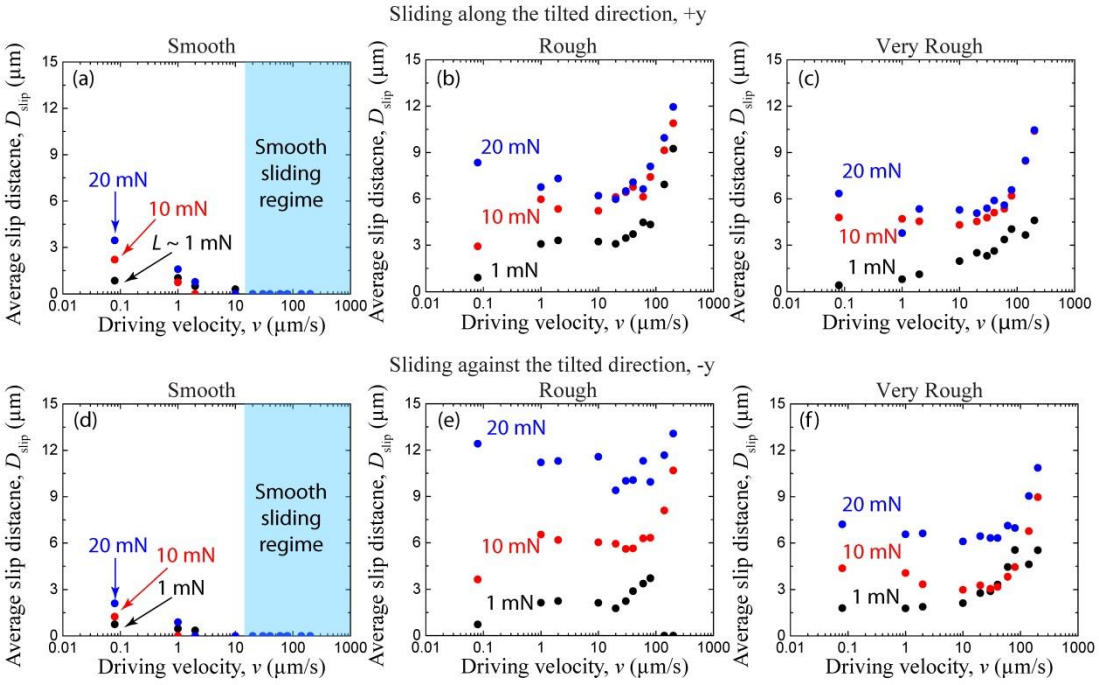

Figure S6.1 Average slip distances, D_{slip}, for three varying loads (1 (black), 10 (red), and 20 mN (blue)) as a function of shear driving velocity, v, for sliding of the smooth (a and d),

rough (b and e), and very rough (c and f) glass disks along the direction of tilt (+y) and against the direction of tilt (-y) of the PDMS micro-flaps.

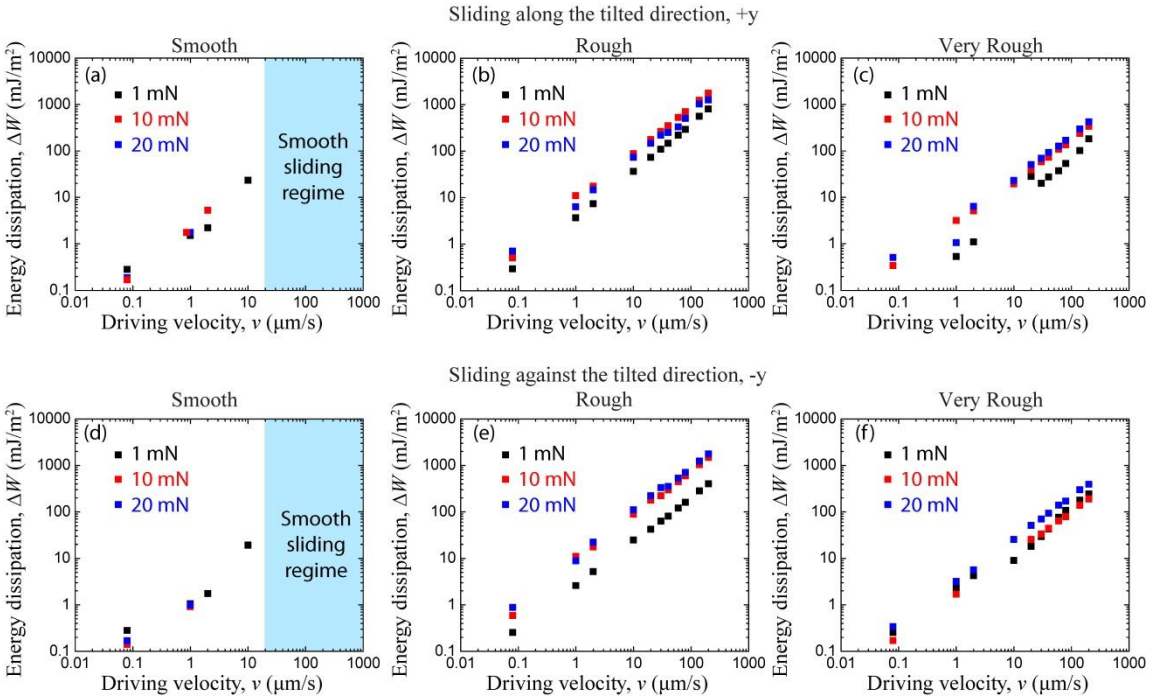

Figure S6.2 Work of adhesion, ΔW, during *Avalanche stick-slip* (or energy dissipation during *Avalanche rupture* of the adhesive interface, not the thermodynamic work of adhesion), for three varying loads (1 (black), 10 (red), and 20 mN (blue)) as a function of shear driving velocity, v, for the sliding of smooth (a and d), rough (b and e), and very rough (c and f) glass disks along the direction of tilt (+y) and against the direction of tilt (-y) of the PDMS micro-flaps.

6.8 References

1. Autumn K, *et al.* (2000) Adhesive force of a single gecko foot-hair. *Nature* 405(6787):681-685.

2. Autumn K & Peattie AM (2002) Mechanisms of adhesion in geckos. *Integrative and Comparative Biology* 42(6):1081-1090.

3. Autumn K, *et al.* (2002) Evidence for van der Waals adhesion in gecko setae. *Proceedings of the National Academy of Sciences of the United States of America* 99(19):12252-12256.

4. Das S, *et al.* (2013) JKR Theory for the Stick Slip Peeling and Adhesion Hysteresis of Gecko Mimetic Patterned Surfaces with a Smooth Glass Surface. *Langmuir* 29(48):15006-15012.

5. Gillies AG & Fearing RS (2014) Simulation of synthetic gecko arrays shearing on rough surfaces. *Journal of the Royal Society Interface* 11(95):20140021.

6. Autumn K, Dittmore A, Santos D, Spenko M, & Cutkosky M (2006) Frictional adhesion: a new angle on gecko attachment. *Journal of Experimental Biology* 209(18):3569-3579.

7. Puthoff JB, *et al.* (2013) Dynamic friction in natural and synthetic gecko setal arrays. *Soft Matter* 9(19):4855-4863.

8. Zhao BX, *et al.* (2008) Adhesion and friction force coupling of gecko setal arrays: Implications for structured adhesive surfaces. *Langmuir* 24(4):1517-1524.

9. Gravish N, *et al.* (2010) Rate-dependent frictional adhesion in natural and synthetic gecko setae. *Journal of the Royal Society Interface* 7(43):259-269.

10. Canas N, *et al.* (2012) Effect of nano- and micro-roughness on adhesion of bioinspired micropatterned surfaces. *Acta Biomaterialia* 8(1):282-288.

11. Geim AK, *et al.* (2003) Microfabricated adhesive mimicking gecko foot-hair. *Nature Materials* 2(7):461-463.

12. Murphy MP, Kim S, & Sitti M (2009) Enhanced Adhesion by Gecko-Inspired Hierarchical Fibrillar Adhesives. *ACS Applied Materials & Interfaces* 1(4):849-855.

13. Yu J, *et al.* (2011) Gecko-Inspired Dry Adhesive for Robotic Applications. *Advanced Functional Materials* 21(16):3010-3018.

14. Zhou M, *et al.* (2012) Design of gecko-inspired fibrillar surfaces with strong attachment and easy-removal properties: a numerical analysis of peel-zone. *Journal of the Royal Society Interface* 9(75):2424-2436.

15. Xue L, *et al.* (2012) Tailoring normal adhesion of arrays of thermoplastic, spring-like polymer nanorods by shaping nanorod tips. *Langmuir* 28(29):10781-10788.

16. Heepe L & Gorb S (2014) Biologically Inspired Mushroom-Shaped Adhesive Microstructures. *Annual Review of Materials Research* (0).

17. Kim Y, Claus RK, Limanto F, Fearing RS, & Maboudian R (2013) Friction Characteristics of Polymeric Nanofiber Arrays against Substrates with Tailored Geometry. *Langmuir* 29(26):8395-8401.

18. Rodriguez I, *et al.* (2013) Shear Adhesion Strength of Gecko-Inspired Tapes on Surfaces with Variable Roughness. *The Journal of Adhesion* 89(12):921-936.

19. Asbeck A, *et al.* (2009) Climbing rough vertical surfaces with hierarchical directional adhesion. *Robotics and Automation, 2009. ICRA'09. IEEE International Conference on*, (IEEE), pp 2675-2680.

20. Tambe NS & Bhushan B (2005) Friction model for the velocity dependence of nanoscale friction. *Nanotechnology* 16(10):2309-2324.

21. Yoshizawa H & Israelachvili J (1993) Fundamental Mechanisms of Interfacial Friction .2. Stick-Slip Friction of Spherical and Chain Molecules. *Journal of Physical Chemistry* 97(43):11300-11313.

22. Yu J, *et al.* (2012) Friction and Adhesion of Gecko-Inspired PDMS Flaps on Rough Surfaces. *Langmuir* 28(31):11527-11534.

23. Israelachvili J, *et al.* (2010) Recent advances in the surface forces apparatus (SFA) technique. *Reports on Progress in Physics* 73(3).

24. Yoshizawa H, Mcguiggan P, & Israelachvili J (1993) Identification of a 2nd Dynamic State during Stick-Slip Motion. *Science* 259(5099):1305-1308.

25. Tysoe W & Spencer N (2004) Why does Amontons' law work so well? (SOC TRIBOLOGISTS & LUBRICATION ENGINEERS 840 BUSSE HIGHWAY, PARK RIDGE, IL 60068 USA).

26. Gnecco E & Meyer E (2007) *Fundamentals of friction and wear* (Springer, Berlin ; New York) pp xi, 714 p.

27. Ishlinskii AY & Kragel'skii IV (1944) Rapid changes during friction. *Zh. Tekh. Fiz.* 14:276-282.

28. Scholz CH & Engelder JT (1976) Role of Asperity Indentation and Plowing in Rock Friction .1. Asperity Creep and Stick-Slip. *International Journal of Rock Mechanics and Mining Sciences* 13(5):149-154.

29. Byerlee JD (1967) Theory of friction based on brittle fracture. *Journal of Applied Physics* 38(7):2928-2934.

30. Carlos Miguez Suarez J & Biasotto Mano E (2000) Brittle–ductile transition of gamma-irradiated recycled polyethylenes blend. *Polymer Testing* 19(6):607-616.

31. Scholz CH (2002) *The mechanics of earthquakes and faulting* (Cambridge university press).

32. Schallamach A (1963) A theory of dynamic rubber friction. *Wear* 6(5):375-382.

33. Schallam.A (1971) How Does Rubber Slide. *Wear* 17(4):301-&.

34. Golden J (1975) A molecular theory of adhesive rubber friction. *Journal of Physics A: Mathematical and General* 8(6):966.

35. Israelachvili JN (2011) *Intermolecular and surface forces: revised third edition* (Academic press).

7. SYNERGISTIC INTERACTIONS BETWEEN GRAFTED HYALURONIC ACID AND LUBRICIN PROVIDE ENHANCED WEAR PROTECTION AND LUBRICATION

7.1 Abstract

Normal (adhesion) and lateral (friction) forces were measured between *physisorbed* and *chemically* grafted layers of hyaluronic acid (HA), an anionic polyelectrolyte in the presence of lubricin (Lub), a mucinous glycoprotein, on mica surfaces using a Surface Forces Apparatus (SFA). This work demonstrates that high friction coefficients between the surfaces do not necessarily correlate with surface damage and that *chemically* grafted HA acts synergistically with Lub to provide friction reduction and enhanced wear protection to the surfaces. Surface immobilization of HA by grafting is necessary for such wear protection. Increasing the concentration of Lub enhances the threshold load that a chemically grafted HA surface can be subjected to before the onset of wear. Addition of Lub does not have any beneficial effect if HA is *physisorbed* to the mica surfaces. Damage occurs at loads less than 1 mN regardless of the amount of Lub, indicating that the molecules in the bulk play little or no role in protecting the surfaces from damage. Lub penetrates into the *chemically* bound HA to form a visco-elastic gel that reduces the coefficient of friction as well as boosts the strength of the surface against abrasive wear (damage).

7.2 Introduction

Osteoarthritis is one of the most frequent and rapidly growing causes of permanent disability in the world. The mechanism of cartilage wear is still unknown and remains a pressing research question within the medical community. Various lubrication mechanisms have been proposed to explain friction and wear in cartilage; however there is no single model that gives a complete picture of the lubrication mechanism. It has been attributed to multiple modes which includes hydrodynamic, elasto-hydrodynamic, weeping (1-3), mixed (4, 5) and boundary (6, 7) lubrication mechanisms. There have been extensive studies on the role of various components (e.g., Hyaluronic acid (HA) (6, 8, 9), Lubricin (Lub) (10-13), lipids (6, 14), etc.) of the synovial fluid to understand their separate roles in the lubrication mechanism. However, the molecular interactions between the different components of synovial fluid (e.g., HA, Lub, lipids etc.) and their synergistic roles in the wear protection and friction reduction mechanisms in articular joints remain a puzzling question.

The articular joint is a highly efficient lubrication system that maintains extremely low friction coefficients (μ = 0.0005-0.04) (15, 16). It consists of porous cartilage surfaces facing each other filled with the lubricating protein molecules and lipids and immersed in the aqueous synovial fluid filling the gap between the two surfaces. Hyaluronic acid (HA), a high molecular weight polysaccharide is the most abundant component of the synovial fluid and provides joint lubrication together with other protein molecules like Lub, a mucinous glycosylated protein (also known as proteoglycan 4, PRG4), various lipids (e.g. mainly phosphatidylcholines, PCs) and glycosaminoglycans (GAGs). HA has been extensively studied and has been seen to act as a potential boundary lubricant when chemically grafted to a surface (6, 17-19) or mechanically trapped (physically attached) (9) to the cartilage surface,

although it shows high friction coefficients (μ = 0.15-0.52) (6, 17). In contrast, free HA shows poor lubricating and wear protection properties.(6, 17-19) Tribological experiments with Lub show that the strength of adsorption (binding strength) to a surface is a crucial parameter that determines the wear protection ability of the glycoprotein (20) and that the surface active component of Lub is responsible for the low friction coefficient between surfaces (11). A multiple-particle-tracking micro-rheology technique showed that Lub cross-links HA and forms an elastic gel-like complex which helps in strain energy dissipation in the synovial fluid (21). This HA-Lub gel was proposed to play an important role in the protection of the cartilage surface against wear (21), however no experimental evidence or quantitative data on the friction behavior between the cartilage surfaces due to the gel formation was provided. However, Lub alone is a critical chondro-protective lubricant (22). Its absence in a mouse model leads to rapid cartilage deterioration and the synovial fluid from humans who genetically lack Lub display a higher concentration of HA (23). Lub in conjunction with HA mediates the interactions at cartilage surfaces and maintains them in a sterically repulsive state (24). Lub also alters the rheological properties of HA by forming a HA-Lub gel which showed a shear thinning behavior (21). Similar strong interaction of Lub with HA has been observed in our SFA experiments. The thin HA-Lub gel complex formed between our model surfaces (mica) showed an increase in the shear viscosity by two orders of magnitude with load.

This work deals with the study of the frictional and wear behavior of model surfaces (e.g., biopolymer coated/ uncoated mica). The boundary lubrication of the surfaces has been studied, and the role of Lub (protein) and HA (polyelectrolyte) during the initiation and spreading (progression, development) of wear has been explored in these experiments. HA,

the viscous component of the human synovial fluid can be both physisorbed or chemisorbed, and either cross-linked or un-cross-linked on the mica surfaces, leading to (at least) four different combinations or scenarios in which the molecules can be organized. Each of the combinations can be useful in terms of reducing the friction forces *and* providing wear resistance or both. Here, we have discussed the important role played by chemically grafted HA along with Lub in not only providing wear protection, but also help reduce friction between the mica surfaces. Conversely, if HA is physisorbed, Lub plays no role in protecting the surfaces from abrasive wear (damage). There is no correlation between the onset of wear and the friction coefficient if the HA-Lub mixture is physisorbed to the surface, in which case the damage occurs at low loads ($F_{\perp}$< 1 mN). However, for chemically grafted HA, increasing the Lub concentration increases the wear protection and also decreases the coefficient of friction.

7.3 Materials and Methods

7.3.1 Preparation of Hyaluronic acid and Lubricin solutions

Hyaluronic acid (HA) with an average molecular weight of 1.6 MDa (Sigma-Aldrich) was used directly without any further purification. A 3 g/L solution of HA was prepared by diluting the polymer in phosphate buffered saline (PBS from Sigma-Aldrich, 120 mM NaCl, 10 mM phosphate salt, 2.7 mM KCl, pH 7.4). The solution was stirred for ~3 h in a warm water bath at 50°C to completely dissolve HA in the PBS buffer. Lubricin (Lub) protein obtained from human synovial fluid as described in reference (25) was diluted in PBS buffer to prepare solutions with concentration of 1, 10 and 100 mg/L. The HA-Lub mixture was prepared by diluting 100 mg/L Lub solution in the 3 g/L HA solution to obtain a

concentration of 10 mg/L of Lub in the final mixture. All the glassware used in the preparation of the solutions was cleaned in ethanol followed by rinsing in Milli-Q® water. The PBS buffer solution was prepared in Milli-Q water as well.

7.3.2 HA grafting

The protocol followed for preparing the grafted layer of HA on the mica surfaces is different from that used in previous work (6) and was as follows: Atomically flat mica sheets (2-5 μm in thicknesses) were glued on two cylindrical glass surfaces, each with a radius of curvature $R \approx 2$ cm. The glued mica surfaces were then activated by water-argon plasma for 10 mins at 40 Watts. (3-Aminopropyl) triethoxysilane (APTES, Sigma-Aldrich) was then vapor deposited on the plasma activated mica surfaces in a sealed vial for ~12 h at 40°C (under vacuum). The resulting APTES-grafted mica surfaces were washed with PBS in order to remove any non-grafted APTES. The thickness of the APTES layer was measured to be ~ 1 nm on each surface in the SFA, which suggests that, a macroscopically uniform molecularly thick layer of APTES was deposited (see supporting Fig. S7.1). The functionalized mica surfaces thus obtained were soaked in the HA solution (3 g/L HA in PBS) for ~ 20 h to obtain the chemically grafted HA layers (see supporting Fig. S7.2). The surfaces were then rinsed thoroughly with PBS buffer to remove any physisorbed HA from the chemically grafted HA layer. In another experiment, force measurements were performed without rinsing the surfaces with PBS (see Fig. 7.2b). For the friction experiments, the HA grafted mica surfaces were not rinsed with PBS in order to mimic the synovial fluid and have free HA in the fluid reservoir between the two mica surfaces.

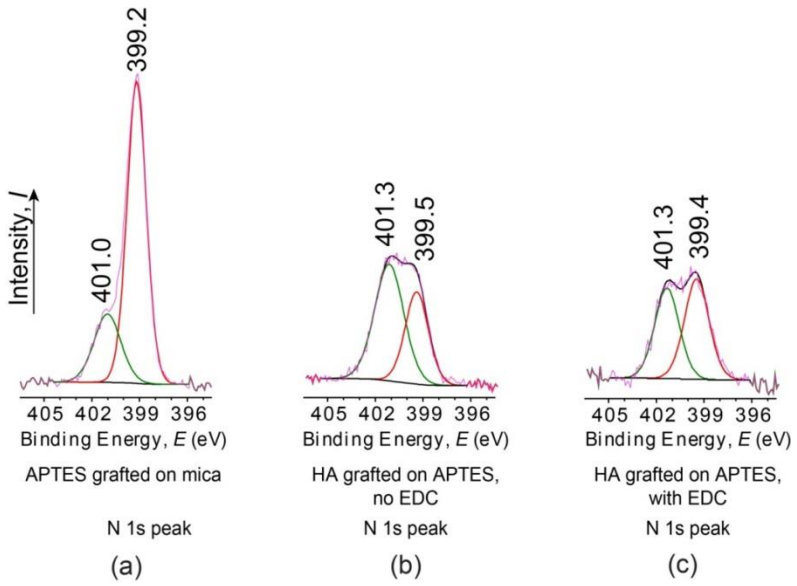

Figure 7.1 High resolution XPS N 1s spectra with Gaussian fits to the peaks upon (a) APTES grafting on the mica surface, (b) HA grafted to APTES on the mica surface without using EDC chemistry, and (c) HA grafted to APTES on the mica surface using EDC chemistry. The survey scans for these surfaces are shown in the supporting Fig. S7.3.

The chemical grafting of HA to the APTES layer on the mica surface was characterized by XPS. XPS measurements were collected from an Axis Ultra XPS (Kratos Analytical, UK) spectrometer. A wide spectrum scan (Binding energy, E = 0 - 600 eV) was obtained with a pass energy of 80 eV (Fig. S7.3). The binding energies were corrected to 285 eV for the C 1s peak. High resolution elemental analysis of the N 1s peak was obtained at 20 eV pass energy with a step size of 0.1 eV and averaged over 10 scans (Fig. 7.1). The electrons were captured at an angle of 70° to make surface sensitive measurements (mica polymer interface). The experimental data was fitted to a Gaussian function. XPS was performed on (1) mica surface grafted with APTES, (2) HA grafted to APTES on the mica surface without using 1-ethyl-(3, 3-dimethylaminopropyl) carbodiiminde hydrochloride

(EDC) chemistry, and (3) HA grafted to APTES on the mica surface using EDC chemistry (26-28) (see supporting Fig. S7.3 and Fig. 7.1). All the above mica surfaces were grafted with APTES under the same condition.

7.3.3 The Surface Forces Apparatus (SFA)

The Surface Forces Apparatus (SFA) was used to measure the normal and frictional forces between two mica surfaces in a cross-cylindrical geometry as a function of the separation distance, *D*, between them (29-32). The mica-mica surface separation distance was measured by multiple beam interferometry (MBI) (33) with angstrom level distance resolution. Two freshly cleaved back-silvered mica surfaces were glued on half cylindrical glass discs ($R \approx 2$) cm with thermoset epoxy resin (Epon 1004F). Before grafting the mica surfaces with HA, mica-mica contact was measured by the SFA in dry air in order to get the reference distance, $D = 0$. The radius of curvature of the contact point was measured from the shape of the fringes obtained by MBI (34). The normal forces were calculated from the deflection of a horizontal double cantilever spring to which the lower surface was attached. The lower cylindrical mica surface can be approached or separated from the upper mica surface by a motor driven spring gear mechanism. When the two surfaces are not interacting, i.e., they are separated by large distances, the change in the separation between them is equal to the distance through which the motor moves the lower surface towards or away from the upper surface. However, once the surfaces are close enough to start interacting with each other, the measured separation distance deviates from the expected separation calibrated when there is no force between the surfaces. This deviation is due to the deflection of the double cantilever spring and is directly proportional to the force acting normally between the

two opposing surfaces. The friction force is calculated from the lateral deflection of a vertical double cantilever spring connected to the upper surface, which is measured using foil strain gauges (35). The lower surface can be sheared against the upper surface with a piezoelectric bimorph device (35) with a shearing amplitude of 10-200 μm. The shearing speed can be modulated by changing the voltage input frequency to the piezoelectric crystal of the bimorph device. In our experiments, a triangular wave input with a peak to peak voltage of 30V was applied with a frequency of 0.01 and 0.1Hz to obtain constant sliding speeds of $v \sim$ 3 and 30 μm/s respectively between the mica surfaces. Wear of the surfaces was visualized from the shapes of the Fringes of Equal Chromatic Order (FECO) (see supporting Fig. S7.4). Thus, the normal loads ($F_{\perp}$), friction force ($F_{\parallel}$), and the film thickness (D) of the HA-Lub mixture were measured *simultaneously* during the friction experiments. The normal force of interaction between the surfaces, $F_{\perp}$ were measured at an approach and separation speeds of 1-2 nm/s.

7.4 Results and Discussion

7.4.1 Chemical grafting of HA to the mica surface

XPS and SFA techniques were employed to confirm the chemical grafting of HA to the mica surfaces. XPS wide spectrum scans (Binding energy, E = 0 - 600 eV) of the surfaces are shown in Fig. S7.3. High resolution N 1s spectral scan of grafted APTES on mica showed a strong peak at 399.2 eV which corresponds to the nitrogen from the free amine, whereas the shoulder peak at 401.0 eV is due to the protonated and the hydrogen bonded amines (36). Reaction of HA with APTES decreased the total N 1s peak intensity (Fig. 7.1b and c). The significant decrease in the low energy fitted N 1s peak at 399.2 eV shows that the free amine

of APTES reacted with the carboxylic group of HA (36) (Fig. 7.1a) in both the cases, i.e. with and without using EDC chemistry. EDC is commonly used to activate the carboxylic acid group (–COOH) of HA for functionalization with amines (26-28). The XPS survey shows that given enough time (~ 20 h) for the reaction, the –COOH of HA forms an amide linkage with the free amine of APTES even without the activation of the –COOH group with EDC. There is an increase in both the intensity and the area of the high energy fitted N 1s peak (Fig. 7.1) at 401.3 eV due to the increase in the number of amide groups from the reaction.

7.4.2 SFA experiments

The adsorption of HA onto the APTES grafted mica surfaces was monitored with the incubation time in the HA solution by measuring the "hard wall" thickness of the HA layer in the SFA (see supporting Fig. S7.2) at a layer of thickness 24 ± 2 nm (at pressure, P ~ 1 MPa) after incubating the APTES grafted mica in 3 g/L HA in PBS. The hard wall measurements were made after the surfaces were rinsed thoroughly in PBS. The refractive index of the chemically grafted HA layer was measured (37) to be 1.4 (~ 53 % hydrated). Thus, we confirmed the formation of a stable grafted layer of HA on the mica surfaces.

7.4.3 Normal forces measured in the SFA

The normal forces $F_{\perp}$ normalized by the surface radius of curvature R were measured for grafted (chemisorbed) HA and physisorbed (not chemically grafted) HA-Lub mixture with and without free HA/Lub in the solution between the surfaces. Table 7.1 shows the different surface and solution conditions and the figures that they refer to.

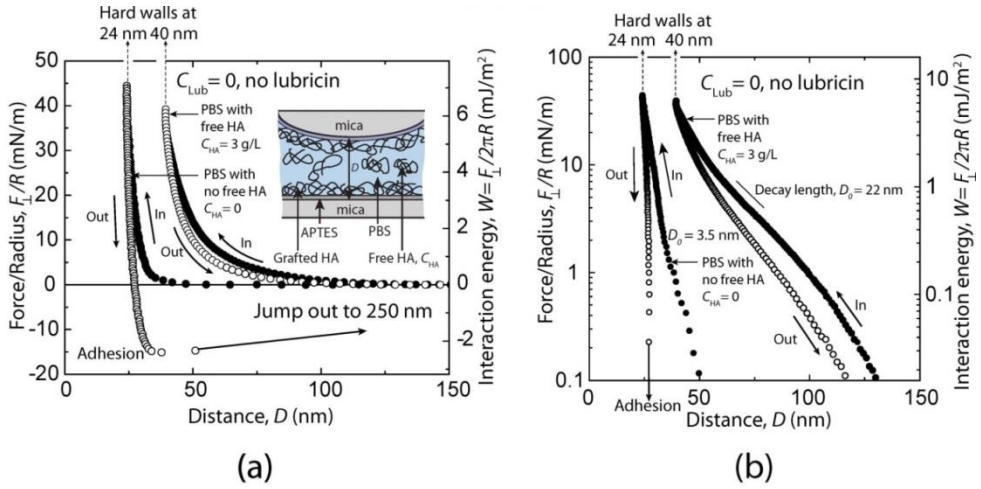

Figure 7.2 (a) Normal force $F_\perp$ normalized by the surface radius of curvature R between HA molecules chemically attached (grafted) on mica as a function of the mica-mica separation distance, D. The black circles represent the forces measured with (C_{HA} = 3 mg/L) and without (C_{HA} = 0) free HA molecules in the PBS buffer (pH = 7.4) between the surfaces. The forces measured between grafted HA molecules with no free HA (C_{HA} = 0) molecules present in the PBS buffer showed a shorter "hard wall" thickness. Forces measured on approach are shown by solid circles and on separation by open circles. (b) The same forces shown on a semi-log plot.

7.4.3.1 Interactions between chemically grafted HA molecules *with* (C_{HA}= 3 g/L) and *without* (C_{HA}= 0) free HA between the surfaces (Fig. 7.2)

The interaction forces between the grafted HA molecules were purely repulsive (Fig. 7.2). Electrostatic forces are expected to play a minor role in the total interaction due to the high ionic strength of the buffer solution and hence small Debye length ≈ 1 nm. The hysteresis between the approach and separation force curves is expected due to the high molecular weight of the polymers and is typically observed in polymer mediated interactions (Fig. 7.2a), especially with high molecular weight polymers.

In the absence of free HA in the solution, the two surfaces adhered with an energy of W = 2.4 mJ/m^2 due to the van der Waals force between the entangled polymer chains on the opposing surfaces (Fig. 7.2a). Such adhesion between the surfaces was not observed when the chemically grafted HA is cross-linked (6). The measured forces were exponential on approach of the two surfaces, with no HA in the solution (C_{HA} = 0), with a decay length of D_0 = 3.5 nm which suggests that the chemically grafted layer of HA is in the collapsed state. The onset of repulsion occurred at a separation distance of about 50 nm (Fig. 7.2b) as a result of the steric repulsion between the tails of the polysaccharide dangling out of the chemically grafted HA chains.

There was no adhesion between the chemically grafted HA layers in the presence of free HA in the solution (C_{HA} = 3 g/L) due to the steric repulsion between the weakly adsorbed free HA on the chemically grafted HA layers. The free HA molecules did not give rise to adhesive bridges between the two grafted HA surfaces even at high compressions, but induced an exponential steric repulsion with a decay length of 22 nm. The presence of trapped HA between the surfaces was also observed from the increase in the hard wall thickness to 40 nm in the force distance curve in Fig. 7.2 as compared to the hard wall thickness of 24 nm when no free HA was present between the surfaces.

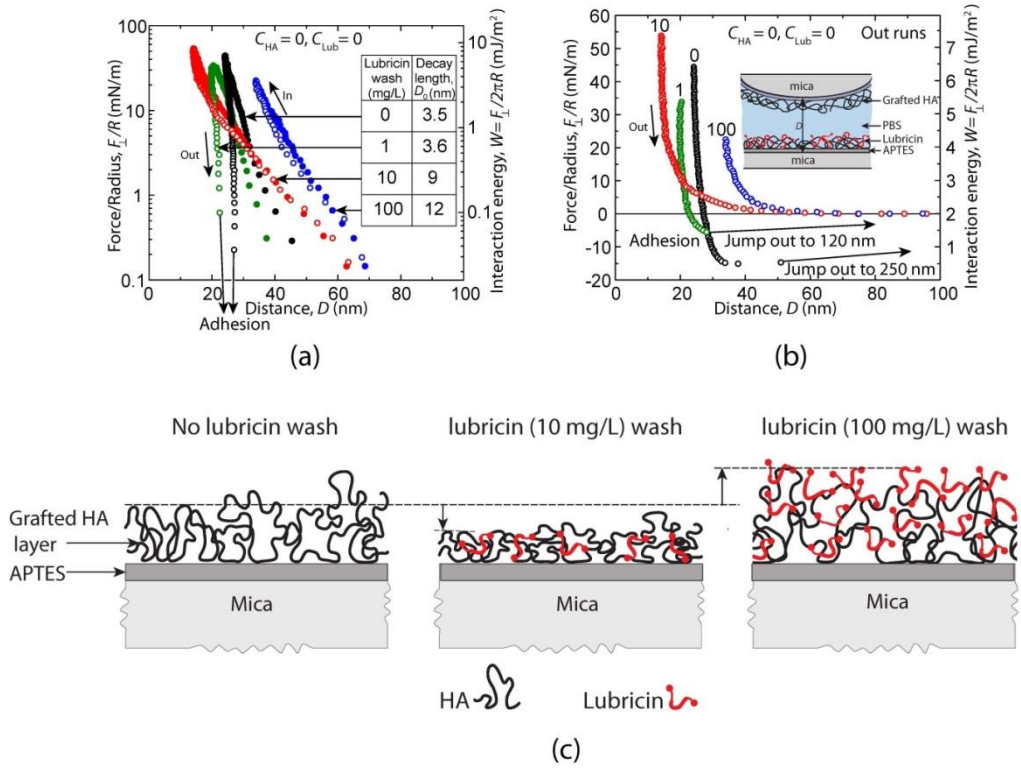

Figure 7.3 (a) Measurement of the normal forces $F_\perp$ normalized by the surface radius of curvature R between two grafted HA layers on mica surface with physisorbed lubricin only on the lower grafted HA layer as a function of the mica-mica separation distance, D. Forces measured on approach are shown by solid circles and on separation by open circles. Incorporation of lubricin causes shrinkage and eventual increase in the thickness of the final hard wall. The reservoir is pure PBS buffer (pH = 7.4) with no free HA ($C_{HA} = 0$). (b) Same experiment as in Fig. 7.2 (a) showing the forces on separation with adhesion between the surfaces when the lower surface was incubated in 1 mg/L lubricin. No adhesion was observed when the lower surface was incubated in 10mg/L and 100 mg/L lubricin in PBS buffer.

7.4.3.2 Grafted HA on mica *without* free HA (C_{HA}= 0) and Lub (C_{Lub} = 0) between the surfaces *with* Lub physisorbed only to the *lower* grafted HA surface (Fig. 7.3)

The normal interaction forces between two grafted (chemisorbed) layers of HA with physisorbed Lub on only one surface were always repulsive on approach due to steric effects (Fig. 7.3a). However, adhesion was measured on separation of the surfaces at low Lub (incubation in C_{Lub} < 10 mg/L outside the SFA) on one of the surfaces only and disappeared when the concentration of Lub was increased (Fig. 7.3b). The measured hard wall thickness decreased from ~ 25 to ~ 15 nm on incubating the chemisorbed HA layer with 1- 10 mg/L Lub in PBS, and swelled to ~ 35 nm after incubation in 100 mg/L Lub (Fig. 7.3a). The measured forces were found to be repeatable at each contact point demonstrating that the Lub bound to one of the HA surfaces is very stable and no transfer of Lub molecules takes place from the lower HA surface to the opposing chemisorbed HA surface.

Lubricin has a net negative charge at pH 7.4 (Zeta potential, ζ = -15.6±2.7 mV). The central domain of Lub is negatively charged and most of the positive charge and hydrophobic residues are carried by the two end domains of the protein. Therefore, it interacts strongly with the negatively charged chemically bound HA chains with the end domains forming a HA-Lub complex. The initial collapse of the HA layer at low C_{Lub} (Fig. 7.3c) is due to the electrostatic and hydrophobic forces resulting in bridging of the HA by Lub. As the concentration of the adsorbed Lub is increased, it cannot bridge anymore due to the saturation of the binding sites on the chemisorbed HA layer. Hence there is a buildup of Lub on the surface which is evident from the increase in the hard wall thickness (Fig. 7.3). The accumulation of Lub on the lower chemisorbed HA surface causes conformational changes of the molecules in that layer, and this is reflected by the increased decay length (Fig. 7.3a)

of the interaction forces with increasing the Lub concentration on that surface. The central negatively charged domain of Lub protrudes out of the HA-Lub complex inducing steric and electrostatic repulsion with the opposing negatively charged chemisorbed HA surface. Hence, there is a decrease in the adhesion energy between the two chemisorbed HA layers with physisorbed Lub to only one of them (asymmetric HA-Lub surfaces) for incubation of that surface in 1 mg/L Lub. At higher incubation concentration (~ 10 mg/L), the adhesion is completely eliminated and by incubation in 100 mg/L Lub, the increased adsorption also pushes out the steric hard wall thickness (Fig. 7.3).

7.4.3.3 Grafted HA on mica *with* free HA (C_{HA} = 1.5-0.36 g/L) and Lub (C_{Lub} = 0.5-55.5 mg/L) between the surfaces and Lub physisorbed to *both* grafted HA surfaces (Fig. 7.4)

The normal forces of interaction measured between symmetric chemisorbed HA layers with physisorbed Lub and HA on both layers were purely repulsive during approach and separation (Fig. 7.4a). These forces were similar to the interactions measured with chemically bound HA with free HA between the surfaces. Introduction of Lub caused the hard wall thickness to decrease from 40 nm (measured with no Lub on or between the surfaces) to 32 nm followed by increase to ~45 nm on increasing the concentration of Lub, C_{Lub} in the reservoir. Initial collapse of the HA layer followed by increase in the hard wall thickness is similar to the asymmetric HA-Lub surfaces described above.

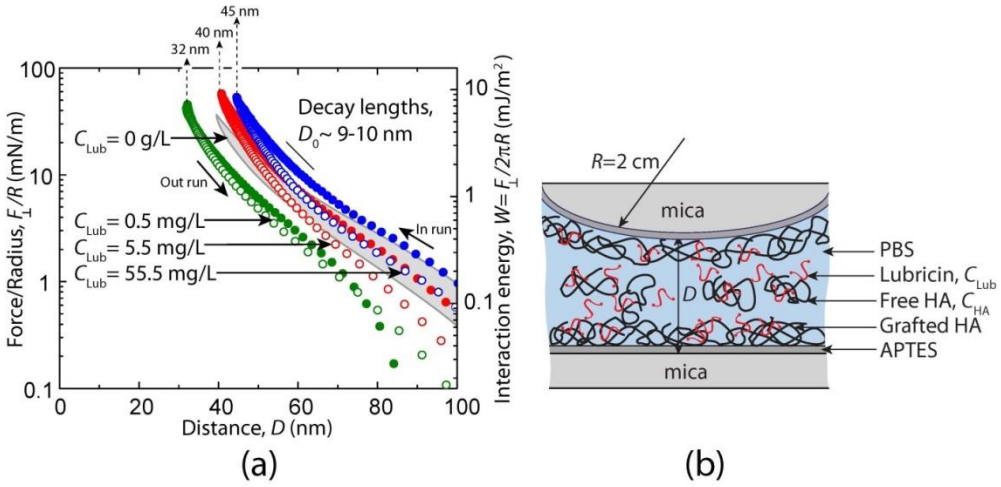

Figure 7.4 Measurement of the normal forces $F_\perp$ and change in the thickness of the final hardwall induced by various concentrations of the lubricin, C_{Lub} injected in the PBS reservoir between the surfaces with free HA molecules (C_{HA} = 0.5-1.5 g/L) in the solution. Forces measured on approach are shown by solid circles and on separation by open circles. In this system, lubricin or HA was not rinsed off with PBS buffer as in the system in Fig. 7.2.

7.4.3.4 Physisorbed HA and Lub on mica *with* free HA (C_{HA} = 2.5-3 g/L) and lubricin (C_{Lub} = 10-250 mg/L) between the surfaces (Fig. 7.5)

The force measured between the mica surfaces with physisorbed HA-Lub complex extended to a distance of 50-60 nm with a decay length of 20 nm (Fig. 7.5). Lub penetrates the free HA molecules with its positively charged and hydrophobic end domains, and increases the net negative charge on its surface which prevents the further adsorption of the free HA-Lub complex to the negatively charged mica surface (at pH 7.4); hence the free HA-Lub complex is expelled out of the gap when the two facing surfaces are brought into contact (D = 0). This is unlike the pure physisorbed HA molecules (no Lub in the system) which tend to form an adsorbed layer and are not expelled from between the mica surfaces under similar compression conditions (6). The short exponential decay length of ~1 nm at a mica-mica

surface separation distance, D < 5 nm is consistent with the Debye length for the PBS buffer (salt concentration of ~ 120 mM) suggesting a DLVO interaction between the surfaces at small separations.

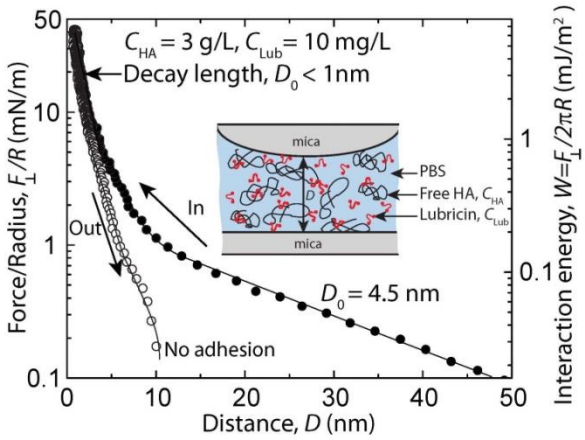

Figure 7.5 Normal force $F_\perp$ normalized by R between physisorbed (not grafted) HA-Lub (C_{HA} = 3 g/L, C_{Lub} = 10 mg/L) mixture on mica as a function of the mica-mica separation distance, D.

7.4.4 Shear forces measured in the SFA

The friction force, $F_\parallel$ were measured as a function of the normal load, $F_\perp$ for the chemically grafted HA as well as for the physisorbed HA-Lub mixture on the mica surfaces with free HA and Lub between the surfaces.

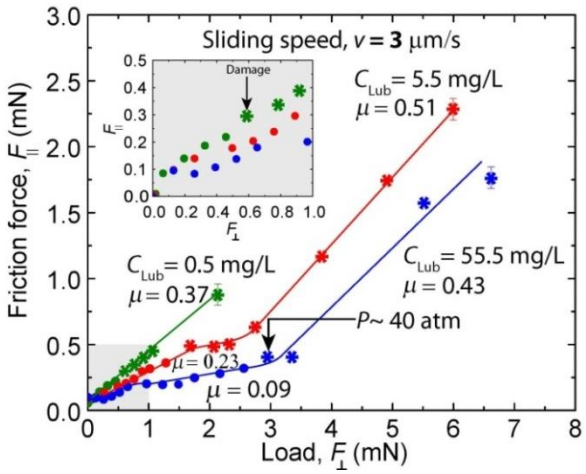

Figure 7.6 Friction forces $F_{\parallel}$ measured as a function of the normal force (load) $F_{\perp}$ between two chemically grafted HA on mica surfaces in PBS buffer with free HA (C_{HA} = 0.5-1.5 g/L) and lubricin in the solution at various concentrations. The surfaces were sheared at a sliding velocity of v = 3 μm/s. The starred points (*) indicate friction measurements after the surfaces became damaged. The inset shows the friction forces at the low load regime ($F_{\perp} < 1$ mN).

7.4.4.1 Grafted HA on mica *with* free HA (C_{HA} = 1.5-0.36 g/L) and Lub (C_{Lub} = 0.5-55.5 mg/L) physisorbed to both the grafted HA surfaces (Fig. 7.6 and 7.7)

HA chemically grafted to the mica surfaces with physisorbed Lub and HA showed excellent lubrication (low friction) and wear protection properties (Fig. 7.6). The measured friction force and wear inception on the surfaces were functions of the lubricin concentration, C_{Lub}, in the bulk. At low concentration of Lub (C_{Lub} < 0.5 mg/L), the surfaces showed higher coefficient of friction of $\mu \approx 0.4$ and surface damage occurred at low loads ($F_{\perp}$ < 0.5 mN, P < 1MPa) (Fig. 7.6). The mica surfaces underwent damage at an applied pressure of about 40 atm (for C_{Lub} = 55.5 mg/L) which is about twice the pressure the surface could withstand before the onset of damage in the absence of Lub for chemically grafted HA on mica (6).

Increasing C_{Lub} caused reduction of μ and increased the threshold load (or pressure) for damage ($F_{\perp}$ = 1.5-2.5 mN) the surfaces could be sheared at before the inception of damage. $F_{\parallel}$ *vs* $F_{\perp}$ showedroughly a linear relationship before and after damage, with higher μ after damage occurred. Before damage occurred, increasing the concentration of Lub decreased the friction coefficients from μ ~ 0.37 for C_{Lub} = 0.5 mg/L to μ ~ 0.09 for C_{Lub} = 55.5 mg/L.

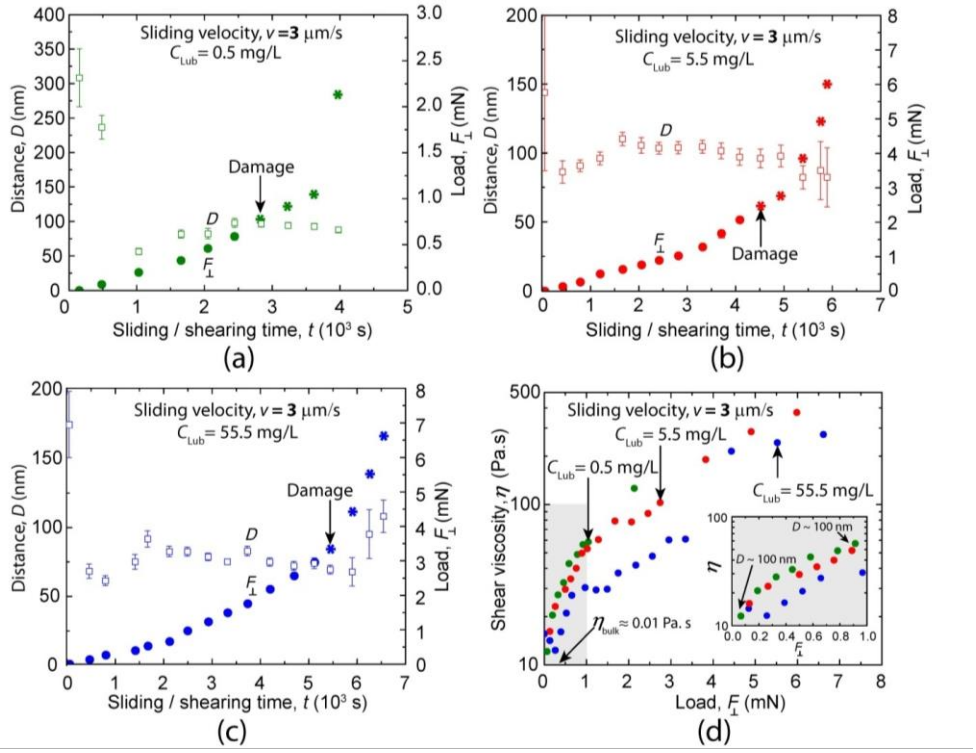

Figure 7.7 (a), (b), (c) Film thickness D measured on shearing the surfaces at a sliding velocity of v = 3 μm/s. The solid circles give the time when shearing was stopped and the load was increased. Shearing was resumed after a loading process was completed. Each of the points on this figure corresponds to the respective film thicknesses at the corresponding normal loads in Fig. 7.6. (d) The measured shear viscosity of the solution between the surfaces at different normal loads for various lubricin concentrations at v = 3μm/s. The starred points (*) indicate friction measurements after the surfaces became damaged.

The HA-Lub gel formed a film of thickness of 50-100 nm after the first few shearing cycles and the thickness of this gel did not change with time or on increasing the load (Fig. 7.7a, b and c). The shear viscosity η of this film is given by (35)

$$\eta = \frac{5F_{\parallel}}{16\pi R v \log(\frac{2R}{D})} \tag{7.1}$$

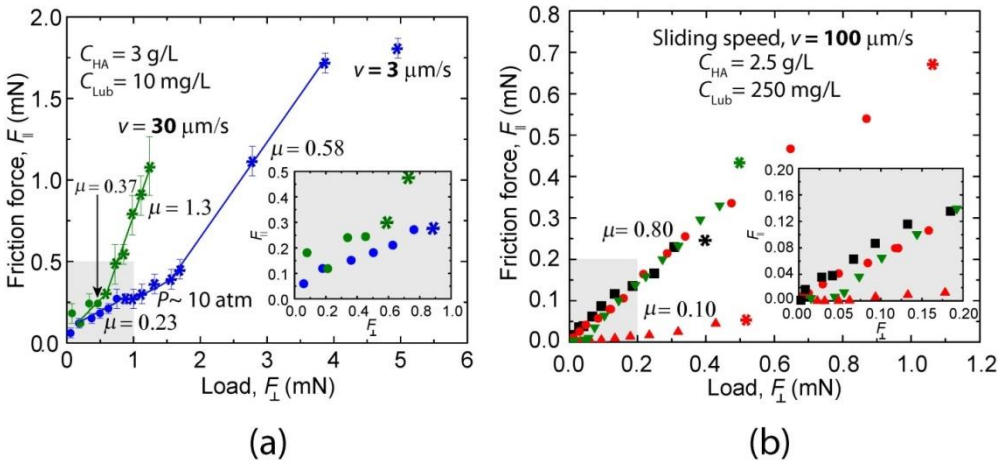

Figure 7.8 (a) Friction forces $F_{\parallel}$measured as a function of the normal force (load) $F_{\perp}$with physisorbed (not grafted) HA-Lub (C_{HA} = 3 g/L, C_{Lub} = 10 mg/L) mixture between the mica surfaces. The surfaces were sheared with a sliding velocity of v = 3 μm/s (blue circles) and 30 μm/s (green circles). The starred points (*) indicate friction measurements after the surfaces became damaged. (b) Friction forces measured with physisorbed (not grafted) HA-Lub (C_{HA} = 2.5 g/L, C_{Lub} = 250 mg/L) mixture between the mica surfaces at a sliding velocity of v = 100 μm/s. Points with same color indicate different contact points on the same surface whereas different colors denote different surfaces. The starred points (*) indicate friction measurements after the surfaces became damaged.

For film thicknesses of less than 100 nm, the shear rate is on the order of 10^4 s^{-1}. This causes jamming (38) of the HA-Lub gel confined between the mica surfaces. At such high shear rates and small confinements, the value of η rise by four orders of magnitude over the bulk value of η ~ 0.01 Pa.s (Fig. 7.7d) (21). The HA-Lub gel undergoes a gradual transition from a liquid- to solid-like behavior between $F_\perp$ ~ 1–6 mN. Such high viscosities have been previously observed in confined polymer melts (35, 39), brush layers (40), and organic liquids (41, 42) at similar shear rates and film thicknesses. The magnitude of η was similar for different C_{Lub} in the bulk reservoir suggesting that the composition of the jammed HA-Lub gel between the surfaces is weakly dependent on the C_{Lub} once the surfaces are sheared for several cycles against each other.

7.4.4.2 Physisorbed HA and Lub on mica *with* free HA (C_{HA}= 2.5-3 g/L) and lubricin (C_{Lub}= 10-250 mg/L) between the surfaces (Fig. 7.8 and 7.9)

HA-Lub mixture physisorbed on to the mica surfaces showed poor wear protection properties. The surfaces already underwent damage at low loads ($F_\perp$ < 1 mN, P~ 10atm) independent of the lubricin concentration or the sliding velocities (Fig. 7.8). Wear occurred at loads less than 1mN for the physisorbed HA-Lub mixture even when the coefficient of friction was low (μ ~ 0.1) (Fig. 7.8b). There was no correlation between μ and C_{Lub} or C_{HA}, or the inception of damage to the mica surface. Shearing the surfaces caused gelation of the physisorbed HA-Lub mixture after several sliding cycles, forming a film between the surfaces of thickness ranging between 50–150 nm (Fig. 7.9a, b). This was similar to the gelation of the HA-Lub complex on the mica surfaces with chemisorbed HA. The physisorbed HA-Lub gel film showed shear thinning behavior since its viscosity decreased as

the sliding velocity v was increased for similar film thicknesses (Fig. 7.9c). The HA-Lub complex is free to slide on the mica surface (the slip plane is on the mica surface) unlike the chemically grafted HA (slip plane is on the chemisorbed HA layer) and hence results in high local shear stresses causing damage to the surfaces. It could also cause regions of high local pressure on the surface due to the formation of nano bumps that can initiate a fracture on shearing the surfaces.

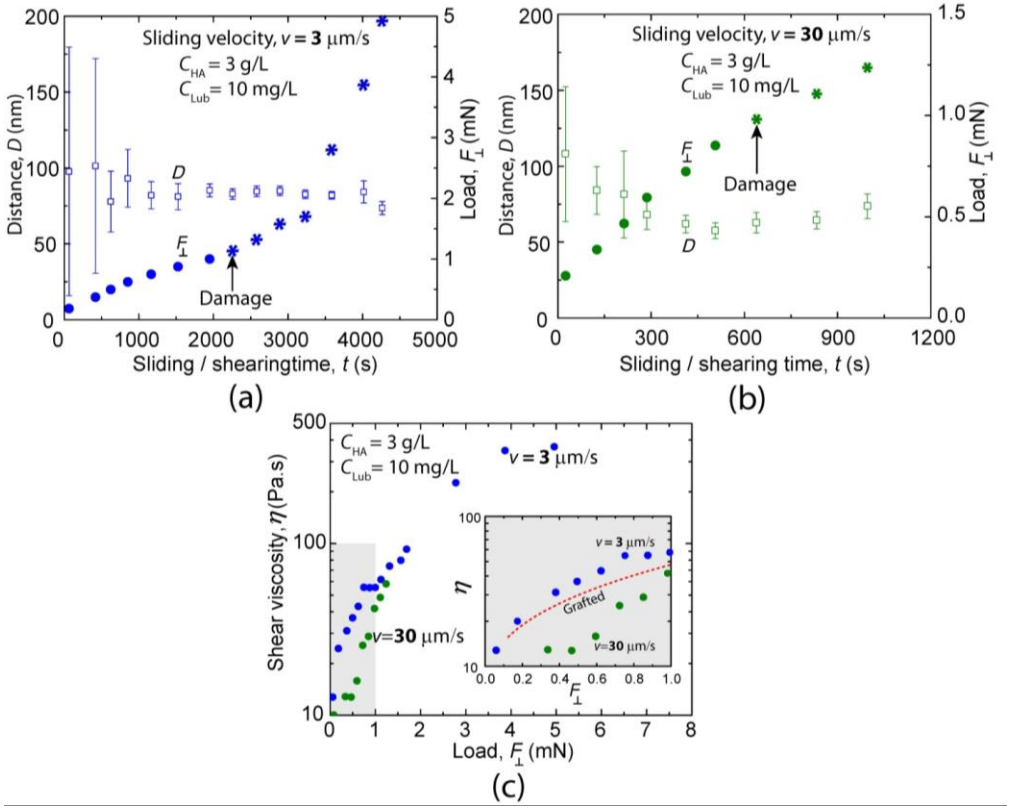

Figure 7.9 (a), (b) Film thickness D measured on shearing the surfaces at a sliding velocity of v = 3 μm/s (blue circles) and 30 μm/s (green circles). The solid circles give the time when the load was increased after a pause in the shearing. Shearing was resumed after a loading process was completed. Each of the points on this figure corresponds to the respective film thicknesses at the corresponding normal loads on Fig. 7.8. (c) The measured shear viscosity of the solution between the surfaces at different normal loads at v = 3 μm/s (blue circles) and

30 μm/s (green circles). For comparison, the red dotted lines indicate the shear viscosity of the film when HA is chemically grafted to the mica surfaces. The starred points (*) indicate friction measurements after the surfaces became damaged.

7.5 Conclusions

Our study shows that chemically grafted HA along with Lub not only provide enhanced wear protection to surfaces, but also helps reduce the friction coefficient. Surface immobilization of HA is necessary for Lub to work synergistically with HA and impart efficient lubricating property to the surface. This is in agreement with the HA "trapping model" recently proposed to explain the lubricating behavior of the polysaccharide in cartilage (9). Increasing the concentration of Lub decreases the coefficient of friction between the surfaces only when the HA is grafted (chemisorbed) to the mica surfaces. It also increases the threshold load the surfaces can withstand before the inception of damage when they are sheared against each other. Physisorbed HA-Lub complex is unable to provide wear protection to mica surfaces similar to pure physisorbed HA on mica. The concentration of Lub plays no role in reducing the friction for the physisorbed HA-Lub mixture and no correlation was found between the friction coefficients and wear protection under physisorption for this system. The possible synergistic action of lipids and GAGs in further enhancing the lubrication properties of chemisorbed HA layers with higher and more physiologic Lub concentrations need investigation.

7.6 Appendix

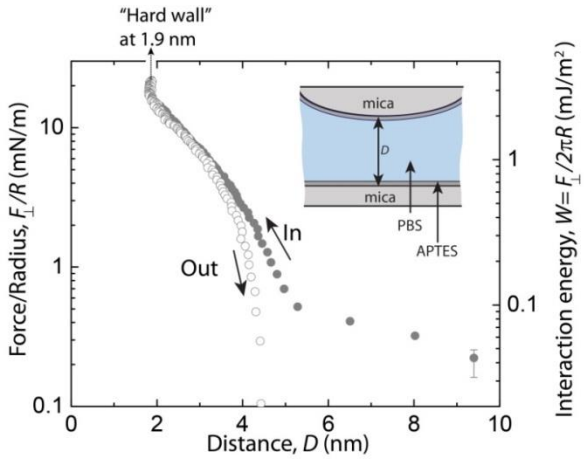

Figure S7.1 Normal force $F_{\perp}$ normalized by R between chemically grafted APTES on the mica surfaces as a function of the mica-mica separation distance, D, with PBS buffer between the surfaces. The force measurements show that a monolayer of APTES was deposited on the mica surfaces.

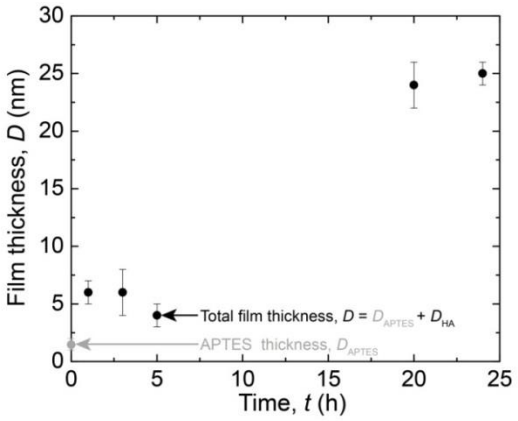

Figure S7.2 "Hard wall" measurements in the SFA to show the growth of the HA film on the mica surface with time, t. The surfaces were rinsed thoroughly in PBS after incubating in HA solution. The error bars indicate the variation in the film thickness of the APTES and HA layer measured at different contact points on the same mica surface.

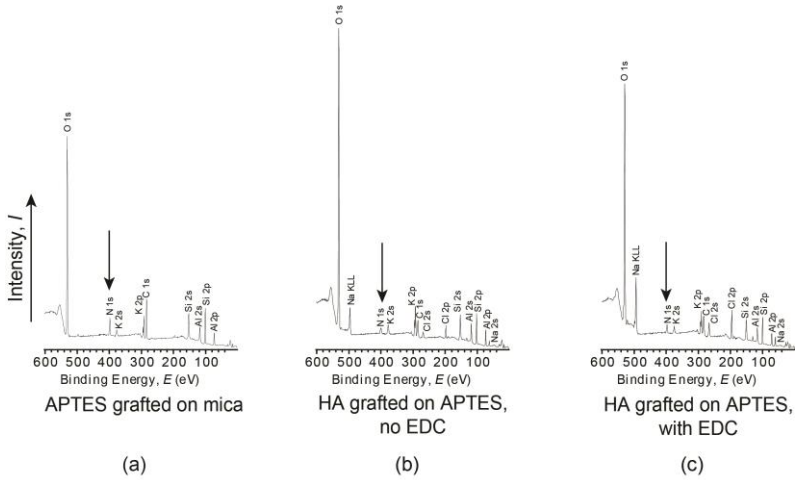

Figure S7.3 XPS survey spectra upon (a) APTES grafting on the mica surface, (b) HA grafted to APTES on the mica surface without using EDC, and (c) HA grafted to APTES on the mica surface using EDC chemistry. The arrows indicate the N 1s peak region in the survey scan which was resolved with high resolution XPS scan (Fig. 7.1).

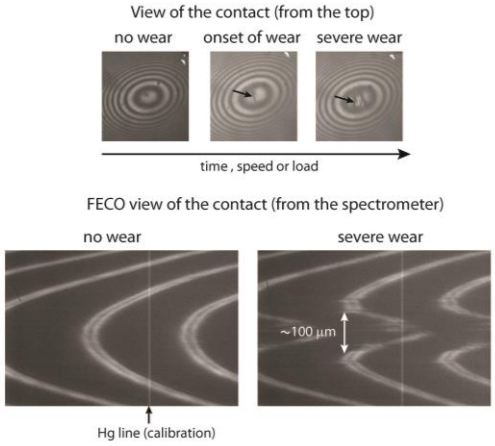

Figure S7.4 Top view images of the surfaces and evolution of the FECO fringe pattern during shearing showing wear tracks in the sliding direction of width <100 µm and height ~200 nm (calculated from the shape of the deformed fringes using the calculations in Ref. (33).

7.7 References

1. Lewis PR & Mccutchen CW (1959) Experimental Evidence for Weeping Lubrication in Mammalian Joints. *Nature* 184(4695):1285-1285.
2. Mow MC & Ling FF (1969) On Weeping Lubrication Theory. *Zeitschrift Fur Angewandte Mathematik Und Physik* 20(2):156-166.
3. Tait DC, Nickel JC, & McLachlan KR (1997) Impulse loading and weeping lubrication on the surface of the TMJ disc. *Journal of Dental Research* 76:3466-3466.
4. Jin ZM (2002) Analysis of mixed lubrication mechanism in metal-on-metal hip joint replacements. *Proceedings of the Institution of Mechanical Engineers Part H-Journal of Engineering in Medicine* 216(H1):85-89.
5. Clarke SJ & Bell MA (2008) Modelling of friction in a ball joint in mixed lubrication. *Proceedings of the Institution of Mechanical Engineers Part C-Journal of Mechanical Engineering Science* 222(2):267-275.
6. Yu J, Banquy X, Greene GW, Lowrey DD, & Israelachvili JN (2012) The Boundary Lubrication of Chemically Grafted and Cross-Linked Hyaluronic Acid in Phosphate Buffered Saline and Lipid Solutions Measured by the Surface Forces Apparatus. *Langmuir* 28(4):2244-2250.
7. Ateshian GA, Wang HQ, & Lai WM (1998) The role of interstitial fluid pressurization and surface porosities on the boundary friction of articular cartilage. *Journal of Tribology-Transactions of the Asme* 120(2):241-248.
8. Swann DA, *et al.* (1974) Role of Hyaluronic-Acid in Joint Lubrication. *Annals of the Rheumatic Diseases* 33(4):318-326.

9. Greene GW, *et al.* (2011) Adaptive mechanically controlled lubrication mechanism found in articular joints. *Proceedings of the National Academy of Sciences* 108(13):5255-5259.

10. Swann DA, Silver FH, Slayter HS, Stafford W, & Shore E (1985) The Molecular-Structure and Lubricating Activity of Lubricin Isolated from Bovine and Human Synovial-Fluids. *Biochemical Journal* 225(1):195-201.

11. Schwarz IM & Hills BA (1998) Surface-active phospholipid as the lubricating component of lubricin. *British Journal of Rheumatology* 37(1):21-26.

12. Zappone B, Ruths M, Greene GW, Jay GD, & Israelachvili JN (2007) Adsorption, lubrication, and wear of lubricin on model surfaces: Polymer brush-like behavior of a glycoprotein. *Biophysical Journal* 92(5):1693-1708.

13. Zappone B, Greene GW, Oroudjev E, Jay GD, & Israelachvili JN (2008) Molecular aspects of boundary lubrication by human lubricin: Effect of disulfide bonds and enzymatic digestion. *Langmuir* 24(4):1495-1508.

14. Freeman MAR, Little TD, & Swanson SAV (1970) Lubrication of Synovial Joints - Possible Significance of Fat. *Proceedings of the Royal Society of Medicine-London* 63(6):579-581.

15. Forster H & Fisher J (1996) The influence of loading time and lubricant on the friction of articular cartilage. *Proc Inst Mech Eng H* 210(2):109-119.

16. Linn FC (1968) Lubrication of animal joints. II. The mechanism. *Journal of Biomechanics* 1(3):193-205.

17. Benz M, Chen NH, & Israelachvili J (2004) Lubrication and wear properties of grafted polyelectrolytes, hyaluronan and hylan, measured in the surface forces apparatus. *Journal of Biomedical Materials Research Part A* 71A(1):6-15.

18. Schmidt TA, Gastelum NS, Nguyen QT, Schumacher BL, & Sah RL (2007) Boundary lubrication of articular cartilage: role of synovial fluid constituents. *Arthritis Rheum* 56(3):882-891.

19. Benz M, Chen NH, Jay G, & Israelachvili JI (2005) Static forces, structure and flow properties of complex fluids in highly confined geometries. *Annals of Biomedical Engineering* 33(1):39-51.

20. Zappone B, Rosenberg KJ, & Israelachvili J (2007) Role of nanometer roughness on the adhesion and friction of a rough polymer surface and a molecularly smooth mica surface. *Tribology Letters* 26(3):191-201.

21. Jay GD, Torres JR, Warman ML, Laderer MC, & Breuer KS (2007) The role of lubricin in the mechanical behavior of synovial fluid. *Proceedings of the National Academy of Sciences of the United States of America* 104(15):6194-6199.

22. Drewniak EI, *et al.* (2012) Cyclic loading increases friction and changes cartilage surface integrity in lubricin-mutant mouse knees. *Arthritis and Rheumatism* 64(2):465-473.

23. Rhee DK, *et al.* (2005) The secreted glycoprotein lubricin protects cartilage surfaces and inhibits synovial cell overgrowth. *Journal of Clinical Investigation* 115(3):622-631.

24. Chang DP, Abu-Lail NI, Guilak F, Jay GD, & Zauscher S (2008) Conformational mechanics, adsorption, and normal force interactions of lubricin and hyaluronic acid on model surfaces. *Langmuir* 24(4):1183-1193.

25. Jay GD, Harris DA, & Cha CJ (2001) Boundary lubrication by lubricin is mediated by O-linked beta(1-3)Gal-GalNAc oligosaccharides. *Glycoconjugate Journal* 18(10):807-815.

26. Nakajima N & Ikada Y (1995) Mechanism of Amide Formation by Carbodiimide for Bioconjugation in Aqueous-Media. *Bioconjugate Chemistry* 6(1):123-130.

27. Follain N, Montanari S, Jeacomine I, Gambarelli S, & Vignon MR (2008) Coupling of amines with polyglucuronic acid: Evidence for amide bond formation. *Carbohydrate Polymers* 74(3):333-343.

28. Danishef.I & Siskovic E (1971) Conversion of Carboxyl Groups of Mucopolysaccharides into Amides of Amino Acid Esters. *Carbohydrate Research* 16(1):199-&.

29. Luengo G, Tsuchiya M, Heuberger M, & Israelachvili J (1997) Thin film rheology and tribology of chocolate. *Journal of Food Science* 62(4):767-812.

30. Luengo G, Israelachvili J, & Granick S (1996) Generalized effects in confined fluids: New friction map for boundary lubrication. *Wear* 200(1-2):328-335.

31. Zeng HB, Tian Y, Zhao BX, Tirrell M, & Israelachvili J (2009) Friction at the Liquid/Liquid Interface of Two Immiscible Polymer Films. *Langmuir* 25(9):4954-4964.

32. Min YJ, Akbulut M, Prud'homme RK, Golan Y, & Israelachvili J (2008) Frictional Properties of Surfactant-Coated Rod-Shaped Nanoparticles in Dry and Humid Dodecane. *Journal of Physical Chemistry B* 112(46):14395-14401.

33. Israelachvili J, *et al.* (2010) Recent advances in the surface forces apparatus (SFA) technique. *Reports on Progress in Physics* 73(3).

34. Heuberger M, Luengo G, & Israelachvili J (1997) Topographic information from multiple beam interferometry in the surface forces apparatus. *Langmuir* 13(14):3839-3848.

35. Luengo G, Schmitt FJ, Hill R, & Israelachvili J (1997) Thin film rheology and tribology of confined polymer melts: Contrasts with bulk properties. *Macromolecules* 30(8):2482-2494.

36. Wang YJ, *et al.* (2009) A study on the performance of hyaluronic acid immobilized chitosan film. *Biomedical Materials* 4(3).

37. Tadmor R, Chen NH, & Israelachvili JN (2003) Thickness and refractive index measurements using multiple beam interference fringes (FECO). *Journal of Colloid and Interface Science* 264(2):548-553.

38. Liu AJ & Nagel SR (2001) *Jamming and rheology : constrained dynamics on microscopic and macroscopic scales* (Taylor & Francis, London ; New York) pp xv, 551 p.

39. McGuiggan PM, Gee ML, Yoshizawa H, Hirz SJ, & Israelachvili JN (2007) Friction studies of polymer lubricated surfaces. *Macromolecules* 40(6):2126-2133.

40. Klein J, *et al.* (1993) Lubrication Forces between Surfaces Bearing Polymer Brushes. *Macromolecules* 26(21):5552-5560.

41. Gee ML, Mcguiggan PM, Israelachvili JN, & Homola AM (1990) Liquid to Solid-Like Transitions of Molecularly Thin-Films under Shear. *Journal of Chemical Physics* 93(3):1895-1906.

42. Demirel AL & Granick S (1996) Glasslike transition of a confined simple fluid. *Physical Review Letters* 77(11):2261-2264.

8. MUSSEL-INSPIRED COMPLEX COACERVATE PROVIDE WEAR PROTECTION TO SURFACES

8.1 Abstract

Complex coacervation is an appealing mechanism for application of underwater adhesives. Coacervates can deliver concentrated polyelectrolytes to surfaces without being diluted or washed away by water and exhibit other qualities conducive to underwater adhesion such as shear thinning, which may help the glue to be extruded; low interfacial energy, which promotes spreading and low viscosity, for ease of application and cross-linking. Mytilus californianus foot protein 1 (mcfp-1) is a natural coating protein found in the cuticle of California mussel byssus threads. The mussel cuticle protects the protease-sensitive collagenous core and is hard, yet extensible. Although it remains unclear whether mussels use coacervation for byssal thread formation, we show that the native mussel protein, mcfp-1, and a surrogate poly-anion, hyaluronic acid (HA), form a complex coacervate. We determined the optimal conditions for coacervation using microscopy techniques, and investigated the interfacial and rheological properties of the optimized, suboptimized and recombinant protein coacervate with a modified surface forces apparatus (SFA). Our work shows that mcfp-1/HA coacervates have a low coefficient of friction (μ ~ 0.3) and excellent wear protection (no damage for loads, $F_{\perp}$< 300 mN). Recombinant mfp1 ($r_{0.2}$mfp1)/HA coacervate exhibits a comparable coefficient of friction (μ ~ 0.3) but shows smaller wear

protection performance (damage at $F_{\perp}$ > 60 mN). The difference likely resides in the post-translational modifications and size of the natural protein. We also show that the 3, 4-dihydroxyphenylalanine (Dopa) residues in $r_{0.2}$mfp1 plays an important role in conferring wear protection to surfaces during shearing and absence of Dopa in the protein results in surface damage at $F_{\perp}$ > 10 mN.

8.2 Introduction

California mussels (*Mytilus californianus*) live a sedentary life “in the fast lane” - on wind and wave-swept shores where wave velocities reach 20-50 m/s (1). A fibrous holdfast known as the byssus (plaque and the thread) mediates the sessile attachment (Fig. 8.1) and resists dislodgement by wave-associated lift and drag forces. Adaptations at multiple length scales have been shown to enhance holdfast tenacity against dislodgement primarily by dissipating energy. These include, but are not limited to, the radial distribution of thread attachment (2, 3), the spatulate morphology of plaques (4), the stiff to compliant gradient in each thread (5), and the reversible yield of threads in tension (6).

Although mussel tenacity is often assumed to result from adhesion forces, frictional forces are arguably more important than adhesion to holdfast performance in drag and lift and has been previously examined for ‘dry’ adhesive systems, e.g., gecko foot attachment to surfaces (7, 8). Indeed, frictional forces are highly context dependent that can promote or subvert tenacity. On the helpful side, a single attached thread and plaque pulled at low angles to the surface (e.g. drag) resists detachment largely by frictional forces, whereas pulled normal to the surface (e.g. lift), a peeling mechanism triggers and causes easy detachment of the plaque from the surface (9, 10). The mussel byssal system is much more than a 'strong

glue'. Hierarchical structures impart toughness and durability and structural interfaces of consideration. Another structure showcasing frictional forces and appropriate to the present study is the byssal cuticle, which is a 10-15 µm-thick coating present on the exterior surface of all threads. The cuticle is a bio-composite with hard spherical granules (diameter ~200 nm in *M. californianus* to ~800 nm in *M. edulis and M. galloprovincialis*) dispersed in a continuous compliant matrix (Fig. 8.1) (11). The cuticle is stiff (E_i 2 GPa) but surprisingly extensible (75 % in *M. edulis* and 120% in *M. californianus*) making it one of the most energy tolerant materials known. Three deleterious modes of friction in the cuticle are 1) abrasion by suspended sand along the exterior surface, 2) deformation of matrix next to granules within the coating, and 3) deformation of cuticle along the interface with the softer collagenous core (E_i 0.4 GPa) (Fig. 8.1) (12).

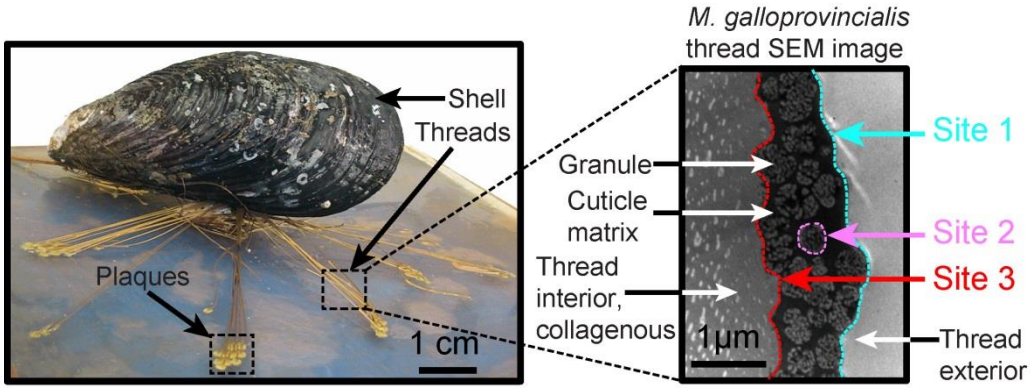

Figure 8.1 Schematics of a mussel (*left*) with the byssus (thread and plaque) securing the mussel shell to a mineral surface. Scanning electron microscope (SEM) image of a thread (*right*) showing the probable failure sites due to frictional stresses at the respective interface. Site 1: Sand-cuticle interface, Site 2: Granule-matrix interface, Site 3: thread interior (collagenous core)-cuticle matrix interface. The SEM image of the thread has been adopted from Ref. (12).

From a molecular perspective, *M. californianus* cuticle contains two proteins: 1) mussel foot protein-1 (mfp-1) is a highly modified, positively charged, intrinsically unstructured protein with 72 decapeptide repeats of the consensus sequence PKISYP**P*TY*K where P* is hydroxyproline, P** is dihydroxyproline and Y* is 3, 4-dihydroxyphenylalanine (Dopa) (13, 14); 2) the other protein is an acidic, chymotrypsin-labile and Ca-binding protein (15, 16) that may be related to the thread matrix protein-1 previously characterized (17). In the present study, we are assuming that cuticle formation by the mussel involves deposition of mfp-1 coacervated with acidic matrix protein to become the continuous matrix. The granules, in contrast, are formed by the condensation of mfp-1 by extensive Dopa-Fe^{3+}-coordination (18). Upon secretion, the matrix coalesces and coats the granules by coacervate driven phase separation of the charge neutralizing polyelectrolytes. In our coacervates, we opted for a polyanion that is acidic, binds calcium and has a mass that is well matched to mfp-1, namely hyaluronic acid (HA) (19, 20).

Despite the reversible deformation of cuticle in tension, the adaptive mechanisms that mitigate damage are unknown for this structure. To address the latter, we studied the effect of mfp-1, particularly in coacervated form, on friction between two mica surfaces in the surface forces apparatus (SFA). *M. californianus* mfp-1, optimally coacervated with hyaluronate, exhibited a friction coefficient of 0.3 and prevented surface damage to mica even at high compressive forces similar to the wear protection conferred by synovial fluid to mica (21). Unexpectedly, coacervated mfp-1 robustly mitigated surface damage to mica during shearing that is independent of the frictional coefficient and far surpasses the performance of coacervated recombinant analogs as well as un-coacervated mfps and hyaluronic acid (HA). Previous studies have shown coacervates to have considerable potential as vehicles for

fabricating new load-bearing materials (22, 23). Our results argue that, at least in optimized mcfp-1/HA coacervates, coacervates per se make significant and unappreciated contributions to damage mitigation to underlying surfaces during load bearing and suggest that achieving damage mitigation relies on careful coordination of interfacial energy, surface adhesion and coacervation.

8.3 Materials and Methods

8.3.1 Turbidimetric measurements of complex coacervates

Turbidimetric measurements were made to quantify coacervate yields under different solution conditions (Fig. 8.2a, b). Each solution was prepared by dissolving the polyelectrolyte (0.3 mg/ml) in sodium acetate buffer (10 mM and pH 3.7 or 4.7 either 10 or 60 mM NaCl). Optimal coacervation has been shown to occur with polymers of matching molecular weights (24). Therefore, $r_{0.2}$mfp-1, 14 KDa was paired with a 35 KDa version of HA whereas the native protein (mfp-1, 92 KDa) was matched with a 76 KDa HA (Lifecore Biomedical, Chaska, MN). The optimal mixing ratio was determined by addition of HA (0.3 mg/ml) into the protein solution (0.3 mg/ml) at varying molar ratios. Ionic strength dependence was investigated at 1:1 weight ratio of fp-1 to HA in 10mM sodium acetate/acetic acid buffer (pH 3.7) and adjusting the NaCl concentration. Charges on mfp-1 and HA at known pH were calculated from Lys pK_a= 10.5 and HA-COOH pK_a= 2.9 (25). Optical microscopy was used to confirm the coacervate phase in the solution (Fig. 8.2c). HA and mfp-1 were mixed just prior to injection (<1min) between a glass slide and coverslip separated by double-sided tape and coacervate formation was monitored with a Zeiss

Axioplan microscopicope equipped with an optronics macrofile CCD camera. Images were taken at 100X magnification 10 min post injection.

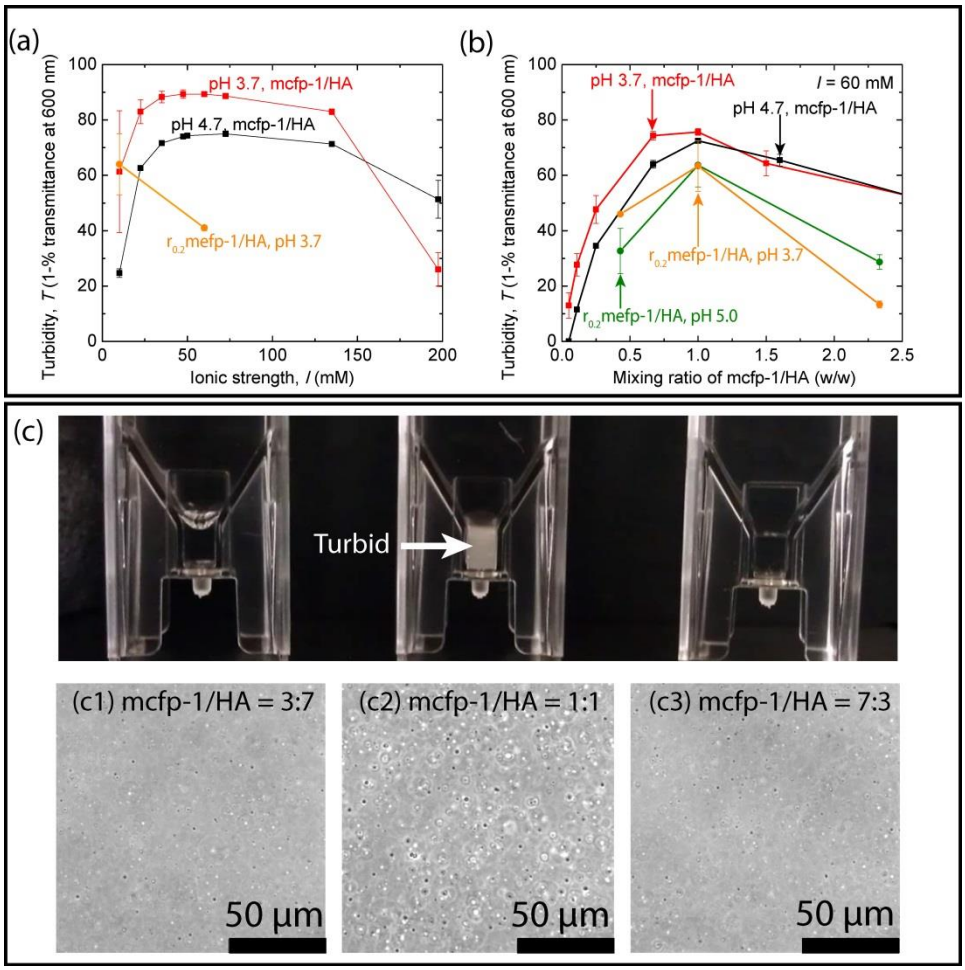

Figure 8.2 Turbidimetric optimization of the coacervation conditions. Coacervation optimization of mcfp-1 or $r_{0.2}$mfp-1 and HA was done with respect to (a) ionic strength and (b) mixing ratio (c) mcfp-1/HA coacervates in the turbidity measuring cell. Bright field images of mcfp-1/HA coacervates in solution with varying mixing ratios (c1) 3:7 (c2) 1:1 (c3) 7:3 mcfp-1/HA.

8.3.2 Measuring normal and lateral interactions

The surface forces apparatus (SFA, SurForce LLC, Santa Barbara) was used to measure the normal and lateral forces between two mica surfaces in a cross-cylindrical geometry as a function of the separation distance, *D*, between them and has been described in section 2.2 of this dissertation. 50–100 μL of coacervate (0.3 mg/mL) was pipetted onto one mica surface. As coacervate micro-droplets coalesced, the condensed coacervate settled onto the mica surface due to its higher density. The settlement effectively separates the dilute water phase from the denser coacervate. The normal forces were calculated from the deflection of a horizontal double cantilever spring to which the lower surface was attached. Lateral (or shear) movement of the bottom surface was accomplished with a bimorph slider, and the friction forces were measured using a friction device (See sec. 2.2). All experiments were performed at room temperature (23 °C).

8.4 Results

8.4.1 Coacervation between the poly-anion and poly-cation

Recombinant (rmefp-1/HA) and native (mcfp-1/HA) coacervate systems were optimized with regard to ionic strength, mixing ratio and pH using turbidimetric technique (Fig. 8.2). The recombinant protein was tested for coacervation with and without the enzymatic modification of tyrosine to Dopa to investigate the role of Dopa in the friction experiments that will be discussed later in this chapter. Both, native and recombinant coacervate systems showed optimal coacervation at a 1:1 (w/w) mixing ratio which corresponds to 0.71:1 cation: anion charge ratio. The native protein coacervated with HA over a wide range of ionic strength showing plateau in the measured turbidity from 40-140

mM NaCl (Fig. 8.2a). Since the rmefp-1 and HA displayed a decrease in turbidity on increasing the ionic strength of the solution from 10 mM to 60 mM NaCl, the optimal salt concentration was determined to be 10 mM (which is the salt concentration of the buffer solution).

8.4.2 Interfacial energy (γ_{eff}) of mcfp-1 and $r_{0.2}$mfp-1 based coacervates

The normal forces ($F_{\perp}$) normalized by the surface radius of curvature (R) were measured between mica surfaces physisorbed with mfp-1/HA coacervates to determine the interfacial energy and nature of physical interactions between the coacervate coated surfaces. Long ranged electrostatic forces are expected to play a minor role in the interaction between the surfaces due to the high ionic strength of the buffer solution (small Debye length < 1 nm). However, short ranged specific coulombic interactions between the poly-anions and poly-cations are persistent and responsible for the stability of the coacervate phase even under high ionic concentrations (I = 50-150 mM, the dispersion is turbid under these conditions, see Fig. 8.2).

The interfacial energy (γ_{eff}) was calculated from the force required to separate two coacervate coated surfaces (Fig. 8.3) and is given by $\gamma_{eff}=F_{ad}/3\pi R$ (10), where F_{ad} is the maximum value of the force required to separate the two surfaces (minima of the potential well of the F/R vs. D plot). The optimized (1:1 protein: HA) recombinant coacervate with Dopa showed higher γ_{eff} ($r_{0.2}$mfp-1-Dopa/HA, γ_{eff} =1.1 ± 0.2 mJ/m^2), compared to the optimized mcfp-1/HA (γ_{eff} = 0.4 ± 0.1 mJ/m^2) or $r_{0.2}$mfp-1/HA coacervate without Dopa (γ_{eff} = 0.5 ± 0.2 mJ/m^2) (Fig. 8.3a). However, the suboptimized mcfp-1/HA coacervate (3:7 or 7:3, mcfp-1:HA) showed γ_{eff} = 1.6 ± 0.2 mJ/m^2, which is significantly higher than that measured for any of the optimized coacervates (Fig. 8.3b). $R_{0.2}$mfp-1/HA coacervate showed

polymer mediated bridging interactions (26) between the surfaces only when Dopa residues were present in the protein (Fig. 8.3a). The native protein (mcfp-1)/HA coacervate always showed a dissipative-bridging adhesion between the surfaces regardless of the optimization conditions (Fig. 8.3b).

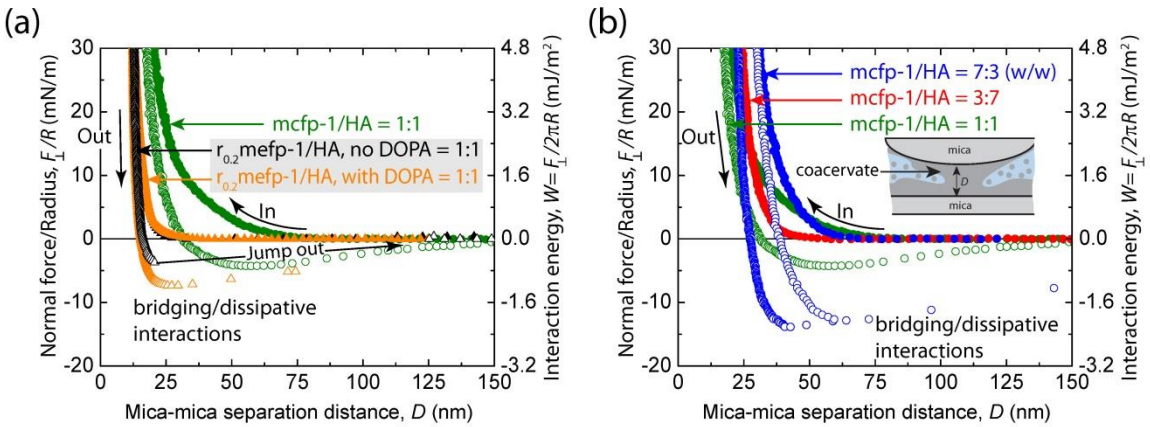

Figure 8.3 Representative normal force $F_\perp$ normalized by the surface radius of curvature R as a function of the mica-mica distance, D with physisorbed fp-1/HA coacervate on mica (a) Comparison between optimized mcfp-1/HA (green circles) and $r_{0.2}$mfp1/HA coacervates with (orange circles) and without (black circles) Dopa residues (b) Comparison between optimized (green circles) and suboptimized (mcfp-1/HA = 7:3 (blue circles) and 3:7 (red circles)) mcfp-1/HA coacervates.

8.4.3 Tribology of mcfp-1 and $r_{0.2}$mfp-1 based coacervates

Lateral (friction) force ($F_{||}$) increased linearly with increasing normal force ($F_\perp$) for all three coacervates (mcfp-1/HA, $r_{0.2}$mfp-1/HA and $r_{0.2}$mfp-1-Dopa/HA) during shearing at v = 100 μm/s and exhibited similar frictional coefficients ($\mu \sim 0.3$) (Fig. 8.4, inset). Despite the

observed damage in all but the mcfp-1/HA coacervates (see below), $F_{\parallel}$ vs. $F_{\perp}$ followed the same trajectory upon decreasing loads even following damage with $\mu \sim 0.3$.

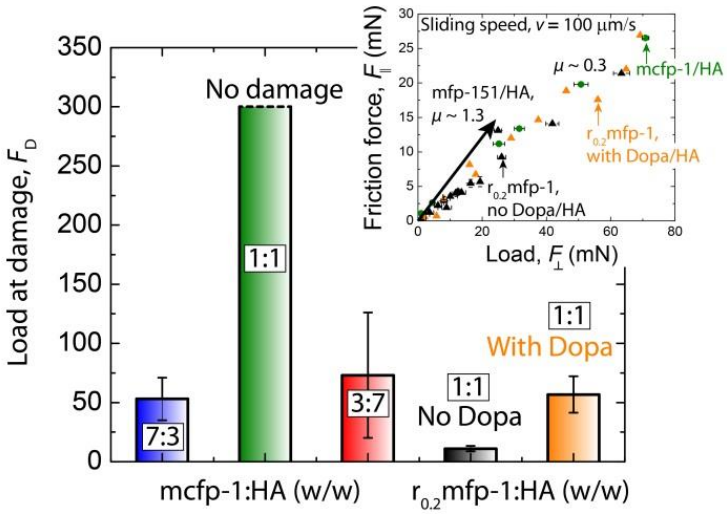

Figure 8.4 Wear protection of mfp-1/HA coacervates as demonstrated by the maximum load (F_D) the mica surfaces can withstand before shear induced damage. *Inset*: Friction force ($F_{\parallel}$) vs. the normal load ($F_{\perp}$) traces for the optimized mfp-1/HA coacervates. Mfp-151/HA coacervate friction trace showing μ = 1.3 for comparison (19).

The ability of a coacervate coating to protect the mica surfaces from wear was determined by the maximum load the surfaces could withstand before damage (F_D) during shearing. Wear of the surfaces was visualized from the shapes of the Fringes of Equal Chromatic Order (FECO) and the onset of wear is indicated by splitting of the FECO fringes (Fig. S8.1). Coacervates of mcfp-1/HA protected mica from detectable damage- even to the maximum applied load of 300 mN (Fig. 8.4), which corresponds to a pressure > 2MPa. In contrast, coacervates of $r_{0.2}$mfp-1/HA succumbed to damage under loads of F_D = 11 ± 3 mN, which improved 5-fold to F_D = 57 ± 18 mN using coacervates based on $r_{0.2}$mfp-1-Dopa/HA

(Fig. 8.4). Mcfp-1/HA coacervates were also tested for shear induced wear protection performance at suboptimized conditions (see Sec. 2.1, suboptimized poly-cation:poly-anion mixing ratio = 7:3 and 3:7). Suboptimized coacervates displayed damage at F_D = 53 ± 18 mN and 73 ± 53 mN for 7:3 mcfp-1/HA and 3:7 mcfp-1/HA mixing ratios, respectively. To summarize, although the friction coefficients between coacervate coated mica surfaces is the same, each coacervate shows different potentials in protecting mica from wear (Fig. 8.4).

8.5 Discussion

Frictional-adhesion (7, 27) plays a crucial role in the attachment of a mussel plaque to rock surfaces in the high energy intertidal zones. Frictional stresses can increase the force needed for detachment of the plaque from the surface by more than an order of magnitude but could also result in abrasive damage to the material. Resistance to shear-induced abrasive wear is essential for marine mussel attachment and the byssus has adapted a thin, hard coating to resist frictional damage from sand particles suspended in the ocean. However, having a hard cuticle to confer wear resistance raises concerns about other damage modes associated with the modulus mismatch between thread's soft cuticle and hard core as well as within the cuticle between the hard granule and soft matrix (Fig. 8.1).

To explore frictional damage mitigation and the potential contribution of complex coacervates in mussel byssus, cuticle matrix mimics were made by coacervating mcfp-1, isolated from *M. californianus*, as well as recombinant analogues ($r_{0.2}$mfp-1 and $r_{0.2}$mfp-1-Dopa) with HA, a commercially available, anionic, Ca^{2+}-binding glycosaminoglycan. Mfp-1/HA matrix-inspired blends were designed to be injectable, deliverable in a concentrated form underwater, and able to coat and protect surfaces. Coacervates of mcfp-1 and HA

showed wear protection to surfaces under 10-fold higher loads than coacervated recombinant analogues and 4-fold higher than suboptimized mcfp-1/HA coacervates (Fig. 8.4). This exceptional damage mitigation is not likely to be adventitious and its possible contribution to the mussel cuticle is discussed below.

Phase separation from bulk solution prevents material loss and allows for dense protein delivery underwater. Complex coacervation is a mechanism of phase separation that relies on charge-charge neutralization and therefore allows for concentrated delivery of charged polyelectrolytes. Coacervation of mcfp-1 and HA occurred immediately upon mixing and persisted over a 10-fold range of salt concentrations, at all polyelectrolyte mixing ratios, and over the tested pH range of 3.3-4.5. To my knowledge, this is the first report on the study of a complex coacervate using native mussel foot protein (mfp). The shorter and smaller $r_{0.2}$mfp-1 constructs both with and without Dopa coacervated with HA, but was more easily destabilized by salt than the mcfp-1 coacervate (Fig. 8.2). The greater salt tolerance of the native protein-HA coacervate may be due to the difference in molecular weights between the native and recombinant proteins ($MW_{mcfp\text{-}1}$ = 92 KDa vs. $MW_{r_{0.2}mfp\text{-}1}$ = 14 KDa). Complex coacervation is less entropically favorable at lower molecular weights (24, 28) suggesting that the entire sequence is important for coacervation. However, both mcfp-1 and $r_{0.2}$mfp-1 coacervate systems allow for concentrated material delivery underwater.

Coating granules, drugs, or perfumes depends critically on interfacial energy (γ_{eff}), and adhesion energy (W_{ad}). In the present context, γ_{eff} denotes the energy required to rupture the coacervate and create new, solvent exposed surface. The low γ_{eff} for a coacervate fluid measured in our study ($\gamma_{eff} \leq 0.5 mJ/m^2$) make mfp-1 containing coacervates ideal for spreading and coating surfaces (29). The efficient spreading and coating of mfp-1 based

coacervates (confirmed by smooth FECO in the SFA, See Fig. S8.1) on mica is reminiscent of granule-matrix configuration in the cuticle.

Native byssal cuticle is well adapted for resisting a variety of modes of frictional wear (as presented in Fig. 1). Indeed, native mcfp-1/HA coacervates mitigate frictional damage to mica surfaces even at normal loads of 300 mN (P > 2 MPa) suggesting that the matrix may plays a crucial role in shear induced damage mitigation in the cuticle. This was unexpected for two reasons: 1) a comparatively high frictional coefficient μ = 0.3 was observed for all coacervates of mfp-1 and HA (synovial fluid, the joint lubricant, has $\mu \sim$ 0.15 in the SFA and provides shear induced wear protection to mica) (21), but also, 2) unlike mature cuticle, these coacervates are still uncross-linked. These results show that a fluid can exhibit wear protection to surfaces regardless of the friction coefficient. It should also be noted that cross-linking of the mfp-1/HA coacervate by metal cation (e.g., Fe^{3+}) could improve the elastic properties of the material and more closely mimic the cuticle matrix. However, in this work, we demonstrate the wear protection performance of an uncross-linked coacervate.

The friction coefficient, μ, is increasingly questioned as a valid measure of surface damage. Several studies of lubricants with low μ, have reported extensive damage to mica (30-32). Indeed, that mfp-1/HA coacervates made from native and recombinant proteins all have μ = 0.3, yet vary >10-fold in damage mitigation, supports the notion that μ is not relevant to damage and has been reported previously (31, 33). Instead, damage mitigation by lubricants seems to be related to how well they adhere to surfaces. Grafting of polymers to surfaces has shown to be essential for improving wear protection during shearing (31). Lubricants with engineered covalent or non-covalent affinity tethers significantly reduce surface damage (34).

Mfps adheres to mica through bidentate hydrogen bonding of the Dopa residue to the siloxane interface and electrostatic interaction of the positively charged lysine with negatively charged mica interface. In the absence of Dopa, $r_{0.2}$mfp-1 is unable to coat mica effectively since the lysine moieties are recruited in forming coacervate with HA. Hence, shearing the surfaces with non-Dopa-lated $r_{0.2}$mfp-1 causes the frictional stresses to act directly on mica and damage the surface. The surface damage occurs at a low shearing loads ($F_{\perp}$ < 10 mN) since mica is unable to endure shear stresses (35) and hence a good candidate for measuring wear protection performance of the coacervates. Dopa containing $r_{0.2}$mfp-1/HA coacervate redistributes with $r_{0.2}$mfp-1-Dopa bound to the surfaces and $r_{0.2}$mfp-1-Dopa/HA coacervate sandwiched in between. This would result in the formation of a tough mfp-1 protein coating or a molecular kevlar on the surface of mica and the frictional stresses will be dissipated in the HA-layer bound to mfp-1 through specific coulombic interactions (Fig. 8.5). Thus, Dopa containing $r_{0.2}$mfp-1 confers superior shear induced wear protection (F_D < 60 mN) to mica compared to the protein without Dopa (F_D < 10 mN). It should also be noted that $r_{0.2}$mfp-1-Dopa coacervate shows a bridging interaction between the coating films (Fig. 8.3) and results in the dissipation of shear stresses in the entangled polymer network (Fig. 8.5) unlike $r_{0.2}$mfp-1 (no Dopa)/HA coacervate that shows a sharp jump out instability.

The native mcfp-1/HA coacervate showed outstanding wear protection (no wear recorded) to the surface and is due to the high Dopa content (~92 Dopa residues, hence superior adhesion to mica) and comparatively bigger size ($MW_{mcfp\text{-}1}$ = 92KDa vs. $MW_{r_{0.2}mfp\text{-}1}$ = 14KDa) than its recombinant analogue. Hence, it is unreasonable to compare the properties of the native mcfp-1/HA to $r_{0.2}$mfp-1-Dopa/HA coacervate. In this spirit, we compare the sub-optimized native mcfp-1/HA coacervate, which showed significantly poorer wear

protection to mica, with the optimized coacervate. This behavior can be explained based on the adhesion contribution to the shear stress at the interface. The sub-optimized mcfp-1/HA coacervate has excess mcfp-1 or HA depending on the mixing ratios. The protein (mcfp-1) or the polysaccharide (HA) that is not involved in charge-charge neutralization (coacervate formation) is now involved in entanglement (through van der Waals, electrostatic and hydrophobic interactions) with the polymers on the opposing surface and results in a significantly higher bridging-adhesion (or cohesion) between the surfaces. This is evident from the high work of adhesion, $W_{ad} = 2\ \gamma_{eff} = 3.2$ mJ/m^2 measured between the sub-optimized coacervates (Fig. 8.3b). Hence, although the sub-optimized coacervates show dissipative-bridging interactions, strong adhesion between the surfaces overwhelms and causes the shear stresses to migrate to the mica surface resulting in damage during shearing. The above results are also in agreement with a similar wear protection mechanism conferred by synovial protein lubricin in synergy with HA (either grafted or physisorbed to mica) (31) where adhesion contribution to friction between HA films is mitigated by lubricin. To summarize, matrix-inspired blends are deliverable in a concentrated form underwater and are able to spread, coat and protect surfaces from wear.

Cuticle matrix proteins are thought to undergo cross-linking by Ca^{2+} and Fe^{3+} complexation (18, 36). As no such processing was included in our mfp-1/HA coacervates, they were not expected to show compressive load-bearing properties. The excellent mitigation of frictional damage by coacervates of mcfp-1/HA raises the interesting possibility that maintaining coacervates in all or part of the cuticle matrix could be adaptively beneficial to damage control as well as self-healing (fluids spontaneously self-heal). Our results reveal a significant untapped potential for coacervates in applications that require both adhesion and

lubrication. Such applications include artificial joints, contact lenses, dental sealants, and hair and skin conditioners.

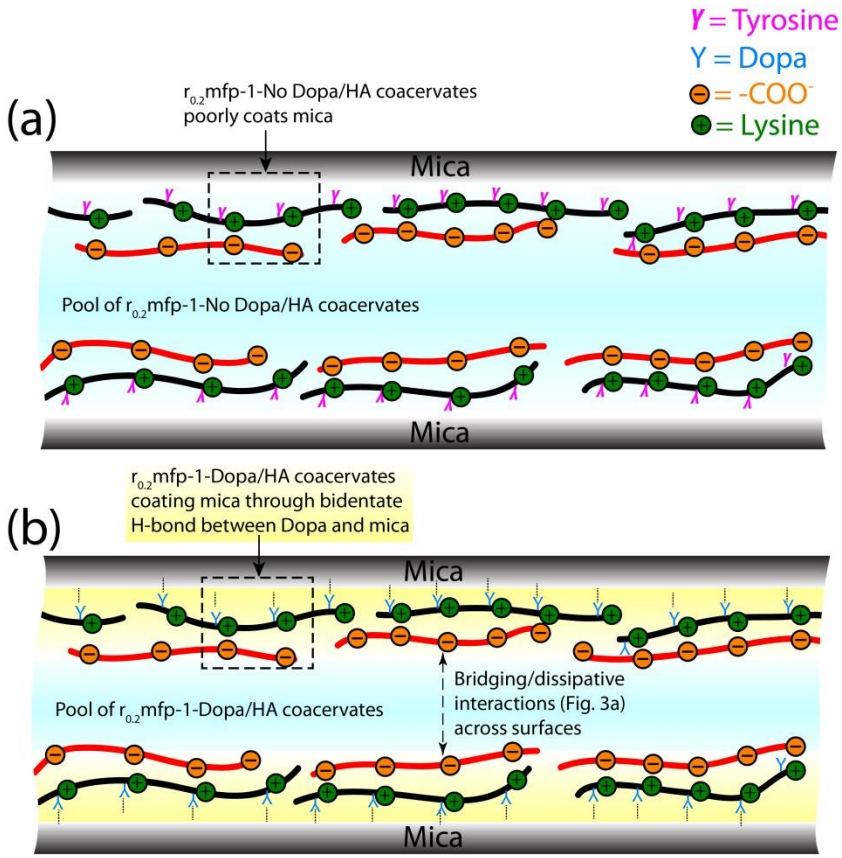

Figure 8.5 Schematics of the (a) $r_{0.2}$mfp-1-No Dopa/HA and (b) $r_{0.2}$mfp-1-Dopa/HA coacervates between mica surfaces. Dopa anchors the coacervate to the surface (Yellow shaded region) and shields it from shear stresses thus protecting the surface from shear induced damage at high loads (F_D < 60 mN) unlike the recombinant protein-No Dopa/HA coacervate (F_D < 10 mN).

8.6 Conclusions

Mussel cuticle matrix-inspired blends of mfp-1 and HA were shown to be deliverable in a concentrated form underwater (as complex coacervates), spread and coat surfaces ($\gamma_{eff} \leq$

1mJ/m^2) and serve to dissipate energy while protecting surfaces from wear. Exceptional damage mitigation of mcfp-1 containing coacervates against shear induced wear, even at normal pressures of P > 2 MPa ($F_\perp$ upto 300 mN in this work), suggests that coacervates can make significant and unappreciated contributions to damage mitigation during load bearing in the mussel byssus. We propose that during compression, coacervated mfp-1 and HA redistribute, mfp-1 binds preferentially to the surfaces due to the Dopa residues in the protein and mfp-1/HA coacervate sandwiched in between. In this way, the slip-plane is shifted up from the surface to the coacervate layer. In contrast, the coacervate layer, enriched as it is in highly hydrated HA, behaves as incompressible 'molecular ball bearings'. The wear protection in mcfp-1/HA coacervates suggests that retention of a fluidic component in the cuticular matrix may substantially contribute to damage mitigation in the mussel byssus.

8.7 Appendix

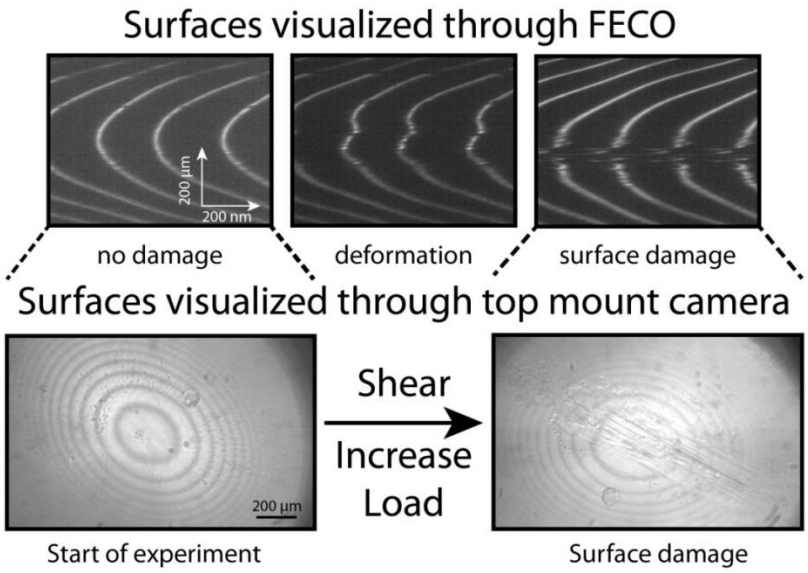

Figure S8.1 The mica surfaces coated with coacervate as visualized through FECO and top mount camera. The FECO view has ‘nm’ and ‘µm’ resolution along the horizontal and vertical direction respectively as shown in the figure (*top left*).

8.8 References

1. Denny M, Miller L, Stokes M, Hunt L, & Helmuth B (2003) Extreme water velocities: topographical amplification of wave-induced flow in the surf zone of rocky shores. *Limnology and Oceanography* 48(1; NUMB 1):1-8.
2. Bell EC & Gosline JM (1997) Strategies for life in flow: tenacity, morphometry, and probability of dislodgment of two Mytilus species. *Marine Ecology Progress Series* 159:197-208.
3. Qin Z & Buehler MJ (2013) Impact tolerance in mussel thread networks by heterogeneous material distribution. *Nature Communications* 4.
4. del Campo A, Greiner C, & Arzt E (2007) Contact shape controls adhesion of bioinspired fibrillar surfaces. *Langmuir* 23(20):10235-10243.
5. Bertoldi K & Boyce MC (2007) Mechanics of the hysteretic large strain behavior of mussel byssus threads. *Journal of Materials Science* 42(21):8943-8956.
6. Waite JH, Qin X-X, & Coyne KJ (1998) The peculiar collagens of mussel byssus. *Matrix Biology* 17(2):93-106.
7. Autumn K, Dittmore A, Santos D, Spenko M, & Cutkosky M (2006) Frictional adhesion: a new angle on gecko attachment. *Journal of Experimental Biology* 209(18):3569-3579.
8. Gravish N, *et al.* (2010) Rate-dependent frictional adhesion in natural and synthetic gecko setae. *Journal of the Royal Society Interface* 7(43):259-269.
9. Begley MR, Collino RR, Israelachvili JN, & McMeeking RM (2013) Peeling of a tape with large deformations and frictional sliding. *Journal of the Mechanics and Physics of Solids* 61(5):1265-1279.

10. Israelachvili JN (2011) Intermolecular and Surface Forces, 3rd Edition. *Intermolecular and Surface Forces, 3rd Edition*:1-674.

11. Harrington MJ & Waite JH (2007) Holdfast heroics: comparing the molecular and mechanical properties of Mytilus californianus byssal threads. *Journal of Experimental Biology* 210(24):4307-4318.

12. Holten-Andersen N, Fantner GE, Hohlbauch S, Waite JH, & Zok FW (2007) Protective coatings on extensible biofibres. *Nature Materials* 6(9):669-672.

13. Waite JH, Housley TJ, & Tanzer ML (1985) Peptide Repeats in a Mussel Glue Protein - Theme and Variations. *Biochemistry* 24(19):5010-5014.

14. Taylor SW, Waite JH, Ross MM, Shabanowitz J, & Hunt DF (1994) Trans-2, 3-cis-3, 4-dihydroxyproline, a new naturally occurring amino acid, is the sixth residue in the tandemly repeated consensus decapeptides of an adhesive protein from Mytilus edulis. *Journal of the American Chemical Society* 116(23):10803-10804.

15. Holten-Andersen N, Zhao H, & Waite JH (2009) Stiff Coatings on Compliant Biofibers: The Cuticle of Mytilus californianus Byssal Threads. *Biochemistry* 48(12):2752-2759.

16. Zuccarello LV (1981) Ultrastructural and cytochemical study on the enzyme gland of the foot of a mollusc. *Tissue and Cell* 13(4):701-713.

17. Sagert J & Waite JH (2009) Hyperunstable matrix proteins in the byssus of Mytilus galloprovincialis. *Journal of Experimental Biology* 212(14):2224-2236.

18. Harrington MJ, Masic A, Holten-Andersen N, Waite JH, & Fratzl P (2010) Iron-Clad Fibers: A Metal-Based Biological Strategy for Hard Flexible Coatings. *Science* 328(5975):216-220.

19. Hwang DS, *et al.* (2010) Viscosity and interfacial properties in a mussel-inspired adhesive coacervate. *Soft Matter* 6(14):3232-3236.

20. Hwang DS, Waite JH, & Tirrell M (2010) Promotion of osteoblast proliferation on complex coacervation-based hyaluronic acid–recombinant mussel adhesive protein coatings on titanium. *Biomaterials* 31(6):1080-1084.

21. Banquy X, Lee DW, Das S, Hogan J, & Israelachvili JN (2014) Shear-Induced Aggregation of Mammalian Synovial Fluid Components under Boundary Lubrication Conditions. *Advanced Functional Materials*.

22. Urry D, Harris R, & Long M (1981) Compounding of elastin polypentapeptide to collagen analogue: a potential elastomeric prosthetic material. *Artificial Cells, Blood Substitutes and Biotechnology* 9(3):181-194.

23. Urry DW (1984) Elastomeric composite material comprising a polypeptide. (Google Patents).

24. Chollakup R, Beck JB, Dirnberger K, Tirrell M, & Eisenbach CD (2013) Polyelectrolyte molecular weight and salt effects on the phase behavior and coacervation of aqueous solutions of poly (acrylic acid) sodium salt and poly (allylamine) hydrochloride. *Macromolecules* 46(6):2376-2390.

25. Reed CE, Li X, & Reed WF (1989) The effects of pH on hyaluronate as observed by light scattering. *Biopolymers* 28(11):1981-2000.

26. Das S, Donaldson SH, Kaufman Y, & Israelachvili JN (2013) Interaction of adsorbed polymers with supported cationic bilayers. *Rsc Advances* 3(43):20405-20411.

27. Das S, *et al.* (2013) JKR Theory for the Stick Slip Peeling and Adhesion Hysteresis of Gecko Mimetic Patterned Surfaces with a Smooth Glass Surface. *Langmuir* 29(48):15006-15012.

28. Wang Y, Kimura K, Dubin PL, & Jaeger W (2000) Polyelectrolyte-micelle coacervation: effects of micelle surface charge density, polymer molecular weight, and polymer/surfactant ratio. *Macromolecules* 33(9):3324-3331.

29. Priftis D, Farina R, & Tirrell M (2012) Interfacial Energy of Polypeptide Complex Coacervates Measured via Capillary Adhesion†. *Langmuir* 28(23):8721-8729.

30. Homola AM, Israelachvili JN, McGuiggan PM, & Gee ML (1990) Fundamental experimental studies in tribology: the transition from "interfacial" friction of undamaged molecularly smooth surfaces to "normal" friction with wear. *Wear* 136(1):65-83.

31. Das S, *et al.* (2013) Synergistic Interactions between Grafted Hyaluronic Acid and Lubricin Provide Enhanced Wear Protection and Lubrication. *Biomacromolecules* 14(5):1669-1677.

32. Yu J, Banquy X, Greene GW, Lowrey DD, & Israelachvili JN (2011) The boundary lubrication of chemically grafted and cross-linked hyaluronic acid in phosphate buffered saline and lipid solutions measured by the surface forces apparatus. *Langmuir* 28(4):2244-2250.

33. Lee DW, *et al.* (2014) Effects of molecular weight of grafted hyaluronic acid on wear initiation. *Acta Biomaterialia* 10(5):1817-1823.

34. Singh A, *et al.* (2014) Enhanced lubrication on tissue and biomaterial surfaces through peptide-mediated binding of hyaluronic acid. *Nature Materials*.

35. Liu Y, Wu T, & Evans DF (1994) Lateral force microscopy study on the shear properties of self-assembled monolayers of dialkylammonium surfactant on mica. *Langmuir* 10(7):2241-2245.

36. Taylor SW, Chase DB, Emptage MH, Nelson MJ, & Waite JH (1996) Ferric ion complexes of a DOPA-containing adhesive protein from Mytilus edulis. *Inorganic Chemistry* 35(26):7572-7577.

9. ENGINEERING SOLUTIONS FOR APPLICATIONS

In the previous chapters, we encountered many different biological and synthetic systems mimicking nature and discussed the possible mechanisms that govern the interaction between proteins, polymers and surfaces. The underwater adhesive mechanisms of mussel foot proteins (mfps) excited numerous scientists in the last decade to overcome fundamental challenges to engineer durable adhesion in a wet environment. Mfp-5 exhibited the highest interaction energy (1) with highest catechol contents (up to ~30%) among the mfps and mfp-3 has shown a capability of self-coacervation, a critical step for mussels to deliver mfps as a fluid phase underwater (2). Although materials with self-mending and adhesive properties have been engineered by means of mussel-inspired, metal-chelating catechol-functionalized polymer network, biological adhesion in wet conditions, as occurs in self-assembled holdfast proteins in mussels is due to factors beyond Dopa chemistry as shown in chapter 4. Researchers have been successful in engineering bacteria to produce sticky proteins that show superior performance over that used by the marine mussels (3). However, they are limited by the quantity and the cost of the adhesive material that can be synthesized commercially. The performance of these adhesives was also not gauged to test the bonding strength between macro-scale (order of millimeter to centimeters) surfaces and demonstrate the binding efficacy of the wet super glue. Until date, to my knowledge, no one reported or

developed wet synthetic adhesive materials that can surpass the supreme sticking capability of the 'underwater glue' secreted by the marine mussels. In this chapter, I will introduce synthetic small single molecules mimicking the mussel foot proteins that can be used as underwater glue.

9.1 Small molecular underwater adhesives inspired by mussels

We recapitulated chemical features (e.g., hydrophobicity, aromaticity, and zwitterionic properties) of a mussel foot protein-5, mfp-5 (Mol. wt. ~10 kDa), in an order of magnitude smaller synthetic small molecules (Mol. wt. ~ 400 g/mol).

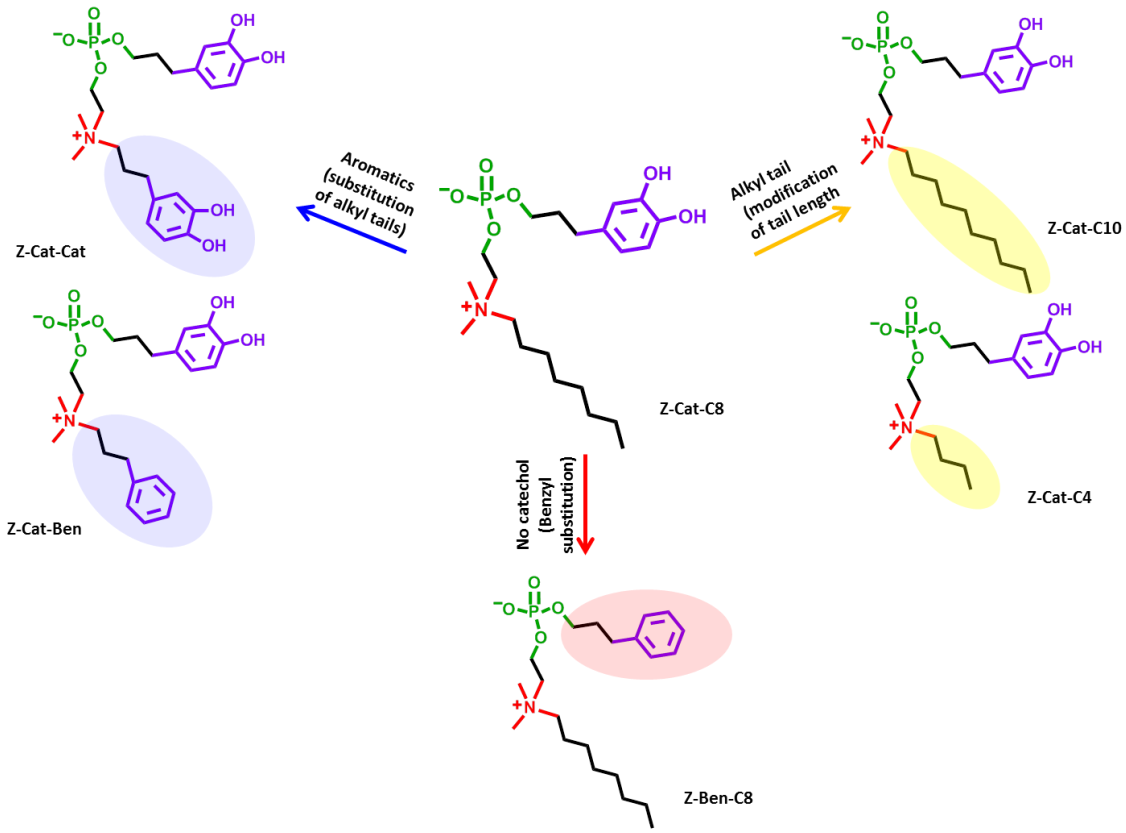

Figure 9.1 Small zwitterionic molecules inspired by mfp-5.

Six small molecules were designed and synthesized (Fig. 9.1) and aqueous colloidal dispersions were prepared for each molecule in deoxygenated deionized (DI) water (5 mM and 0.5 mM solutions). The interfacial properties of the aqueous colloidal dispersions was studies using the surface forces apparatus (SFA), quartz crystal microbalance with dissipation (QCM-D), atomic force microscopy (AFM), dynamic light scattering (DLS), cyclic voltammetry (CV), zeta-potential and surface tension measurements. In the following section, I will report a few characterization data for some of the synthetic molecules since this is a work still under progress.

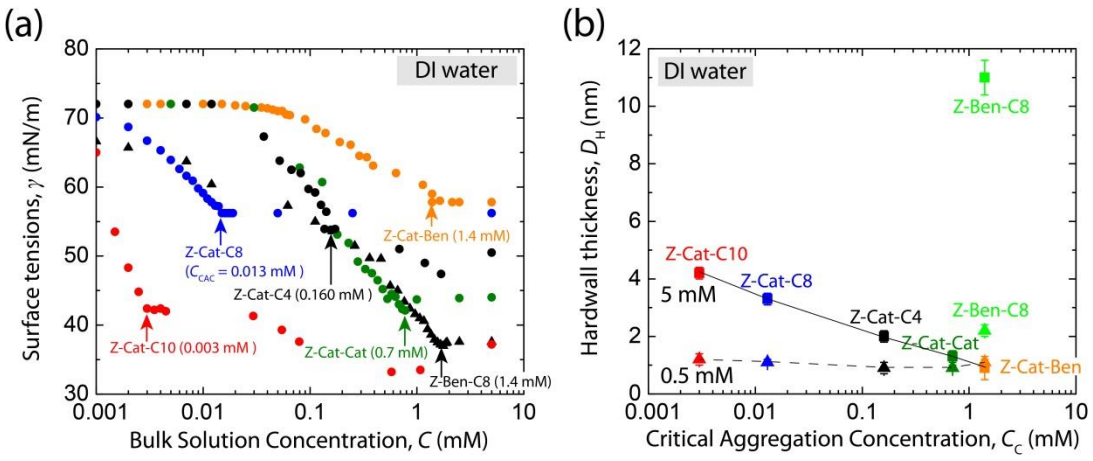

Figure 9.2 (a) Critical aggregation concentration (CAC) of the mussel-inspired small molecules (b) a plot of CAC vs. Hardwall thickness measured in the SFA.

The critical aggregation concentration of each sample was measured by the Wilhelmy plate technique (Fig. 9.2a). Decreasing hydrophobicity by reducing the alkyl tail length increases critical aggregation concentration (CAC) from C10 to C4. It should be noted that the molecule with 4 carbon tail length presumably does not aggregate and undergoes some phase transition giving rise to a peculiar shape of the surface tension vs. concentration plot.

Interestingly, increasing hydrophobicity by substitutions (1) of alkyl groups with aromatic groups and (2) of catechol with benzene increased CAC. The aggregation behavior of these molecules is still under investigation and transmission electron microscopy (TEM) will be used to visualize the structure of the aggregates to gain a fundamental insight of the self-assembly behavior of the material in dispersions.

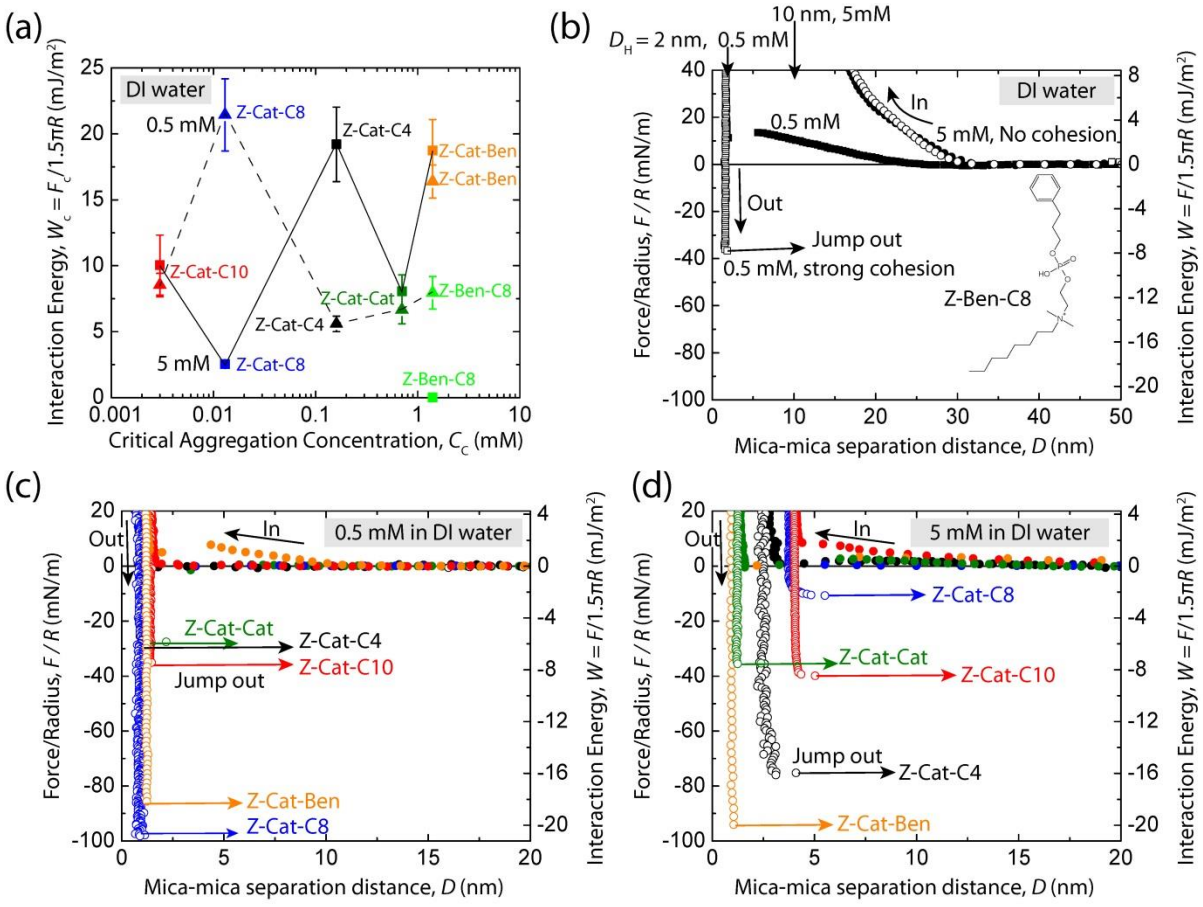

Figure 9.3 (a) A plot of interaction energy vs. CAC measured by SFA (b) Effect of deposition concentration on the normalized force-distance profiles of Z-Ben-C8. Force-distance profiles between mica surfaces deposited with Z-Cat-C8, -C10, -C4, -Cat, -Ben from (c) 0.5 mM and (d) 5 mM colloidal dispersion.

Preliminary SFA measurements (Fig. 9.3a) show that the adhesion energy between mica surfaces coated with the zwitterionic molecules is stronger than that measured for recently developed protein amyloid (3) that mimics the mussel foot adhesive proteins. The hardwall thickness (D_H), i.e., thickness of two absorbed molecular layers on the top and bottom mica surfaces in SFA deposited by dispersions of each molecule was measured. A plot of the hardwall thickness vs. CAC is shown in Fig. 9.2b. Z-Ben-C8 (without catechol) follows a regular bilayer absorption pattern of a general surfactant that forms bilayer (~ 1-2 nm) when its concentration is below CAC whereas that forms multilayers (4-5 nm) when its concentration is above CAC. On the other hand, catechol-carrying molecules show unique behavior that Z-Cat-C8 and Z-Cat-C10 formed ~ 1 nm thick monolayer both below and above CAC at 0.005 and 0.5 mM for Z-Cat-C8 and 0.001 mM and 0.5 mM for Z-Cat-C-10, respectively (note: the results for Z-Cat-C8 and Z-Cat-C10 below CAC are not shown in the figures since the study finished just now). However, when the concentration is orders of magnitude above CAC in 5 mM solution, Z-Cat-C8 form bilayers (~ 4 nm). At 5 mM concentrations, CAC of Z-Cat-C10, -C8, and -C4 were correlated to the hardwall thickness and hydrophobicity of the molecules, whereas 0.5 mM formed same ~ 1 nm hard wall (presumably ~0.5 nm thick monolayer on each side). More interestingly, the hardwall thicknesses of Z-Cat-Cat and Z-Cat-Ben were independent of CAC; monolayer formed regardless of concentration although the CAC of those is similar to CAC of Z-Ben-C8.

In cyclic voltammetry, the dispersions increase oxidative stability of catechol functionalities significantly compared to methyl catechol in DI water (no aggregation), suggesting unique shielding effects of the dispersion (Fig. 9.4). In fact, the redox stability of these molecules was superior to the mfps and peptides (see chapter 3 and 4). Zeta potentials

(ξ) of the dispersions also exhibit different surface charges and densities from -100 mV to 0 mV, suggesting different constructions of each molecular aggregates (e.g., $\xi_{\text{Z-Cat-C10}}$ = 0 mV, $\xi_{\text{Z-Cat-C8}}$ = -40 mV, $\xi_{\text{Z-Cat-Ben}}$ = -90 mV).

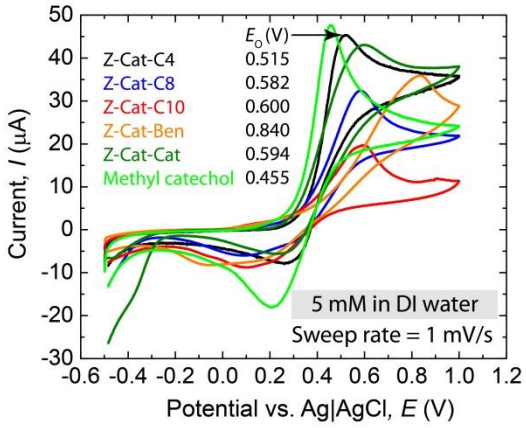

Figure 9.4 Cyclic voltammetry (CV) measurements on colloidal dispersions of 5 mM solution of the synthetic 'mfp-5 mimetic' molecules in DI water showing enhanced resistant to oxidation (increase in the oxidation potential, E_0) of the catechol residues in the molecules.

With regard to the interaction energy as measured by SFA, the catechol containing molecules behave differently from the control (Z-Ben-C8). Z-Ben-C8 shows general bilayer repulsion and jump-in patterns during the approach and separation of two surfaces (Fig. 9.3b) whereas catechol-containing molecules do not show a significant repulsion or no repulsion at all. In addition, interaction energy of Z-Cat-C10, Z-Cat-Cat, and Z-Cat-Ben are independent from the deposition concentration. Moreover, Z-Cat-C8 and Z-Cat-Ben exhibit very strong interaction energy when the deposition is done at ≤ 0.5 mM in DI water. QCM measurements show that all of these synthetic molecules adsorb strongly not only to titania (TiO_2) surface, but also to silica (SiO_2) surfaces unlike the mfps. AFM demonstrate that depositing the molecules at a lower concentration changes the coverage of the molecules on a mica surface

(Fig. 9.5). However, for similar deposition conditions, depending on the catechol content and length of the hydrocarbon tail, the molecules either formed a molecularly smooth defect free bilayer like surface or small pools of aggregates on mica.

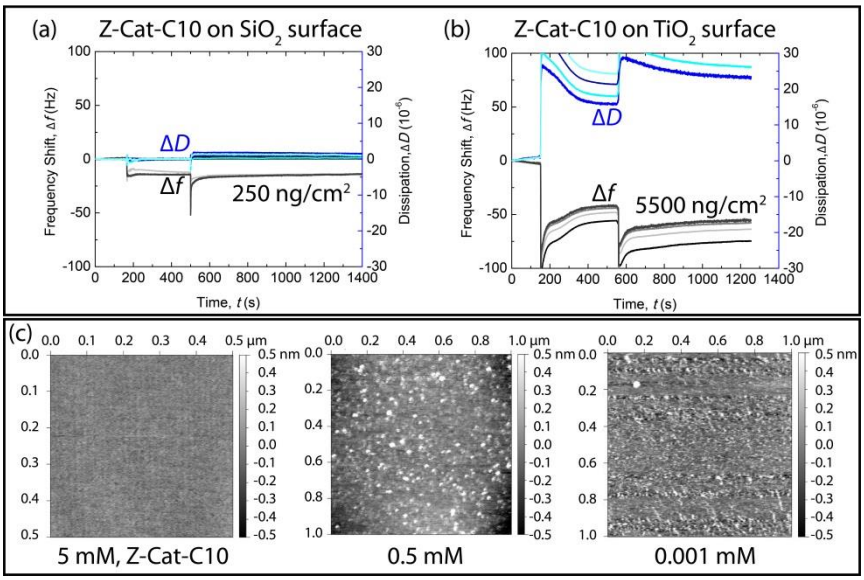

Figure 9.5 QCM-D experiments showing the adsorption of Z-Cat-C10 onto (a) SiO_2 and (b) TiO_2 surfaces. The dissipation (ΔD) of the adsorbed film of Z-Cat-C10 molecules did not change on silica surface (rigid film). However, the adsorbed layer on titania showed significant change in ΔD indicating the formation of a visco-elastic hydrated film. (c) AFM scans of a mica surface adsorbed with Z-Cat-C10 from a solution (in DI water) of varying concentrations (0.001-5 mM). At high deposition concentrations, the molecules form a defect free smooth bilayer on mica. Low deposition concentrations caused the molecules to form small aggregates on the surface. SFA measurements with Z-Cat-C10 showed that the adhesive interaction between two mica surfaces did not change for deposition of the molecules at C = 0.001 (< CAC of Z-Cat-C10, see Fig. 9.2a), 0.5 and 5 mM concentrations, however, the thickness of the adsorbed layer decreased progressively from ~ 4 nm to 1 nm respectively (Fig. 9.3c, d).

The adhesive strength of the synthetic molecules at the macro-scale was demonstrated by gluing two steel plates under water (Fig. 9.6a). One of the surfaces was coated with un-oxidized Z-Cat-C10 whereas the molecules on the other surface were deliberately oxidized with sodium periodate. The two steel plates were then pressed together underwater and allowed to heal for 10 min. This initiates the formation of cross-links (catechol cross-links with quinone) between the molecules on each surface and bonds the two surfaces firmly. Our macro-scale lab adhesion test showed that Z-Cat-C10 prevented the failure of the bond between the steel plates for a load upto 1.1 kg (Fig. 9.6a). As a control, the double sided scotch® tape from 3M could hold the steel plates only for a load upto 0.3 kg provided the surfaces were bonded under dry conditions (The scotch tapes does not perform under wet or moist environment).

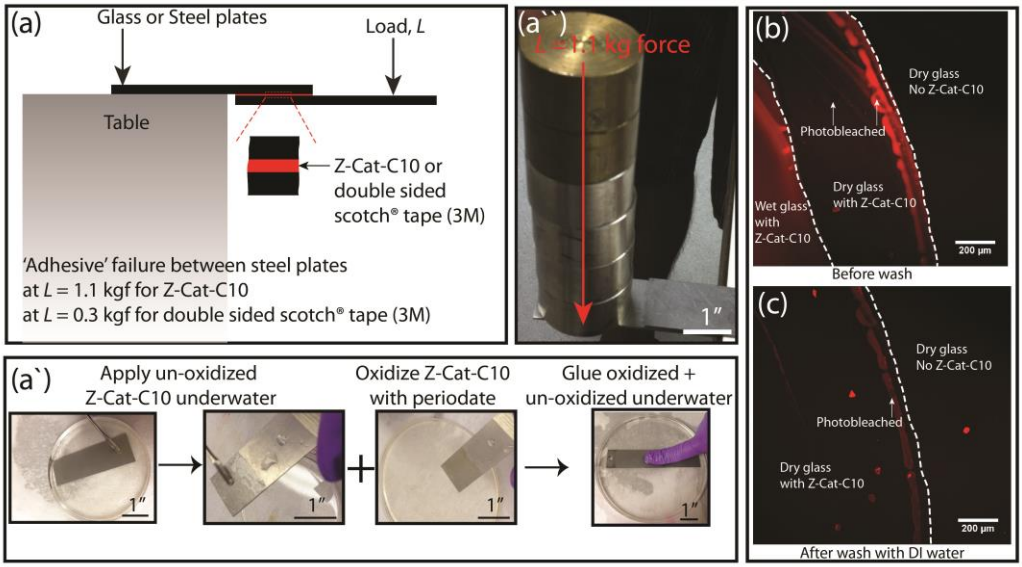

Figure 9.6 (a) A macro-scale lab adhesion test to show the bond strength between two steel plates glued underwater by Z-Cat-C10 (a`, a``) As a control, the same plates were glued outside water in dry atmosphere with a double sided scotch® tape from 3M and the load bearing tests were performed. Our synthetic molecule allowed the bond between the steel

plates to withstand ~3-4 times more load before failure compared to the scotch tape. Fluorescent images (a) of a silica surface coated with Z-Cat-C10 in DI water tagged with Rhodamine 6G (b) after washing the Z-Cat-C10 coated silica thoroughly with DI water. The mussel inspired single molecular adhesive is adhered to silica and is not washed off by water.

Z-Cat-C10 is also not washed off from a coated silica surface and is 'permanently' attached to it as shown in fig. 9.6b, c. This demonstrates that single molecular adhesives can serve as an inspiration for the development of underwater *Magic markers*. *Thus the synthetic wet adhesive molecules reported in this dissertation holds considerable promise for the design of tunable systems for applications in underwater protective coatings, medical adhesives and drug delivery*.

9.2 Gecko-mimetic: Prototype Foot-Placement for Robotic Applications

Understanding the factors, structures and materials that give rise to high adhesion and friction forces (both needed for moving on ceilings and walls) is essential for the development of gecko-mimetic robots. So far no one has been able to reproduce the behavior of a 'fully functioning gecko' (defined below), and in particular the way the gecko manages to combine the surface adhesion-friction properties of its toe pads (spatulae, seta, etc.) with the structure of the feet and body, as well as articulate the whole system (in space and time) to enable the gecko walk, run, or remain totally stationary (without slipping) on both walls and ceilings, both rough and smooth surfaces, of totally different compositions or chemistries, such as hydrophobic or hydrophilic. In addition, the gecko can move very rapidly (at meters/sec, taking 10 ms to grip or 'step down', and 10 ms to detach or 'step up') on both walls and ceilings, and in a very energy-efficient way. All of these features, appearing

together, are quite remarkable and quite unlike any normal 'good' adhesive tape or 'high friction' material. Below is a list of what I consider to be the essential properties for a 'fully functioning biomimetic gecko robot':

(1) *Switchable adhesion:* Rapid high adhesion and equally rapid detachment (low, zero or even negative adhesion, i.e., repulsion), via a mechanism that is independent of whether the surface is a wall (vertical) or horizontal (ceiling).

(2) *Switchable friction:* Similar to switchable adhesion, involving rapid high friction (lateral sticking) and equally rapid relaxation via peeling, bending or rolling away, again via a mechanism that works equally well on walls and ceilings. On the fundamental level, it is not always appreciated that high adhesion does not necessarily mean or lead to high friction, and vice versa. Thus, achieving aim (1) does not necessarily mean that aim (2) has also been achieved.

(3) *Low energy articulation:* That is, not energetically costly to run. Interestingly, an important (and also fundamental) challenge arises here when designing the 'ideal' robot, because while the energy dissipation (during a step cycle) must be low, the transient adhesion and friction forces must be high.

(4) *Satisfactory testing conditions (on different surfaces, environments), and some other essential requirements:* The device must work on both smooth and rough surfaces, on surfaces of quite different chemical compositions (e.g., both hydrophobic and hydrophilic), and in both dry and humid atmospheres. The pads must be self-cleaning, i.e., not pick up and retain dust particles.

On the macroscopic scale, in the area of device fabrication, Murphy et al. (4) demonstrated a robot that walks on walls, with symmetrical pillars (rather than asymmetric,

e.g., tilted, ones), with terminal flat ends. Such a device can only work on totally smooth surfaces, and is very energy-demanding since the full adhesion force and energy have to be overcome on detaching, as in Fig. 9.7a (which is a slow process due to the nature of the local elastic or viscoelastic deformation). Tsukagoshi et al. (5) demonstrated a device that is essentially a miniature car whose wheels are made of a soft elastomeric adhesive material. This device can roll on walls, but again at high energy cost because the back end of the rolling junction has to be continuously detached with a high 'rolling friction' energy, as in Fig. 9.7c. The device is also very slow due to the viscoelastic nature of the wheel material, which requires it to operate at low Deborah numbers or else the adhesion energy will exceed the thermodynamic value, often by as much as three orders of magnitude.

In spite of these advances, no fabricated surface or device currently successfully mimics the gecko's foot pads or articulates in the way the gecko does. And no device has yet been shown to function on both walls and ceilings, only on walls (except for a short time on ceilings before the adhesion is lost); and in any practical situation the battery will be too heavy or will soon run out of energy – probably the greatest current limitation of electric cars.

9.2.1 Fundamental scientific aspects of frictional-adhesion

Before my proposal to achieve a 'fully functioning' articulated device that satisfies the criteria (challenges) listed above, it is worth reflecting on some subtle but crucially important fundamental scientific aspects of the adhesion and friction forces and energies of different types of structures and materials that must be taken into account as we proceed. We must bear in mind that geckos spend time, as well as walk or run, on both walls (requiring high

friction) and ceilings (requiring high *adhesion*), and that these two are not generally simply related (6).

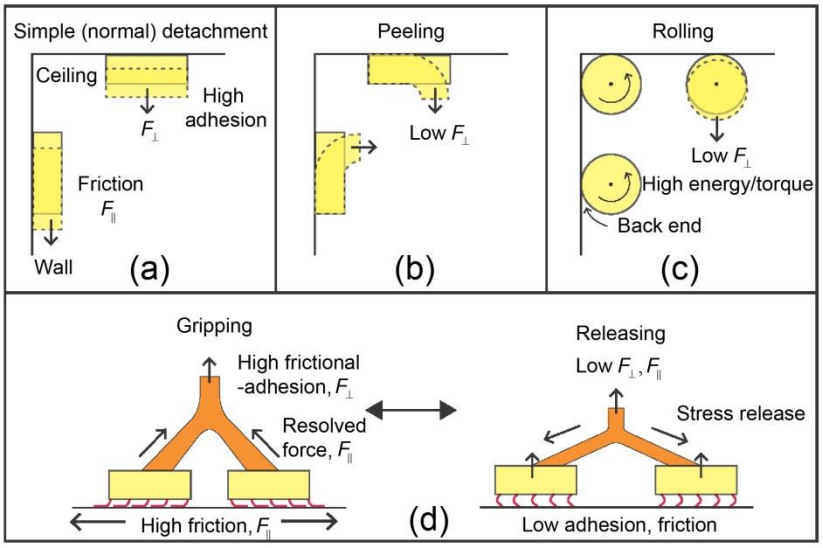

Figure 9.7 Different types of geometries and articulations where one surface moves (adheres, detaches, slides, peels, or rolls) along or away or between surfaces in the ways shown. Scenario (d) is the most promising one for a fully-functioning, low energy, biomimetic gecko device, as further discussed below. Gripping' corresponds to actuation with tilt/flat face and 'releasing' corresponds to actuation against tilt/curved face.

Of the 4 different mechanisms shown in Fig. 9.7, only that shown in panel (d) satisfies all the criteria for a single toe pad (the whole device is discussed later below). Thus, Fig. 9.7a – simple *detachment*, which is analogous to removing a rigid adhering ceramic plate, from strong adhesion and/or friction forces) is energetically very costly; Fig. 9.7b – *peeling* away, like an elastic tape, requires less force to detach, but both the adhesion and friction are now low and not easy to control; Fig. 9.7c – *rolling*: the viscoelastic nature of such materials make them slow and energetically very inefficient, where the adhesion energy

or force needed to lift the back end gives rise to high 'rolling friction' forces and energies). Such a structure will also slowly peel away from a ceiling and eventually fall detach (fall, as illustrated). Finally, Fig. 9.7d – *tilted structures* with anisotropic articulation: different *gripping* and *releasing* configurations allow for high frictional-adhesion on gripping, falling to almost zero on releasing on almost any surface, which can be carried out simply, rapidly, and requiring minimal energy/force to be articulated (see chapter 5 and 6 for frictional-adhesion properties of the tilted micro-flaps).

9.2.2 The solution: Proposed mechanisms and design features

While it may be too early to propose the ultimate (optimum) structure and articulation mechanism, I show in Fig. 9.8 one such device that appears to satisfy all the required conditions listed and discussed above, and that I believe is a scientifically sound and practically viable starting point.

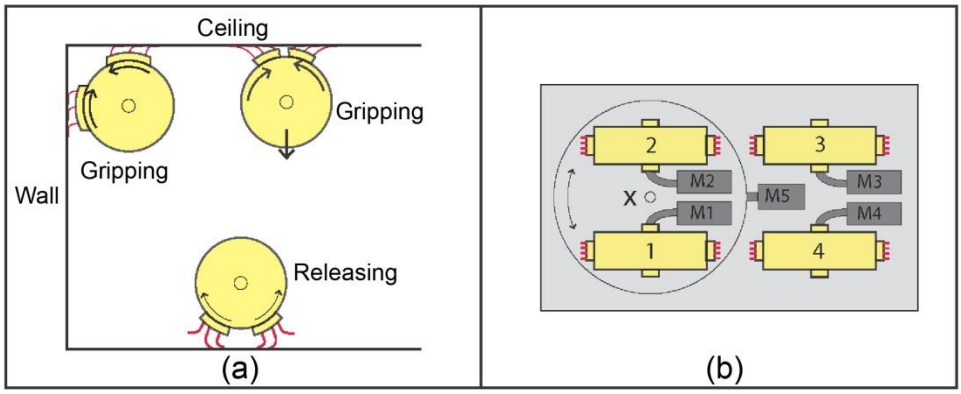

Figure 9.8 Proposed articulation of biomimetic gecko foot and its pads (a) and their integration into the whole device (b), exhibiting high frictional-adhesion for feet in the 'gripping mode' ((a), and foot-pads 1 and 3 in (b)), and low friction and adhesion when in the 'detachment/releasing' mode ((a), and feet 2 and 4 in (b)). In panel (b), motors M1-M4

control the feet and pads on 1 and 4, and motor M5 rotates the base supporting feet 1 and 2 about the axis X for turning and steering.

Figures 9.9 and 9.10 illustrate and summarize the most important features exhibited by geckos that are mimicked by the proposed mechanism of Fig. 9.7d. The proposed mechanisms nicely mimic, and are also a reflection of the repetitive/snake-like motion of geckos (Fig. 9.10b).

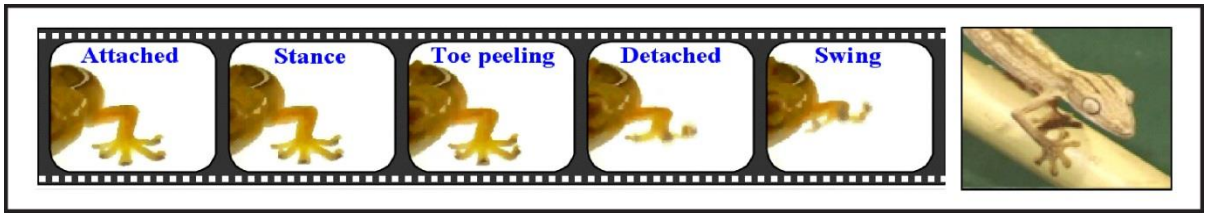

Figure 9.9 Important points to notice about the way a gecko positions itself and moves are illustrated in these snapshots of a gecko lifting its foot: (1) the body is low, close to the ground, allowing the gecko to apply a lateral (shear, frictional) force pulling its diagonally opposite feet together (the diagonally opposite foot not shown, but see Fig. 9.10a); (2) the toes on each foot radiate out in all directions, allowing the toes to be to be pulled inwards, but unable to move due to the high 'adhesion-controlled' (not load-controlled) 'frictional-adhesion' force, thereby providing good grip irrespective of whether the surface is vertical (a wall) or horizontal (a ceiling), at any angle, or even curved (see right panel). In the proposed design (Fig. 9.8a), two opposing toes, instead of five, per foot are suggested as being sufficient for this purpose; (3) to lift the foot the toes peel away (upwards) *from the tips* – a highly unusual mechanism, and on close examination, it is clear that the inward gripping stress is also released (reversed) during this process, as was illustrated schematically in Fig. 9.7d, suggesting that geckos employ both peeling and/or tension releasing on detaching the toe pads.

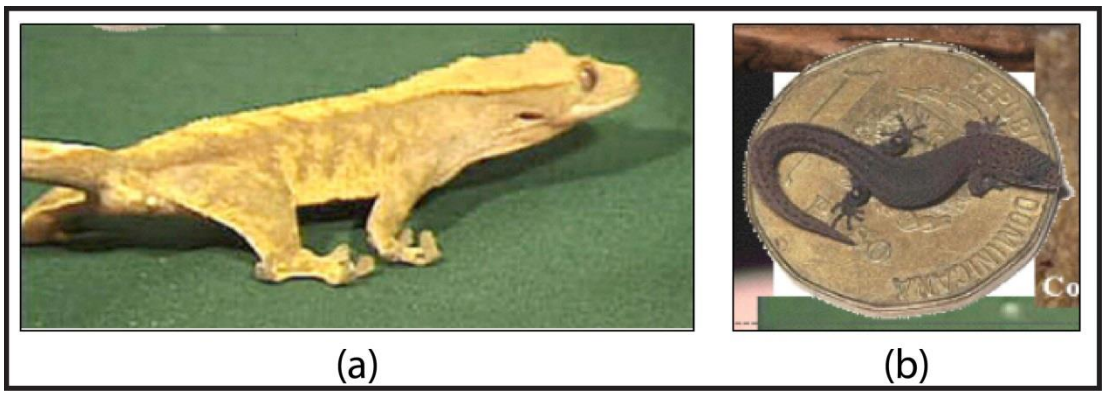

Figure 9.10 Further examples of the diagonally coordinated feet of geckos during the motion, especially when moving quickly. (a) Example of the peeling away of the tips of the toes just prior to lift-off, as the gecko releases the frictional-adhesion gripping forces (cf. Fig. 9.7d). (b) Typical repetition (snake-like) motion of geckos, where diagonally opposite feet are in frictional-adhesion gripping contact at any one time while the other two feet are detached and moving forward. Thus both the (diagonally opposite) feet and toes (on any single foot) can grip in a coordinated way to maximize or optimize the frictional-adhesion depending on the surfaces and conditions.

Thus, as was illustrated in Fig. 9.7d, Figs 9.9 and 9.10 show that the strong adhesion is actually produced by a weak (non-specific van der Waals force only) adhesion interaction between the foot pads (β-keratin protein) and the surface, which translates into a high (lateral) friction force which in turn – when resolved in the normal direction – results in an effectively high 'frictional-adhesion force' (in addition to the large actual friction force). In other words, the gripping forces are large in all directions, and independent of the angle of the surfaces. The gecko simply needs to relax the lateral grip, either by peeling or simply by relaxing the tension on the toes, to reduce both the adhesion and friction forces (on both walls and ceilings) to zero. *The development of anisotropic fibrillar synthetic adhesives and understanding of fiber articulation in these adhesives can thus serve as an inspiration for the*

design and testing of suitable foot-pad placement (gripping and releasing) strategies for robotic applications.

9.3 References

1. Danner EW, Kan Y, Hammer MU, Israelachvili JN, & Waite JH (2012) Adhesion of mussel foot protein mefp-5 to mica: an underwater superglue. *Biochemistry* 51(33):6511-6518.
2. Wei W, Yu J, Broomell C, Israelachvili JN, & Waite JH (2012) Hydrophobic enhancement of dopa-mediated adhesion in a mussel foot protein. *Journal of the American Chemical Society* 135(1):377-383.
3. Zhong C, *et al.* (2014) Strong underwater adhesives made by self-assembling multi-protein nanofibres. *Nature nanotechnology*.
4. Murphy MP, Kute C, Mengüç Y, & Sitti M (2011) Waalbot II: adhesion recovery and improved performance of a climbing robot using fibrillar adhesives. *The International Journal of Robotics Research* 30(1):118-133.
5. Tsukagoshi H, Chiba H, & Kitagawa A (2009) Gel-type sticky mobile inspector to traverse on the rugged wall and ceiling. *Robotics and Automation, 2009. ICRA'09. IEEE International Conference on*, (IEEE), pp 1591-1592.
6. Israelachvili JN (2011) Intermolecular and Surface Forces, 3rd Edition. *Intermolecular and Surface Forces, 3rd Edition*:1-674.